7-2-2011

High redshift QSOs and cool dwarfs in the Deep Lens Survey

Paul Thorman

Paul Thorman
Candidate

Physics and Astronomy
Department

This dissertation is approved, and it is acceptable in quality and form for publication:

Approved by the Dissertation Committee:

David Coombs, Chairperson

John T. McGraw

Jeremy Mould

Rhian Jones

HIGH REDSHIFT QSOS AND COOL DWARFS IN THE DEEP LENS SURVEY

BY

PAUL THORMAN

B.S., Physics, University of Cincinnati, 1998
M.S., Physics, University of Cincinnati, 2002

DISSERTATION

Submitted in Partial Fulfillment of the
Requirements for the Degree of

Doctor of Philosophy
Physics

The University of New Mexico
Albuquerque, New Mexico

June, 2011

ACKNOWLEDGEMENTS

I wish to thank:

my wife, Brianna, for her patience;

my advisor, Dinesh, for his support;

my committee, for their helpful advice;

and the University of New Mexico and the Physics and Astronomy department, for giving me a second chance to succeed in science.

HIGH REDSHIFT QSOS AND COOL DWARFS IN THE DEEP LENS SURVEY

by

Paul Thorman

B.S., Physics, University of Cincinnati, 1998
M.S., Physics, University of Cincinnati, 2002
Ph.D., Physics, University of New Mexico, June 2011

ABSTRACT

The Deep Lens Survey, a 20 deg^2 optical survey, was used to search for two types of rare, very red objects: faint high-redshift (z > 5.4) quasars, which trace structure formation in the early Universe and can be used to study reionization; and ultracool dwarf stars and brown dwarfs, the most numerous constituents of our own Galaxy, which are seldom detected beyond the solar neighborhood due to their low luminosities. To distinguish between these two populations, we added near-infrared imaging to a portion of the Deep Lens Survey area, covering 1.12 deg^2 with survey J-band (1.2 μm) imaging, and successfully targeting 181 out of a planned 280 very red targets over an additional 2.4 deg^2. These observations were reduced and cataloged, producing colors or color limits for 1626 very red objects in the field. The colors were corrected using a combination of outside photometric standards and internal checks, and a model for the colors of the target populations was created from existing measurements in the literature. The relative classification probabilities were estimated for each object by using a color model, and those probabilities were used to generate Monte Carlo realizations of the populations, either for comparison to a simulated Galaxy (for ultracool dwarfs) or for the calculation of a luminosity function (for high-redshift QSOs).

For QSOs, the results were consistent with the most recent work on faint QSOs: we measured a bright-end power-law slope of $\beta = -3.11 \pm 0.8$ for the luminosity function. Citing the similarity to earlier results for brighter QSOs, we rule out QSOs as the dominant source of ionizing photons at the time of reionization (although they may have contributed at the 10-20% level).

For ultracool dwarfs, the model that best reproduced our measured magnitudes was a sech^2 vertical disk profile with $Z_0 = 575^{+465}_{-155}$ for the earliest spectral type range (M9-L2), with hints of a lower scale height for later spectral types. We integrate a range of best-fit models to predict the number of ultracool dwarfs to be found in future surveys, and estimate the errors introduced into current surveys by over-simplified models of the Galaxy.

Spectroscopic observations were obtained for a few of our very red objects; these are displayed and analyzed. Although none of the targeted objects was definitively identified as a QSO, they showed interesting and unusual spectral features nonetheless.

The methods demonstrated here for probabilistic classification of galactic and extragalactic objects will be essential to exploit the full potential of future wide deep surveys, such as LSST. These surveys will reach such faint objects that spectroscopy will be difficult or impossible for many years to come, yet we have shown that the imaging alone, augmented when necessary with follow-up photometry in specific bands, can provide the classifications needed to explore these unknown populations.

Contents

List of Figures

List of Tables

Chapter 1

Introduction

Astronomy, like other observational sciences, has been guided largely by instrumental capabilities throughout its history – new instruments open up new discovery space, whether through increased wavelength range, better sensitivity, or larger area, and allow us to look outward to more distant galaxies, or to the faintest nearby stars and brown dwarfs. While there are a few exceptions (spectroscopy was not initially limited by telescope size or quality, but awaited the discovery of its usefulness, for example), the major discoveries in astronomy have followed from the development of more sensitive and larger photon collection and measuring devices: the development of sensitive film emulsions in the mid-19$^{\rm th}$ century led to astrophotography and photographic spectroscopy; the introduction of photomultiplier tubes in the 1940s led to standardized photometric systems; and since the late 1970s, ever-larger CCD detectors have brought photon counting to survey-sized areas. Looking forward, the most exciting projects planned for the next decade are successors to the spectacularly productive Sloan Digital Sky Survey: yet larger surveys such as LSST and Pan-STARRS, which will use huge CCD arrays to digitize the sky quickly and efficiently.

The research in this dissertation is based on the Deep Lens Survey (DLS), one of the major projects undertaken with the generation of large-format silicon CCDs introduced in the late 1990s (see Chapter 4). Some of the most exciting science in the DLS concerns the very reddest objects, those which are detected in the z'-band (the longest-wavelength filter in the DLS); these objects include the coolest red stars and the highest-redshift galaxies and quasars that the survey can detect. At wavelengths longer than 1 micron, silicon is increasingly transparent, requiring greater detector thicknesses for absorption. This physical limit on the red sensitivity of CCDs can be circumvented by the use of thick chips, but the increased thickness eventually degrades the localization ability of the detector, as electrons generated deep in the silicon are poorly captured by the pixel electrodes, leading to blurred images. This 1 μm silicon limit has shaped the survey capabilities of the Sloan Digital Sky Survey, the DLS, the Canada-France-Hawaii Telescope Legacy Survey, and many others, by

determining the location of the reddest practical band to be included in the main survey. As deep surveys search objects of higher redshift, prominent spectral features pass through various broad photometric bands in turn, but once those features pass redward of 1 micron, they will no longer be captured in the main survey data, and will require additional follow-up imaging to continue tracking their progress to greater cosmological distances.

QSOs and high-redshift galaxies are sources of ionizing radiation, due both to emission from active galactic nuclei and to blackbody emission from young, massive stars. For sources of ionizing radiation, the most obvious spectral feature is the Lyman-α emission line, at 1216 Å in the rest frame. The silicon cutoff allows this emission line to be detected only up to redshift ~ 6.4, which sets the practical limit on the most distant QSOs and Lyman-emitting galaxies which can be detected in a conventional CCD survey. Newer instruments, such as WFC3 on the Hubble Space Telescope, have extended their infrared sensitivity beyond 1 micron, and are now probing redshifts beyond 6.4 by re-examining ultra-deep fields (Bouwens et al., 2009; McLure et al., 2009). Like most projects at the edge of technical capability, surveys of very red objects encounter a unique set of difficulties. Because the 9000 Å long-pass z' filter transmits photons to which the detector is hardly sensitive at all, most surveys choose not to spend the additional integration time to bring z' to the same depth as its bluer counterparts (where the silicon is more sensitive). This was particularly evident in the DLS, where the neighboring bluer filter, the Cousins R-band, was given special attention and integration time, so that it could be used to measure shapes for weak gravitational lensing. As a result, R is more than 3 magnitudes deeper than z' in the DLS. The z' images were also taken during poor weather conditions, to take advantage of the relative insensitivity of the infrared to poor weather; however, the long-pass z' filter encloses a prominent water vapor absorption feature, which can be strongly and non-linearly dependent on the airmass and weather conditions, making photometric calibration very difficult (see Chapter 5). One final challenge

for the z' filter is fringing: the thinned CCDs used for the DLS are approximately 15 microns thick, and light with wavelengths ≈1 micron is quite likely to penetrate the entire depth of the detector, be reflected from the rear surface, and be re-absorbed elsewhere in the chip, leading to interference fringes and a general degradation of the image quality. Nevertheless, the impressive depth of the R-band imaging allows objects as red as $(R - z') \approx 3.5$ to be detected in both R and z' all the way to the detection limit in z'. These two-band detections are more reliable than the one-band z'-only detections used in $i' - z'$ dropout searches for high-redshift QSOs, which are frequently merely variable or moving objects. Two-band detections also ensure that every object has not only a magnitude, but also at least one measured color $(R - z')$ in the catalog, which will be used to improve sample completeness and provide background rejection.

This dissertation concerns the reddest point sources, $(R - z') > 2$, which fall into two categories: unresolved QSOs (Chapter 2) where the Lyman-α break has been redshifted into the z'-band (corresponding roughly to $5.4 < z < 6.4$), and ultracool stars and brown dwarfs in our own galaxy (Chapter 3). These objects have nothing in common astrophysically — even the source of their red colors is different. For brown dwarfs, the red color is a result of $T < 2200K$ blackbody emission, further reddened by molecular absorption; for the high-redshift QSOs, the color comes from Lyman-α emission, with Gunn-Peterson absorption enhancing the contrast on the blueward side. But because both types of objects are unresolved red $(R-z')$ sources in the DLS main imaging, there is nothing to distinguish them without additional wavelength data. The most obvious candidate, radio emission (the original discovery method for QSOs!) is inconclusive in this case, as the rate of radio-loudness among high-z QSOs is ≤10% (Jiang et al., 2007). Instead, we can take advantage of the differing sources of the continuum radiation to distinguish our two populations: the ultracool dwarfs should show strong emission into the near-IR, rising to a thermal peak between 1.3 μm and 3.4 μm, tempered only by increasing infrared absorption from water

vapor, methane, and eventually ammonia. By contrast, the non-thermal emission from the central engine of a QSO falls off with increasing wavelength beyond Lyman-α, although this continuum is overlaid with emission features which can introduce substantial color scatter. Because this color difference between QSOs and cool dwarfs appears only redward of Lyman-α, we will require data from outside the DLS, using detectors with greater infrared sensitivity than silicon CCDs can provide.

At the same time that $40' \times 40'$ CCD array detectors were being constructed, a new generation of near-infrared detectors, based on HgCd or HgCdTe discharge capacitors, was being deployed. These detectors are sensitive to radiation throughout the near-infrared (NIR) atmospheric "windows", the wavelength ranges between the copious H_2O, CO_2, and CH_4 absorption bands that make ground-based observations difficult. While measurements in any of these bands, J, H, or K, could likely distinguish between QSOs and ultracool dwarfs, observational constraints argue for the J-band as the most efficient additional observation to be made. The night sky shines brightly at NIR wavelengths, and longer wavelengths have more thermal emission. In order to maintain dynamic range, a detector observing the 2.2 μm K-band must be read out every few seconds, while the 1.2 μm J-band can be integrated for 60 s or more, depending on the season. Observations with J-band have much lower readout overhead as a result, and reduced sky emission also allows deeper imaging in the same exposure time, even excluding overhead. In light of these advantages, J-band was chosen as the most efficient way to extend the DLS. This imaging was carried out over two separate observing runs, with similar instruments (WIRC and FLAMINGOS) on the Palomar 5 m and Kitt Peak 4 m telescopes. The Palomar imaging was "survey mode," in that the observations were meant to cover a uniform area of the DLS, with no specific targets; the FLAMINGOS run was targeted specifically at $(R - z') > 2$ objects from the DLS early stacks[1]. The results from the J imaging were used to select candidate $z \approx 7$ QSOs for J and K follow-up at Keck, and to find

[1]DLS final stacks and catalogs were not available for the chosen field, F1, at the time of the original proposal; however, the field was conveniently situated for fall observing in the North.

targets for queue spectroscopy using the Hobby Eberly Telescope (see Chapter 10).

In addition to their use as a targeting survey, the $Rz'J$ colors from this study can be used to characterize the populations of ultracool dwarfs and QSOs in a probabilistic fashion, assigning most likely spectral types according to models, and comparing to theoretical predictions (see Chapter 8 and Chapter 9).

The QSO analysis focuses on retrieving the high-redshift luminosity function, a measure of the relative prevalence of QSOs of different brightnesses. These QSOs are some of the most distant observable structures in the Universe, and their luminosities are dependent on the manner and efficiency of their formation, giving us information about the underlying mass distribution at even higher redshifts. QSOs are also a major contributor to the ionizing flux budget of the Universe, although they are not currently believed to have been the dominant source at the time of reionization (Willott et al., 2007). While wide-area, shallow surveys have discovered the rarest, extremely bright high-z QSOs ($M_{1450} < -26$), smaller, deep surveys like the DLS can detect the fainter QSOs that will show how the luminosity function is evolving with time. The QSO luminosity function typically follows a broken power law, with one power law for QSOs brighter than the "break luminosity", L^*, and a second power law for faint QSOs. It has been suggested (Hopkins et al., 2006) that the explanation for the QSO luminosity function lies in the duty cycle of QSOs, the time between the start of active feeding and the time when feedback from ionization and radiation pressure returns the QSO to a quiescent state; their surmise was that L^* represents the brightness of the median actively feeding QSO, which is an essential tracer of the growth of supermassive black holes over cosmic time. These fainter, more numerous QSOs are the dominant emitters of ionizing flux at lower redshift, so finding their counterparts at high redshift is very important to understanding reionization.

The analysis of brown dwarf candidates aims to determine their distribution in the Galaxy. While the all-sky NIR imaging of 2MASS has revealed the population of brown dwarfs in the 20 pc solar neighborhood (Cruz et al., 2007), only a few

studies have attempted to characterize field brown dwarfs at any significant distance from the Sun (Ryan et al., 2005; Pirzkal et al., 2005). As the lowest-mass debris of star formation, newborn brown dwarfs are a matter of interest for modeling of gas fragmentation and star clusters; however, a proper determination of the mass function for cluster brown dwarfs is dependent on proper modeling and rejection of foreground disk brown dwarfs (Caballero et al., 2008). The extra depth and very red ($R - z'$) sensitivity of the DLS allow us to select brown dwarfs at distances of hundreds of parsecs, giving us a chance to observe their characteristic fall-off with vertical distance (away from the Galactic midplane) in a way that shallower surveys cannot. A proper measurement of this vertical scale height can be used to model foregrounds for cluster surveys, estimate brown dwarf backgrounds for color-selected high-redshift surveys, and determine the total mass contribution of this largely invisible population.

These techniques are now being extended to the entire area of the Deep Lens Survey, which will make it one of the largest deep optical and NIR data sets currently available.

Chapter 2

Quasars: History and Theory

2.1 Discovery

Quasi-stellar radio sources, or quasars, were first noted in the Third Cambridge (3C) catalog of radio sources in the late 1950s. The name derived from the faint, unresolved optical counterparts of these radio sources, originally designated "radio stars" (Matthews and Sandage, 1963) until optical spectra showed that they had extremely large redshifts (e.g. $z = 0.158$ for 3C273; Schmidt, 1963) as well as very unusual optical and UV colors. Continuing photometric surveys using the $(U - B)$, $(B - V)$ colors of the first four quasars uncovered a population of radio-quiet high-redshift point sources ("quasi-stellar galaxies" or QSGs), with substantially greater volume density than the radio-loud quasars (Sandage, 1965). The term "quasi-stellar object" (QSO) was eventually adopted to describe the entire population of radio-loud and radio-quiet objects. Sandage originally estimated that radio-loud QSOs made up 0.2% of the total population; the current estimate of the rate of radio-loudness is between 10% and 20%, and the fraction of radio-loud QSOs increases for lower redshifts and brighter QSOs (Jiang et al., 2007). Because nearly all QSOs have at least some radio emission, an arbitrary cutoff of $R > 10$ has been used to define "radio-loud", where R is the ratio of flux at 6 cm to that at 2500 Å (both corrected to the object's rest frame).

Using the Hubble Law to convert redshifts to distances implied extremely large luminosities for these QSOs (100 times greater than the radio galaxies of the day), which led some scientists to search for an alternative to cosmological redshifts (e.g. gravitational redshift, sources falling into local galaxies; Arp, 1966), but these ideas were ruled out when absorption lines in host galaxies were detected (Stockton et al., 1979) with identical redshifts to their quasars. The direct imaging of host galaxies (Wyckoff et al., 1980; Tyson et al., 1982) confirmed that QSOs were simply a variety of active galaxy, brighter and more distant than the usual Seyfert galaxies (Seyfert, 1943), and with a larger fraction of their light generated by the nucleus (which

(a) M77, a Seyfert galaxy. Courtesy HST Archive.

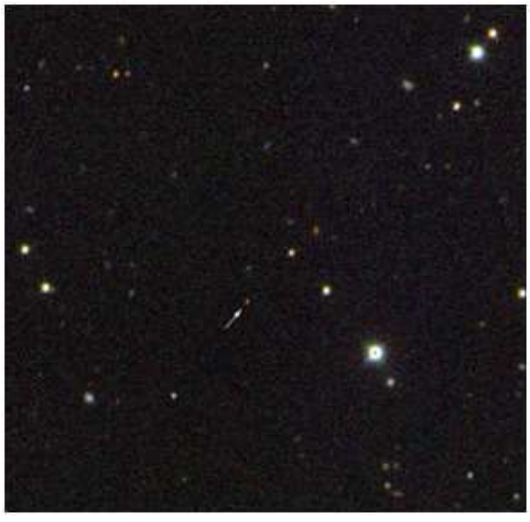

(b) SDSSJ0326-0033, a redshift 5 QSO discovered in 1998. Courtesy SDSS.

Figure 2.1: Nearby and distant active galaxies.

led to the initial non-detection of the host galaxies.) QSOs have been detected with redshifts as high as 6.43 (Willott et al., 2007), and at the low-redshift extreme ($z < 0.06$), they transition smoothly into active galaxies (e.g. The Cologne Nearby Quasar Sample.) The term QSO is generally reserved for active galaxies where the nucleus is the predominant radiation source.

2.2 Spectral Features

The redshifts of QSOs were originally determined from hydrogen emission lines, which are prominent in the typical QSO spectrum (Figure 2.2). Metal emission lines, including strong C and O lines, are also observed up to very high redshifts. These lines are overlaid on a power-law continuum, which is typical of non-thermal emission. Vanden Berk et al. (2001) found a power-law index of $\alpha \simeq -0.5$, which can be used to estimate continuum fluxes, in the absence of emission lines. QSOs, like Seyfert galaxies, are divided into Type I and Type II based on the presence of both

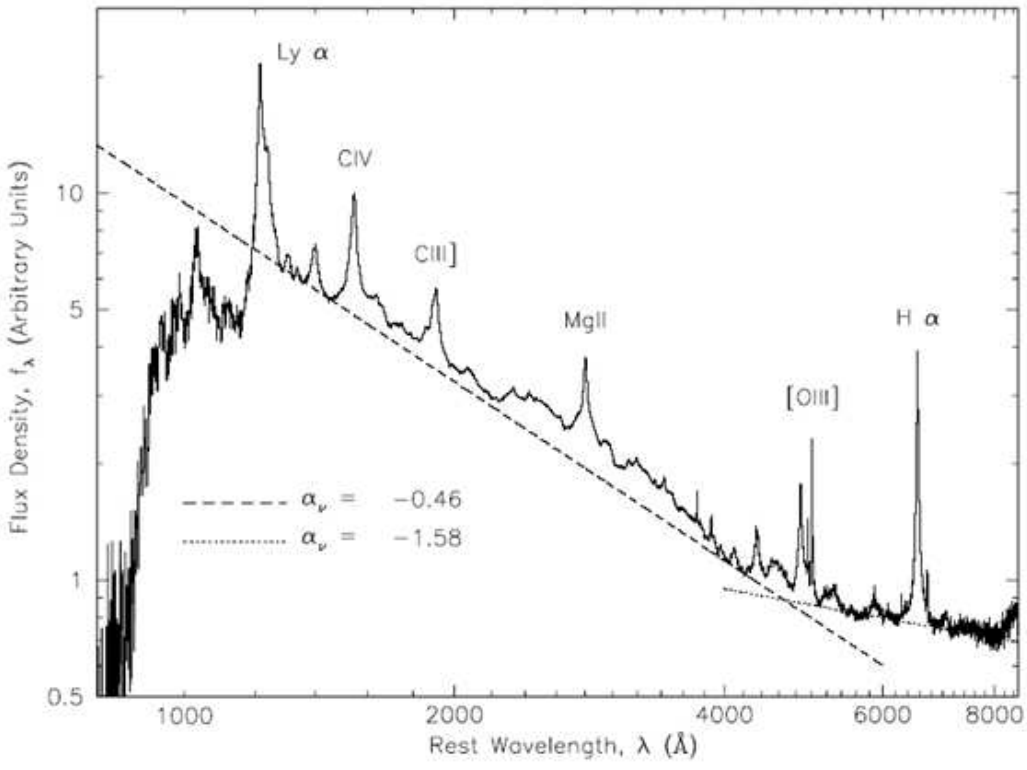

Figure 2.2: Composite QSO spectrum based on the median of over 2200 QSOs from the SDSS. From Vanden Berk et al. (2001).

broad and narrow emission lines (Type I) or only narrow lines (Type II). According to the current standard model of active galactic nuclei (AGN), the broadening of the emission lines is due to extremely high rotational velocity ($> 10,000$ km s^{-1}) in the inner parts of the accretion disk around a supermassive black hole, while the narrow emission lines come from slower-moving (500 km s^{-1}) outer parts of the nucleus. Under this model, the central region of a Type II nucleus is obscured by dust, possibly due to our line of sight passing through a dusty torus (although the mechanism for maintaining obscuration over significant time-scales is not fully understood.) Like most extinction effects, this obscuration is most significant in the rest-frame UV and blue optical, where the QSO's distinctive Lyman-α emission line is located; as a result, optically-selected QSO samples (e.g. Fan et al., 2004) appear

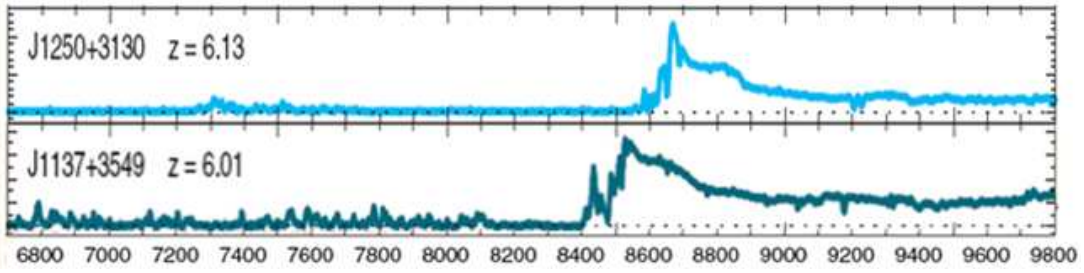

Figure 2.3: Two spectra from typical high-redshift QSOs, clearly showing the Gunn-Peterson absorption blueward of the Lyman-alpha emission line. Adapted from Fan et al. (2006).

to be biased toward unobscured Type I QSOs, while samples selected based on rest-frame infrared emission (Siana et al., 2008) are more uniform (although limited in redshift range by the smaller intrinsic QSO luminosity at NIR wavelengths.)

The spectra of QSOs typically show absorption features due to neutral hydrogen along the line of sight. These absorbers are characterized according to their densities: cold, low-density clouds ($N_{\rm HI} < 10^{17}{\rm cm}^{-2}$) make up the "Lyman-$\alpha$ forest" of narrow line absorption, while moderate-density systems ($10^{17}{\rm cm}^{-2} < N_{\rm HI} < 10^{20}{\rm cm}^{-2}$) begin to show a strong break at the 912 Å Lyman limit (in the rest-frame of the cloud), and the densest systems ($N_{\rm HI} > 10^{20}{\rm cm}^{-2}$) show absorption profiles widened by damping. Of particular interest is the behavior of this phenomenon at the highest redshifts: all QSOs above redshift 6 show a complete absorption trough on the blue side of the broad Lyman-α emission line, giving it an asymmetrical shape (Figure 2.3). This has been interpreted as a signature that the Universe at that time had a larger fraction of neutral hydrogen than we see today (Gunn and Peterson, 1965), although even a tiny fraction of HI ($\sim 10^{-4}$) is sufficient to produce a complete Gunn-Peterson effect. Displaying this change in the intergalactic medium over cosmic time is just one of the ways that QSO observations have contributed to the field of cosmology. Galaxies along the line of sight to QSOs can also produce absorption line systems such as MgII (e.g. Churchill et al., 1999) which have demonstrated the presence of cold gas

at distances several times the light-radii of the galaxies, but with such low levels of correlation to other observed galaxy properties that no one galactic process has been implicated in their creation. Although bright QSOs are easier to use for these absorption studies, both the bright QSOs and the coincidental alignments are rare, relative to the commoner faint QSOs; providing additional lines of sight is one way in which the search for fainter QSOs can expand the possibilities of QSO science.

The presence of QSOs at these high redshifts also links them to the reionization of the Universe, when the neutral hydrogen atoms that were formed at the time of recombination were converted to HII, and the intergalactic medium (IGM) became transparent at optical wavelengths. Some sort of reionization had been predicted due to the non-detection of HI radio emission from the IGM (Kaufman, 1965) and the absence of the Gunn-Peterson trough in $z = 2$ QSOs (Ginzburg and Ozernoi, 1966; Weymann, 1967). The effects of sources of ionizing radiation were at first dismissed, but later calculations (Couchman, 1985) predicted that ionizing radiation could have a significant reheating effect on the IGM, creating spheres of HII that would grow and overlap. The necessary reionization budget (2.5×10^{51} ionizing photons s^{-1} Mpc^{-3}) and the contribution of a population of QSOs were calculated by Madau et al. (1999), and found to be strongly dependent on the parameters of the high-z QSO luminosity function.

2.3 Luminosity function

The spatial density of QSOs of a given intrinsic optical luminosity is parametrized by the QSO optical luminosity function. This density distribution has not remained constant throughout the history of the Universe, but has fluctuated as the QSOs themselves have evolved: near the peak of QSO density, around redshift 2-3, there are now enough known QSOs to discern a double power law distribution (e.g. Boyle et al., 1988; Pei, 1995; Boyle et al., 2000; Croom et al., 2004; Richards et al., 2006).

This double-power law is described by two indices, α and β, plus a break luminosity, L^*, that is allowed to vary with redshift:

$$\phi(L,z) = \frac{\phi(L^*)/L^*}{\left(\frac{L}{L^*}\right)^{-\alpha} + \left(\frac{L}{L^*}\right)^{-\beta}} \tag{2.1}$$

$$\phi(M,z) = \frac{\phi(M^*)}{10^{0.4(-\alpha+1)(M-M^*)} + 10^{0.4(-\beta+1)(M-M^*)}} \tag{2.2}$$

The power-law fits in equations 2.1 and 2.2 are stated in terms of $\phi(L,z)$ or $\phi(M,z)$, the instantaneous luminosity function, defined as the number of QSOs per comoving Mpc^3 per redshift per magnitude (or luminosity); but the luminosity function is sometimes characterized by $\Psi(M,z)$, the cumulative luminosity function, which has been integrated over magnitude to give the total number of QSOs above some detection limit, M, at a given redshift, z. For both the high-z QSO sample from SDSS (Fan et al., 2004) and the larger analysis of photometric quasars in SDSS DR3 (Richards et al., 2006), the number of QSOs observed that were fainter than L^* was considered too small to properly fit a double power-law, so only the bright-end index, β, was determined. This was then combined with an assumed faint-end power-law slope ($\alpha = -1.58$) to determine the contribution of QSOs to reionization (Figure 2.4).

Before this luminosity function can be properly observed, observational biases must be removed. Most samples of QSOs are limited not by redshift or intrinsic luminosity, but by observed flux, which biases them toward faint, nearby sources, while neglecting all but the brightest distant sources (classic Malmquist bias). Such an uncorrected sample would indicate, for example, that the spatial density of QSOs fell off dramatically with distance, while the average intrinsic luminosity increased with distance. A method for correcting this was introduced by Schmidt (1968), and is referred to as the $1/V_a$ estimator. The idea is simple and elegant: calculate the enclosed comoving volume from the observer out to the redshift at which an object was observed (call this V), and compare it to the enclosed comoving volume out to the maximum redshift at which an object of that luminosity could have been observed by your survey (the available volume, V_a). The ratio should be an unbiased measure

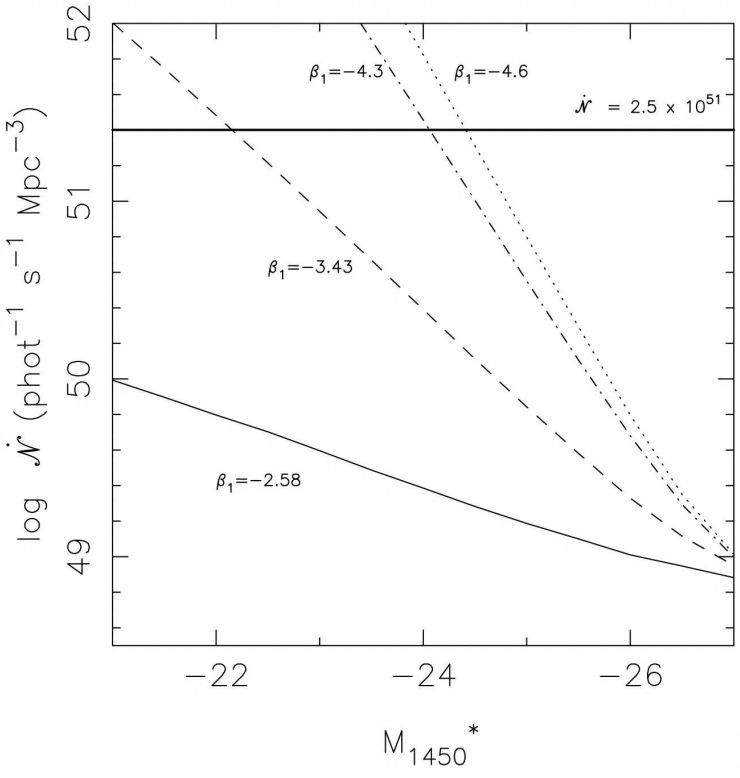

Figure 2.4: The ionizing flux provided by QSOs at $z = 6$, for various values of the bright-end index β; the line at 2.5×10^{51} photons s^{-1} Mpc^{-3} indicates the required flux to accomplish reionization. A faint-end slope of $\alpha = -1.58$ is assumed for QSOs fainter than the stated M^*. From Fan et al. (2001a).

of the distribution of QSOs, as an unchanging density distribution will have a mean value $\left\langle \frac{V}{V_a} \right\rangle = \frac{1}{2}$. Schmidt immediately used this measure to determine that the density of QSOs was increasing out to redshift 1. The method was later extended to provide not only the density as a function of redshift, but a true luminosity function, by which we mean

$$\phi(L, z) \equiv \frac{\partial^2 N}{\partial V \partial L}(L, z), \tag{2.3}$$

where the luminosity function ϕ gives the number density of QSOs, N, as a function of luminosity, L, and redshift, z. If the luminosity bins are small, we can approximate

this by

$$\phi \simeq \frac{1}{\Delta L} \sum_{i=1}^{N} \frac{1}{V_a(i)}, \tag{2.4}$$

where the index, i, runs over the number of detected QSOs, N. The work of Page and Carrera (2000) refined the concept further, taking into account that the faintest bins in the survey (as well as the brightest) would be very poorly handled by the $1/V_a$ estimator, as the actual flux limit was unlikely to trace a boundary of constant L or V, but rather one of constant measured magnitude, causing these bins to appear artificially empty of objects (when in fact they were merely incompletely searched). This problem is exacerbated in calculations using multiple surveys, as it causes problems in any bin containing either the brightest or the faintest objects in any of the surveys. They suggested replacing this estimate with

$$\phi \simeq \frac{N}{\int_{L_{min}}^{L_{max}} \int_{z_{min}(L)}^{z_{max}(L)} \frac{\mathrm{d}V}{\mathrm{d}z} \mathrm{d}z \; \mathrm{d}L}, \tag{2.5}$$

where the integral is over the L and z limits of a given bin, N is the number of QSOs in the bin, and $\frac{\mathrm{d}V}{\mathrm{d}z}$ is the volume element with redshift, which can be easily computed given a particular choice of cosmological model. However, this expression will retain residual errors from the change in detection likelihood within each luminosity or redshift bin, as described in Butkevich et al. (2005).

Due to advances in computing and automated source categorization, newer QSO surveys have added a further refinement to this estimator. For example, the Sloan Digital Sky Survey now has 1,000,000 photometrically-identified QSOs, of which about 100,000 have confirmatory spectra. Using this spectroscopically-confirmed subset (as well as objects with matching radio detections) as a fiduciary sample, the SDSS team has simulated an entire population of QSOs, and processed the simulated data using the SDSS automated selection pipeline to determine their selection efficiency empirically, both as a function of redshift and as a function of intrinsic luminosity (Richards et al., 2006). This detailed completeness measurement allows them to use bins of width 0.05 in redshift space, and luminosity bins only 0.1 mag-

nitudes wide, which minimize the bias due to changes in detection efficiency within a bin. (A similar completeness simulation has been undertaken for our work; see section 8.3.)

2.4 Estimating our QSO density

At very high redshifts ($z > 5.7$) the luminosity function has been based on only a few dozen QSOs, mostly found as i'-dropouts in the SDSS (Fan et al., 2004). To estimate how much the Deep Lens Survey (DLS) can contribute to knowledge of the luminosity function, we must estimate the number of QSOs to be found in the survey. Leaving the intricacies of the observations aside until Chapter 4, the pertinent properties of the DLS data are these: the search area, referred to as Field 1 or F1, consists of 4 sq. deg. of z' imaging to a planned 5σ point source depth of 23.5–24.5 magnitudes (AB). This compares to an initial SDSS search area of around 4500 sq. deg. to a z' depth of 20.5 magnitudes (AB). A second 4 sq. deg. field, F2, has observations from the Spitzer Space Telescope's IRAC instrument, which can be combined with the DLS z' and other imaging for a mid-infrared QSO search. Although this section shows that we can hope to find only similar numbers of QSOs to the SDSS search, DLS is sensitive to much fainter QSOs, which allows the luminosity function to be extended toward the faint end, possibly even locating the break luminosity, L^*.

In order to predict the numbers of QSOs we might find, we must estimate their density at our target redshift. Earlier studies have used an exponential decline to model the total number of QSOs as a function of redshift, which contributes to the normalization parameter Ψ^*: their best-fit function for $\Psi(M, z)$ predicts that QSO density falls off as $10^{-0.5z}$ with increasing redshift (Fan, Strauss, et al. 2001). Combining this with their cumulative QSO luminosity function gives

$$\Psi(M_{1450}, z) = \Psi^* 10^{-0.5(z-6.07)} 10^{-0.4[M_{1450}+26](\beta+1)}, \tag{2.6}$$

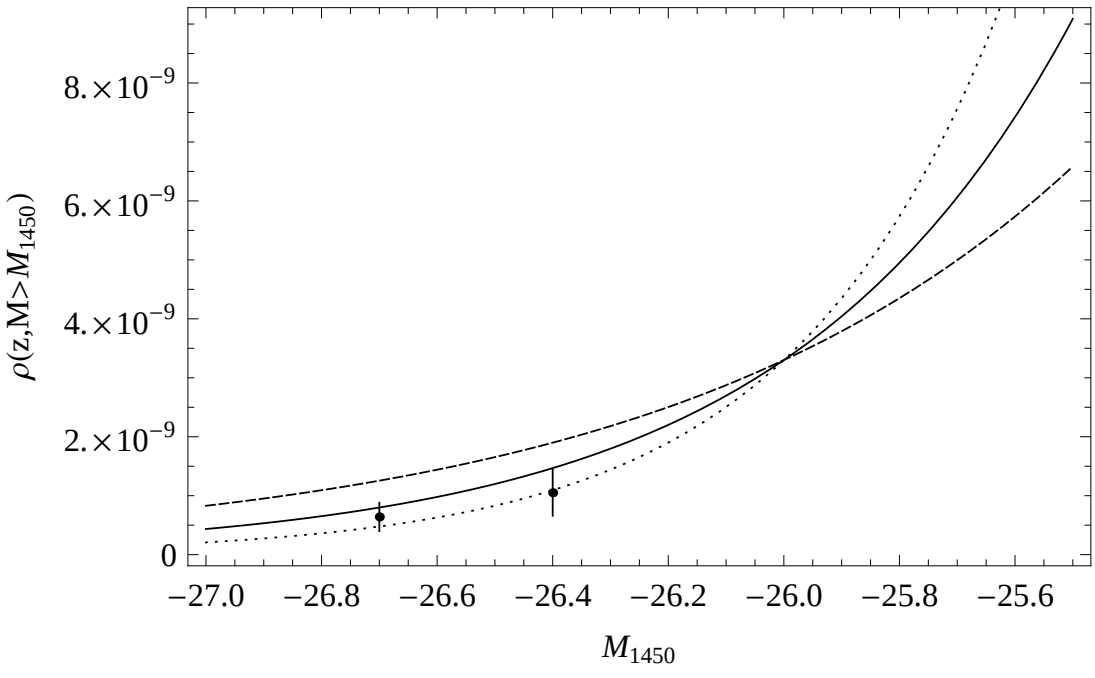

Figure 2.5: A plot of the cumulative luminosity function at $z \approx 6.07$ from Fan et al. (2004). The solid line is their best-fit value for $\beta = -3.2$, while the dashed and dotted lines show the low and high ends of their 68% confidence limits for $\beta(-2.5, -4.0)$. The points with error bars are two stated values of the cumulative luminosity function from the text of the paper.

where M_{1450} is the magnitude measured at a wavelength of 1450 Å, in the object's rest-frame.

A plot of the cumulative QSO density at high redshift is shown in Figure 2.5, using the best-fit SDSS value for the bright-end power-law index ($\beta = -3.2^{-2.5}_{-4.0}$). To obtain a surface density of high-z QSOs, this luminosity function must be integrated over the detectable range of magnitudes at each redshift to obtain a QSO density per comoving Mpc^3:

$$\rho(z, M < M_{lim}) = \int_{-\inf}^{M_{lim}} \Psi^* 10^{-0.5(z-6.07)} 10^{-0.4[M+26](\beta+1)} dM \qquad (2.7)$$

In this case, M_{lim} (Figure 2.7(d)) must be calculated from the depth of the survey, the distance modulus, and the K-correction (see Figure 2.7(b)) before the integration

Table 2.1: Luminosity function calculations for SDSS.

Completeness contour	Effective z' limit (AB)	QSOs per sq. deg.	QSOs in SDSS imaging
Actual		1.97×10^{-3}	9
5%	20.5	7.17×10^{-3}	32.8
50%	20.0	2.35×10^{-3}	10.8
80%	19.6	1.16×10^{-3}	5.30

can be carried out. Then we can use this ρ to get

$$\text{detected QSOs (whole-sky)} = \int_{5.4}^{6.5} \rho(z, M < M_{lim}) \frac{\mathrm{d}V(z)}{\mathrm{d}z} \mathrm{d}z. \tag{2.8}$$

This can be converted to a surface density of detected quasars per square degree using the number of square degrees in 4π steradians ($\simeq$ 41253 sq. deg.).We can check this procedure by comparing to existing surveys: the SDSS main survey detected 9 QSOs at $5.7 < z < 6.5$ in 4578 sq. deg. of imaging to $z_{AB} = 20.5$ mag. Substituting this limiting value for z produces the detection limit shown by the dotted line in Figure 6; however, the SDSS QSO survey also had detailed completeness limits, which they characterized by the fraction of simulated QSOs recovered in each redshift and luminosity bin. The dotted line in Figure 2.7(d) is an excellent match for the 5% QSO recovery contour in Fan et al. (2003); to investigate the effect of different detection contours, the calculation has been run with the magnitude limits corresponding to the 5%, 50%, and 80% contours, with the results shown in Table 2.1.

In order to duplicate the number of QSOs actually detected, we must assume that the effective depth of the SDSS is $z'_{AB} = 19.85$, an overall reduction of 0.65 magnitudes from the nominal 5σ limit. If we assume a comparable reduction in the depth of the DLS F1 imaging, the DLS limit would be $z'_{AB} = 22.9$. If we take the redshift range to be $5.4 < z < 6.5$, the predicted density of QSOs in DLS F1 would be at least 2.15 per sq. deg., of which 0.94 per sq. deg. would lie above redshift 5.7.

We can also compare this calculation to the results from the AGN & Galaxy

Table 2.2: Luminosity function calculations for AGES.

Limit	Effective z' limit (AB)	QSOs per sq. deg.	QSOs in AGES imaging
Actual		0.4	3
Stated 3σ z' limit / Reddest QSO limit	22.5	0.94	7.1
5σ z' limit	21.95	0.31	2.3
Bluest QSO [3.6] limit	21.4	0.10	0.76

Evolution Survey (AGES; Cool et al., 2006), which used 8.5 sq. deg. of matched $B_W RI$ optical imaging from the NOAO Deep Wide Field Survey (NDWFS), added 7.5 sq. deg. of z' imaging to a 3σ limit of 22.5 (AB), and matched those to 4-band mid-infrared survey imaging from the Spitzer Space Telescopes IRAC Shallow Survey (Eisenhardt et al., 2004). Their spectroscopic follow-up confirmed three QSOs above redshift 5.39, detected in at least four bands: R, z, [3.6μm], and [4.5μm]. However, the ($z-$[3.6]) colors of the observed QSOs vary from 0.21 to 1.66 magnitudes, while the detection limit in the [3.6] band is only 21.2 magnitudes; thus, it is likely to be the limiting band for these detections. If this bluest color is adopted for QSOs, the z' limit is moved to 21.4, while the reddest color would be detected right down to the $z = 22.5$ limit. The luminosity function results are shown in Table 2.2. The number of actual QSO detections (3) is most consistent with an effective depth of z'=22.1 (between the two extremes of QSO colors, and close to the 5σ limit), and all the QSOs are brighter than that limit in practice, but the numbers are too small to make a stronger statement.

The IRAC imaging for DLS F2 should be about 0.16 mag deeper than the IRAC Shallow Survey, based on their relative exposure times, so the magnitude limits can be adjusted accordingly. The calculations for a variety of possible limiting magnitudes are shown in Table 2.3, and a plot of density vs. depth is shown in Figure 2.7.

Table 2.3: Luminosity function calculations for DLS.

Limit	Effective z' limit (AB)	QSOs per sq. deg.	QSOs in DLS field
Maximum 5σ z' limit	24.5	53.8	215
Minimum 5σ z' limit	23.5	7.10	22.7
Reddest QSO [3.6] limit (F2)	23.0	2.57	10.3
Bluest QSO [3.6] limit (F2)	21.6	0.15	0.60

As shown in these calculations, a deep, small-area survey such as DLS can detect numbers of QSOs comparable to a much larger survey like SDSS, provided that the additional depth and the steepness of the QSO luminosity function outweigh the disadvantage of smaller area. The QSOs found by these searches will complement the brighter SDSS QSOs, sampling a completely different part of the luminosity function and allowing the characteristic break luminosity and total ionizing flux to be determined for the entire QSO population.

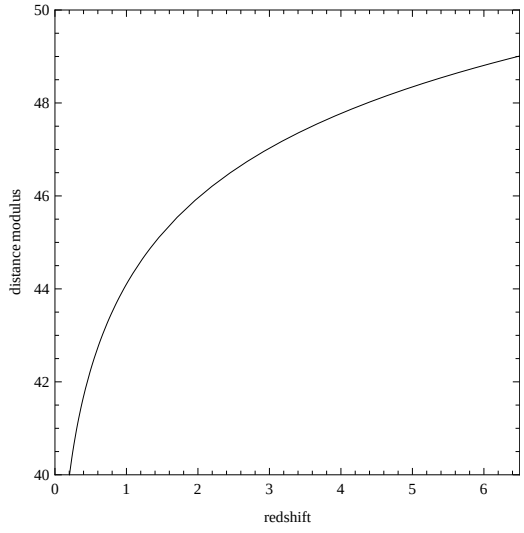

(a) Distance modulus for the adopted cosmology ($\Omega_\Lambda = 0.7$, $\Omega_m = 0.3$, $h = 70$). Calculated using relations from Hogg (1999); Hogg et al. (2002a).

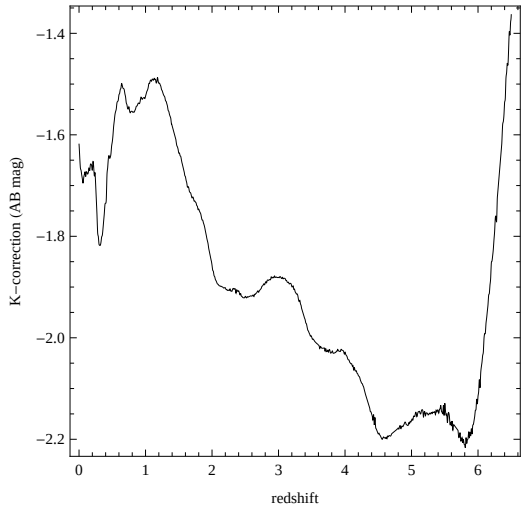

(b) K-correction for the median QSO spectrum of Vanden Berk et al. (2001) (Figure 2.2) with the IGM absorption from Songaila (2004).

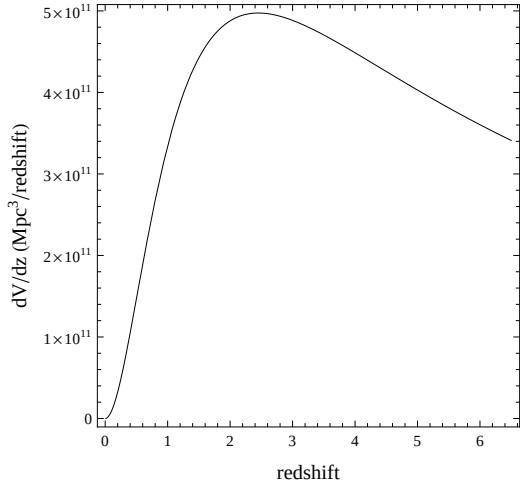

(c) Change in comoving volume as a function of redshift, again assuming the standard cosmology.

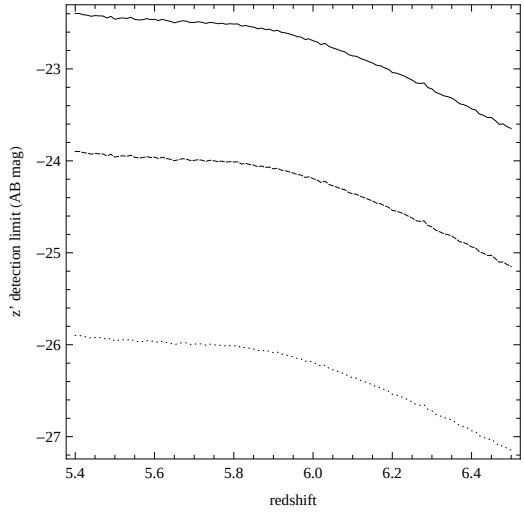

(d) Limiting magnitudes in z', showing the depth in M_{1450} as a function of redshift for the Deep Lens Survey (solid line, assuming z_{AB} to 24), AGES 3σ limit (dashed line), and SDSS (dotted line).

Figure 2.6: Calculated magnitude properties for QSOs.

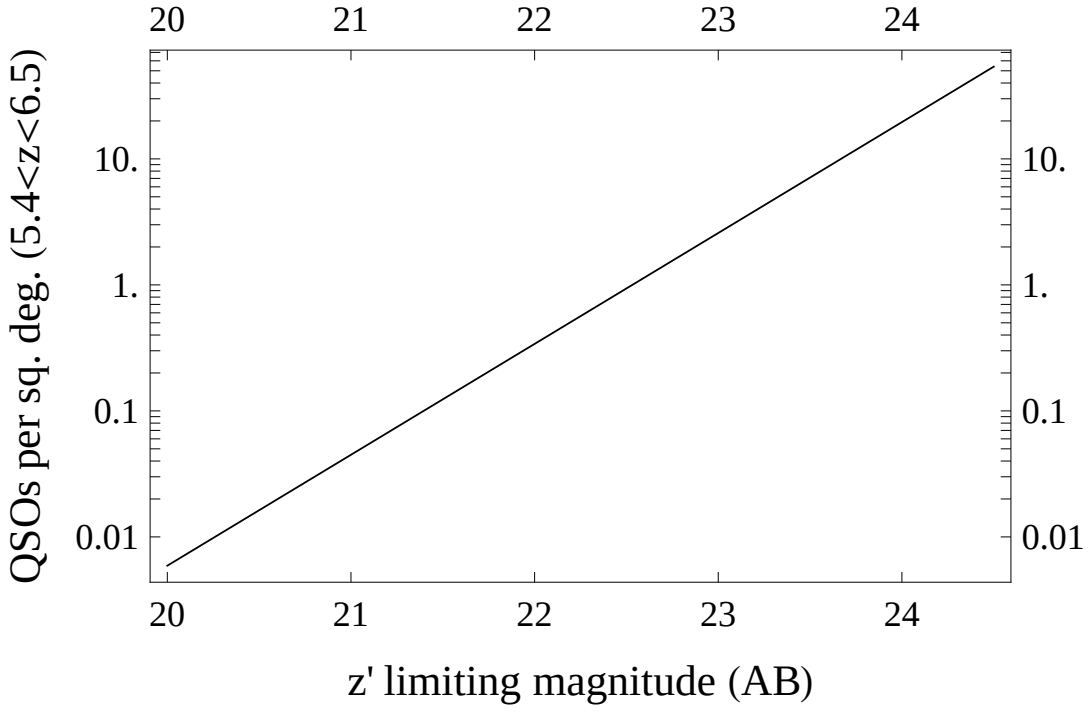

Figure 2.7: QSOs per square degree as a function of z' magnitude, using the best-fit bright-end slope for the luminosity function from Fan et al. (2004).

Chapter 3

Brown Dwarfs: History and Theory

The distinction between giant and dwarf stars has been known since at least Hertzsprung (1910) and Russell (1910), who used newly available photographic parallaxes to determine that stars within a spectral class did not always share the same intrinsic luminosity. Although the understanding of stellar interiors was incomplete at that time, Russell did come to the conclusion that these different luminosity classes represented different stages in stellar evolution (albeit completely different stages from our current understanding), and the idea of the main sequence was solidly established by the time Eddington (1917) correctly predicted the luminosities of the smallest M dwarfs he considered plausible ($0.2M_{\odot}$). The addition of Gamow's (1938) detailed description of nuclear fusion as a stellar energy source made it possible to explain stellar luminosities from basic physics, and also provided a natural low-mass limit for what could qualify as a main sequence star — any body which supports itself against gravity by using energy from fusion to maintain hydrostatic equilibrium. The concept of degenerate stellar-mass objects, supported by the mutual repulsion of their Fermi gas components, was also well established (Chandrasekhar, 1931) as an explanation for white dwarfs, but as there were no known degenerate sub-stellar objects (brown dwarfs) to which to apply these models, there was no immediate push to calculate their properties.

Nevertheless, the properties of brown dwarfs were predicted before they were ever discovered, using numerical simulations of stars of very low masses[1]. The solutions of the polytrope equation (Kumar, 1963) indicated that electron degeneracy would support newborn stars below a certain mass (0.08 $M_{\odot}$, according to early convective calculations; Hayashi and Nakano, 1963), preventing the core temperature and pressure from ever reaching the levels needed for proton-proton fusion. After a few later-disproven candidates (notably VB 10, a dM8 which spent several years as the faintest known object outside the solar system; Liebert et al., 1978; Schweitzer et al., 1996), two very faint red companions to brighter stars were discovered, each with its

[1] An excellent review of the history and current state of cool dwarf science can be found in Reid and Hawley (2005).

own unusual spectral features, and both quite distinct from the M dwarfs: GD 165B and Gl 229B.

The brighter of the two, GD 165B, was discovered by Becklin and Zuckerman (1988), and a spectrum was obtained (Fig. 3.1) which showed the unexpected absence of the TiO absorption bands which define the M dwarf spectral class (Kirkpatrick et al., 1993) and the presence of very pressure-broadened resonance lines of KI and NaI. When later observations indicated the existence of a significant population of such objects, the new spectral class "L" was defined to describe them (Kirkpatrick et al., 1999).

The cooler of the two prototypes was discovered as a proper motion companion to Gl 229 (Nakajima et al., 1995), and was shown to have molecular absorption bands corresponding to methane and water absorption (Oppenheimer et al., 1995), and an even lower effective temperature than GD 165B ($T_{\rm eff} < 1000K$). This object became the prototype for the "T" dwarf spectral class.

At present, no fewer than 752 L and T dwarfs have been confirmed[2], mostly detected by combining large-area CCD imaging from SDSS with large-area near-IR imaging from 2MASS, and searching for point sources with specific non-stellar colors. The resulting sample is believed to be nearly complete, containing every M8–L7 dwarf to 20 pc (Cruz et al., 2007) within the area of SDSS, but is understandably limited by the relatively shallow 2MASS imaging ($J = 15.8$, 10σ point sources). More recently, the UKIDSS Large Area Survey[3] has begun imaging 4000 sq. deg. of the SDSS footprint to $J = 20$, which should make better use of the SDSS z'-band imaging ($z' = 20.5$, 95% repeatability) for detecting L and T dwarfs (even the bluest of which would be expected to have $z'_{AB} - J_{Vega} > 2.4$). Ideally, the optical observations should be deeper than the infrared observations, to ensure that every red object is detected in more than just one band; the DLS observations are excellent

[2]http://www.dwarfarchives.org
[3]http://www.ukidss.org/surveys/surveys.html

for this purpose, as the detection limits in our bands correspond well to the predicted colors of dwarfs, yielding a large number of 3-band-detected brown dwarf candidates (see Chapter 10).

By using the DLS+J imaging to search for fainter brown dwarfs (> 4 magnitudes beyond SDSS+2MASS), we expand our search to two additional populations: intrinsically fainter objects and more distant objects. Although the small search area of the DLS disadvantages it in the search for nearby, intrinsically faint objects, the sample of distant brown dwarfs is essential in constructing a complete model of the Galaxy. The population of L and T dwarfs is only well-known within 20 pc of the Sun, with the remainder of the Galactic distribution very poorly constrained, which leads to large uncertainties in the total number and mass of this most numerous component of the Galaxy. Without direct measurements, we are at risk of "inventing" the Galaxy based solely on our own neighborhood. Dwarfs at larger distances from the Galactic midplane are also likely to be older and more metal-poor — a different population than the local cool dwarfs — and the cooling of brown dwarfs over time allows them to be used as chronometers of star formation throughout the history of the Galaxy (Burgasser, 2004). Only by searching for these distant brown dwarfs can we construct an accurate model of the cool dwarfs of the Galaxy, describing their current spatial distribution, which is related to the initial mass function for the smallest substellar objects and the history of star formation as a whole.

3.1 Model Atmospheres and Cooling

Since brown dwarfs never attain p-p fusion (although they are expected to destroy their primordial deuterium), they must inevitably cool and fade over Gyr timescales. Accordingly, there is no unique mass-luminosity relation for brown dwarfs, as there is for main-sequence stars; the luminosity and temperature of a brown dwarf will decrease as it ages, and it will change to progressively later spectral types as its

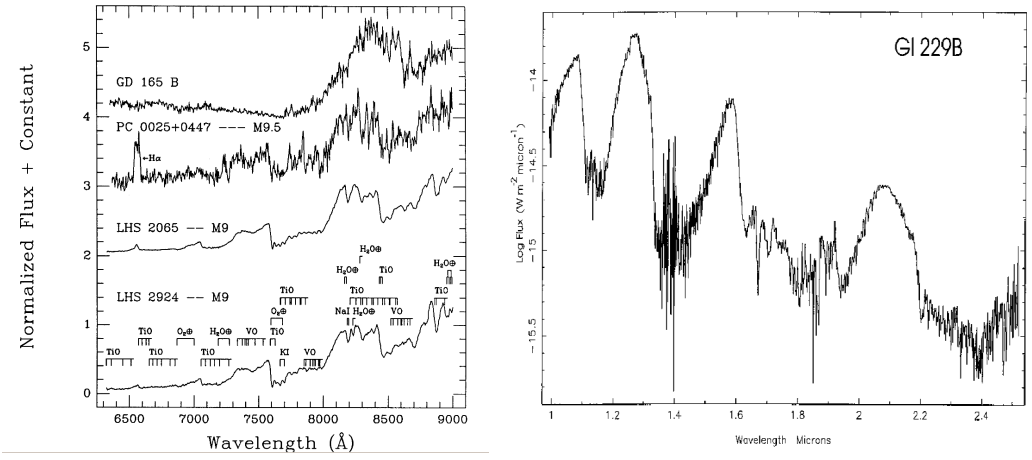

Figure 3.1: Spectra of the prototypical L and T dwarfs, GD 165B (left) and Gl 229B (right). Note the absence of the TiO absorption bands at 7100 Åand 7400 Åin GD 165B, and the 2.2 μm CH_4 absorption and 1.4 μm H_2O absorption in GL 229B. Figures are from Kirkpatrick et al. (1993) and Geballe et al. (1996).

atmosphere cools and molecular species form dust and clouds, and eventually precipitate out entirely. In cool star atmospheres, the hydrogen is bound up into H_2 or metal hydride (CaH, MgH, FeH) molecules, leaving the oxygen (in stars of reasonably high metallicity) in TiO, VO, and H_2O molecules (Allard et al., 1997, and references therein). M3 and later dwarf stars in particular show CaOH absorption (Boeshaar, 1976), which can be used to distinguish them from more distant M giants, one of the few ways in which this background can be reduced. Like most of the molecular species in M dwarfs, the band structure of CaOH has not been reproduced from theory, and is frequently estimated using a band model (assuming nearly complete opacity in a continuous band, e.g. Brett, 1989), which can overestimate the total opacity by neglecting the photons that escape between absorption lines.

In order to model the M-L transition, it is necessary to combine a model of the fully-convective stellar atmosphere with TiO and H_2O opacities with a model of the metal absorption lines, which blanket whole ranges of the optical spectrum. Models originally included line blanketing as a coarsely-gridded "Opacity Distribution

Function" (e.g. Kurucz, 1970), but more recent models have used finer grids and added effects from laboratory TiO measurements and telluric water vapor corrections (Baraffe et al., 2003), allowing them to reproduce the fluxes over a wide range of wavelengths. Despite these improvements, the "cloudy" models of Burrows et al. (2006) predict optical $(r - i)$ colors of L dwarfs which differ from actual spectra by $\approx$1 mag (Fig. 3.2), although the same models reproduce the infrared colors well. The complex, layered structure of cloudy brown dwarf atmospheres makes it difficult to simultaneously model different parts of the spectrum, coming as they do from different layers of the atmosphere, and passing through absorbing layers of different opacities (many of which have never been measured in the laboratory.) Since these measurements come from physically separate regions of the star, their temperatures may vary significantly, making T_{eff} estimates highly model-dependent, in the absence of genuine bolometric measurements. This adds to the uncertainty in the cooling rates of brown dwarfs, as their radiation balance cannot be confidently characterized in the absence of a reliable T_{eff}. Nevertheless, the atmosphere models of Baraffe et al. (2003) have been used to create cooling curves, showing the temperature of a given mass brown dwarf as it cools over time (Fig. 3.3). These cooling curves are an essential part of our expectations for various spectral types, as they determine the time that a given object can be expected to remain detectable before cooling completely; however, the dissimilarity to the actual measured colors of L and T dwarfs, particularly in the optical range that includes our R-band data, makes the current models inappropriate for use in constructing models of brown dwarf colors. Instead, we will use measured spectra of known dwarfs to determine their colors in our filter system (see Chapter 7 for details.)

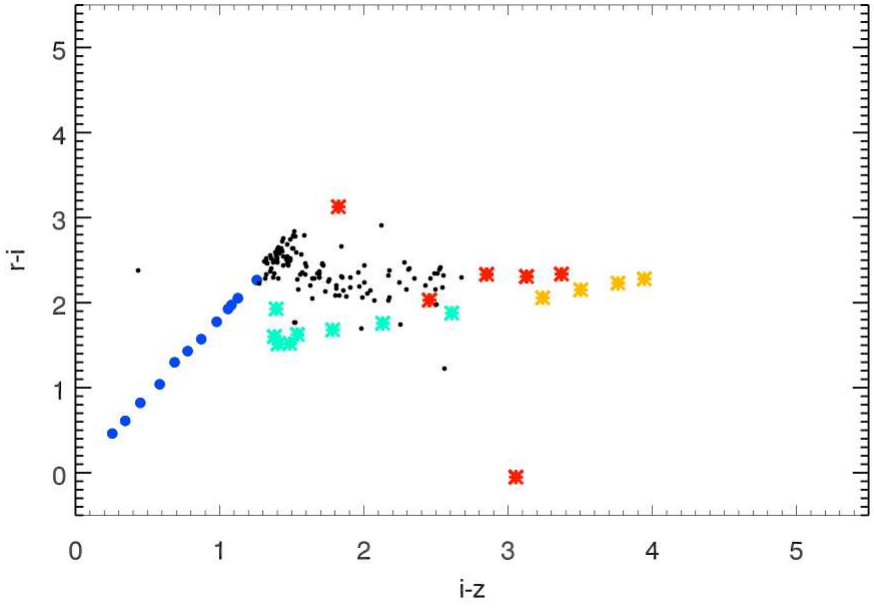

Figure 3.2: Comparison of model $(r-i)$ and $(i-z)$ colors for L dwarfs (cyan asterisks) to synthesized photometry from L dwarf spectra (black points). The model L dwarfs are from Burrows et al. (2006), the spectra are drawn from the brown dwarf library (see Chapter 7 for complete references.) Blue points show measured colors for M dwarfs from Bochanski et al. (2007), while orange and red asterisks are T and Y dwarf models from Burrows et al. (2006) and Burrows et al. (2003), respectively. Plot by K. Covey and the LSST Cool Stars group.

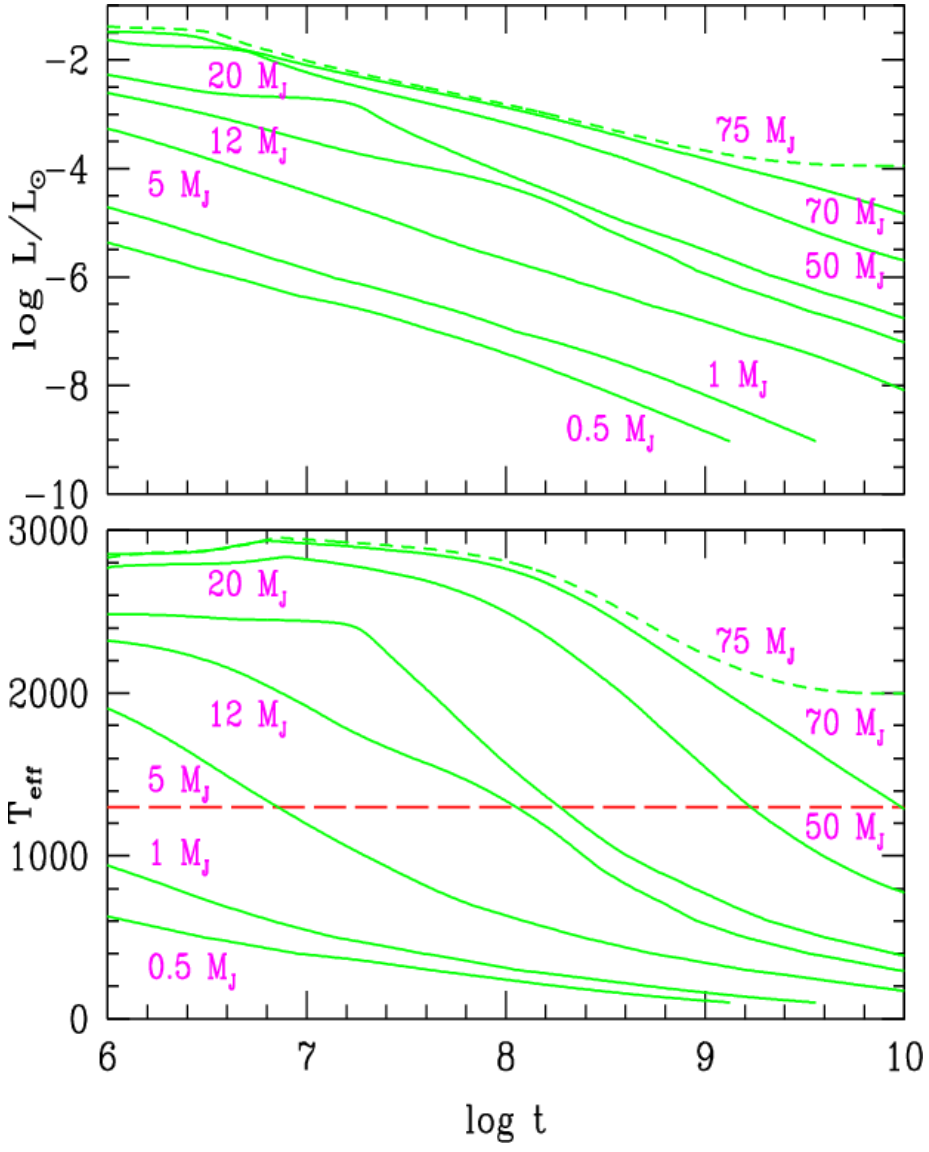

Figure 3.3: Cooling curves for brown dwarfs and exoplanets, showing luminosity and effective temperature as a function of log time (in years.) The upper limit for brown dwarf masses, the mass above which a star's lithium stockpile will be destroyed, is around 75 Jupiter masses (M_J), while the lower limit, below which even deuterium fusion cannot occur, is approximately 12 M_J. Plot from Baraffe et al. (2003). Note that even the most massive brown dwarfs (solid lines) cool below the 1600K L-T transition in ≈4 Gyr, while the lowest-mass brown dwarfs will cool to spectral type T within only 60 Myr. The dashed green line representing the lowest-mass star with sustained fusion eventually stabilizes at T_{eff}=2000K. The dashed red line indicates the limit below which the Baraffe COND models are appropriate (indicating that the dust in in the atmosphere has settled below the photosphere).

3.2 Predicting the Distribution

Based on the cooling curves, we expect to find that the L-type brown dwarfs are relatively young, in galactic terms — certainly younger than the slightly more massive late-M and early-L hydrogen-burning stars, which are expected to date all the way back to the formation of the galaxy. These different populations are found in the highly flattened Galactic disk, where the density of stars decreases rapidly with height above the Galactic midplane. This decrease is characterized by a scale height, defined as the vertical distance required to measure a certain fractional reduction in number density ($\frac{1}{e}$, for exponential models). M dwarfs are found in an old (10 Gyr) stellar disk, with a large scale height (>400 pc; Jurić et al., 2008), as well as in a low-density thick disk, with a scale height of ≈1 kpc (Oort, 1952). The L-type brown dwarf population will be younger, and have had less time to be scattered out of the galactic disk (most likely by interactions with giant molecular clouds, or through ejection of the lowest-mass members of multiple star systems), so a decrease in the scale height would be expected for the population of substellar objects, relative to the stellar scale height — a departure from the overall trend of increasing scale height with decreasing luminosity that is seen throughout the main sequence.

Our sample must be analyzed using a model for the disk of the galaxy. One possible model (de Grijs and Peletier, 1997), based on the infrared light curves of the stellar components of edge-on spiral galaxies, is an azimuthally symmetric ellipsoid with

$$n(r, \theta, z) = n_0 \exp(\frac{r}{R_0})\exp(\frac{z}{Z_S}) \tag{3.1}$$

where n_0 is the density at the galactic midplane, r is the radial distance from the center of the Galaxy, R_0 is the scale radius (≈ 2600 pc; Jurić et al., 2008), z is the distance perpendicular to the plane of the Galaxy, and Z_S is the exponential scale height of the disk.

This profile is quite similar to the one used by Pirzkal et al. (2005) based on Reid

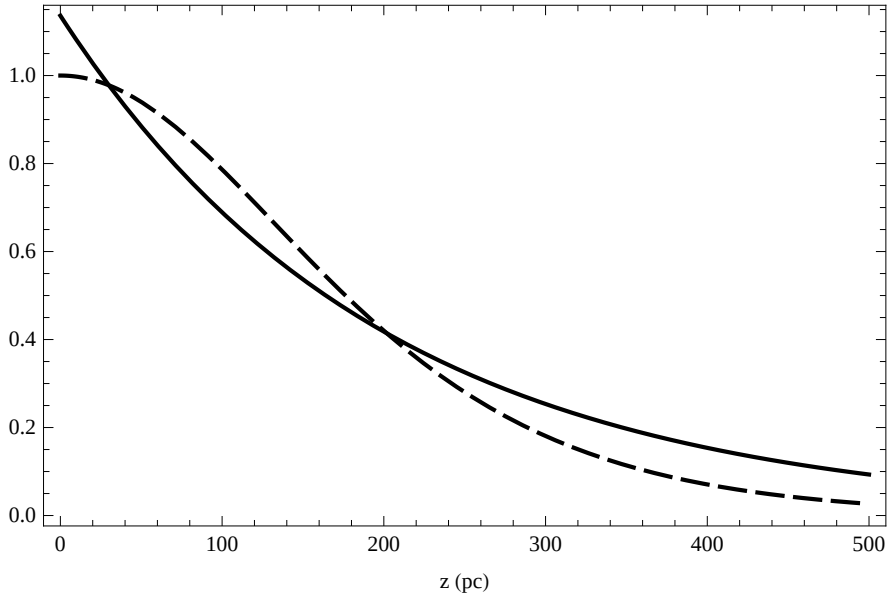

Figure 3.4: Exponential (solid line) and isothermal (dashed line) density profiles for a $Z_S = Z_0 = 200$ pc scale height, normalized to have the same value at the distance of the Sun from the galactic plane (≈ 30 pc).

et al. (2000); they used an isothermal disk for the vertical component of the galaxy, which has

$$n(z) \propto n_0 \ \mathrm{sech}^2 \frac{z}{Z_0} \tag{3.2}$$

where Z_0 is no longer e-folding height of the disk (the height for sech^2 to decrease to $1/e$ of its value at the midplane is not Z_0, but 1.08 Z_0.) This profile is the steady-state solution of the collisionless Boltzmann equation in the case of the isothermal disk, so we will be adopting the sech^2 profile due to its strong physical motivation (and more realistic shape near the midplane, which is important for observations in the southern galactic hemisphere.) As a practical matter, the two profiles are very similar (within $\approx 10\%$; see Fig. 3.4), with the greatest discrepancy near $\frac{Z_0}{2}$.

Given a choice of density profile and a measurement of the local density, we can predict the number of objects of each spectral type which should be detected in the DLS imaging. Following Caballero et al. (2008), we will integrate the number

density in a truncated cone representing our survey area, stretching from the closest heliocentric distance at which an object of that type remains unsaturated in all three survey filters, to the farthest heliocentric distance at which it could be detected in the z' filter. To carry out the volume density integral, we set up a heliocentric coordinate system, denoting the distance from the Sun as d, and using the galactic longitude l and latitude b as our angular coordinates. In this system, our cylindrical galactic coordinates r and z can be expressed as

$$\begin{aligned} r &= \sqrt{R_{\odot}^2 + d^2 \cos^2 b - 2R_{\odot} d \cos b \cos l} \\ z &= d \sin b + z_{\odot}. \end{aligned} \tag{3.3}$$

The thin disk profile from Jurić et al. (2008), based on photometric stellar distances in the SDSS, indicates that the Sun is located 24 ± 5 pc north of the midplane of the Galaxy. We will need to determine n_0, the density at the Galactic midplane, based on $\mathrm{n_{local}}$, the density of L and T dwarfs as determined by surveys of the solar neighborhood. The spatial densities by spectral type in Caballero et al. (2008) are based on Cruz et al. (2003), which used a 20 pc distance-limited sample to determine local late M dwarf densities, while the L and T dwarf densities are based on the mass function normalization from Reid et al. (1999), which used an 8 pc distance-limited sample. To correct these local values to the density at the midplane, it is necessary to integrate the model distribution function over a sphere of the correct radius, centered on the Sun. The density integral over this sphere is analytically difficult, but can be carried out numerically, and the resulting ratio $\frac{n_{\mathrm{local}}}{n_0}$ for the 20 pc sphere is plotted in Figure 3.5.

The local density has been measured by Cruz et al. (2007) for spectral types M8–L7, and has been estimated for early and late T dwarfs by Metchev et al. (2008) (see Table 3.1). This normalization can be combined with our completeness (P(detection $\mid m_z$), the probability of correctly detecting an object, given its

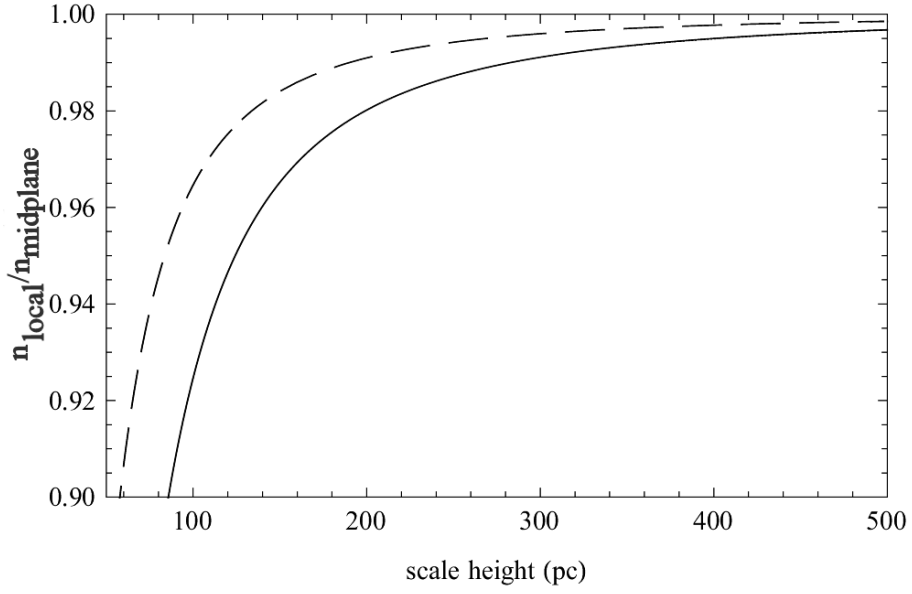

Figure 3.5: The ratio $n_{\rm local}/n_0$, plotted as a function of vertical scale height Z_0 (solid line). The approximation used in Caballero et al. (2008), $n_0 \simeq n_{\rm local} \exp(z_\odot/z_0)$ is also shown (dashed line).

apparent magnitude m_z) and the absolute magnitude of each type of object, then integrated over all distances reached by the DLS to determine the total predicted number of objects of each spectral type, for a given scale height. The scale heights from the literature are 350 ± 50 pc (Ryan et al., 2005) and 400 ± 100 pc (Pirzkal et al., 2005).

Using the methods outlined in Chapter 8, the completeness as a function of apparent magnitude has been combined with the scale height and the absolute magnitude scale from Dahn et al. (2002) and integrated in 1 pc bins to produce normalized probability distribution functions (PDFs) for the detection of an object along our line-of-sight, given a spectral type, distance bin, and scale height (Figure 3.6). In order to match these distributions to the local density of objects, we sum the closest probability bins up to 20 pc, then multiply by the factor needed to reproduce the number of objects of the same spectral type within 20 pc, predicted from the densities above. The simplifying assumption that the average density within 20 pc

Spectral Type	$n_{\rm local}$ (10^{-3} pc^{-3})	Spectral Type	$n_{\rm local}$ (10^{-3} pc^{-3})	Spectral Type	$n_{\rm local}$ (10^{-3} pc^{-3})
M7	2.21	L0	0.352	T0	0.111
M8	1.58	L1	0.475	T1	0.122
M9	0.912	L2	0.552	T2	0.205
		L3	0.460	T3	0.399
		L4	0.452	T4	0.719
		L5	0.480	T5	1.20
		L6	0.433	T6	1.75
		L7	0.355	T7	2.44
		L8	0.255		
		L9	0.170		

Table 3.1: Local space density of spectral types, using model-based densities from Caballero et al. (2008), scaled to the total counts of Cruz et al. (2007) for M and L dwarfs, and Metchev et al. (2008) for T dwarfs.

is the same as the density integrated along our line-of-sight to 20 pc affects the calculation only at the 1% level. This rescaled PDF is then summed over all distances (out to 2500 pc, well beyond our maximum detection distance) to determine the total number of objects to be detected in the DLS imaging, if it were to cover the entire sky. For the final step, we estimate the effective area of the survey: 3.5 DLS subfields completely surveyed over their 8192×8192 pixel central regions, plus 5.5 DLS subfields surveyed to 64% target completeness over their entire area, comes to approximately 2.76 deg^2. Using this effective area, we can predict the total number of detections of each spectral type, shown in Table 3.2.

Scale Height (pc)	M9–L2	L2–L5	L5–L9	T0–T8
350 (Ryan)	70.7	5.77	1.20	0.426
400 (Pirzkal)	80.0	6.25	1.27	0.444

Table 3.2: Predicted number counts for cool dwarfs in DLS F1.

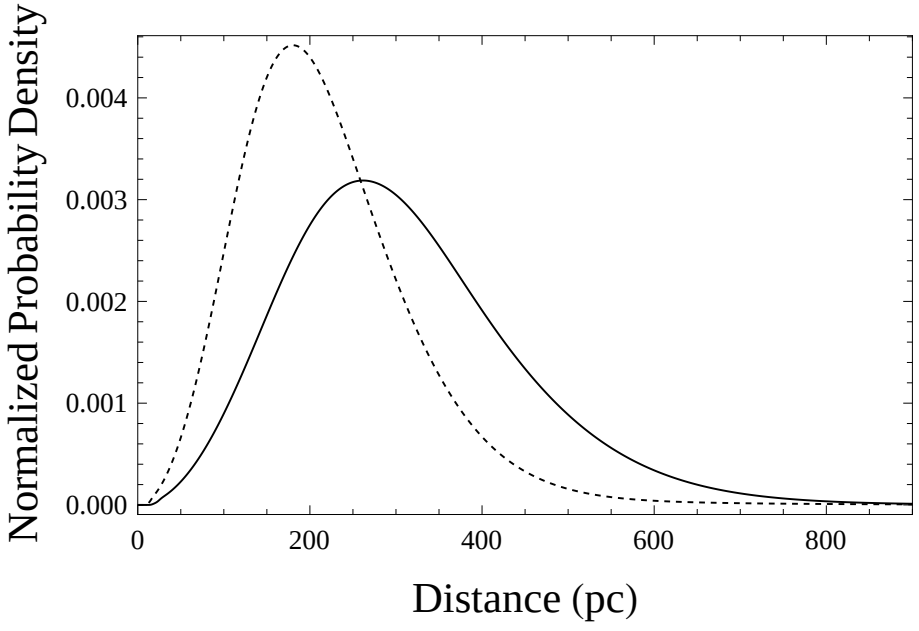

Figure 3.6: Examples of PDFs for object detection in the DLS. The solid curve is the detection probability for an M9–L2 object in a model with a 350 pc scale height, while the dashed curve is for an L2–L5 object in a model with a 400 pc scale height. Note that the brighter objects are likely to be detected out to nearly one scale height, while the fainter L dwarfs are limited by the survey completeness at much shorter distances.

Chapter 4

Observations

4.1 Optical Observations

The Deep Lens Survey was conceived and designed primarily to carry out measurements of weak lensing shear around massive galaxy clusters (Wittman et al., 2006). The original survey proposal asked for time to image seven $2^\circ \times 2^\circ$ fields in four optical and near-infrared bands (B, V, R, and z'); the approved plan included 5 of those 7 original fields (see Table 4.1). These fields were selected to have low galactic extinction and few bright stars, so they are preferentially at high galactic latitude (no field is less than 35° from the galactic plane). However, faint stars are needed as standards for weak lensing, to correct any shape distortion in the images, so the chosen fields also do not lie directly out of the Galactic plane. Fields 1 and 4 (F1 and F4) were chosen to overlap with existing redshift surveys, to help with calibrating the DLS photometric redshifts: the Caltech Faint Galaxy Redshift Survey (Cohen et al., 1999) and the 2dF Galaxy Redshift Survey (Colless et al., 2001). The remaining fields were chosen to be regularly spaced in right ascension, to make possible split-night observations on two fields, while the northern and southern hemisphere fields were chosen to avoid scheduling conflicts. The original campaign was planned for 86 10-hour observing nights (reduced to 81 nights in the absence of F6 and F7.) The observations were made using the NOAO 8K×8K MOSAIC CCD cameras at Kitt Peak's Mayall telescope for F1 and F2, and Cerro Tololo's Blanco telescope for F3, F4, and F5. Each DLS field contained nine subfields (denoted p11 through p33), with comparatively little overlapping imaging between subfields. Twenty dithered exposures of 600 s (900 s in R) were used to create a stacked mosaic, with a median 5σ point source depth of 26.2 in R (Vega-based magnitude, as will be used throughout this research). These exposures were also used to create "sky flats" for the MOSAIC imagers, using diffuse sky glow to determine the relative sensitivity of each detector pixel. The use of imaging runs separated by one month was intended to detect faint transient objects using a real-time transient detection pipeline, but faint transients proved interesting even on a night-to-night basis (Kulkarni and Rau, 2006).

Field Name	R.A.	Decl.	Gal. Longitude	Gal. Latitude
DLS F1	00:53:25.3	+12:33:55	123.6898	-50.3035
DLS F2	09:19:32.4	+30:00:00	196.2496	43.7979
DLS F3	05:20:00.0	-49:00:00	255.5101	-34.8171
DLS F4	10:52:00.0	-05:00:00	256.4834	46.8162
DLS F5	13:59:20.0	-11:03:00	328.5095	48.4209

Table 4.1: Field positions for the Deep Lens Survey.

In order to carry out weak lensing measurements, two kinds of data are needed: deep imaging for shape determination and multi-band photometry for redshift estimation. Redshift estimation is dependent on having a long baseline in wavelength space, so the chosen filters (B, V, R, and z', see Fig. 4.1) cover nearly all of the wavelengths detectable by standard CCDs. The shape estimation, for a ground-based survey, will depend critically on the seeing, so the chosen filter for deep shape imaging was R-band. Redder filters tend to have better seeing due to reduced refraction by atmospheric disturbances, but the z' band was impractical for quality measurement due to the low CCD quantum efficiency at 1 μm and fringing produced by sky emission lines, so R was the logical choice. The deep R imaging was carried out at times of best seeing and lowest airmass, which resulted in a narrower point spread function, and deeper effective imaging for the same exposure time. The original goal for the survey was a 1σ sky background of 29 mag arcsec^{-2} (Vega-based) in the BVR bands, which would correspond to a 5σ limit of $R = 26.8$ in an aperture twice the average R FWHM of $0''.7$. The z'-band imaging is substantially shallower, with parts of F1 no deeper than $z' = 23.5$ (Vega-based), and suffers substantially from scattered light around bright stars and residual noise from sky defringing. The CCD quantum efficiency is less than 40% at such red wavelengths, and the z' filter used on the MOSAIC imager, like most first-generation z' filters, is simply a red-pass filter, with no stop at the red end to provide a sharp cut-off to the filter's long-wavelength sensitivity. In practice, this means that colors of red objects in z' filters can vary

by up to 0.15 magnitudes due to the CCD sensitivity (e.g. the L dwarf colors from Dahn 2002). The broad z' filter also fails to correspond to any particular "window" in atmospheric transmission; there are major telluric absorption features in the middle of the band, which can vary dramatically depending on observing conditions (and z' was relegated to some of the worst observing conditions in the DLS, due to its perceived insensitivity to sky illumination and poor seeing). One other possible issue arises with red-pass filters and CCDs: although the quantum efficiency of the CCD is falling with increasing wavelength, as photons lack the energy to excite electrons into the conduction bands, a relatively warm CCD can contain phonons with enough energy to make up the difference, allowing uncertain sensitivities of a few percent well beyond 1 μm (Tyson, J.A. priv. comm.). While this would pose no problem for a filter profile such as the V-band, where the red cut-off of the filter prevents low-energy photons from ever reaching the detector, the z' filter is designed to allow these near-IR photons through, relying on the CCD to reject them. As a result, red standards are essential in determining the actual color response of the z' filter, which can be quite complex. See Chapter 5 for the procedure used to calibrate the DLS z' filter for this study.

4.2 Near-IR Observations

In order to distinguish between cool dwarf stars, brown dwarfs, and high-redshift QSOs, $(R - z')$ colors must be supplemented with near-infrared (NIR) colors. While photometric searches for objects with prominent spectral breaks (e.g. QSOs, Lyman-break galaxies) can be carried out using dropout searches in the reddest band of a survey, they will have fewer misidentifications and spurious objects if every object is detected in more than one band. For $z > 5.4$ QSOs, that means including at least one NIR band: J, H, or K. While K (2.2 μm) is frequently used for this purpose, its high thermal background makes deep imaging difficult. The J-band (1.2 μm) has

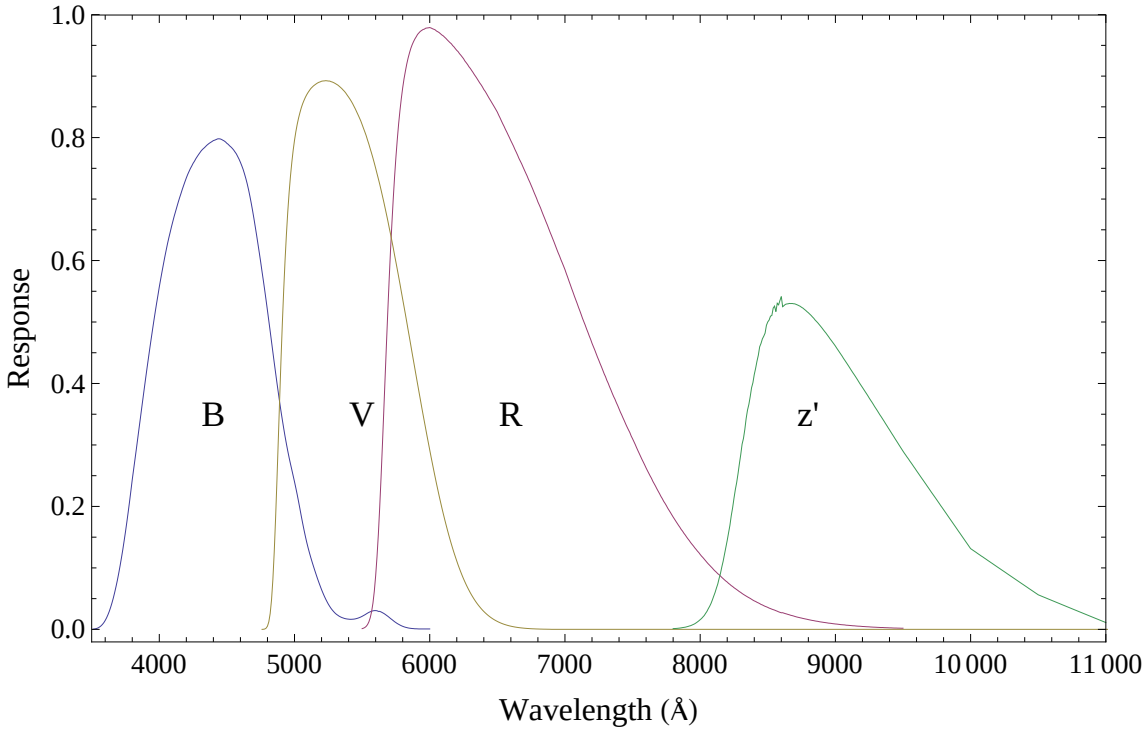

Figure 4.1: Published sensitivity of the combined CCD and filter for the KPNO MOSAIC camera, from the Kitt Peak website.

the additional advantage that it can be used for $(z' - J)$ dropout surveys, which are sensitive to the as-yet-undiscovered redshift 7 QSOs, as well as extremely red objects such as T dwarfs (although for a larger survey, $(z' - K)$ dropouts can be combined with radio detections to search for high-redshift radio galaxies; Schmidt, 2007). With these goals in mind, P. Thorman and Dr. D.J. Thompson have imaged 40% of DLS F1 (1.12 deg^2) in the J band to a depth of $J = 21.4$ (5σ point source) using the Palomar WIRC instrument, a 2048×2048 Hawaii-II HgCdTe near-infrared detector mounted on the 200-inch Hale telescope (described in Wilson et al., 2003). Multiple 60 s dithered exposures were used for sky subtraction, which is a major issue at NIR wavelengths. The pixel scale of WIRC is very similar to MOSAIC, so 16 dithered pointings were required to cover a single DLS subfield. Over three nights in August 2004, 56 of these dithered pointings were completed in DLS F1, covering 3.5 of the 9

subfields (Table 4.2). In addition to the use of these data in this dissertation, Dr. D.J. Thompson also carried out a dropout search for redshift 7 QSOs, including follow-up J and K imaging (to rule out ultracool dwarfs and transients) and spectroscopy at the Keck observatories, but no $z > 6.5$ QSOs were found in the field.

The next logical step was to continue the search in the rest of DLS F1, but survey imaging in J was time-consuming, especially with the relatively small fields-of-view of the NIR cameras available at the time. Instead, Dr. D. Loomba, Dr. I. Dell'Antonio, and P. Thorman submitted a proposal for targeted imaging of the remaining 60% of F1, focusing only on very red ($R - z'$) objects found in the Deep Lens Survey images (Figure 4.2). We were granted 8 nights with the FLAMINGOS instrument (Elston, 1998) on the Mayall 4 m telescope at KPNO. Due to poor weather, only four nights' observations were successful, but 181 of the 280 planned targets (64%) were observed to their intended depth in J (Figure 4.3). Similarly to the WIRC observing run, 60 s dithered exposures were used for sky subtraction, and a total of 51 pointings were observed (Table 4.4), to a median depth of $J = 20.44$. Later, these J images were optimally weighted, remapped to the DLS orientation and pixel scale using the IRAF *geomap* and *geotran* tasks, and combined with the WIRC J-band images to create a master J image for each DLS subfield, which was used to create the final $Rz'J$ catalogs (see Chapter 6). These final J-band images had RMS position residuals of ~ 0.3 pixels ($0''.07$) with respect to the DLS images.

Month	Year	Filter(s)
November	1999	R,z'
December	1999	R,z'
November	2000	R,z'
December	2000	R,z'
November	2001	R,z'
December	2001	z'
September	2002	z'
November	2002	z'
December	2002	R,z'
January	2003	R,z'
October	2003	R,z'
January	2004	R
August	2004	J
September	2004	R,z'
August	2006	J

Table 4.2: Observing runs for DLS F1, including the original DLS observations and our added J-band observing runs.

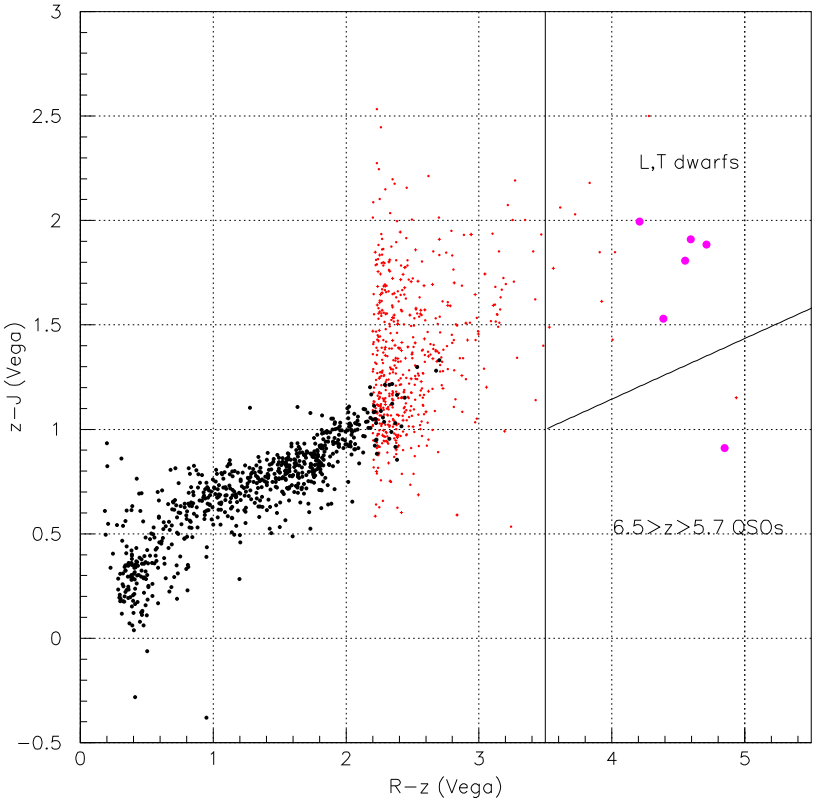

Figure 4.2: Color-color plot from 0.6 sq. deg. of combined DLS and WIRC J-band imaging. The small crosses (red) are $J > 21.5$ dropouts, while the large circles (magenta) are R dropouts. The solid line indicates the original ($R - z' > 3.5$) limit for targeting the observations, but the actual FLAMINGOS imaging recovered a sample very similar to the red crosses. The approximate locations of high-z QSOs and L & T dwarfs are shown on the right.

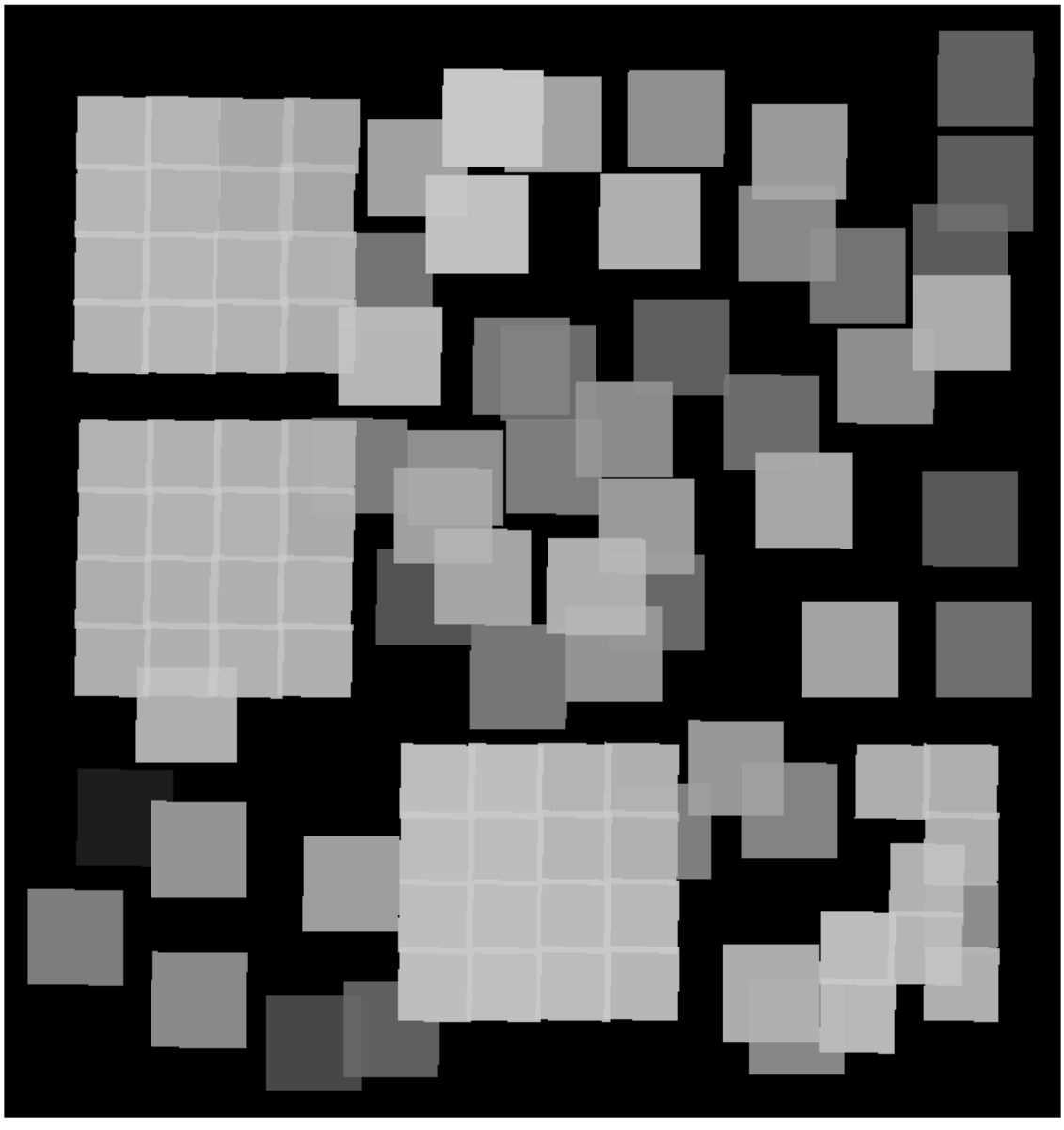

Figure 4.3: Exposure map for DLS F1 J-band imaging, with deepest imaging shown in white, shallowest in black. Angular scale is one DLS field, $2^\circ \times 2^\circ$. Note the regular tiling of the Palomar WIRC survey imaging, compared to the variable depth of the pointed KPNO observations.

	R.A.	Decl.	Exp. Time(s)	Desired 5σ	FWHM (pix)	Noise RMS 1 pix (ADU)	Zero-point	$5\ \sigma$ $2\times$FWHM
1	12.4190	13.5486	1	17.15	4.2	11.5	25.84	19.26
2	13.8387	11.5625	2	17.75	4.5	12.1	25.23	18.52
3	13.6526	12.9865	3186	21.69	3.4	2.8	26.44	21.62
4	13.0669	13.4827	1637	21.32	4.0	5.9	26.26	20.46
5	13.2291	12.5245	2221	21.49	3.3	3.2	26.43	21.50
6	13.6057	13.3697	3238	21.70	3.6	2.4	25.70	20.99
7	12.7990	12.6829	2063	21.45	3.5	3.9	26.43	21.22
8	14.0786	11.9735	1106	21.11	4.0	5.9	26.38	20.58
9	13.5092	12.7338	670	20.84	2.8	6.1	26.35	20.90
10	13.1510	12.8343	676	20.84	3.1	5.5	26.36	20.91
11	13.1336	12.6314	1637	21.32	3.7	5.0	26.41	20.87
12	12.5927	12.9439	532	20.71	3.1	6.6	26.41	20.76
13	13.0582	13.0014	267	20.34	4.6	11.7	25.85	19.15
14	12.8353	12.0425	4065	21.82	4.4	7.7	26.42	20.23
15	12.8337	11.6724	1417	21.25	3.2	3.3	26.40	21.47
16	13.3565	12.9673	1129	21.12	3.6	4.5	25.37	19.98
17	13.4032	12.3308	280	20.37	5.2	7.8	25.11	18.72
18	13.4328	12.5326	1538	21.29	3.1	5.3	26.41	21.00
19	12.8734	12.8404	258	20.32	4.4	11.2	26.02	19.42
20	13.6918	12.7600	197	20.18	4.5	10.5	26.32	19.77
21	12.4766	13.1925	180	20.13	5.0	11.7	25.74	18.95
22	13.6011	12.4847	2569	21.57	4.7	4.0	26.15	20.60
23	13.6767	11.5910	40	19.31	4.9	10.9	25.54	18.85
24	13.4615	13.2563	3279	21.70	3.4	2.0	26.34	21.89
25	14.2356	12.0254	610	20.79	4.2	5.5	23.65	17.87
26	14.0721	11.6542	816	20.95	3.7	5.6	26.10	20.44
27	13.5242	12.6477	1230	21.17	2.7	4.1	26.31	21.33
28	12.6395	13.1508	130	19.95	3.9	11.3	26.41	19.93
29	13.4126	13.4772	4090	21.82	3.2	2.0	26.38	21.56
30	12.4365	12.6457	178	20.12	3.1	4.3	24.65	19.47
31	13.0759	13.2546	6288	22.06	3.1	2.6	26.32	21.69
32	13.3222	12.7548	105	19.83	4.3	4.7	25.54	19.91
33	13.0132	12.0006	209	20.21	3.2	9.6	26.32	20.23

Continued on next page

Table 4.3: Field positions and depths for the FLAMINGOS observations.

	R.A.	Decl.	Exp. Time(s)	Desired 5σ	FWHM (pix)	Noise RMS 1 pix (ADU)	Zero-point	$5\ \sigma$ $2\times$FWHM
34	12.6246	12.3752	1233	21.17	3.4	4.1	26.35	21.12
35	13.2449	13.4580	1435	21.25	3.3	3.9	26.35	21.21
36	12.4189	13.3325	4	18.04	4.1	10.0	25.74	19.34
37	12.8336	13.2245	620	20.80	4.3	6.7	26.24	20.22
38	14.0287	11.7800	49	19.42	2.9	9.8	24.69	18.69
39	13.2029	12.3584	1729	21.35	4.2	4.0	26.01	20.58
41	12.4225	12.3728	4	18.00	4.2	9.8	26.04	19.63
42	12.4063	13.0460	2355	21.52	3.2	2.9	26.35	21.56
43	13.6853	13.1343	52	19.45	4.1	11.9	26.31	19.72
45	13.7386	11.8954	266	20.34	3.2	4.3	26.25	21.03
49	12.7247	13.4007	976	21.04	3.6	4.6	26.33	20.91
54	14.0291	12.2392	2520	21.56	3.4	3.0	26.35	21.46
58	14.2827	11.7875	67	19.59	3.2	10.5	26.32	20.14
65	12.9431	12.1311	14	18.74	4.1	10.4	26.10	19.66
68	13.6840	11.7317	8	18.44	3.5	16.8	26.33	19.54
74	13.0271	12.4709	43	19.34	3.5	17.0	26.35	19.54
O 21	13.5542	12.7863	300	20.73	3.5	7.7	26.34	20.39
O 23	13.2890	12.9523	540	20.58	3.5	5.5	26.31	20.73

Table 4.4: Field positions and depths for the FLAMINGOS observations. Every field that was observed is listed, regardless of whether full depth for candidate identification was reached. Fields O21 and O23 were re-observed to recover candidates which had been missed in the original imaging due to telescope pointing errors.

4.3 Mid-IR Observations

The final data set used in this analysis comes from the Spitzer Space Telescope's InfraRed Array Camera (IRAC; Hora et al., 2000), which uses a combination of InSb and arsenic-doped silicon (Si:As) detectors to carry out simultaneous observations in two of four broad-band filters: 3.6 μm, 4.5 μm, 5.8 μm, and 8.0 μm ([Ch1]-[Ch4]). Observations at these wavelengths are very difficult from the ground due to the atmosphere's near-complete opacity and tremendous thermal emission from the atmosphere and observatory, so even a modest 0.8 m space telescope like Spitzer can easily outperform much larger telescopes on the ground. Dr. G.W. Wilson, of the DLS team, spearheaded a proposal to image all of F2 to 120 s depth using IRAC, which was approved and completed in 2006, with the data released publicly one year later. We have cataloged the released IRAC mosaics in each IRAC channel using Source Extractor (Bertin and Arnouts, 1996), and performed a positional cross-match among R, z', [Ch1], and [Ch2]. The resulting colors were compared to the observed colors of objects in the GOODS field, as plotted in Cool et al. (2006), and found to be in good agreement once the shift from AB to Vega magnitudes was accounted for (Figure 4.4). The modal 5σ detections in [Ch1] and [Ch2] were 5.0 and 6.5 MJy/sr, respectively, which are equivalent to magnitude limits of 15.5 (18.3 AB) and 14.7 (18.0 AB), comparable to the depths of the GOODS wide-field 90 s Spitzer imaging. These catalogs allowed QSO candidates to be selected from DLS F2 according to a refined version of the criteria used by the AGES team, which will be described in Chapter 10. Unfortunately for the brown dwarf search, typical L dwarfs have mid-IR colors very similar to main sequence stars (Patten et al., 2006), which makes them difficult to distinguish without near-IR imaging. For that reason, the present brown dwarf analysis will include only the brown dwarf population selected using the J imaging in F1, with no additional sources from F2.

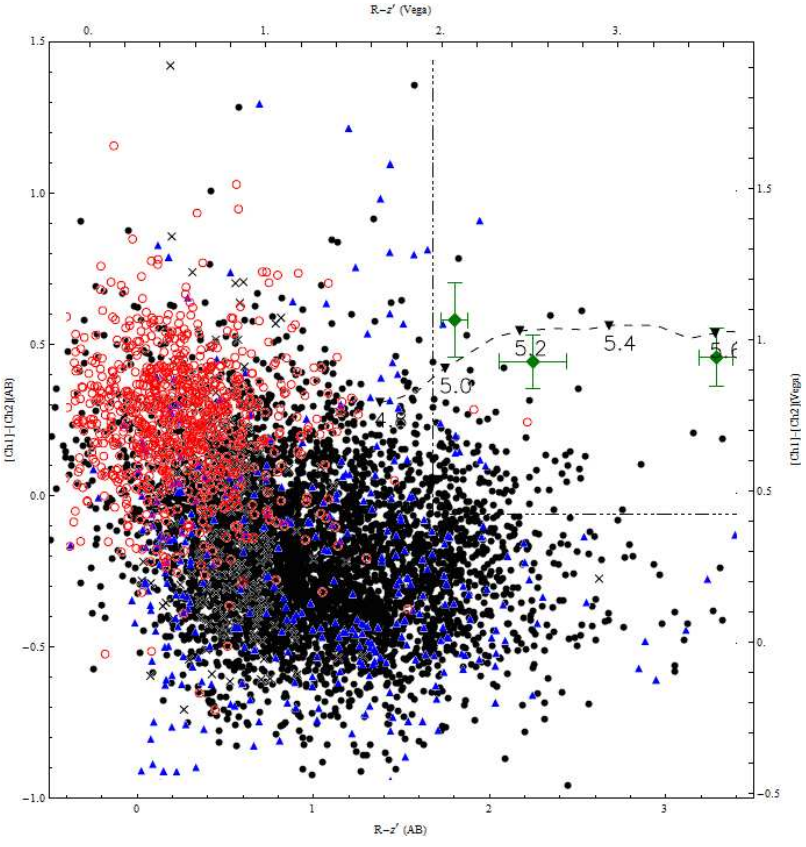

Figure 4.4: Color-color plot of $(R - z')$ vs. [Ch1]−[Ch2] for all matched objects from the 2006 release subfields of the Deep Lens Survey (black points), compared to the same colors from Cool et al. (2006). The AGES survey includes spectroscopic identifications: blue triangles are stars, black X symbols are low redshift galaxies ($0.01 < z < 0.5$), and the red circles are $z > 1$ sources, mostly AGN. The green triangles with error bars are the three high-z QSOs identified using the color criterion shown by the dot-dashed rectangle.

Chapter 5

Calibrating the DLS z-band

The goal of photometric calibration is to produce a catalog of magnitudes which have been corrected for atmospheric (and possibly galactic) extinction, the throughput of the optical system, and the sensitivity of the detector; and so represent a true measure of the intrinsic brightness of an object incident at the top of the atmosphere. The calibration plan for the DLS was based on the use of standard stars: stars located in equatorial fields for easy access from either hemisphere, which have highly accurate photomultiplier tube measurements of the photon flux made by Landolt (1992). His system of filters included B, V, and R filters, with the V and R similar to the DLS versions, and a slightly more blue-sensitive B than the DLS B filter. The same standard stars were used in z', although Landolt did not measure with such a filter: the magnitudes were synthesized using the formulae from Fukugita et al. (1996a), which related Johnson-Cousins BVR magnitudes to SDSS ugriz magnitudes with a series of simple color relations determined from library spectrum convolution. (Although Fukugita's published z' filter curve is a poor match to the actual SDSS z' filter, due to their eventual use of thick, front-illuminated CCDs, it is a reasonable representation of the MOSAIC CCD response.) These Landolt standard star fields were observed regularly, at a variety of airmasses, between science pointings during DLS observing runs. In the original DLS data reduction, the set of all available standard stars in a given filter was used to solve for the magnitude zero-point, regardless of when the original calibration image was taken; this may introduce systematic error in the event of long-term drift in the observational setup, by averaging over variations in detector temperature, water vapor column density, even over different telescopes entirely, in the case of fields accessible from both hemispheres. A more optimal reduction method might use only the calibration data with the smallest separation from the science observations, both in time and in observing conditions.

Landolt's measurements were intended to duplicate Johnson and Morgan's original magnitude system, in which a main sequence star of type A0 would have zero

color. These tabulated magnitudes for the calibration stars were then used to solve

$$m_{tabulated} = m_{instrumental} + a + b(B-V) + c(B-V)^2 + d(1 - airmass) \qquad (5.1)$$

for each filter, where the instrumental magnitudes are those measured from the flux at the instrument, a is a zero-point offset to be determined, b and c are "color terms", first- and second-order corrections to the predicted instrumental magnitude based on the tabulated $(B-V)$ color of each star, and d describes the extinction of starlight by the Earth's atmosphere. The catalog magnitudes to be assigned to each object were then obtained from

$$m_{catalog} = m_{instrumental} + a + d(1 - airmass)$$

This is the equivalent of changing each tabulated "standard star" magnitude by the appropriate color terms to bring it into the native magnitude system of the new survey:

$$\begin{aligned} m_{Landolt} - b(B-V) - c(B-V)^2 &= m_{instrumental} + a + d(1 - airmass) \\ &= m_{inst} + m_0 \end{aligned}$$

5.1 Correcting for Seeing

A cursory plot of bright (but not saturated) objects from the existing releases of the Deep Lens Survey catalog will show minor variations in color between the subfields of the DLS (Figures 5.2(a) & 5.2(b)).

The majority of this variation is due to using the dual-image mode of Source Extractor, which uses objects which are detected in one image as the basis for measurements on a different image, often from a different filter. Although this method allows the deepest images (usually R-band) to be used for detection purposes, the colors it produces are unreliable due to loss of flux outside the detection-band isophote when other bands are observed in poorer seeing.

To determine whether the entire difference in Source Extractor magnitudes between subfields (and even within a subfield) could be attributed to this effect, a curve-of-growth fit was used to determine the true magnitudes of objects in the Source Extractor catalogs, based on a list of their fluxes in a variety of fixed apertures. Each object in the Source Extractor catalog was fitted as the sum of two normal distributions in flux, which might correspond to observations made under different conditions. The fit was made to a radially-symmetric flux profile normalized to unity over all space:

$$f_{total}(r) = c_1(1 - e^{\frac{r^2}{2\sigma_1^2}}) + c_2(1 - e^{\frac{r^2}{2\sigma_2^2}}) \tag{5.2}$$

so that the normalization values c_1 and c_2 are simply the flux attributed to each Gaussian profile, and σ_1 and σ_2 are determined by a simultaneous least-squares fit.

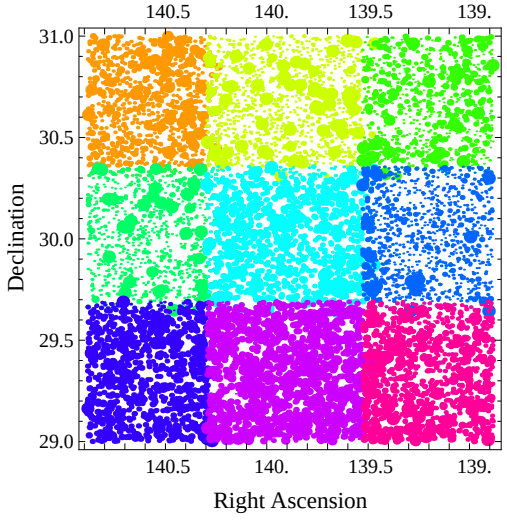

(a) Sky position for SDSS stars which were also detected in the DLS. Point size corresponds to the *size* parameter returned by ellipto (Bernstein and Jarvis, 2002). Ellipto is a software program that measures various parameters related to the size and shape of objects.

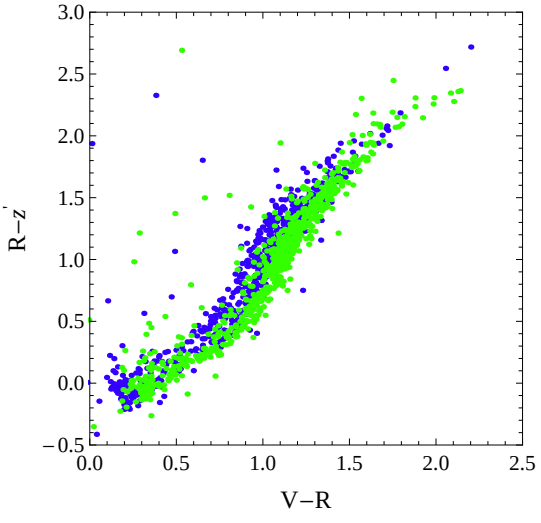

(b) The color-color diagram for the green and blue subfields (p13 and p31), illustrating the inconsistent colors between subfields in F2.

Figure 5.1: Variation in F2.

Although star profiles are not perfectly symmetrical (with ellipticities up to $\approx 0.1 - 0.15$), these profiles should still provide a better measure of the total flux than any single aperture sum. These fluxes can then be converted to magnitudes, assuming the zero-points calculated by the DLS pipeline, and compared to some outside standard of photometry to determine the accuracy of those zero-points. Since F2 is included in Data Release 7 of the Sloan Digital Sky Survey[1] (SDSS), approximately 400 stars per subfield can be cross-matched by position, and used as standards for this purpose (subject to the natural variations in stellar colors with metallicity and age). The SDSS star database, which includes all objects identified as stellar by the SDSS pipeline, was used for this match, and a flag cut was made against the DLS objects in order to exclude saturated sources.

The result was not unexpected: the DLS z' magnitudes obtained by curve-of-growth fitting, using the zero-points originally determined from the Landolt standard stars, agreed with the magnitudes from the SDSS catalog to within 0.03 magnitudes mean residual, regardless of the seeing in the particular subfield. Single-image Source Extractor mag_auto (Kron adaptive elliptical aperture; Kron, 1980) magnitudes, which are measured on the z' image using object isophotes determined on that same z' image, had a constant aperture correction of 0.10 magnitudes; while dual-image Source Extractor magnitudes (which use the Kron apertures determined from R to measure the z'-band flux) had a mean z' residual of 0.20 magnitudes in good seeing, and 0.25 magnitudes in poor seeing (Figures 5.2 and 5.3).

This issue of seeing across bands has been resolved using the Colorpro package (Coe et al., 2006, see Chapter 6). The conclusion was that the DLS zero-points are reliable enough for use, but that great care must be taken in using the output of Source Extractor (and dual-image mode should be avoided when working with object colors.) A small residual remains in the zero-points between widely-separated subfields (e.g. p13 and p31) as there is no overlapping imaging to ensure consistency

[1] http://www.sdss.org

of photometry between them; however, this effect is substantially smaller than the effect due to apertures and seeing (< 0.07 magnitudes between the most discrepant subfields), and will be addressed in future DLS data releases.

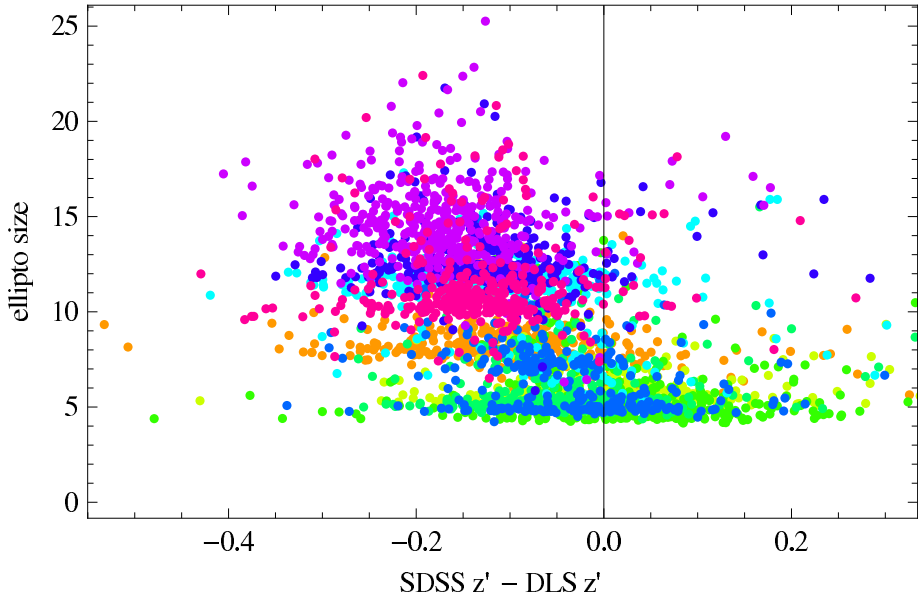

Figure 5.2: Color residuals between DLS (as cataloged in dual-image mode by Source Extractor) and SDSS, as a function of ellipto size (a measure of the object's size in pixels; Bernstein and Jarvis, 2002), color-coded by subfield (colors are the same as Figure 5.2(a)). The correlation between lost flux and ellipto size within a subfield (as seen in the presence of two tiers within the green and blue points, center) is evidence that the effect is predominantly aperture-based, not a problem of subfield calibration.

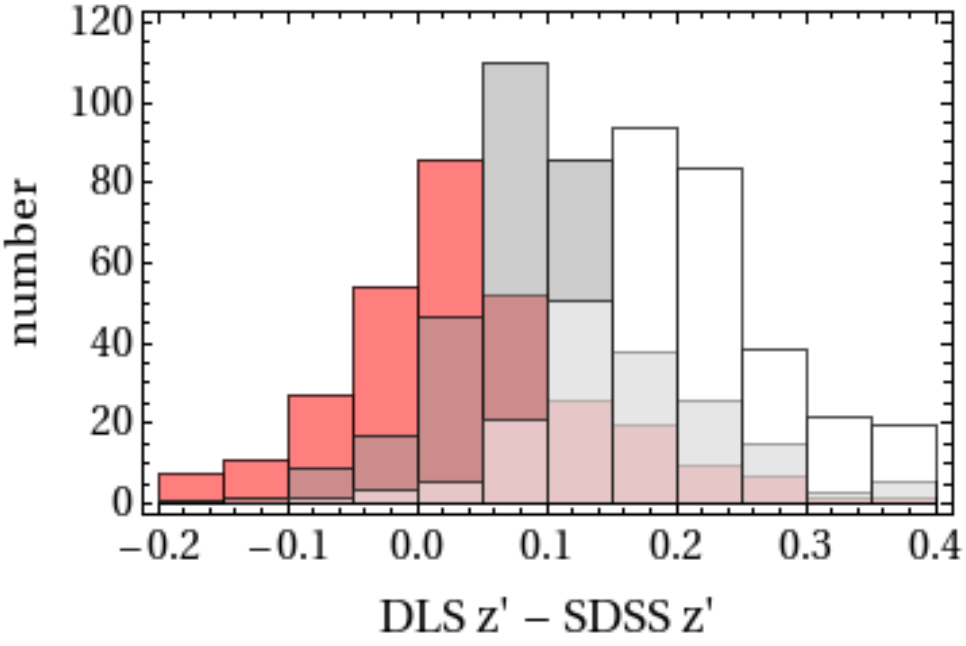

(a) Histogram of residuals in p11.

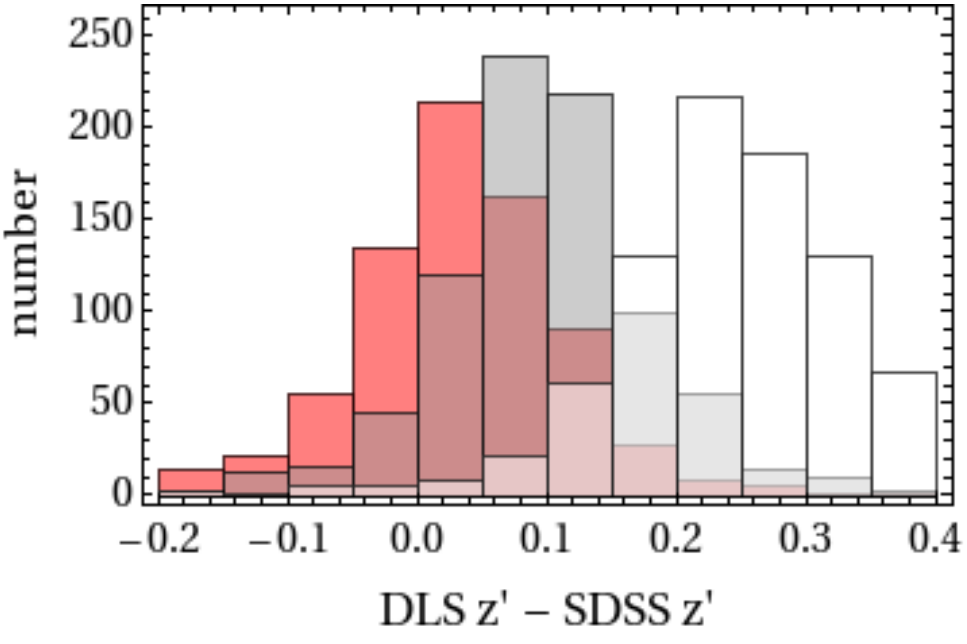

(b) Histogram of residuals in p32.

Figure 5.3: $z_{DLS} - z_{SDSS}$ residuals under good (p11) and bad (p32) seeing conditions. The red histogram shows the distribution of residuals using a two gaussian fit to the curve-of-growth, which does the best job of recovering the SDSS magnitudes; gray is single-image mag_auto from Source Extractor; white is Source Extractor in dual-image mode, detecting on R while measuring on z', which does a particularly poor job under bad seeing conditions.

5.2 Correcting for the CCDs

While the z' filters themselves are nearly identical between SDSS and DLS, both merely long-pass filters, the CCDs can differ somewhat in red-end sensitivity due to design differences: although the original intent of the SDSS collaboration (as expressed in Fukugita et al., 1996a) was to use thinned, back-illuminated CCDs, with UV-sensitive anti-reflective (AR) coating, for all five bands of SDSS, cost and availability concerns caused them to downgrade the actual z' CCDs to front-illuminated, thick CCDs (Gunn et al., 1998). Front illumination is a major handicap for any CCD imager, as it means that the electronic structure — the gates, the readout channels, and the conductors — lies between the science target and the bulk of the silicon detector. It also makes the application of anti-reflective coatings difficult by creating an uneven surface. The thicker CCDs, however, are a boon for near-infrared imaging: they provide a longer path length within the silicon for each photon, allowing low-energy photons with longer penetration lengths a better chance of interacting with a phonon before exiting the detector (the advantages of thinned CCDs are primarily for short-wavelength photons which get absorbed in a very thin surface layer). The net result is a thick CCD with much poorer overall quantum efficiency (QE), but slightly greater red-end sensitivity than a thinned CCD.

The MOSAIC camera, on the other hand, uses an array of 8 thinned CCDs, which have documented variations in sensitivity from chip to chip, and the z' observations were typically left to the worst atmospheric conditions, as they were not essential to the primary goals of the DLS. As an infrared band, z' is expected to suffer less from moonlight and poor seeing conditions, and its only planned use in the weak lensing mission of the DLS was to determine photometric redshifts for the thousands of cataloged background objects, not to measure any sort of high-quality shape parameters. Due to differences in z' system throughput, which affect different types of stellar spectra differently, color terms (like those detailed in Equation 5.1) were

always expected to be necessary for any comparison between SDSS and DLS.

However, the data from F2 did not match with expectations from the filter curve (Figure 5.4). The SDSS magnitudes were slightly brighter on average than the DLS Colorpro magnitudes, with the effect stronger for late-type stars than for early (according to the spectral types determined from SDSS colors, using the color-type relations from Covey et al., 2007). This effect was independent of the seeing in a particular subfield. This was quite the opposite effect that would have been predicted based on the mean published QE of the MOSAIC CCDs, which were expected to be more red-sensitive than the SDSS chips. The Earth's atmosphere is another possible culprit in this unexpectedly low red-end sensitivity. The z'-band covers the range from 7800 Å to 11000 Å, which contains a pair of major H_2O absorption features centered at roughly 9050 Å and 9500 Å. These features are strongly and non-linearly dependent on the column density of water vapor during the observation. Given this significant disagreement between predicted and measured color relations, we had to consider the possibility that one of the the published filter curves (either DLS or SDSS) was incorrect. The SDSS z' filter has been carefully characterized using a monochromatic illumination system throughout the life of the survey (Doi et al., 2010), so our efforts turned to recovering the effective DLS z' filter curve from the existing data.

5.3 Inverting the Problem

Determining the actual filter curve, given the measured fluxes, is a typical inversion problem, belonging to the class of Fredholm equations of the first kind (Arfken and Weber, 2005):

$$\int f(x,t)g(t)dt = h(x) \tag{5.3}$$

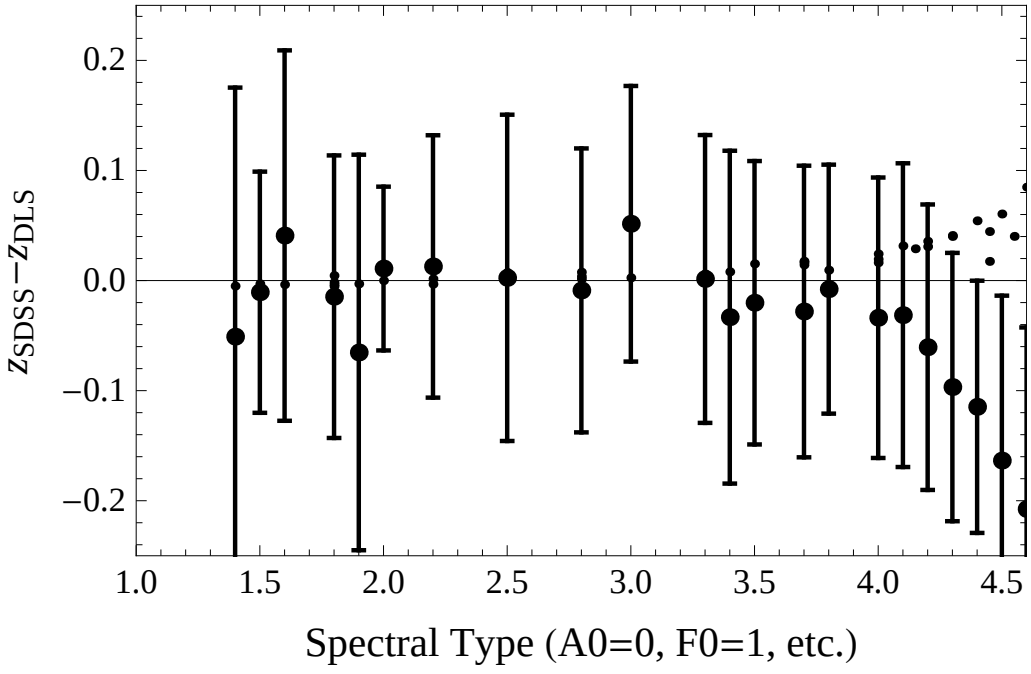

Figure 5.4: Comparison of predicted to measured star colors as a function of spectral type. The small points are the predicted colors from the BPGS and Pickles spectral atlases; the large points with error bars show the measured mean and standard deviation in the measured sample for each spectral type. A mean offset for each subfield has been removed by subtracting the mean $\Delta z'$ for objects of spectral type F-K.

In this particular case, f could be the spectrum of the xth star as a function of t (wavelength or frequency), g is the unknown filter, and h is the measured flux response for that star. Equation 5.3 can be solved in discrete form by convolving the kernel functions f with a set of basis functions, $\tau(t)$, then solving the resulting matrix in a least-squares sense (if an exact solution is not available, as in our case, due to irreducible measurement error).

$$f_{ij} \equiv \int f_i(t)\tau(t)dt$$

$$\sum_j f_{ij}g_j = h_i$$

$$min||f_{ij}g_j - h_i||^2$$

The difficulty in solving an integral inversion equation is conceptually simple: the process of integration destroys the frequency/wavelength information content of the filter and spectrum, leaving only the sum. For a general family of curves $g(t)$, this information will not be fully recoverable from the integrated values, and will have to be imposed on the solution in the form of constraints. Given a simple and general basis, such as a set of step functions in wavelength:

$$\begin{aligned} \tau_j(t) = \quad & 1 \quad \text{for } t_j < t < t_j + \Delta t \\ & 0 \quad \text{otherwise} \end{aligned}$$

the solution of the matrix will seize on the most diagnostic wavelength bin (i.e. the one whose values most accurately track the relation shown in the response vector) and weight it heavily, to the exclusion of all other bins. If positivity is not enforced, the solution will probably include negative sensitivity for some parts of the filter, a clearly unphysical prospect (as seen in our own preliminary results). Restrictions which can be introduced include a maximum value for the second derivative, which can be imposed through the use of the Laplacian filter on discrete lists:

$$\begin{aligned} \frac{d^2y}{di^2} &\approx (y_{i+1} - y_i) - (y_i - y_{i-1}) \\ &= y_{i+1} - 2y_i + y_{i-1}. \end{aligned}$$

The norm of the filter vector can also be restricted to some fixed value, to avoid runaway outliers.

However, in the particular case of the DLS z' filter, none of these regularization methods was sufficient to restrict the free solution to something reasonable. Possible reasons for this failure include the small number of independent measurements (only 12 fitted spectral types appear in the SDSS imaging of F2) and the large intrinsic scatter in the measured colors of the stars, which left this procedure in the position of fitting a large number of filter sensitivity bins using only 12 actual data: the 12 differences between the synthesized star colors for each spectral type and the

corresponding mean (or median) measured colors for the SDSS stars of that spectral type. Clearly, a much more restrictive family of curves would need to be fitted to these simple data.

Instead of building the filter from independent segments, we altered the existing filter curve in reasonable ways. First, the atmospheric absorption was varied, particularly the water vapor column density; this proved insufficient to bring the filter color predictions into agreement with the measured data. An unrealistic amount of water vapor was required (more than 10^3 times the baseline value) and the goodness-of-fit was still increasing with column density. This indicated that more than atmospheric absorption was necessary to correct the z' filter, so we turned to a model for adjusting the quantum efficiency. In order to dampen the red-end sensitivity while maintaining a realistic filter shape, with continuous derivatives, we multiplied the baseline QE by a sigmoid function:

$$\frac{1}{1 + e^{(x-\mu)/a}}$$

This function varies smoothly from 1 to 0 with a decrease centered at μ and width controlled by a. These parameters were then determined for the z' filter by minimizing

$$\sum_i (z_{SDSS} - z_{DLS}) - (z_{SDSSfilter} - z_{DLSfilter}(a, \mu))$$

where i runs over all observed stars, and the $z_{SDSSfilter}$ are synthesized from the Pickles (1997) standard stars, assuming that the SDSS throughput curve is correct. The $z_{(DLSfilter)}(a, \mu)$ were then synthesized for each possible filter curve, the differences between the standard stars and the synthesized stars computed, and the best-fit sigmoid found. This procedure provided an adequate fit for the observed colors, but had the decided disadvantage of lacking any explicit physical underpinnings.

5.4 A Physical Solution

The underlying physical explanation for the difference in the red-end sensitivities most likely lies in the detector temperature. The quantum efficiency of any band-gap device is sensitive to temperature, because of the thermal properties of the charge carriers; but the red-end sensitivity of a silicon CCD is not primarily direct-gap based (the photons have insufficient energy for a direct excitation). Instead, the electrons are excited using an indirect-gap interaction, combining the incoming photon with a phonon in the silicon crystal, which can either add or remove energy and momentum. By adding momentum to the incipient electron, this phonon can shift the electron from the zero-momentum state, where the photon's energy is insufficient for excitation into the conduction band; to a state with non-zero momentum, where the band-gap is narrower, and the photon's energy will suffice to excite it. This complex temperature and wavelength dependence has been modeled for silicon (Rajkanan et al., 1979) based on measurements from NASA's early CCD detectors. The form of the absorption coefficient was assumed, but the number and energy of the direct and indirect gaps was allowed to vary until they found the fit satisfactory. The absorption coefficient (the e-folding depth for decrease of incident light intensity) was modeled by Rajkanan et al. (1979) in the following form:

$$\begin{aligned} \alpha(T) &= \alpha_{direct} + \alpha_{indirect} \\ &= A_{direct}(\hbar\omega - E_{direct}(T))^2 \\ &+ \sum_{i,j} C_i A_j(T) \left[\frac{\{\hbar\omega - E_{gj}(T) + E_{pi}\}^2}{e^{E_{pi}/k_B T} - 1} + \rho_i \frac{\{\hbar\omega - E_{gj}(T) - E_{pi}\}^2}{1 - e^{-E_{pi}/k_B T}} \right] \end{aligned} \tag{5.4}$$

The subscript i runs over possible phonon energies E_{pi}, while the j subscript corresponds to different indirect band gaps E_{gj}. The first term inside the large square brackets corresponds to absorption of a phonon of energy E_{pi}, which process is allowed for any incoming photon whose energy lies in the range $\{E_{gj}(T) - E_{pi}\} \leq \hbar\omega \leq \{E_{gj}(T) + E_{pi}\}$, while the second term represents the emission of a phonon to carry away excess energy; this is only allowed for $\hbar\omega \geq \{E_{gj} + E_{pi}\}$. In equation 5.4,

the terms must be allowed or disallowed manually, as they do not naturally vanish for forbidden energies. As a result, the function has discontinuities in all derivatives. The temperature dependence of the band gap energies was taken from Varshni (1967), and assumes the form

$$E_g(T) = E_g(0) - \left[\frac{\beta T^2}{T+\gamma}\right]. \tag{5.5}$$

Rajkanan et al. then determined the proportionality constants in eqn. 5.4 and the optimal band gap energies by a least-squares fit to the NASA absorption data. In order to convert this α into a quantum efficiency, it is merely necessary to consider the fraction of photons absorbed in a CCD of thickness d:

$$I = I_0 e^{-\alpha d} \qquad \text{(definition of } \alpha\text{)} \tag{5.6}$$

$$QE(T,\lambda) = 1 - \frac{I}{I_0} = 1 - e^{-\alpha(T,\lambda)d} \tag{5.7}$$

Making the assumption that our discrepant value for the QE of the MOSAIC CCD was due in some part to temperature, we compared the QE curve from our measured temperature of operation (168K), which is based on the FITS header CCDTEMP keyword, and the SDSS standard operating temperature (193K Gunn et al., 1998), to see whether the predicted stellar color differences matched what we observed between DLS and SDSS. This difference being inadequate to explain our sensitivity discrepancy, we considered that the MOSAIC CCD might have been tested at room temperature (293K), and determined the necessary thickness for a best-fit to the published z' filter curve provided by KPNO . The resulting thickness (14.8 μm) was consistent with the published thickness of the thinned, back-illuminated CCDs manufactured by SITe (14–16 μm, Clampin et al., 1998), which are of the same type used in the MOSAIC imagers. The original SITe specifications document (Scientific Imaging Technologies Inc., 1995) for the CCD also contains the room-temperature QE, not a cryogenic version (understandable, since the manufacturer would have

no way to know what cooling package would be attached to the detector.) This room-temperature QE is consistent with the published MOSAIC z' filter curve (Figure 5.5). Replacing the published curve with the theoretical silicon sensitivity at

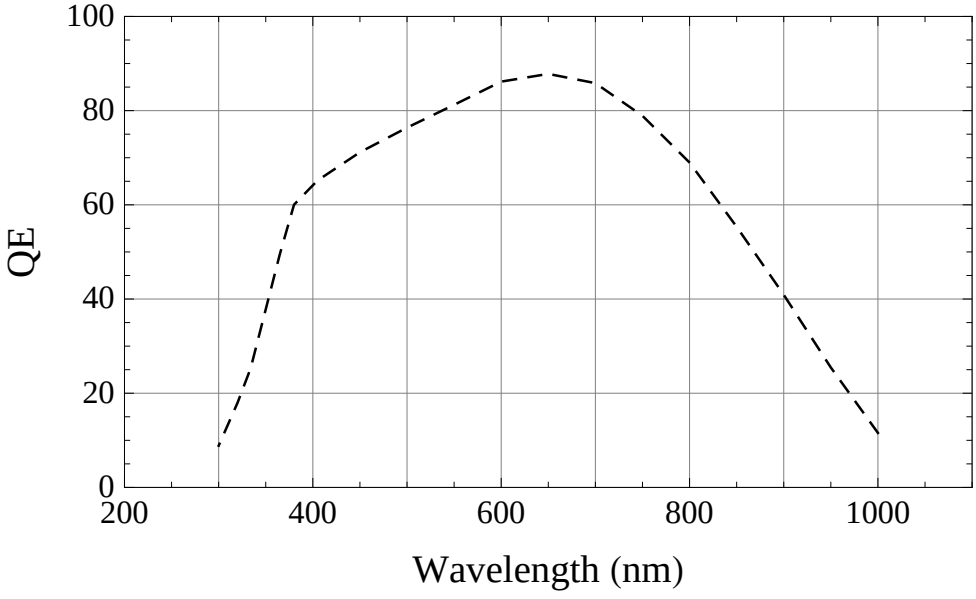

(a) Published QE for the average of the 8 MOSAIC CCDs.

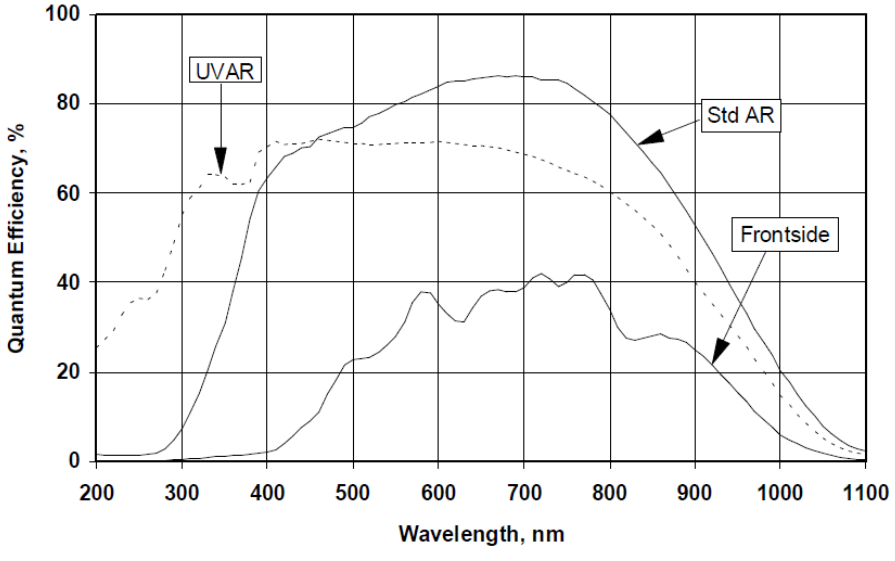

(b) Room temperature QE for MOSAIC CCDs, from the manufacturer.

Figure 5.5: Quantum efficiency for the MOSAIC CCDs.

the MOSAIC operating temperature and applying a standard atmospheric absorption profile (Figure 5.6) recovers the stellar colors much more satisfactorily than the published MOSAIC throughput, and this filter will be adopted from now on.

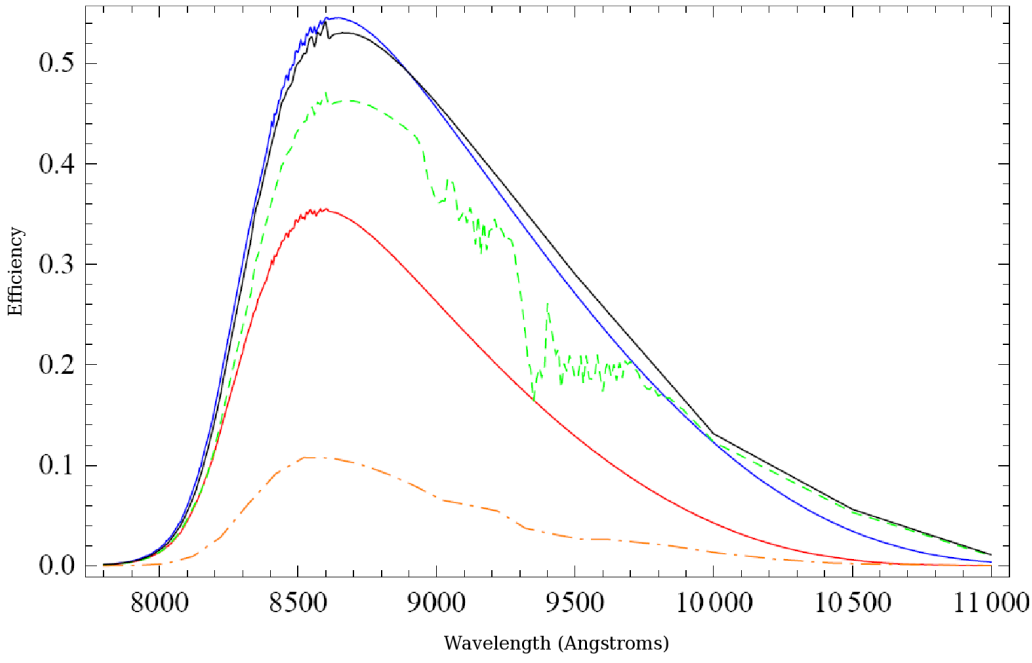

Figure 5.6: Total system throughput (filter plus CCD response) as a function of wavelength for several z filters. The black and blue lines are the published MOSAIC sensitivity and the theoretical sensitivity at 298K, respectively; the dashed green line is the published curve with atmosphere included, which was used to model the stars in Figure 3. The red curve is the theoretical sensitivity at 168K, while the dot-dashed orange curve is the SDSS z response. We have adopted the red curve as our underlying CCD sensitivity for the remainder of this work.

Chapter 6

Creating the RzJ Catalogs

6.1 Cataloging the Fields

A scientifically useful catalog needs a few common features, regardless of the intended research targets: it must be reasonably complete, and preferably have its incompleteness quantified; it should contain as few false positives as possible; and the measurements contained should have their own reliable error estimates. One method for simplifying the completeness calculation is to use a single detection image or passband. If a band is available where the objects are sure or nearly sure to be detected, then the area and depth of that image can serve as the limits for the survey as a whole. For this dissertation the z'-band was selected as the detection band, despite its various flaws in image quality and its inferior depth to R. Unlike J, the z'-band imaging covers the entire DLS area, not just selected portions. And while the R-band imaging is deeper and has better seeing and less degradation from sky effects such as fringing, the extreme $(R - J)$ color of our objects argues against using either of the two extremes of wavelength for detection, to avoid unnecessary one-band detections. The z' image is particularly useful for detection of high-redshift QSOs, for which the Lyman-α peak falls in that wavelength range.

For Deep Lens Survey Field 1 (F1), the unreleased R- and z'-band stacks were used for cataloging, along with all available J-band data from the 2004 Palomar WIRC and 2006 Kitt Peak FLAMINGOS observing runs. The R and z' images were cataloged using Source Extractor in single image mode, with reduced deblending compared to the Deep Lens Survey release catalogs, and the addition of noise-based weighting for detection thresholds, using the WEIGHT_TYPE = BACKGROUND option in SExtractor. This method uses a measurement of the noise on the science image itself to determine the proper relative pixel weights; standard DLS release catalogs use pixel weight maps based on the measured RMS of pixels that contributed to the total stack, but those were not available at the time of this catalog construction. Without the noise-based weighting, a large number of spurious detections are

generated in the low-depth edge regions of the DLS z' images. A relatively stringent detection threshold of 9 contiguous pixels more than 1.5σ above the background was used to reduce unwanted false detections. The shape of each detected object was also measured using the DLS implementation of the ellipto adaptive weighted-moment algorithm (Bernstein and Jarvis, 2002), which takes an input catalog in the simple *fiat* ASCII catalog format used by the DLS, and makes measurements at each object location on the original image pixels.

Matching Overview: These $Rz'J$ catalogs must be matched in a consistent way which allows for the possibility that an object may be detected in one, two, or all three bands. This was done by matching R to z' (the catalogs called rzmatch) and z' to J (zjmatch) separately; these catalogs should include all 2-band detected objects (and two copies of every 3-band detection). By matching to R and J separately, we allow the possibility of very red brown dwarfs, which might lack an R detection, and of blue QSO candidates, which would not appear in J. However, some z'-detected objects are too faint to be detected independently in R, or in J, but an aperture magnitude can still be calculated using the pixels at the object's location in the other bands. To include objects which were not detected in R or J alone, but where an aperture magnitude can still be measured, two more sets of catalogs were created (rznomatch and zjnomatch). Each object in these catalogs was checked by eye to ensure that the detection was not the result of (or contaminated by) an image artifact in R or J, producing the "clean" versions of each catalog. Frequent examples of image artifacts included false detections in R due to scattered light around bright stars, and persistence artifacts in J, where bright stars leave an imprint in subsequent images. These clean catalogs were then combined into one catalog (a trivial matter, since each object was uniquely matched to a z' detection), called the zcheck catalog. This catalog was then checked by eye to ensure that the z' detections were valid (resulting in the zcheck.clean catalog) and duplicates from overlap between subfields were removed, resulting in the final catalog. Each step is reviewed in detail

Table 6.1: Number of objects in each checked $Rz'J$ catalog for DLS F1.

Catalog Name	Raw detections	Clean detections	% clean detections	Description
rzmatch	2070	1578	76.2%	Matched detections in R and z' catalogs
rznomatch	5420	630	11.6%	z' detections with no matching R detections
zjmatch	2011	852	42.4%	Matched detections in z' and J catalogs
zjnomatch	1345	480	35.7%	z' detections with no matching J detections
zcheck	2208	1721	77.9%	All objects with acceptable $(R - z')$ colors
Less duplicates: 1626 objects in data set				

below, while the numbers of objects can be found in Table 6.1 and the decision tree summarized here can be found in Figure 6.1.

Rzmatch: These R and z' catalogs were matched to one another using the assumption of no significant proper motion offsets ($< 1''$) between R and z'; the R and z' stacks were based on multiple observing runs from 1999 to 2004, so any object with a genuine motion should appear as an extended source in both. In order to avoid multiple matches for objects resolved in R but unresolved in z', a matching algorithm was adopted to require that for a given z' object, an R object was accepted as a match only if the R object was the closest match to z' and the z' object was also the closest match to R. Otherwise, the z' object was considered

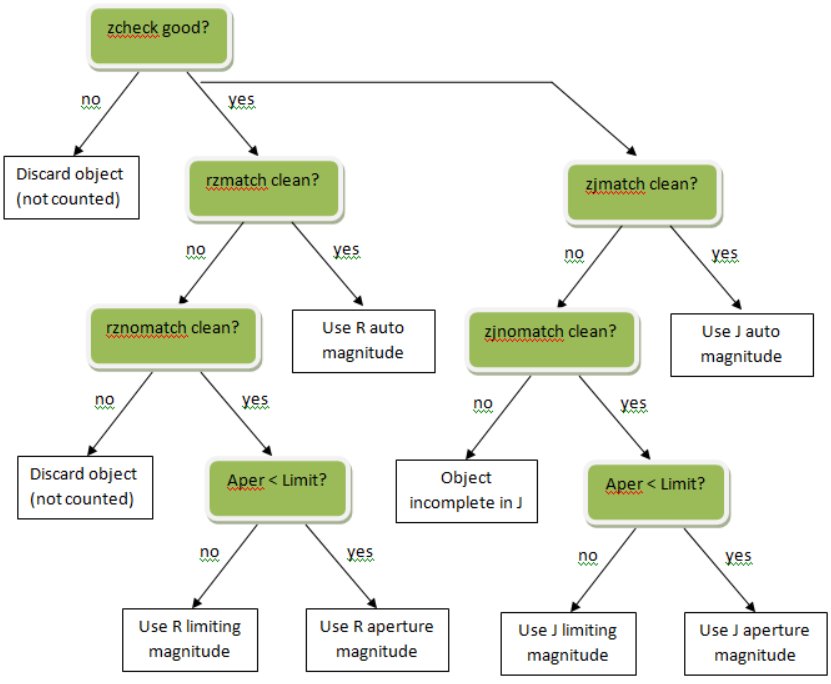

Figure 6.1: Decision tree for catalog creation, based on object quality and matching.

unmatched, but not yet discarded. For matched R and z' objects, the MAG_AUTO adaptive aperture magnitudes were used to determine whether this object would have a corrected $(R-z')$ color redder than 2.0, which corresponds to stars with a spectral type later than M3, or Type I (unobscured) QSOs with a redshift greater than 5.0. (While obscured QSOs can be reddened due to dust absorption in their host galaxy, we do not expect to detect Type II QSOs at these redshifts due to the accompanying decrease in luminosity due to dust.) These 2070 red objects matching to less than $1''$ in R and z' were provisionally accepted, using their MAG_AUTO values, and called the "rzmatch" data set. These matched objects were then visually checked separately against the R and z' images, looking for image artifacts and bad matches (an unlikely problem, due to the restrictive $1''$ limit, but still possible, particularly due to object confusion and blurring in the z' image as compared to the deeper, better-seeing R image). Any object which had no obvious defects in its isophote, and no reason to reject the object match, was passed on as part of the set "rzmatch.clean" (1578

objects), for which MAG_AUTO would be used.

Rznomatch: Objects detected in z' for which the matching algorithm returned no best R match (or no R match at all within $1''$) were not discarded. They were given a second chance to pass using aperture magnitudes, measured in 10-pixel ($2.57''$) apertures on the R images, centered at the location of every z' detection using SExtractor in dual-image mode with z' detection parameters identical to the first catalog, to ensure perfect matching of objects in the catalogs. These R-band aperture magnitudes were "aperture corrected" to bring the aperture magnitudes into line with the presumed correct magnitudes (in this case, MAG_AUTO) for a sample of stars in the field (selected to have small size and ellipticity for their magnitudes).The corrected R magnitudes were then used to determine whether a given z' object would have a corrected $(R - z')$ color redder than 2.0, using MAG_AUTO for z'. These 555 objects, which had been rejected from the .rzmatch catalogs as having bad matches or unreliable isophotes, along with 4865 objects with no match in R, but with aperture magnitudes indicating $(R - z') > 2.0$, became the "rznomatch" data set. These were visually checked by plotting the z' isophotes over the R image, to check for image artifacts in R or contamination of the aperture magnitude by nearby objects. (Image artifacts and contamination in z' would be handled at a later step.) Those which had no apparent defects were considered the "rznomatch.clean" data set (630 objects), for which corrected R aperture magnitudes would be used. Any object which failed at this step was discarded, as having no reliable $(R - z')$ color of any kind.

zJmatch and zJnomatch: Similarly, the combined J-band images for each Deep Lens Survey subfield were cataloged in J using SExtractor in single-image mode; however, the weighting of the J image for detection thresholds was not estimated based on the noise levels, but taken directly from the exposure map, which should be a good estimator of inverse variance. Any object which was a member of either the .rzmatch.clean or .rznomatch.clean data set, that is, any object with a measurable $(R - z')$ color, regardless of its source, was checked for a matching

J detection within 20 pixels (5.1″) using the same best-match algorithm outlined above. These became the ".zjmatch" data set (2011 objects), which was visually checked against z' and J simultaneously, looking for incorrect matching and J image artifacts which could invalidate the J-band MAG_AUTO photometry. As with the R catalog, anything with an acceptable J MAG_AUTO magnitude was kept as "zjmatch.clean" (852 objects), while those with bad matches, or those which were not imaged in J, were given another chance using aperture magnitudes. These 1345 "zjnomatch" objects were visually checked using the z' isophotes on the J image to see whether a valid aperture magnitude could be obtained in J. If the aperture was free of defects, and was part of the area imaged in J, then those objects became part of the "zjnomatch.clean" data set (580 objects), for which MAG_APER could be used for J, once corrected using the aperture correction from the stellar locus. The J detection limits vary greatly across the image, so they were determined from measurements of the RMS noise in a matched aperture on the interpolated noise maps generated by Source Extractor, and some are unreliable due to artifacts in the RMS measurement, so for unmatched J objects with acceptably clean apertures, the aperture magnitude was used when it was less than the limiting magnitude, or when it was less than the zero-point of the image, whichever was less. If the aperture magnitude was greater than the limiting magnitude, but less than the zero-point, the limiting magnitude was used, while if the measured limit and the aperture magnitude were both fainter than the zero-point of the field, the object was considered incomplete, with no $(z' - J)$ color determined. Unlike the R matching procedure, even the 776 objects not imaged in J (or with no valid way of determining their correct $(z' - J)$ color) cannot be discarded at this step, as they will be an important part of determining the survey's completeness in J.

zcheck and zcheck.clean: Next, every object which had a measurable $(R - z')$ magnitude (the .rzmatch.clean and rznomatch.clean data sets, totaling 2208 objects) was checked simultaneously against R and z', using the R and z' isophotes for objects

with matches, and the z' isophote on both images for unmatched objects. Although these objects had already been checked for image defects in R, the possibilities of image defects in z' or spurious positional matches had still to be considered. Objects were marked as having either an acceptable $(R - z')$ match and z' isophote (marked once); or a bad match or isophote, but still a usable z' aperture magnitude (marked twice); or rejected completely as having no usable z' magnitude, or being a z' imaging artifact (no mark). These formed the ".zcheck.clean" catalog (1721 objects), which are the only objects which were considered for study. A final check was made to remove 111 duplicate objects (any objects within 2 pixels or $0.51''$ of one another), due to the overlapping imaging at the edges of the Deep Lens Survey subfields. These duplicates also allowed a check on the reproducibility of the z' magnitudes: 61.2% of the duplicates had magnitude differences smaller than their joint 1σ error bars, only slightly less than the expected number. These duplicate objects were handled hierarchically for each color: automatic magnitudes were preferred to aperture magnitudes, which were preferred to 5σ limits (or area not imaged in J). Ties between adjoining fields were broken by preferring the measured magnitude with the lower quoted magnitude error. The index numbers were chosen to match with the J field, and the chosen duplicates were placed in the field from which the J detection came, since the J magnitudes from FLAMINGOS and WIRC were handled differently (different processing, different zero-points). The summary of the 2008 catalogs is in Table 6.1.

6.1.1 Possible selection effects

Unintended selection effects can be introduced at nearly any step in the above procedure. The detection step has been made intentionally reliant on the z'-band images, so that only their noise and artifact properties will affect the catalogs; these noise and artifact properties have been modeled in detail with the point source recovery test described in Chapter 8. However, the detection threshold used (9 adjacent pix-

els at 1.5σ above the background), while essential to keeping the number of false detections down, is slightly more restrictive than the default 6 pixel detection area, and results in a slightly higher overall detection threshold in good seeing than bad seeing (due to the concentration of the signal in fewer pixels.) In simulations with Gaussian noise, an average signal-to-noise ratio of 4.68 in a 2.5xFWHM-diameter aperture was required in order to produce the 9 contiguous pixels greater than 1.5σ above the background in good seeing ($0.7'' = 2.72$ pixels FWHM), while a S/N of only 4.24 was sufficient to obtain those 9 pixels in poor seeing ($1.5'' = 5.84$ pixels FWHM.) Because a standard test star (fixed FWHM) was used for the point-source recovery test, it would be possible for a small depth discrepancy ($\pm 0.05^m$) to remain between the actual stars in an image and the simulated stars.

The matching is also position-dependent, which makes it reliant on accurate astrometry and small proper motions. The DLS image stacks were constructed from multiple exposures taken between 1999 and 2004, which could allow as much as 5 years' worth of proper motion to accrue during the course of the survey. For large proper motions ($> 0''.4$/yr), the images taken at different epochs will not overlap, which could result in the object appearing multiple times in the stack, or worse, being removed entirely by the process of outlier rejection (assuming that images without the object outnumber images with the object at each location). Smaller proper motions ($\approx 0''.2$/yr) will more likely result in a blurred version of the object appearing in the stack, where the overlapping portions of the object from different exposures are retained (but there is still the possibility that flux from the outer edges was lost in the image stacking process). If this dissertation were directed primarily at high-proper-motion objects, it would have been necessary to catalog each exposure separately, to fit for changes in position for each object. Instead, the more distant set of candidates (high-z QSOs) is expected to exhibit no proper motion whatsoever, while the nearer candidates (brown dwarfs and cool stars) lie tens of parsecs away (an L5 dwarf closer than 18 pc would be saturated in the z'-band). These cool dwarfs

may have significant proper motions – an L0 dwarf at the z' saturation limit would need only 68 km/s in transverse velocity to show a proper motion of $0''.4$/yr – but the magnitude distribution of candidate objects (as seen in Chapter 8) is dominated by fainter, more distant objects, due to the greater volume searched at larger distances. Although it is possible that the search is biased against nearby objects due to their large proper motions, the majority of the search volume is located at distances of hundreds of parsecs, where proper motions for these stars should have no effect on their detection.

6.2 Recalibrating the Catalogs

The product of the above cataloging procedure was a highly reliable catalog of red objects in all of F1, which were included whether or not they had been targeted in the FLAMINGOS campaign, or even imaged in J-band. However, a comparison of the $(R - z')$ and $(z' - J)$ colors of stellar objects to their predicted colors, simulated from the stellar libraries of Pickles (1997) and Bruzual, Persson, Gunn, & Stryker[1], showed a substantial mismatch in the location of notable features in the stellar locus, relative to the location of objects of known spectral type (e.g. the 3-band-imaged objects from Dr. D.J. Thompson's NIRC observing run, whose $z'JK$ colors are highly diagnostic of spectral type; see Chapter 10). This failure to match the stellar locus could not be corrected by a simple displacement along one or the other color axis, as would be introduced by an incorrect zero-point or a misapplied aperture correction, but required a stretch along one or both axes. A fit of this type would require some knowledge of the correct magnitudes and colors of objects in the field, in order to constrain these additional parameters, and might better be addressed by identifying the underlying causes of the miscalibration and correcting them, rather than trying to fit the final results in an *ad hoc* manner. Some of the discrepancy

[1] ftp://ftp.stsci.edu/cdbs/grid/bpgs/

was eventually corrected by adjusting the z' filter used in the color simulations (see Chapter 5), while the remainder was handled in the manner described below.

In order to calibrate the 2008 Source Extractor catalogs, in which the objects had been visually verified, they were first positionally matched to the Colorpro catalogs, which have more reliable $(R - z')$ colors. Colorpro is a cataloging method developed by Coe et al. (2006), to combine data from images with significantly different point spread functions (PSFs), as with our R and z' data, while correctly determining object colors. In short, Source Extractor catalogs are created using the best-seeing image, and a segmentation map is saved, which assigns each pixel in the R-band image to an object. This segmentation map is then convolved with a difference kernel derived from the measured PSF in the poorer-seeing images, which results in a segmentation map assigning each pixel in the poor-seeing image to an object in the good-seeing image. Source Extractor then conducts forced photometry on precisely those pixels in the poorer-seeing image which correspond to the same object in the good-seeing image, which ensures that the isophotal magnitudes are corrected for the difference in seeing. The Colorpro catalogs were matched to the existing DLS star catalogs (stardb), to reduce contamination from non-star sources. These stardb catalogs consist of objects selected in each DLS field for their small size and ellipticity, given their magnitude, and should be a nearly pure sample of stars. They were created to aid with the astrometric calibration and PSF circularization used by the DLS weak lensing method (Wittman et al., 2006). The sky locations of the matched stars are shown in Figure 6.2.

Spectral types were then assigned to these stars based on their 4-band Colorpro colors, and their colors were corrected in two iterative steps: 1) a shift to minimize the least-squares difference between the sample stars and the colors of equivalent library standard stars and 2) removing stars of discrepant color (beyond a fixed number of standard deviations from the mean). These steps were repeated until the sample converged (no stars clipped). This provided color shifts $\{\Delta(B - V)$, $\Delta(V - R)$, and

$\Delta(R - z')\}$ to bring the Colorpro colors into line with the synthesized star colors. To determine the overall magnitude calibration, the star sample was matched to the J imaging from WIRC and FLAMINGOS, and the $(z' - J)$ color corrected to the colors of synthesized stars, using the spectral types determined from the DLS $BVRz'$ colors. The J-band MAG_AUTO magnitudes were confirmed to match 2MASS to within ± 0.02 magnitudes RMS, and $\Delta(z' - J)$ and $\Delta(R - z')$ were determined to be +0.19 and -0.11 magnitudes, respectively. At this point, the $(z' - J)$ offset was applied to Colorpro z', and the sum of the $(R - z')$ and $(z' - J)$ offsets applied to Colorpro R, resulting in a set of Colorpro and NIR $Rz'J$ magnitudes normalized using 2MASS.

These corrected Colorpro magnitudes were then used as the standard to which the Source Extractor catalogs would be corrected. The median difference between Colorpro R and MAG_AUTO R was a stable 0.19 ± 0.03 mag, with no dependence on R magnitude (Fig. 6.3), so this offset was applied as a correction to bring Source Extractor R auto magnitudes into line with the corrected Colorpro R. For objects with no reliable auto magnitude, aperture magnitudes were substituted, after including a polynomial correction (Table 6.2) to bring them in line with the auto magnitudes:

$$R_{\rm auto} = R_{\rm aper} + a + bR_{\rm aper} + cR_{\rm aper}^2 + dR_{\rm aper}^3 \tag{6.1}$$

The differences between Colorpro z' and the measured Source Extractor auto magnitudes of the same objects were significant, and varied as a function of z' magnitude (Fig. 6.4), while the aperture magnitudes showed no such trend (only an aperture correction varying with the seeing in a particular DLS subfield; Table 6.3). For this reason, z' aperture magnitudes were preferred over auto magnitudes in the new catalog, the opposite of the original catalog's preference. These were corrected using the median aperture correction, determined separately for each subfield, to match the corrected Colorpro z' magnitudes (Table 6.3). For z' objects with no reliable aperture magnitude, the auto magnitudes were substituted, after correcting

Table 6.2: Polynomial fits for correcting R and z' magnitudes.

Measurement Band	a	b	c	d
R	-8.18	1.01	-0.0498	0.000767
z'	25.4	-3.71	0.179	-0.00285

Table 6.3: z' aperture corrections for each F1 subfield.

Subfield	Median Aperture Correction ($z_{aper} - z_{\mathrm{Colorpro}}$)	Standard Deviation of Corrections
F1p11	0.208	0.037
F1p12	0.152	0.035
F1p13	0.248	0.062
F1p21	0.187	0.072
F1p22	0.181	0.096
F1p23	0.305	0.069
F1p31	0.308	0.045
F1p32	0.210	0.069
F1p33	0.218	0.044

them by a polynomial fit (Table 6.2; Figure 6.5) to bring them into line with the corrected aperture magnitudes:

$$z'_{\mathrm{aper}} = z'_{\mathrm{auto}} + a + bz'_{\mathrm{auto}} + c(z'_{\mathrm{auto}})^2 + d(z'_{\mathrm{auto}})^3 \tag{6.2}$$

The J auto magnitudes required no magnitude-dependent calibrations, but were shifted by a zero-point difference corresponding to the magnification factors of the WIRC and FLAMINGOS images, due to a failure to conserve flux in the original geometric remapping on to the DLS coordinate system, and separate aperture corrections of 0.28 and 0.16 magnitudes for the FLAMINGOS and WIRC subfields were applied.

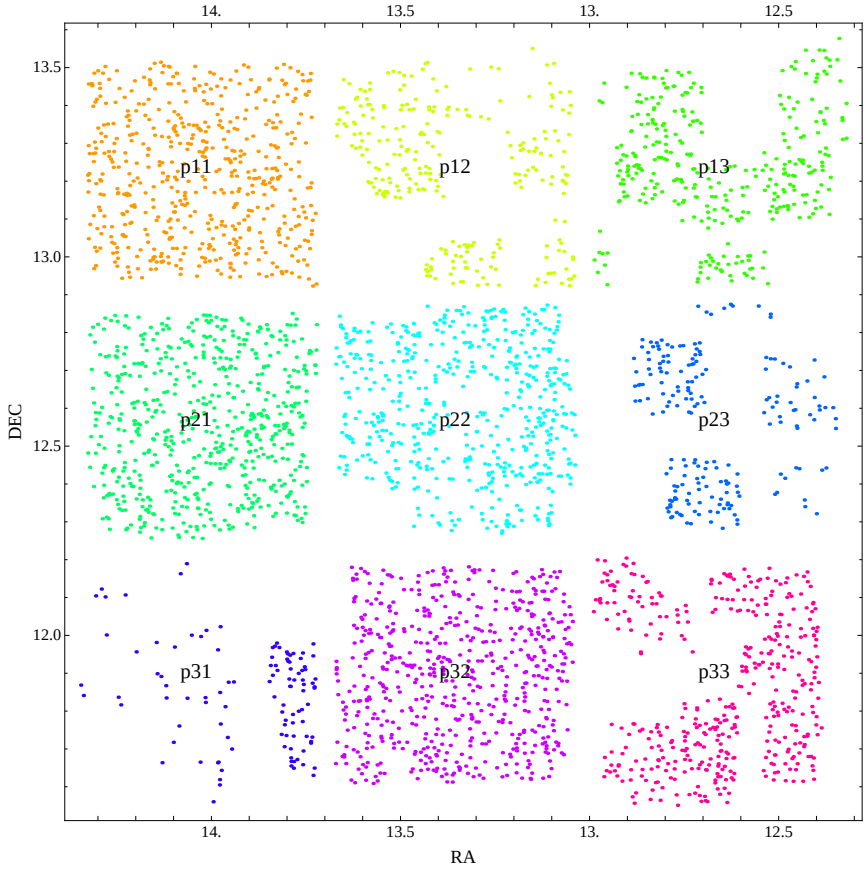

Figure 6.2: Sky positions for objects in the matched Colorpro and F1.stardb catalog, which was used for iterative stellar locus calibration. The stardb stars were originally selected based on size and magnitude, and used for astrometry and PSF circularization routines throughout the DLS. The disparity in density among the subfields is due to the differing depths of the J-band imaging; the WIRC imaging is clearly visible as large blocks of deep survey data, while the FLAMINGOS pointings are sparser and shallower, on average.

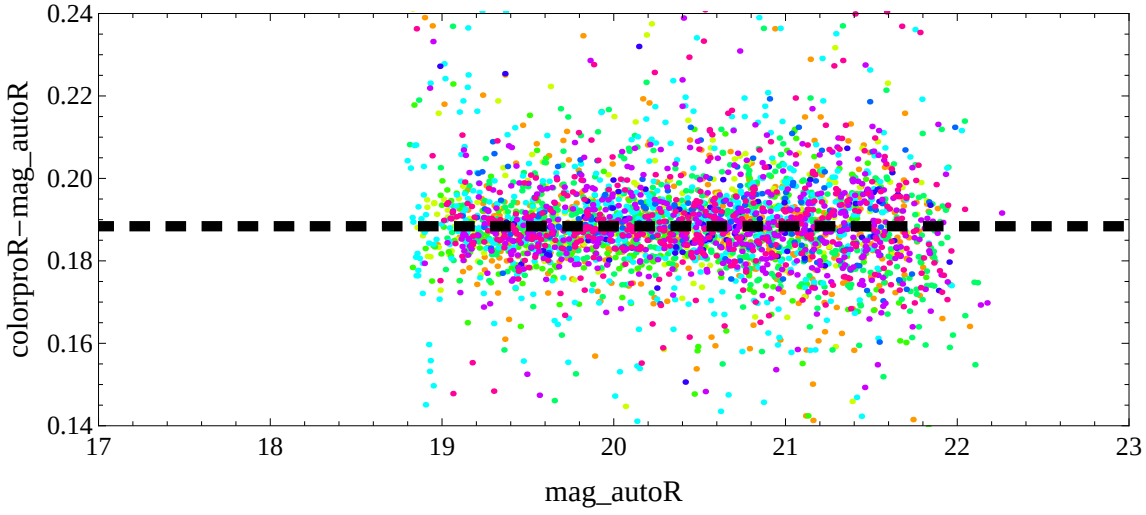

Figure 6.3: Magnitude residual plots for Colorpro vs. Source Extractor MAG AUTO R-band measurements. Aside from a constant offset, no trend with magnitude is evident. Point color indicates the original subfield, as labeled in Figure 6.2.

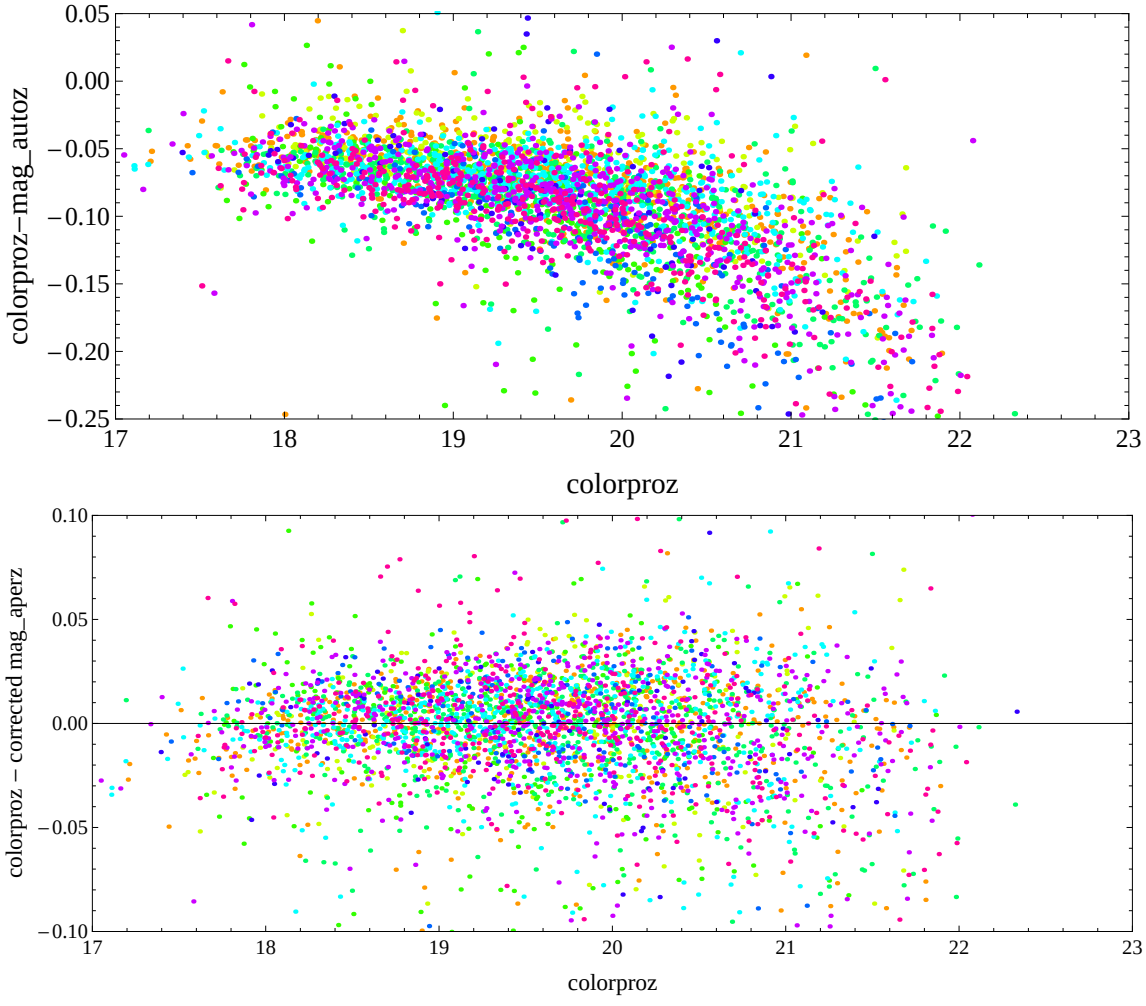

Figure 6.4: Magnitude residual plots for Colorpro vs. Source Extractor MAG AUTO (top) and median-corrected MAG APER (bottom) z'-band measurements. The trend with z' magnitude is clear in the auto magnitudes, while the aperture magnitudes can be well-corrected on a subfield basis (Table 6.3). Point color indicates the original subfield, as labeled in Figure 6.2.

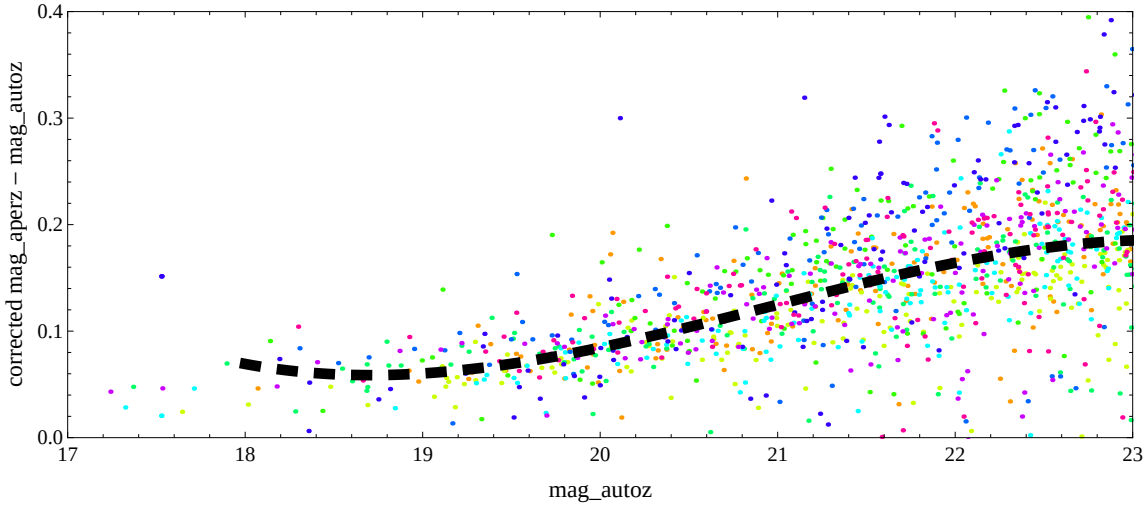

Figure 6.5: Magnitude residual plots comparing Source Extractor MAG AUTO to the median-corrected MAG APER z'-band measurements. The dashed line shows the polynomial fit used to convert auto to aperture magnitudes, for sources lacking them; the large scatter from the trend is why these auto magnitudes were not preferred. Point color indicates the original subfield, as labeled in Figure 6.2.

6.3 Testing the Catalogs with Red Standards

The ideal calibration for the colors and magnitudes of red objects in the DLS would be based on real observations of objects of known spectral type, using the same instrumentation and observing setup as the actual DLS. During the original observing campaign, a small sample of cool stars and brown dwarfs was observed using the MOSAIC camera at KPNO (see Table 6.4). These standards were imaged singly, without dithering, but each image was flat-fielded using the standard sky-flats generated by the DLS pipeline, and the sky background subtracted. Detection was carried out using Source Extractor, generating raw catalogs of instrumental magnitudes. In order to determine the zero points of the images, a cross-match to SDSS was performed on each field, and fields with multiple images were matched and co-added at the catalog level. The SDSS *griz* magnitudes were then used to synthesize BVR photometry for main-sequence stars in the red standard fields, according to the SDSS-to-BVR magnitude relations from Fukugita et al. (1996b). These SDSS reference stars were matched to the MOSAIC images using sky position; then the instrumental magnitudes of the same stars were parametrized with first- and second-order color terms in $(B - V)$, a zero-point for each filter, and a linear airmass term, treating them as the reference stars in Equation 5.1. (The airmass term is not required for the fitting of individual fields where SDSS stars are available, being completely degenerate with the overall zero-point, but it permits the calibration to be extended to fields where SDSS imaging is not available.) The resulting calibrated DLS magnitudes were then combined with the known spectral types of these standards, and added to the other outside sources of photometry for calibration purposes.

As shown in Figures 6.6, 6.7, and 6.8, the measured colors of stars in DLS F2 and our targeted red standards match well with synthesized magnitudes generated by convolving a variety of library stellar spectra with the z' filter curve derived in Chapter 5.

Table 6.4: Exposure times for each red standard object.

Object Name	Exposure time (sec)			
	B	V	R	z'
LHS 2924	900	600	300	10, 60
SDSS J1159+0057	not imaged	not imaged	600	200
SDSS J1257-0113	1200	750	600	500, 200
SDSS J1110+0116	not imaged	not imaged	not imaged	300, 600

Table 6.5: Positions and measured magnitudes in DLS filters for red standard objects.

Object Name	RA (J2000)	Dec	Spec. Type	B	V	R	$z'_{\rm Vega}$
LHS2924	14:28:43	+33:10:37	M9V	22.13 ±0.02	19.82 ±0.01	17.30 ±0.00	13.95 ±0.00
SDSSJ1159+0057	11:59:39	+00:57:27	L0	N/A	N/A	19.66 ±0.01	16.16 ±0.00
SDSSJ1257−0113	12:57:37	−01:13:36	L5	> 24.70	> 24.15	21.78 ±0.04	18.25 ±0.01
SDSSJ1110+0116	11:10:10	+01:16:13	T6	N/A	N/A	N/A	19.65 ±0.04
Errors are photometric only, to the nearest 0.01. Dropouts are reported at 5σ limits.							

The imaged red standards provide an independent check of the standard calibration spectra and the filter throughput curves, and the libraries and sensitivity have proven to be correct. The synthesized colors can now be relied upon in calibrating the remainder of the data.

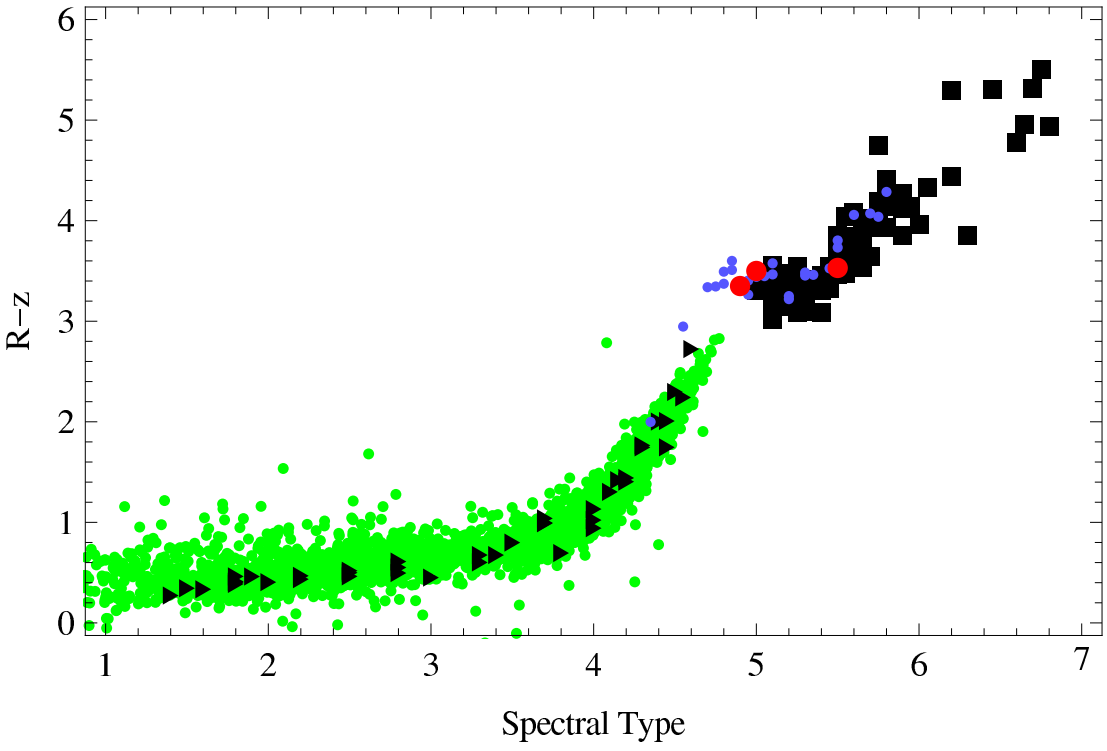

Figure 6.6: $R - z'$ vs. spectral type. Green points: stars from F2, black triangles: library stars, blue points: cool dwarfs and brown dwarfs from Dahn et al. (2002), black squares: synthesized colors from brown dwarf spectra. Red standards are shown as red points. For comparison, a sample of bright stars from F2 has been plotted, with assigned spectral types based on a least-squares fit of their SDSS colors to the model colors from the stellar atlases (Pickles & BPGS). The black squares are synthesized colors from measured spectra of L and T dwarfs (see Section 7.2 for details.) To bridge the gap between the main sequence and the brown dwarfs, measured $(R-z')$ colors from Dahn et al. (2002) have been included. The R filter used for those observations was similar to the MOSAIC R filter, but the z' observations, which were made on a variety of telescopes with differing detectors, were carefully recalibrated by Dahn et al. to the SDSS z' filter using third-order color terms. A first-order fit to the difference between synthesized DLS z' and synthesized SDSS z' for the sample of late M and early L dwarfs has been applied to correct them to the DLS z' filter. The resulting fit was $z'_{DLS} - z'_{SDSS} = -0.0859 - 0.0569 * (\text{spectral type})$, where the spectral types are represented by A0=0.0, F0=1.0, etc. The red points represent the measured $(R - z')$ of the known red standards. Error bars are included in the plot, but are smaller than the points themselves.

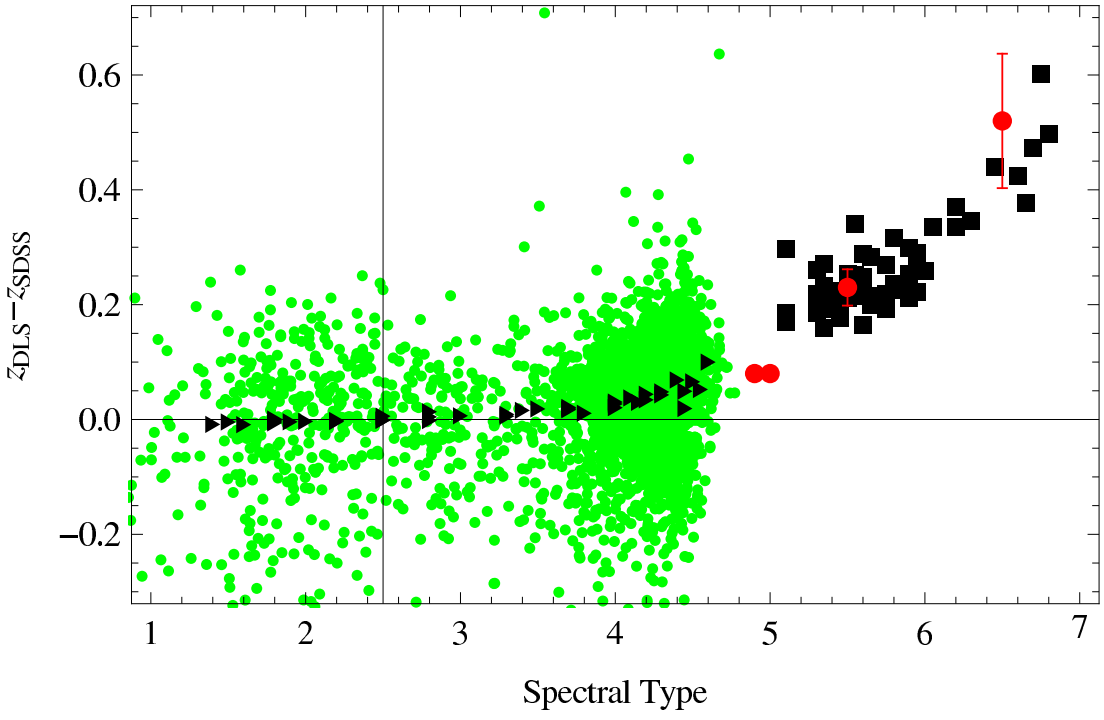

Figure 6.7: DLS z'−SDSS z' vs. spectral type. Green points: stars from F2, black triangles: library stars, black squares: synthesized colors from brown dwarf specta. Red standards are shown as red points with error bars. Figure 6.7 plots the difference between DLS z' and SDSS z' over all spectral types (both magnitudes Vega-based.) As in Figure 6.6, a sample of bright stars from F2 has been included, to show the overall trend in color. These are similar to the stars which were used to construct the DLS z' filter transmission curve, so the green points may be thought of as the calibration data set. The black squares are the synthesized colors for L and T dwarfs, while the red points with error bars show the measured colors of the red standards. Although the red standards were not used in the estimation of the z' filter throughput, the resulting colors are in good agreement with the measured values.

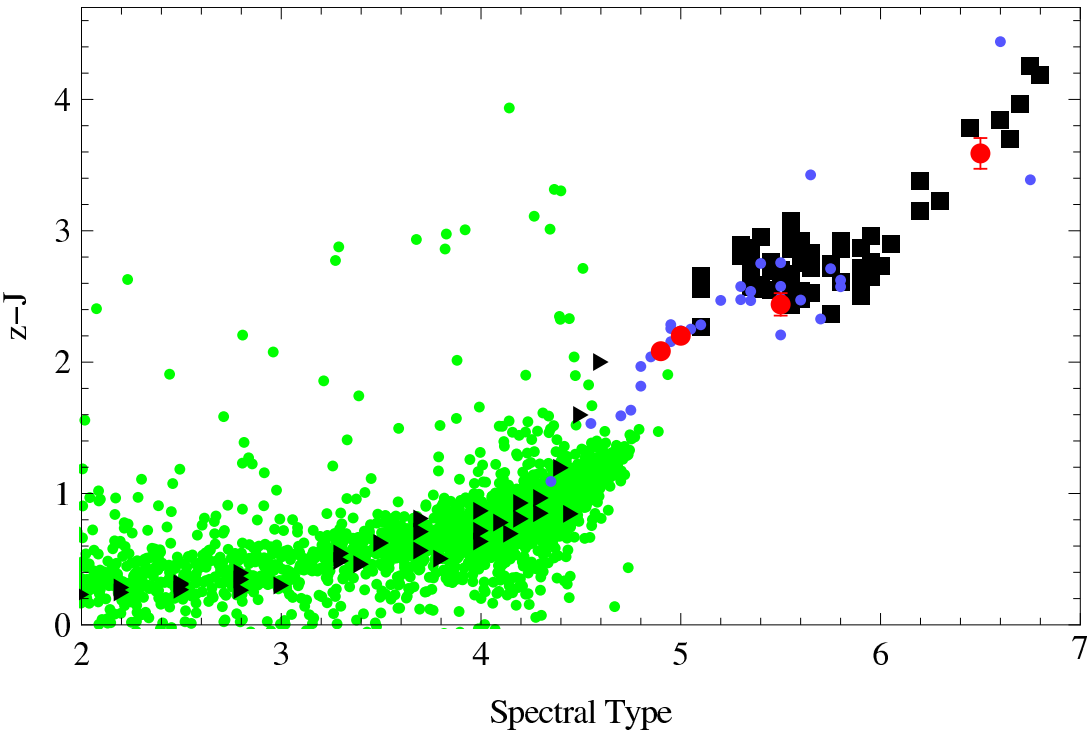

Figure 6.8: $(z' - J)$ vs. spectral type. Green points: stars from F1, black triangles: library stars, blue points: cool dwarfs and brown dwarfs from Dahn et al. (2002), black squares: synthesized colors from brown dwarf spectra. Red standards are shown as red points with error bars. The green points are a sample of size-magnitude selected stars from F1, using both the WIRC and FLAMINGOS J images. The blue points from Dahn 2002 have been included, with the z' filter correction applied. No J correction was applied to the Dahn observations, as they were already corrected to the Mauna Kea Observatory (MKO) J filter standard, which is similar to the filters used on WIRC and FLAMINGOS. However, those filters differ from the 2MASS J filter quite substantially, so in constructing the $z' - J$ for the red standards, the 2MASS J magnitudes were corrected to the MKO system according to the spectral type-color relations from Stephens and Leggett (2004). The resulting points for $(z' - J)$ are plotted in red, with error bars, and agree well with the predicted colors.

Chapter 7

Modeling Target Colors

7.1 Modeling QSO Colors

In order to determine the colors of QSOs in our filter system, we will need a model of the source flux which can be convolved with our filter and CCD response to determine the total measured object brightness. For the QSO model, we will be using the rest-frame spectrum from Vanden Berk et al. (2001) (Figure 2.2), which is a median composite of relatively low-redshift QSO spectra, all corrected to zero redshift. This spectrum, f_λ, will then be redshifted to a variety of values using the typical redshift relation,

$$f_\lambda(\lambda, z) = f_\lambda(\frac{\lambda}{1+z}). \tag{7.1}$$

While the QSO source spectrum is consistent over a large range of redshift (leaving aside minor differences in metallicity and emission line widths), the increasing absorption of the intergalactic medium (IGM) becomes a major factor in determining the colors of QSOs and all other continuum sources at redshifts > 4. As the flux from the QSO passes through intervening HI at lower redshifts, the blue side of any hydrogen emission feature is strongly absorbed, with complete absorption (a "Gunn-Peterson trough"; see Figure 2.3) for QSOs at redshift 6 and above. To model this increasing absorption with redshift, we will be using the average IGM absorption from Songaila (2004), applying the absorption to all flux blueward of the Lyman-α peak at 1218Å (rest-frame). Finally, the resultant QSO spectrum is used to generate colors in the DLS filter set, using the flux relations from Hogg et al. (2002b), transformed to take a spectrum as a function of wavelength rather than frequency:

$$(M_1 - M_2) = -2.5 \log_{10}[\frac{\int f_\lambda(\lambda, z) R_1(\lambda) \lambda \mathrm{d}\lambda}{\int R_1(\lambda) \mathrm{d}\lambda/\lambda} \frac{\int R_2(\lambda) \mathrm{d}\lambda/\lambda}{\int f_\lambda(\lambda, z) R_2(\lambda) \lambda \mathrm{d}\lambda}], \tag{7.2}$$

where R_1 and R_2 are the response functions of the filters. The resulting colors

are naturally in AB magnitudes (Oke, 1972), so a zero-point shift must be applied to bring them into the Vega magnitude system. To determine this shift, we can simply use Equation 7.2, substituting the flux of Vega for f_λ, and fixing one known magnitude (e.g. $V_{AB}(\text{Vega}) \equiv 0.02$), then solve for the remaining zero-point shifts based on the colors of Vega in the filter set.

This provides the QSO $Rz'J$ colors which will be used in the color selection (Figure 7.1). To determine the distribution of colors around the mean, we refer to Willott et al. (2005), where the spectra of 180 low-redshift QSOs were redshifted, intergalactic absorption applied, and their $(z' - J)$ colors determined. A contour enclosing 95% of the spectra was drawn, which we have used to determine the 2σ deviation from average (which is slightly larger for $(z' - J)$ redder than median than for the blue side.) This mean and standard deviation have been used to characterize an asymmetrical distribution, gaussian on each side of the mean, which will be used to generate the likelihood of a given object being a QSO. To reduce the number of calculations required, only objects lying more than 1σ blueward of the stellar locus were included in the probabilities, all other objects being vanishingly unlikely to be QSOs.

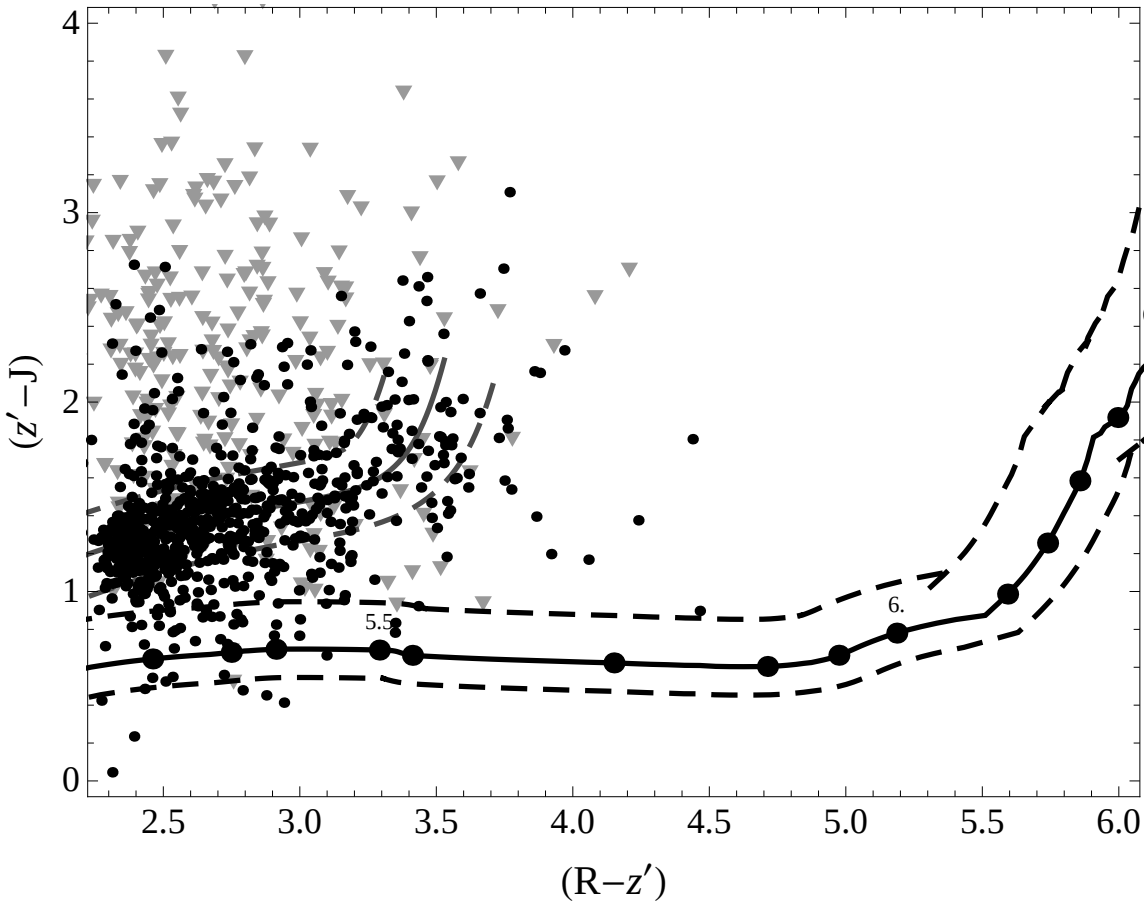

Figure 7.1: DLS $(z' - J)$ vs. $(R - z')$ for QSOs at various redshifts. Text labels indicate z=5.5 and z=6.0, and the 3-band detected and J-dropout samples from F1 are shown as points and triangles, respectively, with J-dropouts marked at the location of the 5σ limit, which is an upper limit for their $(z' - J)$ color. The gray dashed lines at the left indicate 1σ deviations from the stellar locus (dominant mass of black points near $\{2.5, 1.1\}$), while the black dashed lines show 1σ deviations from the QSO track, as determined from the dispersion of redshifted spectral colors in Willott et al. (2005).

7.2 Modeling Cool Dwarf Colors

There are two main methods for determining colors of M, L, and T dwarfs: photometric surveys and spectroscopic surveys. The photometric surveys have the advantages of greater reach and larger sample size, but their utility is limited by how similar their filter set is to the filter set of interest. The spectroscopic data can, in principle, be used to simulate colors on any filter system, but the data are of varying quality, span different ranges of wavelength (depending on the spectrograph used), and may include gaps or unreliable data due to telluric absorption and sky emission. For this study, both photometric and spectroscopic data were used in combination, to create a single model of the color-spectral type relation for cool dwarfs in the DLS.

7.2.1 Photometric Colors

Although several surveys have now discovered significant cool dwarf populations (e.g. DENIS, Delfosse et al. (1997); 2MASS, Kirkpatrick et al. (1999)), the filter sets used have varied significantly. The DENIS survey used the 0.85 μm I filter, quite different from the DLS R-band, along with J and K, while most studies of 2MASS data have combined their JHK magnitudes with optical colors from SDSS (i' and z') or the DSS (the Digitized Sky Survey[1], largely based on the National Geographic Society-Palomar Observatory Sky Survey's blue and red photographic plates). There has been a study (Dahn et al., 2002) of cool dwarfs using a Cousins R filter, similar to the DLS, but with the SDSS z' filter (see Section 5.4 for the differences). Using the inferred z' response for DLS and the published z' sensitivity for SDSS, it should be possible to use cool dwarf spectra to fit a correction: $\Delta z' \equiv z'_{\rm DLS} - z'_{\rm SDSS}$. As shown in Figure 7.2, there is a significant offset between the two z' filters, and a weak dependence on type, which has been modeled with a best-fit line. The results

[1] http://archive.stsci.edu/cgi-bin/dss_form

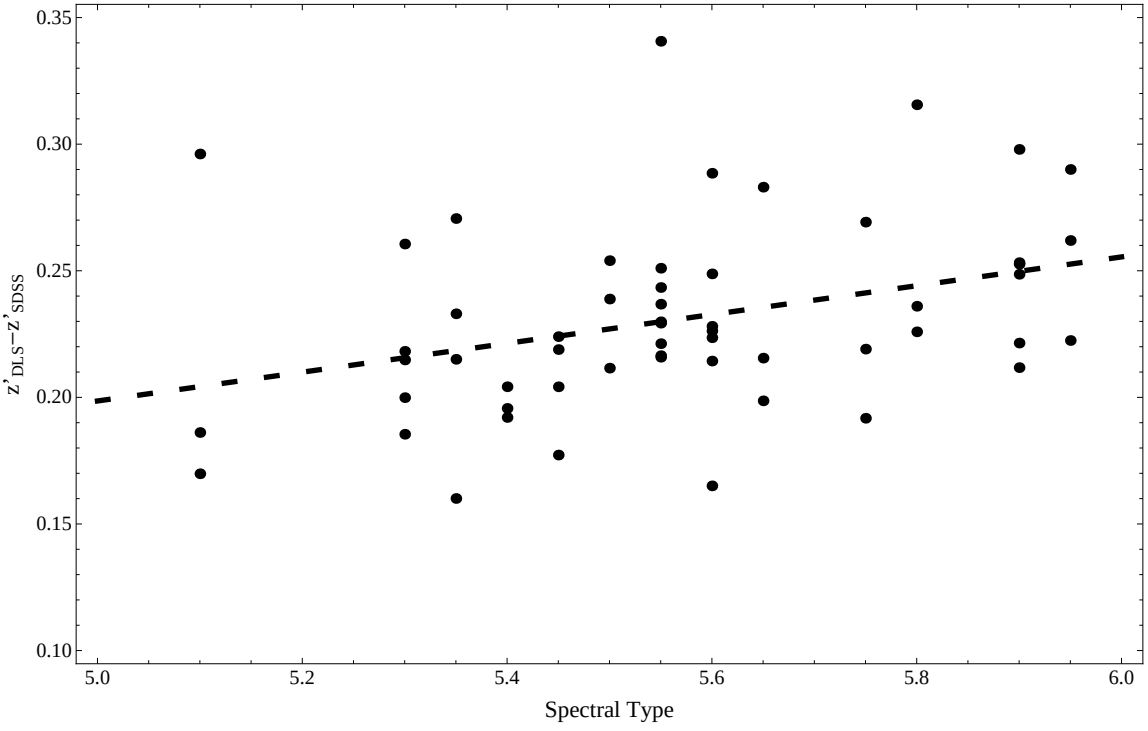

Figure 7.2: DLS z' – SDSS z' calculated from library spectra of various spectral types (L0=5.0). Shown as a dashed line is the linear fit used to correct z' values from Dahn et al. (2002) for use in typing cool dwarfs in the DLS.

are the colors of 27 L dwarfs, converted to $(R-z')$ in the DLS system, which can be combined with the results from the spectroscopic sample.

The objects observed by Dahn et al. (2002) also included six late M dwarfs, which were combined with the simulated colors of the reddest M stars included in the Pickles catalog and fitted with third-order polynomials in both $(R-z')$ and $(z'-J)$, as functions of spectral type. This constituted the "M dwarf" model, which was used to determine whether an object was of type later than M8 (i.e., suitable for the brown dwarf sample), and to obtain approximate spectral types for M3–M8 dwarfs.

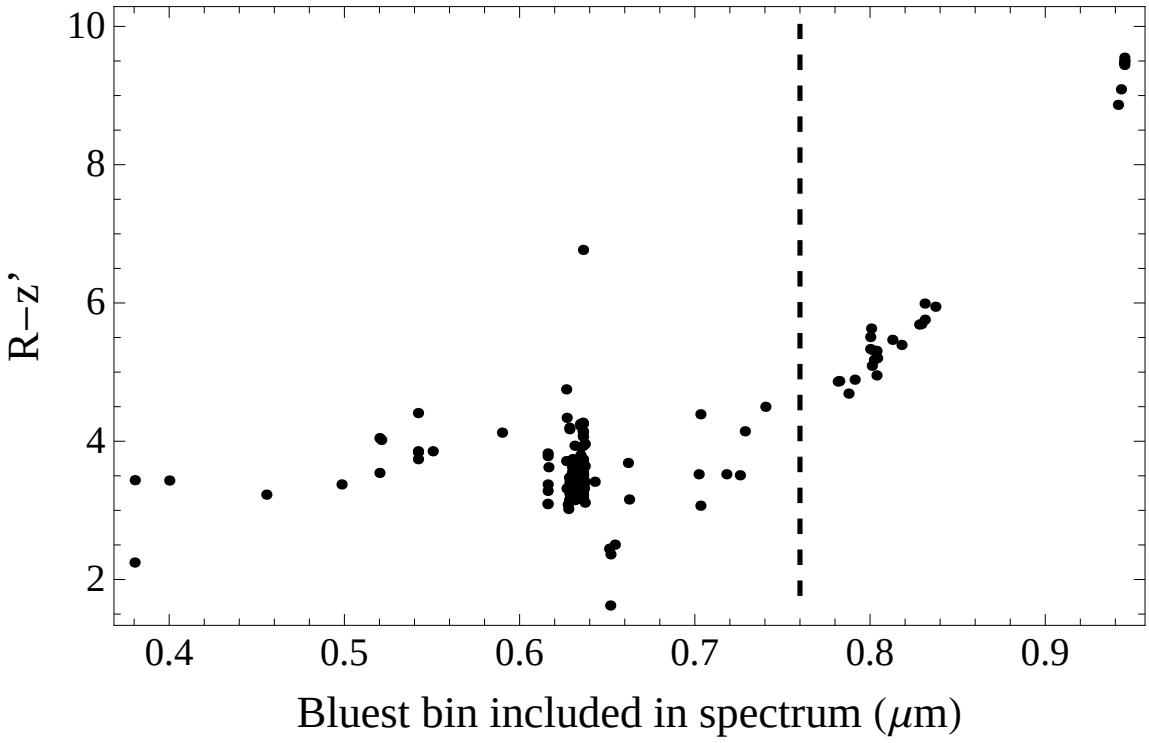

Figure 7.3: $(R-z')$ is plotted here as a function of the wavelength of the bluest data included in a given spectrum. Although the colors have significant scatter, there can be little doubt that spectra which lack data blueward of 0.76 μm are being artificially reddened by missing flux in the R-band.

7.2.2 Spectroscopic Colors

Using published spectra of M, L, and T dwarfs, we can convolve them with the response function of our CCD and filter set to synthesize colors for cool dwarfs in the DLS filters (Equation 7.2). The published spectra were drawn from Chiu et al. (2006), Golimowski et al. (2004), Knapp et al. (2004), McLean et al. (2003), Burgasser et al. (2003), Geballe et al. (2002), Wilson et al. (2001), Reid et al. (2001), Leggett et al. (2001), Noll et al. (2000), Gizis et al. (2000), Kirkpatrick et al. (2000), Tsvetanov et al. (2000), Reid et al. (2000), Martín et al. (1999), Strauss et al. (1999), Kirkpatrick et al. (1999), Leggett et al. (1999), Tinney et al. (1998), Oppenheimer et al. (1998), Golimowski et al. (1998), Ruiz et al. (1997), Kirkpatrick et al. (1997),

and Geballe et al. (1996).

As one might expect from such a heterogeneous sample, the spectra are from a wide variety of telescopes and spectrographs, and have correspondingly different ranges of wavelength where the data are reliable. To avoid using spectra to generate colors for filters in which they had invalid data, the minimum and maximum wavelength for each spectrum were plotted against the derived color. Ideally, there should be no dependence of object color on the range of wavelengths included in the spectrum, only on the spectral type of the object, so any trend in color with limit was taken as a sign that the integration was invalid, and objects beyond such limits were excluded (see Figure 7.3 for an example.)

The $(R - z')$ and $(z' - J)$ colors were calculated for all objects with valid wavelength ranges, and binned into 4 groups by spectral type: M9–L2, L2–L5, L5–L9, and T0–T8. These bins were selected as having relatively little change in $Rz'J$ color within the group, compared to the differences between groups. The T dwarfs have been plotted as a single group, despite having significant internal scatter, for two reasons: only 32 T dwarf spectra were available, making the use of smaller bins questionable; and exceedingly few T dwarfs are predicted to be detected by the DLS (< 0.5 T dwarfs predicted in the whole of F1, as calculated in Section 3.2). The colors of the objects in each group were then used to calculate a mean and standard deviation in each color, which would be used to assign a spectral type to each red object in the DLS sample (Figure 7.4).

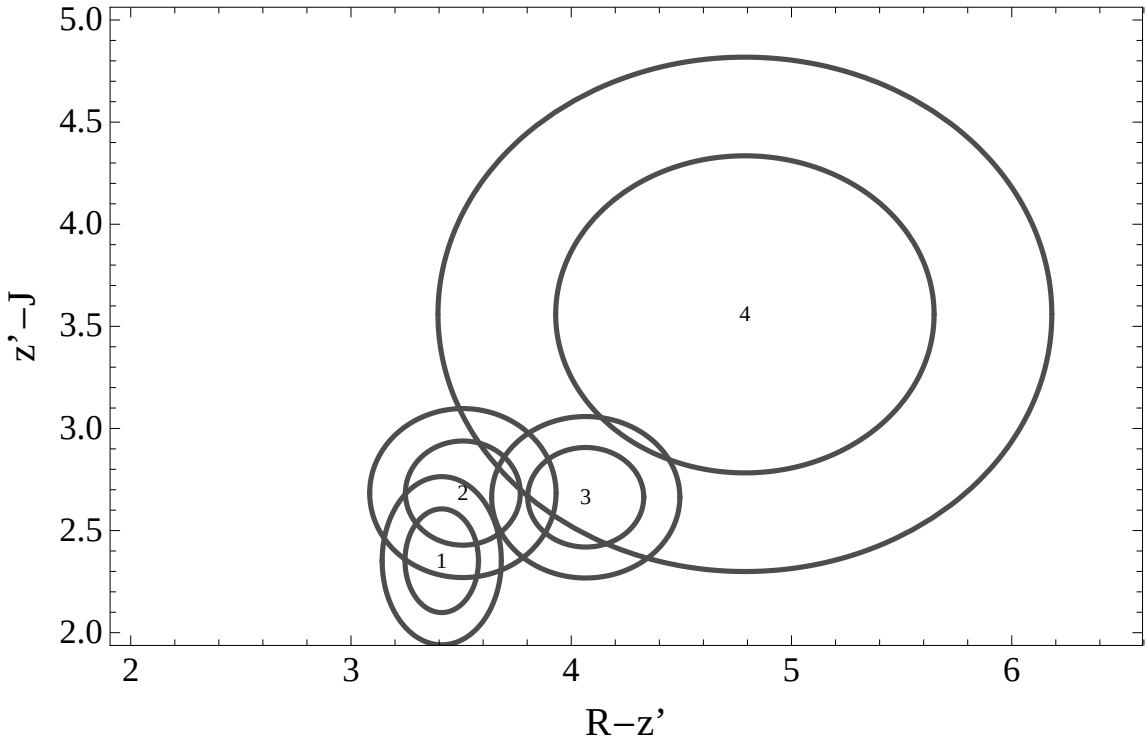

Figure 7.4: $Rz'J$ color-color plot for the brown dwarf color models. Contours indicate 1σ and 2σ from the mean colors of each spectral type bin: (1) M9–L2, (2) L2–L5, (3) L5–L9, and (4) T0–T8.

Chapter 8

Determining the Cool Dwarf Scale Height

In order to realize the goal of calculating the brown dwarf scale height based on our $Rz'J$ catalogs, the sample must be characterized, and each object assigned a probability of being a brown dwarf of a given type (Section 8.1). These probabilities can then be used to generate random realizations of the population, for comparison to a family of galactic models (Section 8.2). The best-fit models are described in Section 8.3, and are converted to exponential models for comparison to older results in Section 8.3.1. Finally, the ramifications of the results for existing and future surveys are considered in Section 8.4.1.

For this study, all objects included in the DLS F1 corrected Rz'J red objects catalog have been divided into four non-exclusive categories (Figure 8.1): the "survey sample," which includes all objects detected with $J < 21$ in the J-band survey imaging from WIRC; the "J-detected sample," which contains every z' object with a matched counterpart in J, including those drawn from the targeted FLAMINGOS imaging; the "J-dropout sample," those objects whose z' locations were imaged in J, but where no J counterpart was detected; and the "z-detected sample," which contains all other objects with measured $(R - z')$ colors, which were not imaged in J. The colors and magnitudes of these samples are shown in Figure 8.2.

8.1 Calculating Type Probabilities

The survey sample serves as our reference for determining the characteristic dispersions and magnitudes of the cool star, brown dwarf, and interloper populations (interlopers include red or reddened galaxies, high-redshift QSOs, and possibly other unknown contaminants.) The cool star and brown dwarf characteristic colors have been modeled using the procedure in Chapter 7, and the corrections described in Chapter 6 have been applied to the Rz'J catalog, to bring it into line with 2MASS photometric and stellar color standards. During catalog creation, each object was flagged with the source of its photometry (auto, aperture, limit, or incomplete); these

flags are used to separate the objects into samples. For example, the survey sample consists of all catalog objects flagged as having J photometry that is neither incomplete nor a 5σ limit, located in the WIRC subfields (p11, p21, p32, and p33), which have a corrected $J < 21$. This sample is used to create the probability distributions that are applied to the other samples in order to assign each object a probability of belonging to a given spectral class, designated $P(\mathrm{T})$ (for probability of type). The survey sample is used for this calibration because its members were not selected using any color, so their colors should be an unbiased representation of the colors of the underlying population. The remaining three object samples each have some observational bias based on $(R - z')$ color: the color was used to determine whether an attempt would be made to image the object in J, slightly altering the likelihood of finding a red or blue $(R - z')$ object in each sample; the J-dropout sample is also biased toward faint magnitudes and large $(z' - J)$. Nevertheless, every object in every sample has a measured R and z', which is used to construct its $P(\mathrm{T})$ based on our color models, so the effect of this observational bias should be minimal.

The survey sample was used to determine the standard deviation of M dwarfs from the model mean. To characterize interlopers, objects were excluded beyond 2.2σ from the M3-M8 dwarf model (Section 7.2), a value chosen to exclude noticeable interloper populations with both redder and bluer colors than the M dwarfs. Each non-interloper object in the survey sample was then assigned a definite spectral class, using the model with the smallest χ^2 value. It was necessary to assign these definite spectral classes for the survey sample, in order to generate the probability distributions to be applied to the other samples.

The survey sample was also used to determine all of the characteristics of the interloper class, including its magnitude distribution (called $P(\mathrm{T}|m_z)$, the probability of type for a given apparent z' magnitude) and two-dimensional probability distributions in $(R - z')$ and $(z' - J)$ colors (henceforward C_1 and C_2), which are called $P(\mathrm{T}|C_1)$, and $P(\mathrm{T}|C_2)$, each one the probability of an object being an interloper

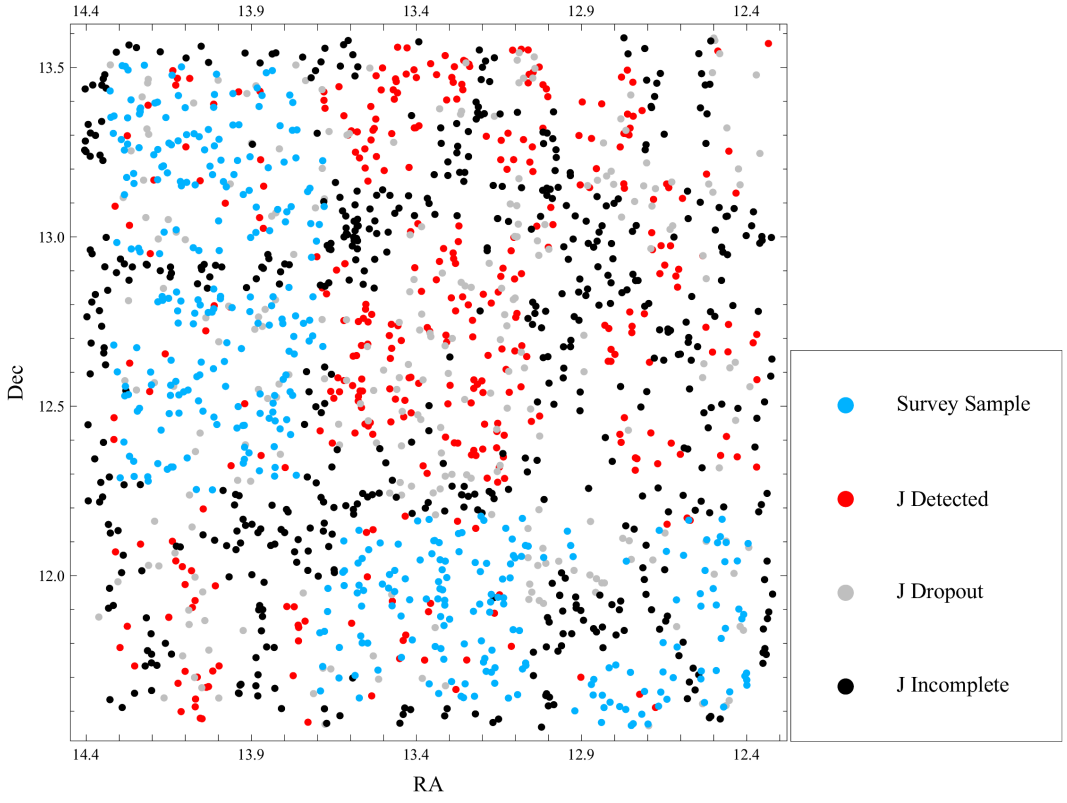

Figure 8.1: Sky positions of the objects in each catalog sample from F1. The blue points trace the WIRC survey imaging, while the red points are mostly objects detected by FLAMINGOS (or very faint WIRC detections). Black points (J Incomplete) trace the DLS F1 area not imaged with WIRC or FLAMINGOS. North is up, east is to the left.

given color C_1 or C_2. However, the fraction of non-dwarf interlopers (objects outside both the 2.2σ stellar locus region and more than 2.2σ from every MLT model) as a function of z' magnitude was essentially identical in the survey and J-detected samples (Fig. 8.3), so the interloper fraction was instead determined from the set of all J-detected objects, using the 2.2σ cut defined on the survey sample to determine interloper status.

Every object in the three remaining samples was then assigned a probability of belonging to each spectral type, based on its $m_{z'}$, C_1, and C_2. For the J-detected

sample, the probability was calculated from

$$P(\mathrm{T}) = \int_1^6 \mathrm{d}C_1 \int_0^6 \mathrm{d}C_2 P(C_1)P(C_2)P(\mathrm{T}|C_1, C_2), \tag{8.1}$$

where the $P(C_1)$ and $P(C_2)$ are joint error distributions (assumed to be Gaussian) about the measured colors, with an error floor of ± 0.02 magnitudes. (See Fig. 8.4.) As seen in the color-color plots, these limits of integration encompass our measured colors. These integrals were carried out numerically using *Mathematica* and the analytical forms of both normal distributions.

For the J-dropout sample, the probability was taken to be

$$P(\mathrm{T}) = \int_{-\infty}^{lim} \mathrm{d}C_2 \iint \mathrm{d}C_1 \mathrm{d}m_{z'} P(C_1)P(m_{z'})P(\mathrm{T}|C_1, C_2, m_{z'}), \tag{8.2}$$

where the $P(C_1)$ and $P(m_{z'})$ are magnitude error distributions about the measured magnitude or color (assumed to be Gaussian), and the C_2 integral is carried out up to the 5σ upper limit. For these objects, the numerical integral was combined with the $P(\mathrm{dwarf}|m_{z'})$ factor for the $m_{z'}$ bin into which the object fell, and the $P(\mathrm{dwarf}|C_1)$ for their $(R - z')$ bin, as calculated from equal-count bins of the J-detected sample (see Fig. 8.5). These integrals are calculated for each model, giving a complete set of normalized probabilities of the object belonging to each type. (See Fig. 8.6.)

For the z-detected sample, where the objects were not imaged in J at all, the integral used was

$$P(\mathrm{T}) = \iint \mathrm{d}(C_1)\mathrm{d}(m_{z'})P(C_1)P(m_{z'})P(\mathrm{T}|C_1, m_{z'}), \tag{8.3}$$

where the $P(\mathrm{T}|C_1, m_{z'})$ has been summed over all values of C_2 to model our complete ignorance of that color. (See Fig. 8.7.)

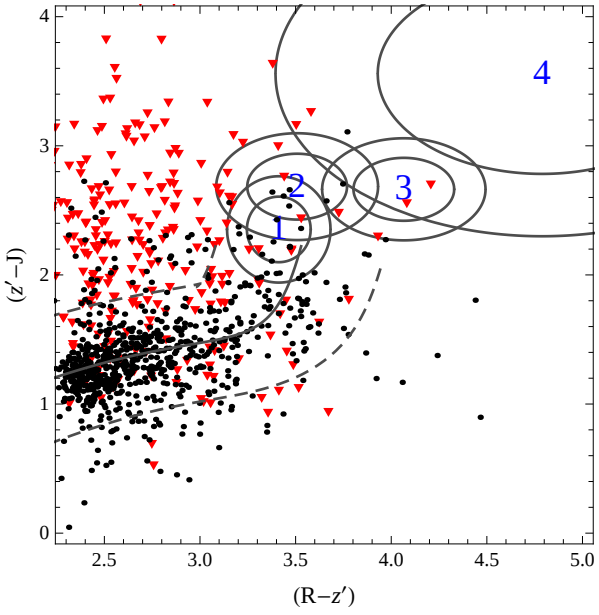

(a) $(R - z')$ vs. $(z' - J)$ for the J-detected sample (black points) and J-dropout sample (red triangles). Track at the lower left indicates the mean stellar locus, with dashed 2.2σ contours, while 1) – 4) are the models for M9–L2, L2–L5, L5–L9, and T dwarfs, respectively, showing 68% and 95% contours.

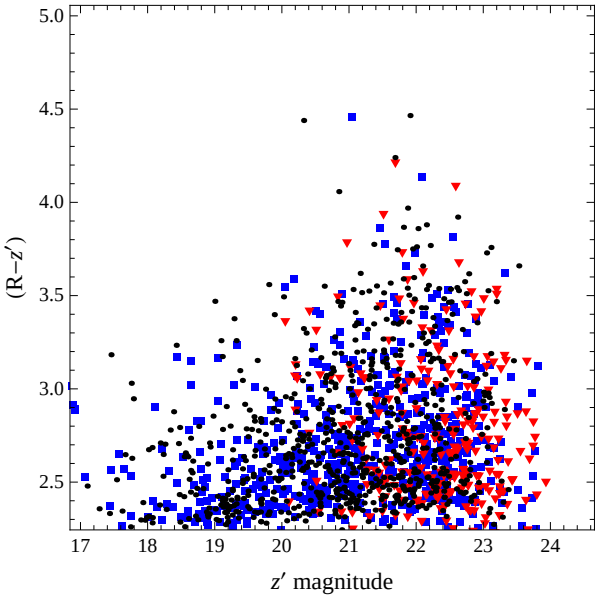

(b) Color-magnitude diagram showing the J-detected and J-dropout samples (symbols same as above) and adding the z'-detected sample (blue squares). J-imaging incompleteness for red objects ranges from 41% for relatively blue sources down to 18% for red sources.

Figure 8.2: Colors and magnitudes of z'-detected objects.

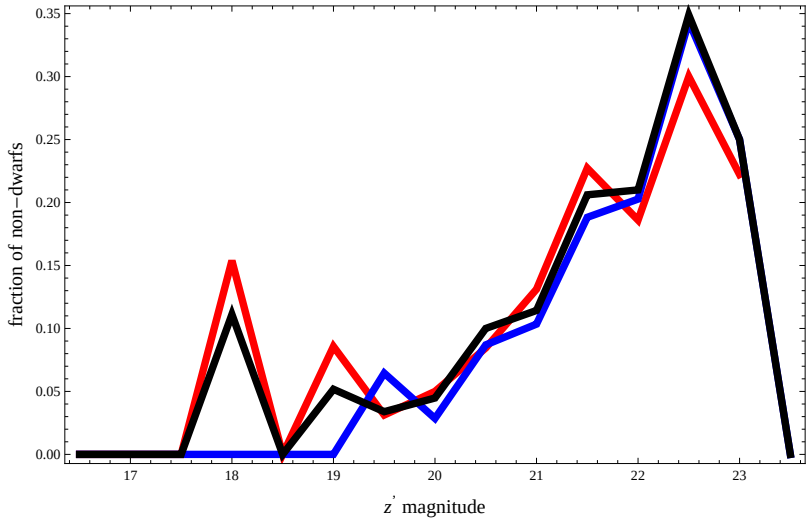

Figure 8.3: Fraction of objects flagged as "interlopers" ($> 2.2\sigma$ from any model) in each magnitude bin. Red is measured on the FLAMINGOS fields only, blue on the WIRC fields only, black on the whole sample. The trend appears similar in all three samples, so all J-detected objects (the largest sample) have been used to determine the interloper rate.

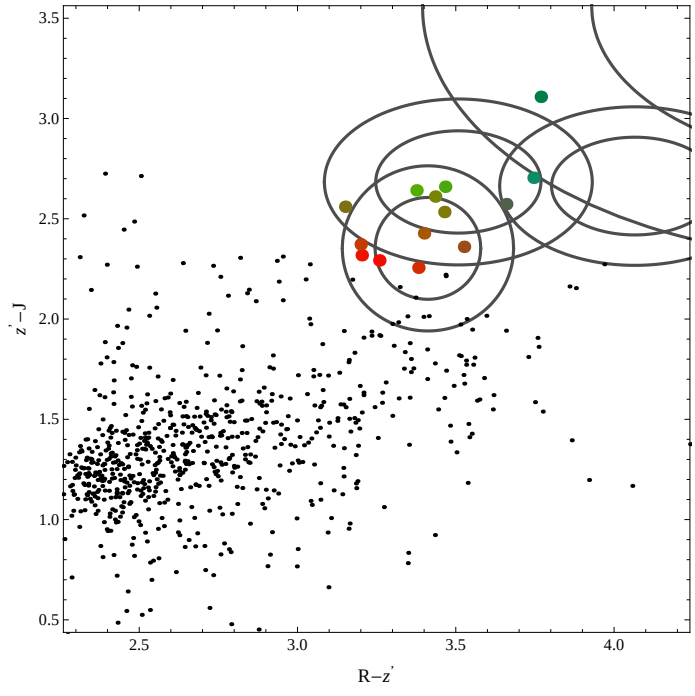

Figure 8.4: Color-color plot for J-detected sample, showing the assigned P(T) for each object later than M9 as an RGB color: red represents the probability that an object is a M9–L2 dwarf, green for L2–L5, blue for L5–L9. Contours show the 1σ and 2σ ranges of each model. The entire J-detected sample is shown with small black points for reference. Black points were not assigned colors or probabilities if they were determined to be of spectral type earlier than M9 in the stellar locus model fit; while this conservative cut may introduce incompleteness in the sample, the greater risk is of the much more common M8 and earlier dwarfs masquerading as M9 and later due to intrinsic color variations or photometric error.

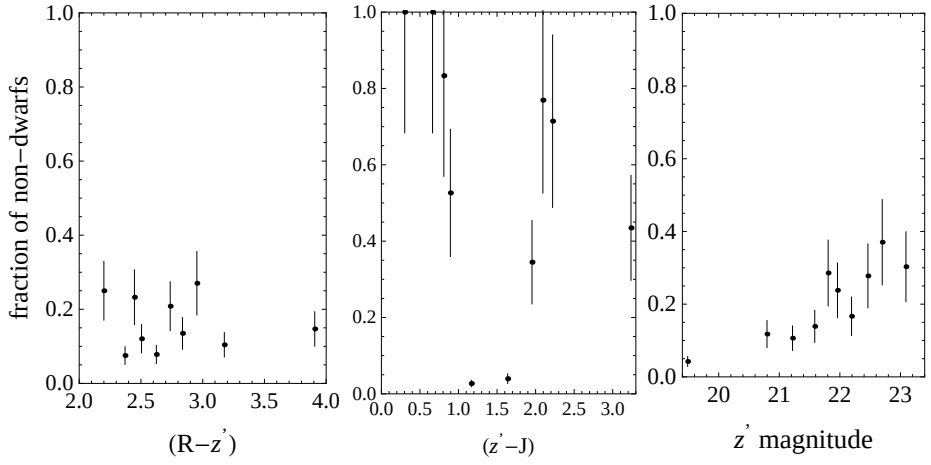

(a) $(R - z')$ (b) $(z' - J)$ (c) z' magnitude

Figure 8.5: Probability that an object is not a dwarf (i.e. an interloper) as a function of color and magnitude. Bins contain equal numbers of outliers, which should result in equal Poisson errors on the outliers in each bin. The dip where $1.0 < (z' - J) < 2.0$ results from the overwhelming stellar locus population at that color, making the presence of non-dwarfs extremely unlikely.

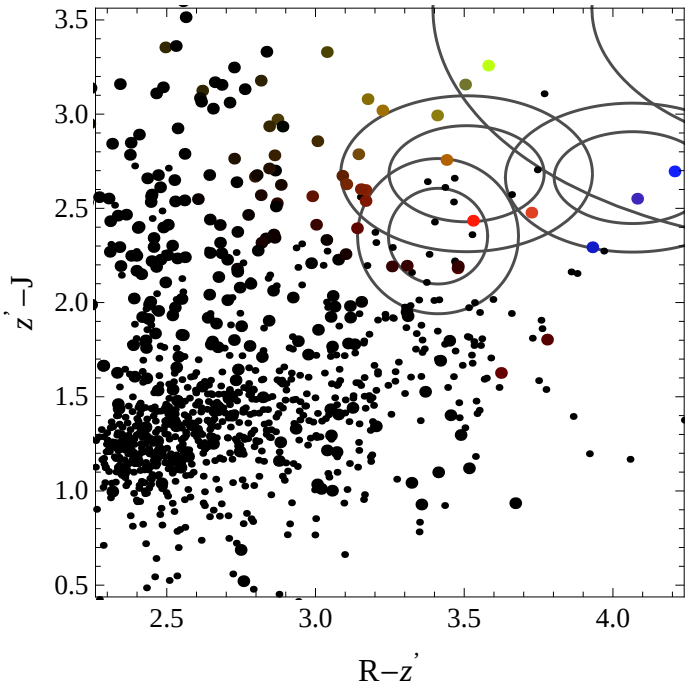

Figure 8.6: Color-color plot for J-dropout sample, showing the assigned P(T) for each dropout object (plotted at the 5σ $(z' - J)$ limit) as an RGB color: red represents the probability that an object is a M9–L2 dwarf, green for L2–L5, blue for L5–L9. Colors have been normalized to the maximum probability in the sample, as these probabilities tend to be very small. Contours show the 1σ and 2σ ranges of each model. The J-detected sample is shown with small black points for reference, while larger black points are J-dropout objects with no significant model probabilities; black points were not assigned colors or probabilities if they were determined to be of spectral type earlier than M9 in the stellar locus model fit; while this conservative cut may introduce incompleteness in the sample, the greater risk is of the much more common M8 and earlier dwarfs masquerading as M9 and later due to intrinsic color variations or photometric error.

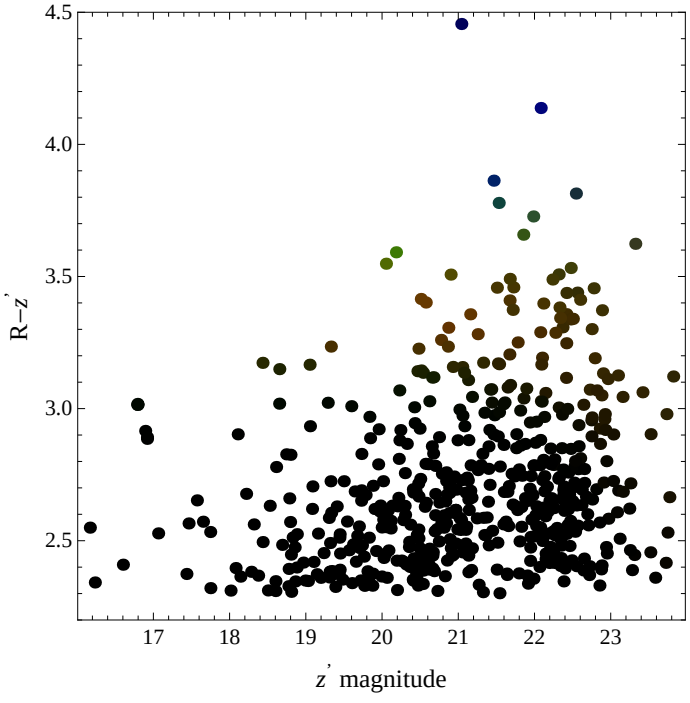

Figure 8.7: Color-magnitude plot for J-incomplete sample, showing the assigned P(T) for each object as an RGB color: red represents the probability that an object is a M9–L2 dwarf, green for L2–L5, blue for L5–L9. Colors have not been normalized to the maximum value in the sample, so their darkness is indicative of low overall probabilities.

8.2 Galactic Model

Although a small number of halo ultracool dwarfs have been detected (Burgasser et al., 2008; Cushing et al., 2009) the field population is expected to be dominated by a single disk component (e.g. Pirzkal et al., 2005), modeled as an isothermal disk with density

$$\rho(r,\theta,z) = \rho_0 \exp\left(-\frac{r}{R_0}\right) \operatorname{sech}^2\left(\frac{z}{Z_0}\right), \tag{8.4}$$

where ρ_0 is the density at the midplane of the galaxy, (r,θ,z) are cylindrical galactocentric coordinates, and R_0 and Z_0 are a scale radius and height, respectively. This scale height should not be confused with the exponential scale height, Z_S, which performs a similar rôle in the simplified exponential model,

$$\rho(r,\theta,z) = \rho_0 \exp\left(-\frac{r}{R_0}\right) \exp\left(-\frac{z}{Z_S}\right). \tag{8.5}$$

While the asymptotic behavior at large z indicates $Z_0 \simeq 2Z_S$, the actual relationship between the two scale heights is somewhat more complex, particularly where z is of the same order of magnitude as the scale height, as it is for our samples. For direct comparison to older surveys, the equivalent exponential scale heights will be calculated in Section 8.3.1. To avoid confusion, Z_0 will be referred to as the scale height, and Z_S as the exponential scale height, throughout this chapter.

Porcel et al. (1998) found $R_0 = 2100$ pc, so for the line of sight through our field we would traverse nearly 5 kpc in the vertical direction for every one scale radius, allowing us to neglect the radial variation in density as long as $Z_S \ll 5000$ pc. This is almost certainly a fair assumption, as the thickest measured part of the galactic stellar disk has a scale height less than 1000 pc.

Following Bahcall (1986), the surface density of stars, A_T of a given type T can be calculated from

$$A_T d\Omega = \int_{-\infty}^{\infty} dm' \int_0^{\infty} dR R^2 P(\mathrm{D}|m') \rho(R,M) \phi(M) d\Omega, \tag{8.6}$$

where $P(\mathrm{D}|m')$ is the completeness as a function of magnitude (probability of detection given m'), ϕ is the luminosity function, and ρ is the spatial distribution as a function of heliocentric distance R. In this integral, the absolute magnitude, M, is replaced with the expression for $M(m', R) \equiv m' - 5\log_{10}(R/10 \text{ pc})$ wherever it appears. Our models will be constructed using the solar neighborhood luminosity function, with no added variation with distance; while this would be a definite misstep for very distant ($R >> Z_0$) brown dwarfs (where we would expect a complete absence of objects just below the hydrogen-burning mass limit, which would cool before they had a chance to be scattered away from the Galactic midplane), the current sample of L2 and later dwarfs is believed to lie within 300 pc of the Sun (see Figure 8.16), and should be reasonably well-represented by the local density.

For a given scale height Z_0, the number of objects between heliocentric distance d and $d + \delta$ is

$$nd\Omega = \rho_0 \int_d^{d+\delta} \mathrm{sech}^2((z_\odot + x\sin b)/Z_0)x^2 \mathrm{d}x d\Omega, \tag{8.7}$$

which can be normalized by the total number of objects to give a probability of an object existing in that particular distance bin (which we will call $P(\mathrm{O}|d)$, the probability of an object existing within a shell of thickness δ located at a heliocentric distance d). We have adopted $z_\odot = 27$ pc north of the Galactic midplane. By comparing observations to this $P(\mathrm{O}|d)$, the scale height can be measured without the need for the effective area A or the midplane density ρ_0, which enter only as normalization constants; the shape of the distance histogram is itself a measure of scale height (Figure 8.8).

It is not sufficient for the object to exist in this distance bin; it must also be detected by the survey. Completeness as a function of apparent magnitude was determined by running Source Extractor on the DLS z' images with 10^4 point sources added at intervals of 0.1 mag, from $z' = 20$ to $z' = 26$, using precisely the same settings as the original z' catalog. Test stars were added on a regular grid, to aid in

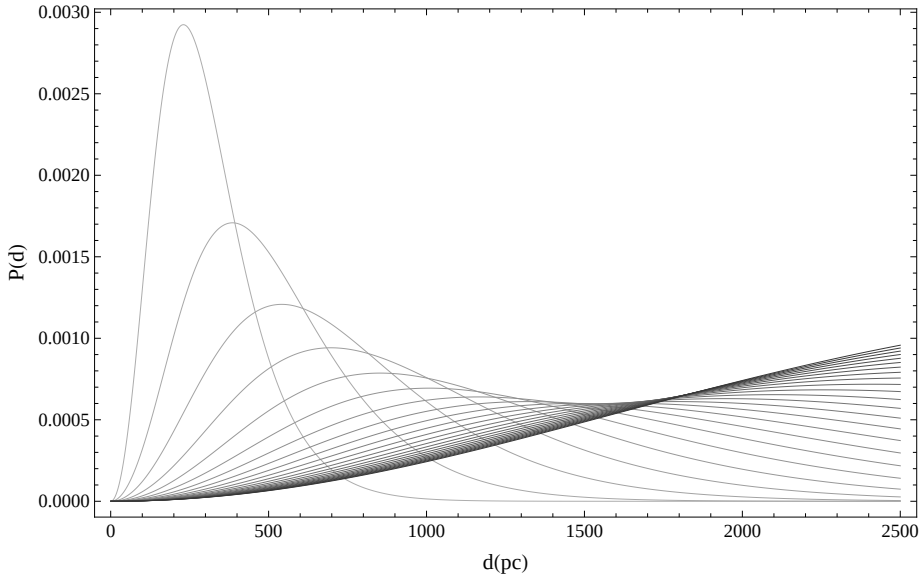

Figure 8.8: Normalized probability distributions for a variety of scale heights, from 150 pc to 2500 pc (narrowest to widest curves). The y-axis gives the normalized probability of finding an object in a given 1 pc bin. The plotted curves are the product of the differential volume ($\propto d^2$) and the density of a sech^2 profile of the given scale height, integrated in 1 pc increments along the line-of-sight of F1.

identifying them in the catalogs, but this causes some unlucky stars to land directly atop imaging artifacts or saturated stars (in which case they are never detected), and others in regions which were not imaged by DLS, and thus have no noise (in which case they are always detected.) Both of these are effects which are location-dependent, not magnitude-dependent, so they would be rightly considered as part of a determination of the area imaged by the DLS, but not as part of a completeness function; objects which were always detected or never detected have therefore been excluded from the analysis. Completeness for all 9 subfields is shown in Figure 8.9; this figure also contains the PSF model, which was created from an observed isolated star from a z' image (its apparent cuspiness is an artifact of plotting pixellated data as a surface). Fairly strong detection criteria have been used in SE (1.5σ in 9 contiguous pixels), reducing the depth of the survey slightly, in order to obtain a larger proportion of clean detections. The completeness will be included as $P(\mathrm{D}|m_z)$

(the probability of a detection, given an object of apparent magnitude $m_{z'}$).

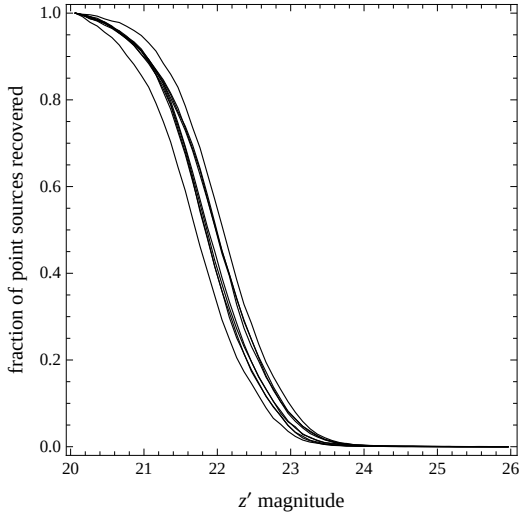

(a) Source Extractor recovery fraction for 10^4 test stars of each input magnitude, in 0.1 magnitude increments. Each $40^{'} \times 40^{'}$ subfield of DLS F1 is plotted separately. Test stars which were always detected or never detected have been excluded from this analysis.

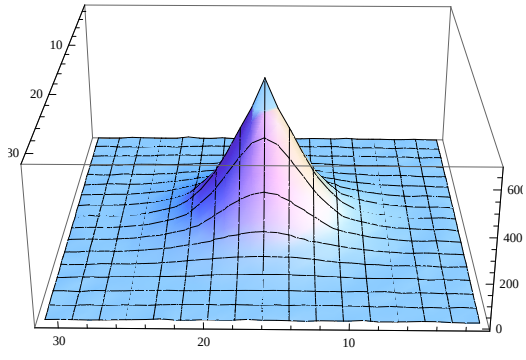

(b) PSF model used for completeness test. The model was created by rotating a selected z' star in 10° increments and coadding it with itself, to generate a very-low-noise, circularly symmetric model of the z' PSF to be co-added with the DLS stacks.

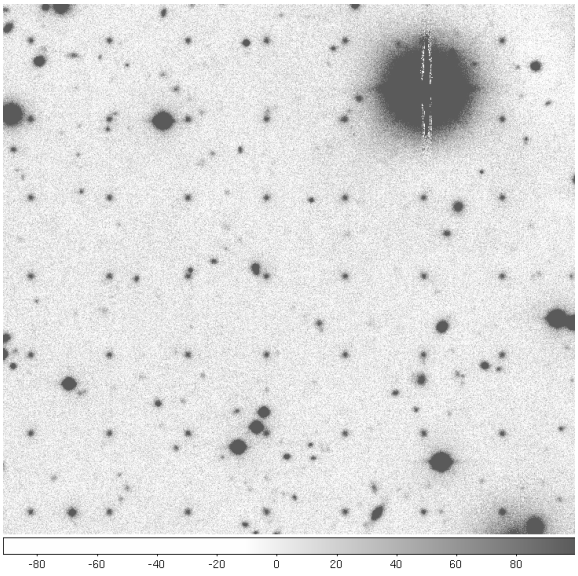

(c) Example DLS image stack (F1p12) with 21$^{\text{st}}$ magnitude stars added on a regular grid, for the completeness test.

Figure 8.9: Components of the completeness test.

The last step handled in the distance model is $P(m_z|d, \mathrm{T})$ (the probability that an object of type T, located at distance d, will have a measured magnitude m_z), which can be determined from the distance modulus and the luminosity function $\phi(M)$. The z'-band luminosity function was determined from the Dahn et al. (2002) M_J/spectral type relation, the spectral library $(z' - J)$ colors, and the relative local density of the spectral types in the solar neighborhood from Cruz et al. (2007). The M_J/spectral type relation was used to estimate the absolute J magnitude of each object in the brown dwarf spectral library which had reliable $(z' - J)$ colors, and the $(z' - J)$ color added to M_J to determine $M_{z'}$. These points were fitted with a second-order function of spectral type, and the RMS scatter was measured to be 0.22 magnitudes, no larger than Dahn's original RMS scatter in the M_J relation. Using this RMS scatter as the width of a normal distribution, each single spectral type (L1, L2, L3, and so on) was weighted by its local space density, summed over a range of spectral types, and normalized to obtain $\phi(M_{z'})$ (or $P(M_{z'}|T)$, the probability of a dwarf of given type having absolute magnitude $M_{z'}$; see Fig. 8.10).

For the T dwarfs, the luminosities and densities from Metchev et al. (2008) were used. Magnitude distributions were constructed for M9–L2, L2–L5, L5–L8, T0–T8, as well as M9–L5, for comparison with earlier studies which binned all late types. The resulting model detection probability,

$$P(\mathrm{D}|\mathrm{T}, d, Z_0) = \int \mathrm{d}m_z P(\mathrm{D}|\mathrm{O}, m_z) P(\mathrm{O}|d, Z_0) P(m_z|d, \mathrm{T}), \tag{8.8}$$

was calculated at 1 pc intervals and normalized to its sum for every model, sampling the scale height at 10 pc intervals. The three terms in the integral are identical to the terms in Equation 8.6: the probability of detection, given that an object of magnitude m_z exists (completeness); the probability of an object existing in a distance bin d given scale height Z_0 (model density); and the probability that an object will have a particular m_z given its distance and type T (luminosity function). Integrating over the whole range of magnitudes detectable by the survey then gives a $P(\mathrm{d})$ which can be measured at the locations of the detected objects to obtain the

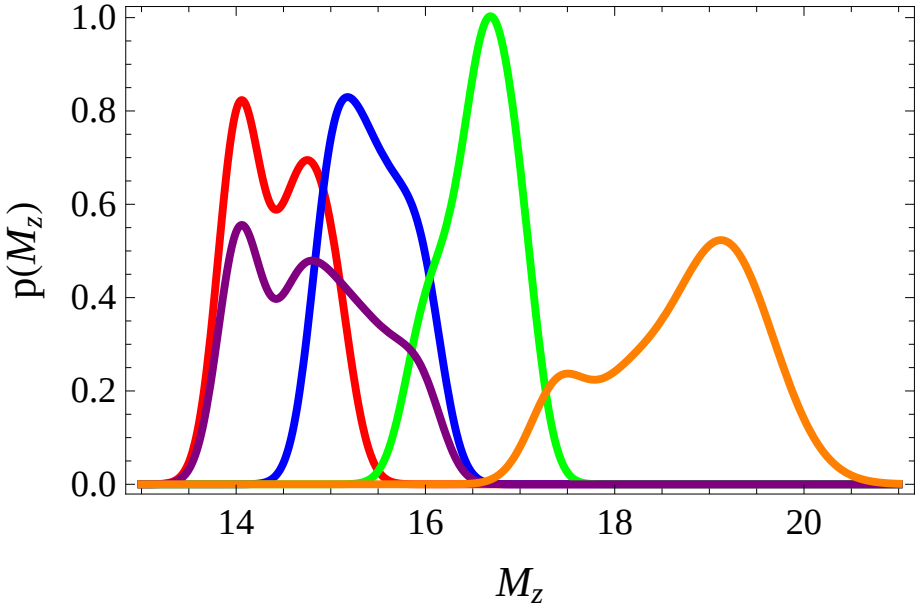

Figure 8.10: Normalized probability of an object having a given absolute magnitude $M_{z'}$, assuming it belongs to a range of spectral types (red: M9–L2, blue: L2–L5, purple: M9–L5, green: L5–L9, orange: T0–T8). These were constructed based on the local luminosity function, by including the same relative proportions of each spectral type as appear in the solar neighborhood sample of Cruz et al. (2007). Absolute z' magnitudes were determined from published M_J values and our calibrated $z' - J$ colors for each spectral type.

total likelihood of those observations. The best-fit models are shown in Figure 8.16.

8.3 Comparison to Data

For each detected object, the type probabilities have been calculated as outlined in Section 8.1. Measured properties of each cool dwarf candidate, along with cut-out images, can be found in Section 10.1. In order to compare the data to the models, a $P(d|T, m_z)$ (the probability that the object lies at distance d) must be calculated for each object. During the completeness testing, a bias in the recovered magnitudes of faint objects was clearly seen (Figure 8.11).

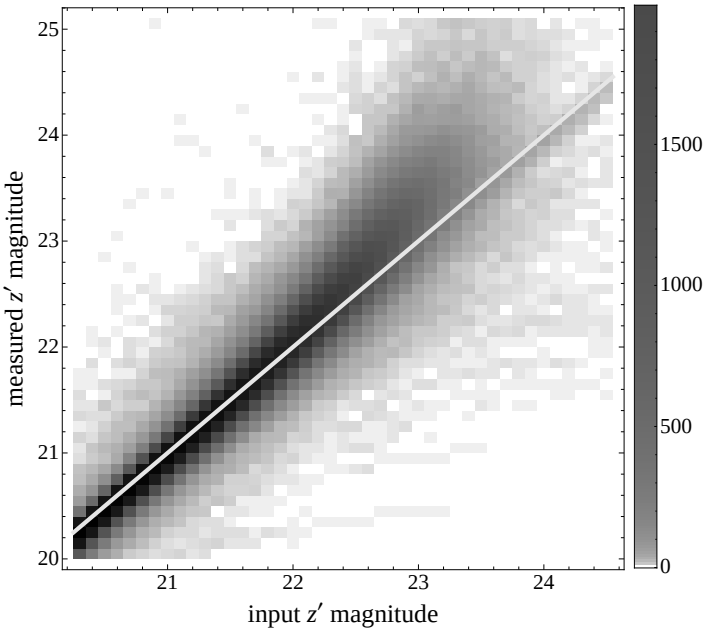

Figure 8.11: Histogram of input and Source Extractor measured magnitudes for 10^4 test stars, shown in 0.1 magnitude bins; the line indicates $m_{\rm input} = m_{\rm output}$. Test stars which were always detected or never detected have been excluded from this analysis.

To prevent this magnitude bias from biasing the distance estimates, the ordinary probability of m_z (typically assumed to be the measured magnitude of each object plus a Gaussian scatter) was replaced by the normalized probability of that object originating in some other magnitude bin. Bins 0.1 magnitude wide in m_z were used for both the true (m_z) and measured (M_z) magnitudes, for objects fainter than $z' = 20.3$; for brighter objects, where nearly all objects were measured in the same 0.1 magnitude bin as their true values, Gaussian errors were adopted, based on the reported Source Extractor magnitudes and errors (with a floor of ± 0.02 mag). For every object, the distance probability distribution was calculated using

$$P(d|\mathrm{T}, \mathrm{M}_z) = \int P(m_z|\mathrm{M}_z) P(m_z|\mathrm{T}, d) \mathrm{d}m_z. \tag{8.9}$$

The integral is replaced with a sum over all possible origination bins for $\mathrm{M}_z > 20.3$. This results in a P(d) for each object and type (e.g. Fig. 8.12).

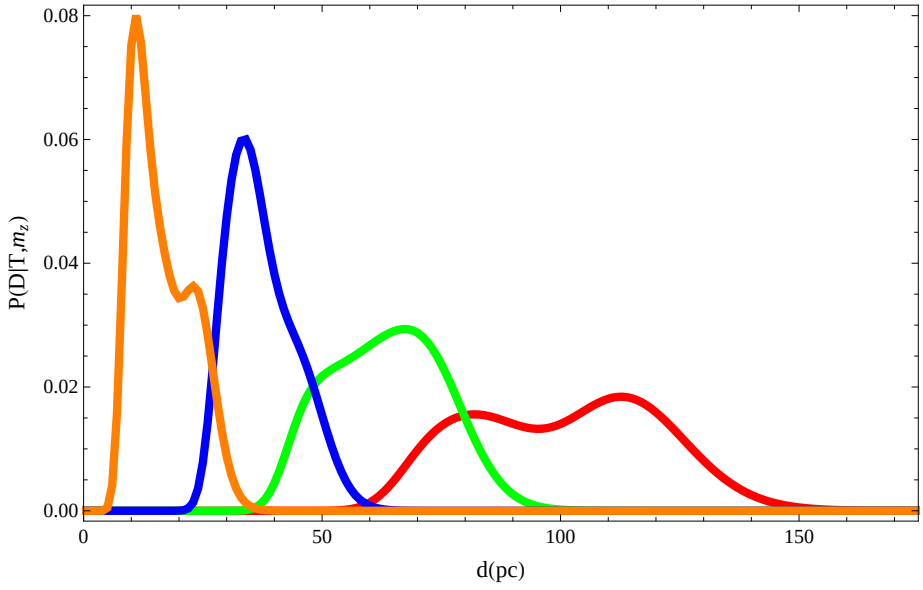

Figure 8.12: The distance probabilities for a single object, one for each possible type (red: M9–L2, blue: L2–L5, green: L5–L9, orange: T0–T8.)

These $P(d)$ and $P(T)$ are used to construct Monte Carlo realizations of the data. A random type is drawn from the $P(T)$ for each object, corrected for the possibility of type misidentification by applying a prior probability of each spectral type based on their local prevalence and the model scale height, and the distance to each object is randomized to a value drawn from its own $P(d|T)$. Two objects which had K_S-band imaging or spectral identification as late L dwarfs (see Chapter 10) were forced to have appropriate spectral types in all realizations.

The probability of a given scale height model being correct is then the simultaneous probability of the observations d_i, or

$$P(Z_0|\mathrm{T}) = \prod_{i=1}^{N} P(\mathrm{D}|\mathrm{T}, d_i, Z_0) \tag{8.10}$$

for each realization. Summing the realizations gives the likelihood density at each value of Z_0. If the chosen type is earlier than M9, or interloper, the object is not included in that realization. This leads to products with more or fewer terms, which must be corrected to allow for a proper comparison. To treat products equally,

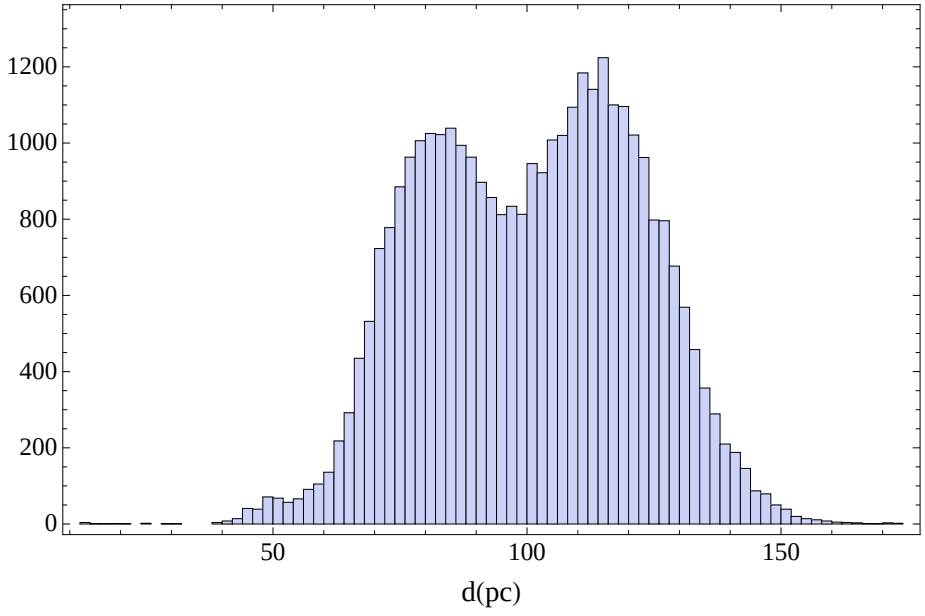

Figure 8.13: Histogram of simulated distances for the object from Fig. 8.12 from 33,333 realizations (1/3 of the total number of simulated realizations.) Based on the distribution, it is clear that the object has been assigned a high probability of belonging to the M9–L2 sample.

regardless of the number of factors, we use a geometric mean:

$$P(Z_0) \propto \left[\prod_{i=1}^{N} P(\mathrm{D}|\mathrm{T}, d_i, Z_0)\right]^{1/N} . \tag{8.11}$$

These probabilities were calculated for 10,000 realizations at each scale height, with the number of dwarfs for each of the four types averaging (52.08, 4.35, 2.14, 1.46), from earliest to latest.

8.3.1 Exponential Models

In order to properly compare results from the DLS with earlier estimates of the scale height which used a simplified exponential model, we have two options: either we can convert the values of Z_0 to the exponential scale height Z_S by using an empirical relation, or we can solve an entirely independent set of exponential models to

determine the best-fit exponential model for each range of spectral types. Whenever possible, we have chosen to fit the exponential models explicitly, as this should lead to the highest-quality values of Z_S; however, in the case of the M9–L2 sample, no exponential model was able to adequately explain the distribution of dwarf distances, and an empirical relation was used out of necessity.

A grid of exponential scale height models was assembled, using the integral in Equation 8.8, but with the exponential profile described in Equation 8.5 used in place of the sech^2 vertical variation. These models were then used to calculate the simultaneous likelihoods of the detections for 10,000 random realizations, with misidentification simulated in each realization as described above. The results are plotted in Figure 8.14, showing well-defined likelihood maxima for the L2–L5 and L5–L9 samples at 324 pc and 195 pc, respectively. The shape of the distance distribution for M9–L2 dwarfs was incompatible with the model predictions, leading to unphysical values of Z_S, so an alternative method was used to convert the measured Z_0 to Z_S. As shown in Figure 8.15, the density peak of the sech^2 distribution (although not its shape) can be matched, as a function of distance, by using a $Z_S = 0.6Z_0$. Applying this factor to Z_0 for the M9–L2 sample yields $Z_S \approx 345$ pc, which will be used for comparison to previous studies.

8.4 Results

The results for each spectral type bin are shown in Table 8.1: the most likely M9–L2 scale height is $Z_0 = 575^{+460}_{-150}$ pc, assuming a flat prior between 50 and 1500 pc for Z_0, while the L2–L5 scale height is only $Z_0 = 175^{+800}_{-70}$ pc, and the most likely L5–L9 scale height is 91 pc (see Figure 8.14 for details). Although very low scale heights are favored for T dwarfs, there is no definitive limit that can be placed on them by this study. The exponential models failed to adequately explain the observed data for M9–L2 dwarfs, but an empirical estimate can be obtained by demanding that the

two models have the same peak density as a function of distance: the equivalent Z_S for our measured Z_0 is 345 pc, which is consistent with both Ryan et al. (2005) and Pirzkal et al. (2005) at the 1σ level (their estimates were 350 ± 50 pc and 400 ± 100 pc, respectively.) The exponential model for L2–L5 dwarfs favored $Z_S = 324^{+740}_{-150}$ pc, not significantly lower than the M9–L2 value, while the most likely exponential scale height for L5–L9 dwarfs drops to $Z_S = 195^{+560}_{-100}$ pc. The poor upper limits for the scale heights based on this method are a natural result of magnitude incompleteness; once $P(\mathrm{D}|m_z)$ becomes the dominant term in the model, the distance distribution becomes insensitive to increasing Z_0 (as $\mathrm{sech}^2(\frac{z}{Z_0}) \rightarrow 1$).

A larger scale height for the M9–L2 sample would be consistent with the idea that a large fraction of this population is old and stellar. Any significant decrease in scale height between M9–L2 and the L2–L5 might indicate that the average hydrogen-burning limit for field L dwarfs lies somewhere between the first and second samples, causing a reversal of the increase in scale height with decreasing temperature that is observed for the main sequence; however, the large positive error bar on the L2–L5 scale height measurement precludes such a strong statement at this time. Although the lower mass of these substellar objects makes them more likely to be scattered out of the galactic plane, their short lifetimes ($\sim$ 1 Gyr, Baraffe et al., 2003) should result in a thinner disk than for more massive, but longer-lived ultracool dwarf stars.

8.4.1 Consequences for deep surveys

Ultracool dwarfs and brown dwarfs are contaminants for ground-based CCD dropout surveys, particularly for unresolved sources like $z > 5.7$ QSOs. The presence of field L and T dwarfs also confounds measurements of the initial mass function based on cluster surveys, unless cluster membership can be kinematically verified. Adopting an exponential scale height value of $Z_S = 330 \pm 3$ pc, as was done in Caballero et al. (2008), rather than using the best-fit sech^2 model for L2–L5 dwarfs, would lead to a

maximum overestimate of 6.1% in the number of field early L dwarfs along the line of sight to σ Orionis, a minor correction. However, a similar error in a survey of the depth of the DLS would result in a $\sim$ 17% reduction in the predicted number of L2 dwarfs, if we integrate the Caballero model and our best-fit out to 288 pc (the detection limit for an L2 dwarf in the DLS), with smaller reductions for later spectral types (due to their closer detection limits). Assume that our eight L2 and later dwarfs are the primary background for a QSO survey (such as the one carried out in Chapter 9) which would be expected to detect only a few QSOs per DLS field, but which lacks our J-band follow-up imaging, and cannot distinguish between brown dwarfs and high-z QSOs. Then this change in the number of L2 dwarfs (from a predicted 9.6 dwarfs down to 8) would introduce nearly as much error into the predicted red object counts as the entire predicted sample of QSOs.

Table 8.1: Comparison of sech^2 and exponential scale heights from the DLS to exponential scale heights from Ryan et al. (2005) and Pirzkal et al. (2005).

Spectral Types	Best-fit scale height (pc)	68% confidence interval (wide prior)	68% confidence interval (narrow prior)
Sech^2 Models	Z_0	Uniform prior 0–2500 pc	Uniform prior 0–1500 pc
M9–L2	575	380–1400	420–1040
L2–L5	175	100–1710	110 –1000
L5–L9	91	$<$ 2340	$<$ 1250
Exponential Models	Z_S	Uniform prior 0–1500 pc	Uniform prior 0–1000 pc
M9–L2	345*		
L2–L5	324	170–1060	180–760
L5–L9	91	100–1110	100–760
Previous Z_S Estimates	Z_S		
Ryan 2005	350$\pm$50		
Pirzkal 2005	400$\pm$100		

*Calculated using Z_0 to Z_S scaling relation, illustrated in Figure 8.15.

This new scale height also allows an updated evaluation of the total mass of L and T dwarfs in the Milky Way (Ryan et al., 2005). The solar neighborhood number density of M9–L9 dwarfs in the Cruz et al. (2007) sample (4.90×10^{-3} pc^{-3}) is substantially lower than the 120×10^{-3} pc^{-3} used by Ryan, but without a unique mass-spectral type relation, the mass function can only be approximated. In the 1–10 Gyr age range, the range of masses for objects above the hydrogen-burning limit is 0.07–0.09 $M_{\odot}$, while substellar L dwarfs range from 0.05–0.07 $M_{\odot}$. Using current values for the density, and restricting the count to M9–L9 dwarfs, we can integrate the single exponential scale height model from Ryan et al. (2005) to calculate $4.12 \pm 0.5 \times 10^9$ total dwarfs, which would have a maximum total mass of $3.30 \pm 0.4 \times 10^8$ M$_{\odot}$, assuming the largest likely mass of $0.08 M_{\odot}$ for each object; or $2.77 \pm 0.4 \times 10^8 M_{\odot}$ if a more moderate value of $0.06 M_{\odot}$ is adopted as the mass of L2 and later dwarfs. Integrating our best-fit model yields only 3.19×10^8 M9–L9 dwarfs, and reduces their total mass to $2.55 \times 10^8 M_{\odot}$ (if $0.08 M_{\odot}$ per dwarf is assumed) or $2.36 \times 10^8 M_{\odot}$ (if $0.06 M_{\odot}$ is adopted as the mass of L2 and later dwarfs). However, a random sampling of 10,000 values of the scale heights from our posterior probability distributions (using a flat prior with $0 < Z_0 < 1000$) indicates that the poor constraints on the L2–L5 and L5–L9 scale heights leave open the possibilty of a much more massive disk of brown dwarfs: $6.14 \pm 1.5 \times 10^9$ dwarfs, with a mass between $4.2 \pm 0.9 \times 10^8$ M$_{\odot}$ and $4.9 \pm 1.2 \times 10^8$ M$_{\odot}$, depending on the masses adopted for the type ranges (as above). This represents as much as a doubling in the total mass of L dwarfs, compared to earlier estimates, but they are nevertheless too few to serve as a significant reserve of baryonic dark matter for the Galaxy. However, the sample of distant T dwarfs in this study cannot rule out the existence of a significant disk of old T dwarfs (some of which might have masses near the hydrogen-burning mass limit), whose mass could rival or exceed the mass of the disk of L dwarfs.

8.4.2 Extrapolation to upcoming surveys

Next-generation deep optical surveys such as the Large Synoptic Survey Telescope[1] (Tyson, 2002) and Pan-STARRS (Kaiser et al., 2002) plan to image nearly the entire sky to unprecedented depths. Taking advantage of red-sensitive detectors and a larger mirror and field-of-view, LSST plans to observe 20,000 sq. deg. to a z' depth $\sim$ 1.7 magnitudes beyond DLS over the course of its 10-year main survey. The 1 micron y-band imaging from the LSST main survey should be able to supplant $(z'-J)$ colors for discrimination between interlopers and ultracool dwarfs. By adding a great deal of area, as well as measurements at a wide variety of galactic latitudes, these surveys should settle the question of the L dwarf scale height definitively, and even allow the study of L dwarf populations of different ages, identified kinematically.

An early estimate of the number of zy-detected brown dwarfs in the LSST sample was $\sim 70,000$, based on the assumption that 10% of the survey's M9 discoveries would lie below the hydrogen-burning mass limit, and using a uniform exponential scale height of $Z_S = 275$ pc to model the distribution of L and later dwarfs. If we assume that one-quarter of the anticipated two-band (zy) L dwarf detections (out of a predicted $\sim 35,600$ L dwarf detections) will belong to a $Z_0 = 175$ pc thin disk component, rather than the $Z_S = 275$ pc thicker disk, and integrate the disk models out to the z-band detection limit of an L5 dwarf (830 pc), we find that this number should be reduced by 13%, to $\sim 30,900$ predicted L dwarf detections. This calculation assumes LSST coverage between galactic longitudes 20° and 200° and for all areas $< 15°$ from the galactic plane, which is being mostly avoided due to source confusion and high extinction.

[1] http://www.lsst.org.

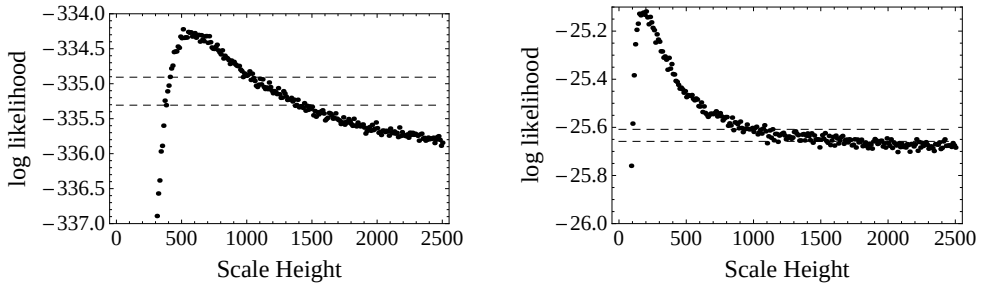

(a) M9–L2

(b) L2–L5

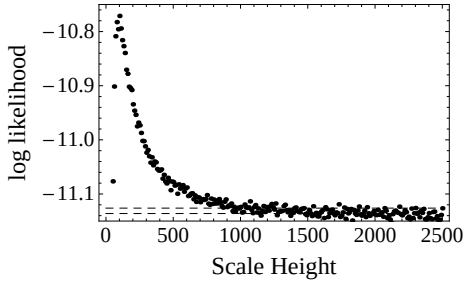

(c) L5–L9

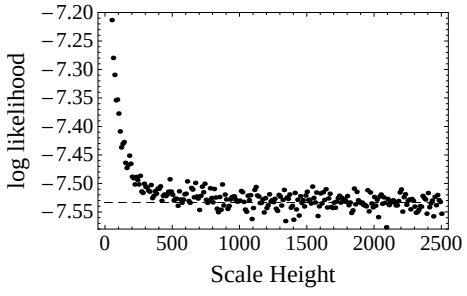

(d) T0–T8

Sech^2 models.

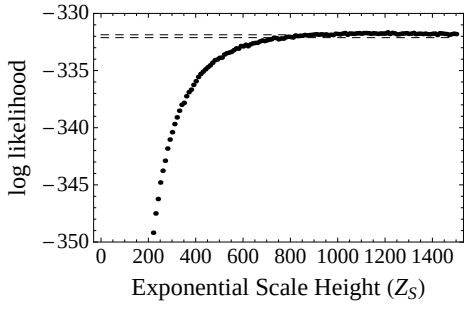

(e) M9–L2

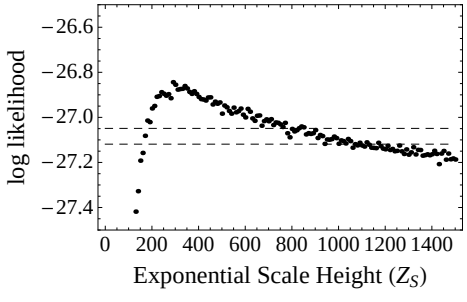

(f) L2–L5

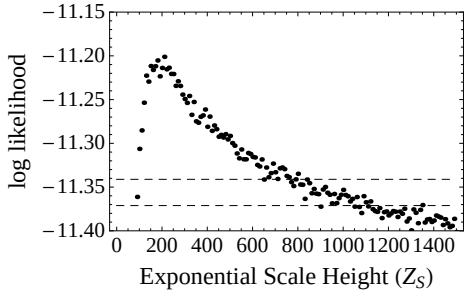

(g) L5–L9

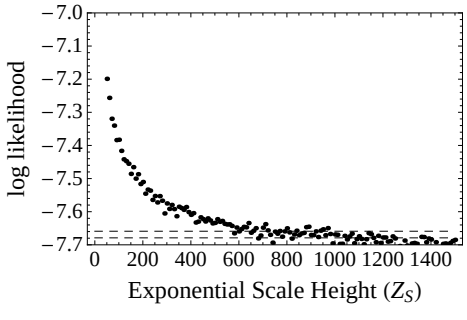

(h) T0–T8

Exponential models.

Figure 8.14: Log-likelihoods for sech^2 (top) and exponential (bottom) models, as a function of Z_0 or Z_S. Dashed lines show 68% confidence intervals using different priors: for the sech^2 models, a constant prior from 0–2500 pc (lower line) and 0–1500 pc (upper line); and for the exponential models, constant priors from 0–2500 pc (lower line) and 0–1000 pc (upper line).

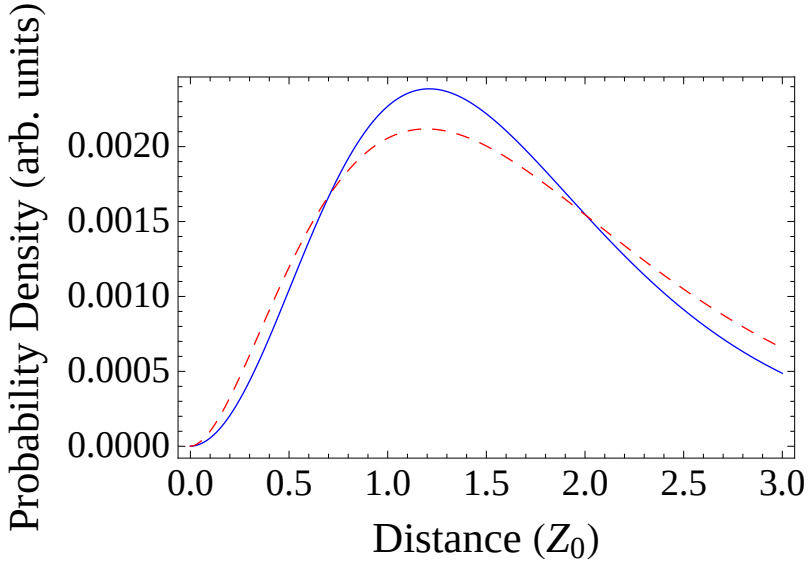

Figure 8.15: Density vs. distance for the sech^2 (solid blue line) and exponential (dashed red line) models. To achieve matching peaks in density, the exponential scale height here has been set to a numerically determined value of $Z_S = 0.6Z_0$, which will be used to convert the Z_0 for the M9–L2 sample to a Z_S value, for comparison with older surveys.

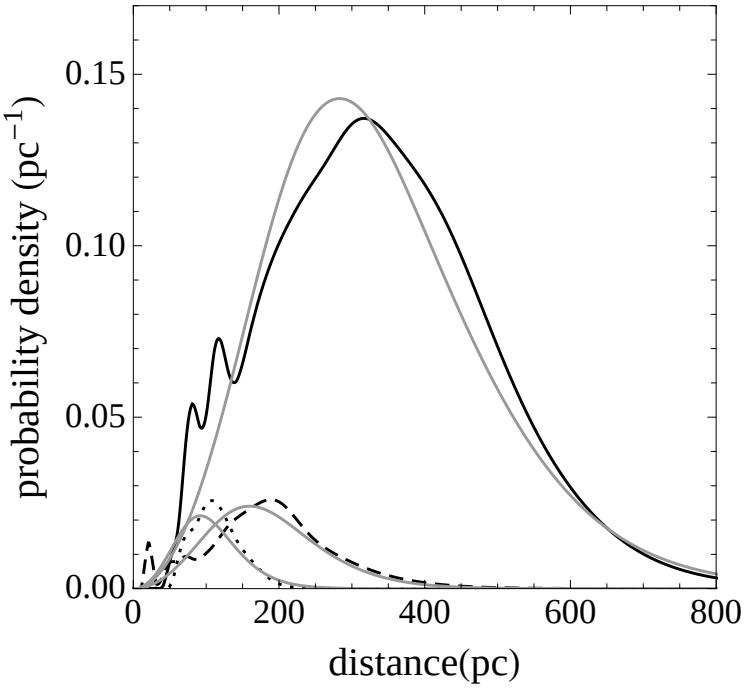

(a) Sech^2 models.

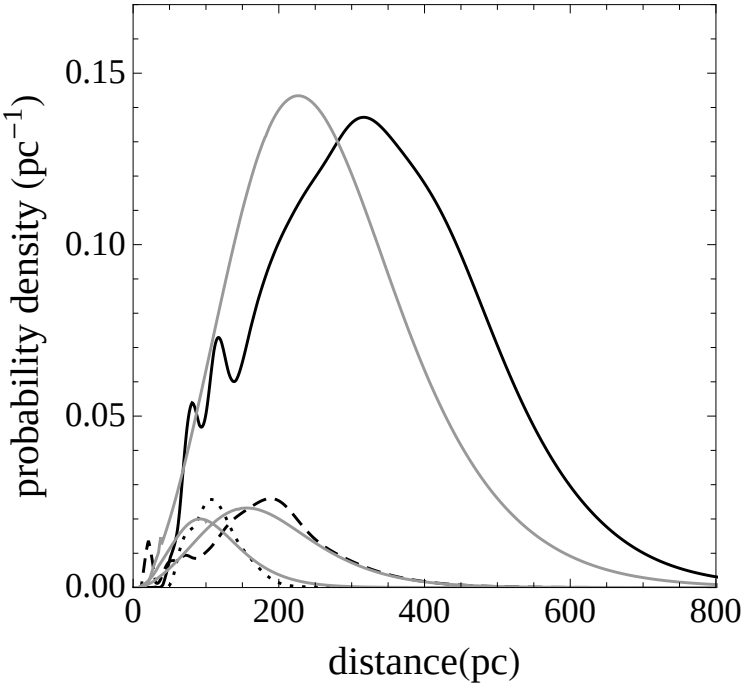

(b) Exponential models.

Figure 8.16: Probability density functions summed over all objects for M9–L2 (solid line), L2–L5 (dashed line), and L5–L9 (dotted line), giving the total probability of finding such an object in the given 1 pc bin. Best-fit models (shown in gray) have been normalized to data using a least-squares fit.

Chapter 9

Constraining the High-z QSO Luminosity Function

By adding J-band imaging to F1, we can now discriminate (at some level) between the dominant population of low-mass stars and brown dwarfs, and the distant, much more rare population of high-redshift QSOs ($z > 5.4$). Using the magnitudes of our sample, along with estimates of the probability that each object is a QSO (called $p(QSO)$), we can calculate the luminosity function for QSOs, which characterizes their prevalence in the early Universe. Although estimates of the high-z QSO luminosity function have been made previously, they typically involve large investments of 8 m telescope time (Willott et al., 2010) or apply to only the brightest QSOs (Jiang et al., 2009). By using photometric identification and redshifts, we can recover the luminosity function for much fainter sources, over a significant area. These techniques will also be essential for future projects, such as LSST, where spectroscopic follow-up to match the optical imaging survey may be impractical for many years to come.

In Section 9.1, we describe how each object in the catalog was assigned a probability of being a high-z QSO. We then use those probabilities to calculate the luminosity function for the WIRC-surveyed portion of F1, using a modified version of Schmidt's $1/V_a$ estimator (Section 9.2). Section 9.3 expands this analysis to the full area of F1, by making some assumptions about the portion of color space over which the sample is complete. Finally, likelihoods for the full two-parameter luminosity function are computed (Section 9.4), and the broader impact of our results is discussed in Section 9.5.

9.1 Characterizing the QSO Sample

In DLS Field 1, we have access to J-band imaging, which can be used to break the $(R - z')$ degeneracy between cool dwarfs and QSOs. Ideally, these QSO candidates would be subjected to spectroscopy, to search for emission lines and validate both their QSO identification and their redshift. Due to the faintness of these candidates,

Survey	area (sq. deg.)	z'-band depth (Vega)
DLS WIRC Surveyed Area	1.03	23.5
DLS WIRC & FLAMINGOS	2.47	23.5
CFHTLS Very Wide	150	20.7
CHFTLS Wide	171	21.9
CFHTLS Deep	4	24.1
SDSS Main	8423	20.0
SDSS Deep	260	20.5

Table 9.1: Areas and depths of earlier high-z QSO searches.

only an 8 m telescope (or larger) can carry out this follow-up, and indeed, a small sample of candidates was observed using the Low-Resolution Spectrograph (LRS; Hill et al., 1998) on the Hobby-Eberly Telescope (HET) at McDonald Observatory (see Chapter 10 for details). However, no QSOs were confirmed from this sample by spectroscopy, owing largely to the difficulty of the observations.

Instead, the QSO candidates in F1 will be assigned QSO probabilities, and the resulting probabilistic counts and magnitudes used to estimate the number of low-luminosity, high-redshift QSOs. Due to our J-band imaging, which brackets the Lyman-α emission feature at redshift 6, we expect very little contamination in our sample from narrow-emission-line galaxies, such as starburst galaxies at intermediate redshift, which have interfered with some narrow-band searches(Kakazu, 2008). Although these ultra-metal-poor galaxies might show higher levels of flux in the z'-band, mimicking the z'-band detection of a QSO, they would be unlikely to also supply enough line flux for an R-band detection (making them R-band dropouts). It might also be possible to mistake a Lyman-break galaxy (LBG; Sunyaev et al., 1978) for a QSO, based on its moderate spectral break at the Lyman limit ($\sim$1 magnitude break at 912Å rest-frame); however, the population of LBGs tends to be tremendously fainter than the population of QSOs, with only rare specimens known

at $I_{AB} < 24$ (Douglas et al., 2009). Some LBGs are also large enough to be resolved in $0.8''$ seeing, even at high redshift, although no explicit selection was made based on object shape in this study. Finally, the same intergalactic absorption that produces the highly asymmetrical Lyman-α line in QSOs also absorbs flux blueward of rest-frame 1216Å for LBGs, creating a Lyman-α break rather than a Lyman limit break. At these high redshifts, any break seen between R and z' would likely be a 1216Å break, requiring the LBG to lie at redshift $\sim$6, implying an even higher luminosity, and making the existence of such interlopers highly unlikely.

Instead, the main contaminant for this sample would be late-type stars, scattered into our color selection by intrinsic color scatter and photometric errors (as in Willott et al., 2009). To eliminate as many of these stars as practicable, proper weighting must be applied in color space: given the calculations in Chapter 2, we expect only a few QSOs per square degree, certainly fewer than 10 in DLS F1, while the $Rz'J$ data set consists of 1626 objects, predominantly M dwarfs. If we assume that the M dwarfs are normally distributed about a mean color track, then a cut made at a distance of 3.2σ would be expected to contribute no more than 1 false positive to the QSO distribution. However, as our sample contains not only 3-band detections, but J-band dropouts, it is important to create a complete color-color model of both QSOs and dwarf stars (see Chapter 7) which can be integrated along the unknown $(z' - J)$ color axis to obtain a probability for J-band dropouts. Each object was represented by a bivariate gaussian distribution, located at its measured position in color-color space. For objects contained in the imaging area, but undetected in J, the 5σ limit was used to construct a normalized probability distribution in $(z' - J)$, by placing an inverted normal distribution, $1 - \frac{e^{-(x-\mu)^2/(2\sigma^2)}}{\sigma\sqrt{2\pi}}$, five standard deviations redder than the measured limit, allowing the probability to go to unity with decreasing $(z' - J)$, then normalizing the resulting distribution over the area where the QSO and star probabilities are non-zero. The resulting convolution integrals represent the probability that a given object is a star or a QSO, assuming equal *prima facie*

probabilities of each population (a clearly incorrect assumption.) In order to correct this, we apply a prior probability for each category, based on its predicted population in DLS F1. Since the vast majority of objects in the field are non-QSOs, only a small error is made by normalizing the sum of the raw star probabilities, $p_i(\mathrm{star}|\ \mathrm{color})$ (the probability that object i is a star, given its color), to the total count of objects in the field:

$$p_i(\mathrm{star}) = \frac{N_{\mathrm{stars}}}{\sum_{i=1}^{n} p_i(\mathrm{star} \mid \mathrm{color})} p_i(\mathrm{star} \mid \mathrm{color}). \tag{9.1}$$

However, the same approximation cannot be used to normalize the QSO probabilities; for these, we normalize to the predicted counts of QSOs in each WIRC-surveyed subfield, given its imaged area and magnitude completeness. For the J-detected sample, where a selection has been made in $Rz'J$ color space, the models are integrated only over the area included in the QSO selection; for the J-dropout objects, the models are integrated over all $(R - z')$, but with a limit in the z' vs. $(z' - J)$ plane corresponding to $J > 21.4$ to replicate the 5σ detection limit (see Fig 9.1 for regions.)

$$p_i(\mathrm{QSO}) = \frac{\int_{zmin}^{zmax} \mathrm{d}z \phi_z(z) \frac{\mathrm{dV}}{\mathrm{dz}}}{\sum^{n} p_i(\mathrm{QSO} \mid \mathrm{color})} p_i(\mathrm{QSO} \mid \mathrm{color}). \tag{9.2}$$

In this equation, $p_i(\mathrm{QSO})$ represents the probability that object i is a QSO, ϕ_z is the luminosity function of QSOs, $\frac{\mathrm{dV}}{\mathrm{dz}}$ is the comoving volume element, derived from the standard cosmology, and $p_i(\mathrm{QSO} \mid \mathrm{color})$ is the unnormalized relative probability that object i is a QSO, based on its colors.

This procedure allows the probabilities to be normalized, but requires foreknowledge of the total number of QSOs predicted in the field, which has been determined using the luminosity function from Willott et al. (2010). Although this use of prior results seems as though it could allow contamination of this study, only the total number of QSOs is affected by this procedure, which is **not** the essential result of this study. The key result, the slope of the luminosity function, is derived from the relative numbers of QSOs in each luminosity bin, and not from the overall normalization of the bins. For this purpose, the QSO probabilities could have been left unnor-

malized; however, for ease of comparison, we have matched the normalization used by the most recent outside QSO studies. This may be considered merely a plotting convenience, to show that the slopes of the power law fits to the luminosity function are similar. Measured properties and cut-out images of the highest-probability QSO candidates can be found in Section 10.2.

9.2 $1/V_a$ Estimator: F1 Survey Sample

Having now all of the derived properties (rest-frame magnitude, redshift, probability, and completeness) for the red objects in the survey area of F1, we can apply the Schmidt (1968) estimator, in the improved form of Avni and Bahcall (1980):

$$\Phi(M_{1450}) = \sum_{j=1}^{N} \frac{1}{V_a^j} \frac{1}{\Delta M_{1450}}, \tag{9.3}$$

where

$$V_a^j \equiv \int_{\Delta M_{1450}} \int_{\Delta z} p(\text{detection}|M_{1450}, z) \frac{\mathrm{d}V}{\mathrm{d}z} \mathrm{d}M_{1450} \mathrm{d}z.$$

is the effective volume surveyed for objects matching the description of object j, ΔM_{1450} is the width of the magnitude bins into which the objects are separated, and $p(\text{detection}|M_{1450}, z)$ is the probability of detecting an object, given its luminosity and redshift (the completeness; see Figure 9.2). In this equation, M_{1450} is the absolute magnitude of an object, measured at rest wavelength 1450Å. Unlike a typical QSO sample, where binning the individual detections is the natural procedure, the result of a probability analysis is a continuous probability distribution in M_{1450}, which can be integrated in bins to obtain the equivalent measure. To construct this continuous distribution, we take

$$PDF(M_{1450}) = \sum_{j=1}^{N} p_j(\text{QSO}) p_j(M_{1450}|m_{z'}, z). \tag{9.4}$$

where $p(M_{1450}|m_{z'}, z)$ is the probability of an object having a luminosity M_{1450}, given its measured magnitude and estimated redshift. To obtain this probability, we take $p(m_{z'})$, calculated from the measured errors on z', and apply the K-correction (Section 2.4) to transform observed-frame z'-band magnitude to rest-frame M_{1450}, taking into account both the colors of the template QSO spectrum and the distance modulus to the estimated redshift.

Following Willott et al. (2010), we adopt a value of $k = -0.47$ from Fan et al. (2001b) for the redshift evolution of the overall QSO volume density, where

$$\Phi(M_{1450}, z) = \frac{10^{k(z-6)}\Phi(M^*_{1450})}{10^{0.4(\alpha+1)(M_{1450}-M^*_{1450})} + 10^{0.4(\beta+1)(M_{1450}-M^*_{1450})}} \tag{9.5}$$

where $\Phi(M^*_{1450})$ is the comoving density of QSOs at the break luminosity, M^*_{1450}, and β is the bright-end power-law index. The faint-end slope of the power law, conventionally represented here by α, is still beyond our power to resolve: many QSOs significantly fainter than the break luminosity are needed, and currently only one is known (and not from our sample). Instead, we will fix α and solve for the best-fit values of the bright-end slope, β, and the characteristic luminosity, M^*. It is important to note that these are not fundamental physical parameters, but only the values of a particular parameterization, and frequently depend on the manner in which the variables are fitted.

For comparison, we will also include the SDSS Deep Stripe sample of Jiang et al. (2009), which fitted a bright-end slope and normalization to the $z = 6$ QLF. The form of the luminosity function used by Jiang was

$$\Phi(M_{1450}) = \Phi^* 10^{-0.4(\beta+1)(M_{1450}+26)}, \tag{9.6}$$

which is equivalent to Equation 9.5 with $\alpha = \beta$, $k = 0$, and $M^* = -26$. In order to compare to our QSO sample, which covers a different redshift range, we have assumed the same redshift evolution as above, with the normalization Φ^* determined

at a stated characteristic magnitude of -26 and an assumed redshift of 6.0. For comparison to our sample, both comparison QLFs have been integrated in one-magnitude bins in M_{1450}.

The results of our binned analysis for the survey subfields are shown in Figure 9.3. For comparison, the results of the SDSS and CFHTQS high-z QSO searches are also plotted, with their best-fit luminosity functions integrated in bins to match the DLS data. The DLS points have been plotted with symmetrical statistical errors; however, as each bin contains less than one integrated QSO probability, the standard Poisson errors on the values might be considered to include zero as the lower 1σ limit for every bin. These can be considered worst-case error estimates. Nevertheless, the points are consistent with both the Jiang et al. (2009) and Willott et al. (2010) luminosity functions, at the 1σ level. Given our detection limits in F1 and large statistical errors, we cannot corroborate the latter paper's detection of a QSO break luminosity at $M_{1450} \approx -25.1$, but neither can our data rule out the double power law. Using the single power-law form, our best-fit slope is $\beta = -2.92 \pm 1.88$ (Figure 9.3, right panel), with the best-fit $\Phi^* = 2.04 \times 10^{-9}\mathrm{Mpc}^{-3}\mathrm{mag}^{-1}$ at $M^* = -26$, with a Monte Carlo error of 0.83 dex (Figure 9.4). (Here, as below, the Monte Carlo error has been determined by selecting random samples of the QSO candidates according to their QSO probabilities, then carrying out the analysis on each random sample.) This is consistent with the normalization that was forced on the probabilities, which can be estimated from

$$\Phi(-26) \approx \frac{\int \Phi(-26, z)\frac{\mathrm{d}V}{\mathrm{d}z}\mathrm{d}z}{\int \frac{\mathrm{d}V}{\mathrm{d}z}\mathrm{d}z} = 2.19 \times 10^{-9}\mathrm{Mpc}^{-3}\mathrm{mag}^{-1},$$

where our best-fit single power law has been assumed, along with the Willott et al. (2010) M^* and Φ^*, in order to determine the normalization at $M_{1450} = -26$. This normalization should be trivially identical to theirs, as their integrated prediction was used to normalize our probabilities; however, the value of β depends only on the relative density of QSO probability in each magnitude bin, so the measurement

of β should be independent of the normalization. Nevertheless, the fact that our QSO power-law slope can be recovered from three DLS subfields that are predicted to contain less than a single QSO may indicate either that the normalization of the current QSO luminosity functions is too low, or that the luminosity function of non-stellar backgrounds in F1 follows the same power law predicted for high-z QSOs.

Possible errors in this determination include contamination from misidentified non-QSO sources in the DLS. As a check on this possibility, we have repeated the binning procedure and comparison to the CFHTQS luminosity function while reddening the $(R - z')$ limits, which eliminates the lowest-redshift part of the QSO track as well. If contamination from stellar sources or red elliptical galaxies were a significant effect, it would be worst for the bluest $(R - z')$ colors, where the stellar $(z' - J)$ colors are closest to QSO colors, and where a moderate intrinsic reddening could scatter an elliptical galaxy at redshift 1 into our $(R - z')$ selection (it would require a color excess of E$(R - z')\sim 0.5$, corresponding to E$(B - V)\sim 0.45$, which would be plausible for a dusty galaxy). The results of moving the color selection 0.1 and 0.2 magnitudes redder in $(R - z')$ are shown in Figure 9.5. The resulting best-fit values for β were not significantly steeper than for the survey sample, -3.42 ± 2.46 and -3.62 ± 2.54 for the respective limits, with most of the change due to the brightest bin (which is strongly affected by the selection criteria.) Neglecting the brightest magnitude bin, the fits for the redder color cuts are $\beta = -3.15 \pm 3.92$ and -3.13 ± 3.86, respectively.

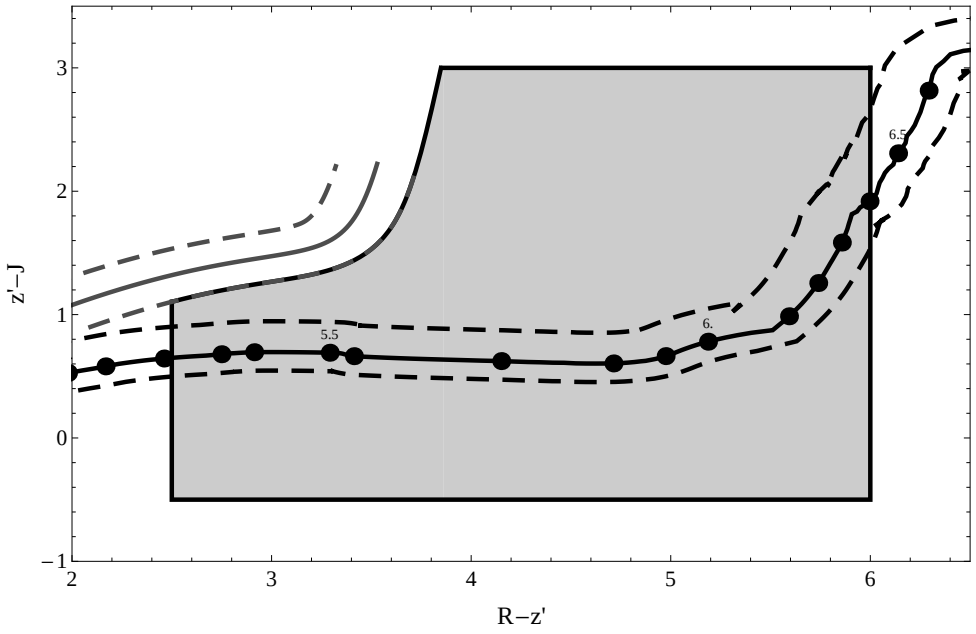

(a) $(z' - J)$ vs. $(R - z')$ color-color plane, showing the selection region for QSOs (shaded) with the stellar locus (upper left, with 1σ spread) and QSO track. Star and QSO models were integrated over this region before normalizing to the total density from Willott et al. (2010). Although the QSO track takes up only a small portion of the shaded area, there are both J-dropouts and J detections found in the space between the stellar and QSO colors, which should be included in the total normalization despite their low QSO probabilities.

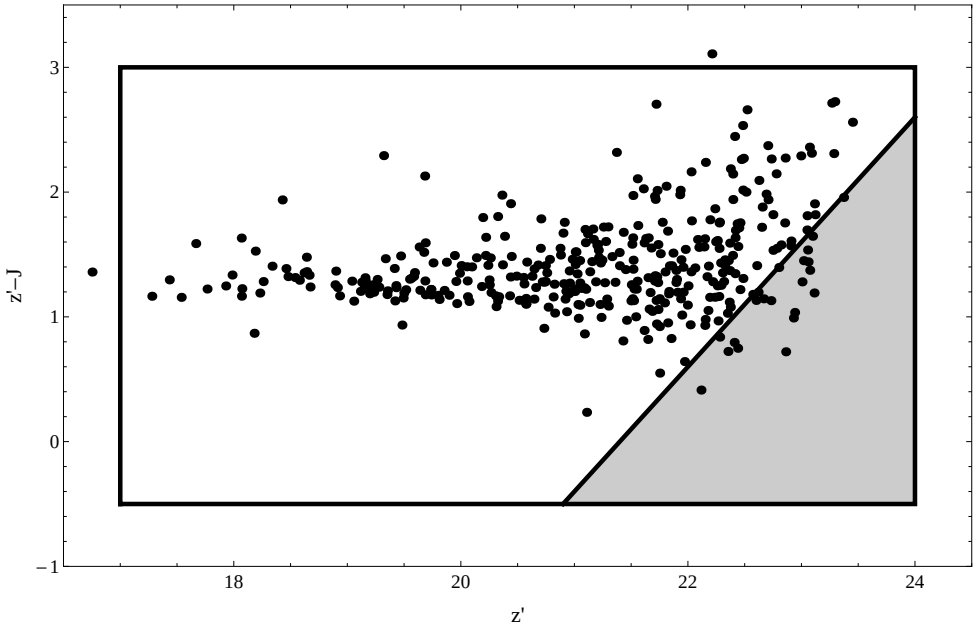

(b) Color-magnitude diagram showing $(z' - J)$ vs. z' integration boxes used for estimating QSO probability normalization in the J-detected (unfilled) and J-dropout (shaded) samples. Plotted for comparison are the colors of all 381 J-detected objects in the WIRC-surveyed DLS F1 subfields.

Figure 9.1: Model integration regions for estimating probability normalization.

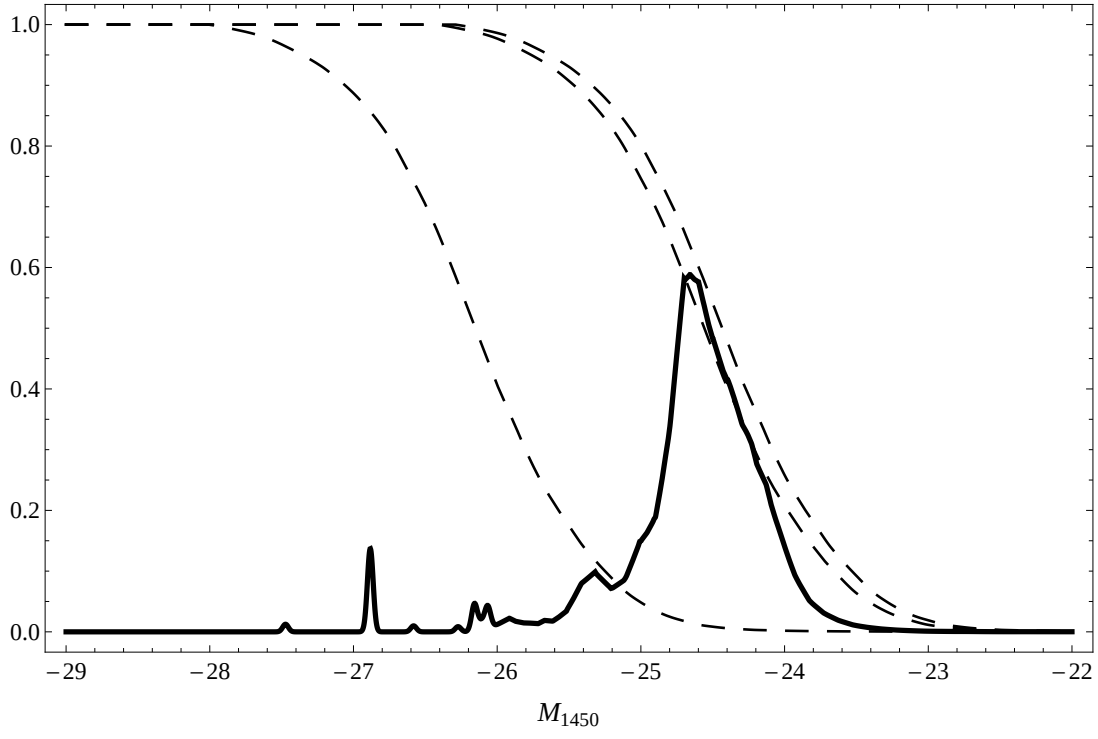

Figure 9.2: Probability density (solid line) and completeness (dashed lines) for the survey area of DLS F1, as a function of M_{1450}. Completeness is shown for redshifts 6.4, 5.7, and 5.2 (left to right). The sharp peaks in the probability density mark the locations of individual high-probability bright QSOs.

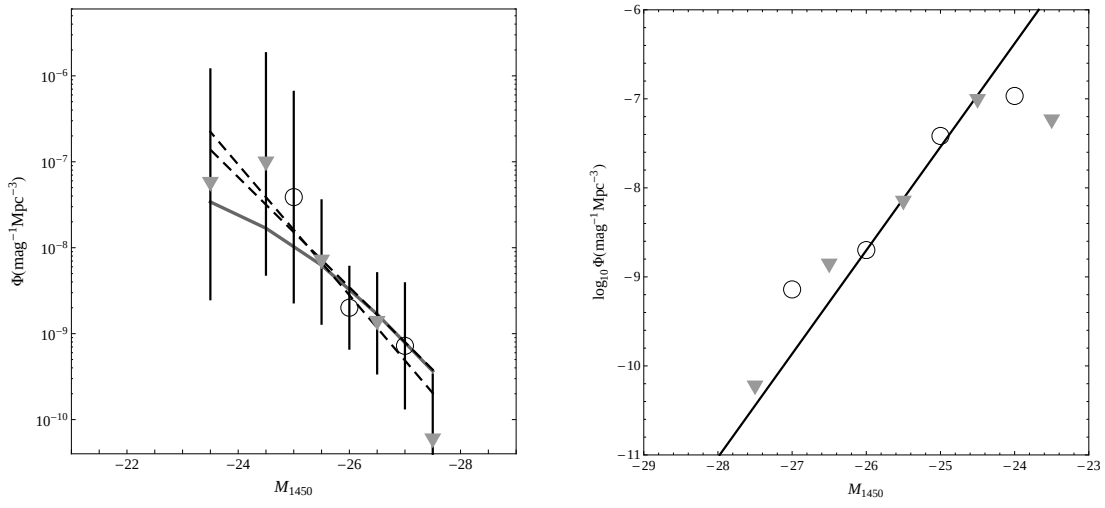

Figure 9.3: Binned luminosity function (left) and best-fit power law (right), determined by a least-squares fit to the logarithm of the density, for two different choices of bins (circles and triangles), using the DLS data. Lines in the left panel show three other measurements of the luminosity function, Willott et al. (2010) in gray, two possible power-law fits from Jiang et al. (2009) as dashed lines, binned to the same resolution as the DLS points. "Worst case" errors are shown (see Table 9.2). The Jiang et al. (2009) power-law fits for $z = 6$ have been extrapolated to our lower redshifts using a $k = -0.47$ redshift evolution, as in Equation 9.5.

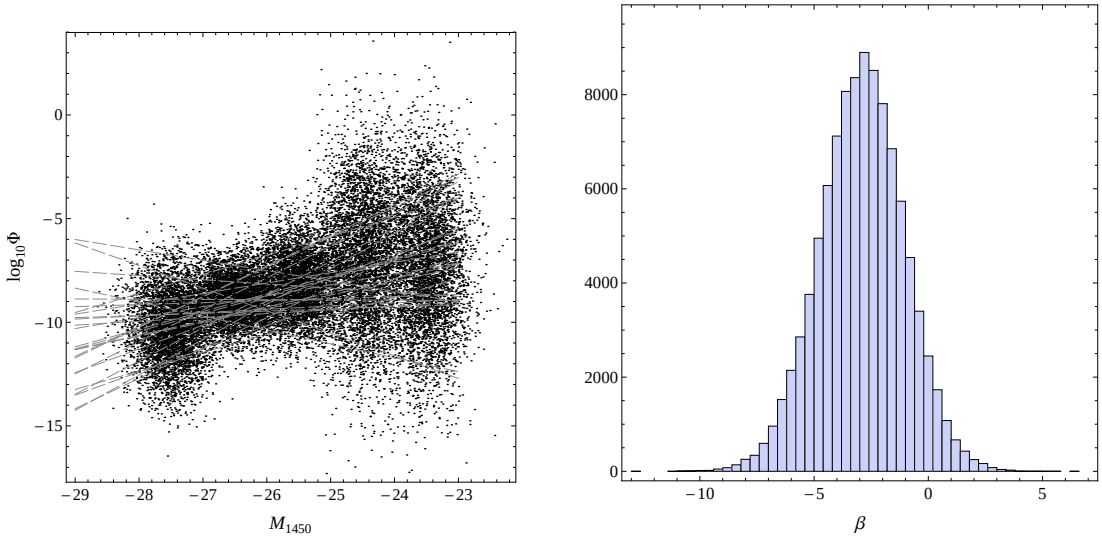

Figure 9.4: **Left:** 5000 of 100,000 random resamplings of the binned DLS QSO counts, with 25 random best-fit lines overplotted. The objects in each luminosity bin were resampled according to the estimated error on the bin count, and the best-fit slope of the power law was recalculated for each realization, to determine the final error distribution. **Right:** Histogram of derived values for β from those resampled data.

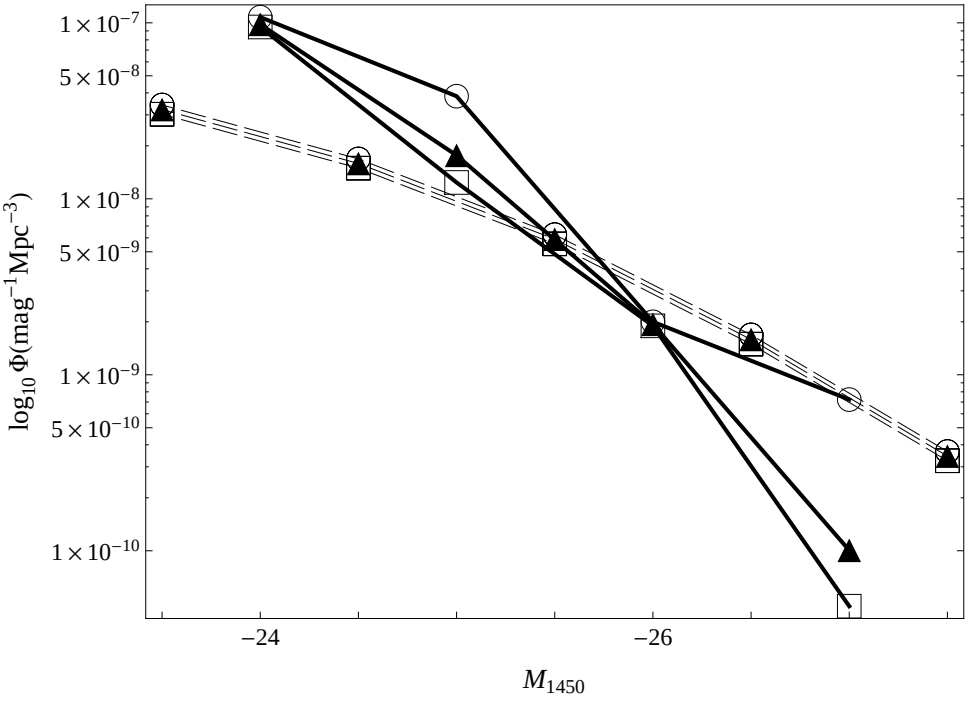

Figure 9.5: Binned survey QSO sample for $(R - z')$>2.5 (circles), 2.6 (triangles), and 2.7 (squares), each sample connected by a solid line. Dashed lines show the corresponding luminosity functions from Willott et al. (2010), with redshift limits adjusted to correct for the change in color selection.

In addition to the worst-case Poisson errors shown in Figure 9.3, two other methods were used to determine the power-law index, β, and its error. First, the best-case Poisson errors were considered. Assuming that each object that contributed to a given M_{1450} bin reduced the bin's error in the usual Poisson manner, the fractional error on each bin can be determined from $\sqrt{n_i}/n_i$, where

$$n_i = \int_{\Delta M_i} \int_{\Delta z} \sum_{j=1}^{N} p_j(M_{1450}|m_{z'}, z) \tag{9.7}$$

and the sum is over all N objects. This gives a lower limit on the errors, assuming every one of our candidates to be a genuine QSO. The resulting errors can be used in a Monte Carlo analysis like the one pictured in Figure 9.4, and the resulting best-fit values are shown in Table 9.2. The power laws fitted from the best-case errors are the most robust against the two different binning options used, but the errors, comparable to the statistical errors in surveys with many more QSOs, are almost certainly an underestimate.

The final analysis method for determining the binned QSO luminosity function is a full Monte Carlo simulation (Figure 9.6), in which the set of QSOs analyzed is drawn randomly from the population, and the jth QSO is included with probability $p_j(QSO)$. This provides a more realistic estimate of the errors, at the cost of computing time. In tests, the mean number of QSOs in each bin was identical to the integrated value of the $p(M_{1450})$, as it should be. However, there were a large number of realizations in which **no** QSOs appeared, or only one, in which case a power law could not be fitted. The omission of these realizations from the results biases the final values somewhat (for example, the mean occupancy of each bin is not equal to the $p(M_{1450})$ in the fittable ensemble of realizations.) Nevertheless, this calculation provides a more realistic estimate of the errors and their distribution, assuming that the underlying probabilities are correct. The Monte Carlo data sets, fitted power laws, and distribution of β are shown in Figures 9.6 and 9.7. The values of β are not adequately captured by a median and standard deviation, but those have been

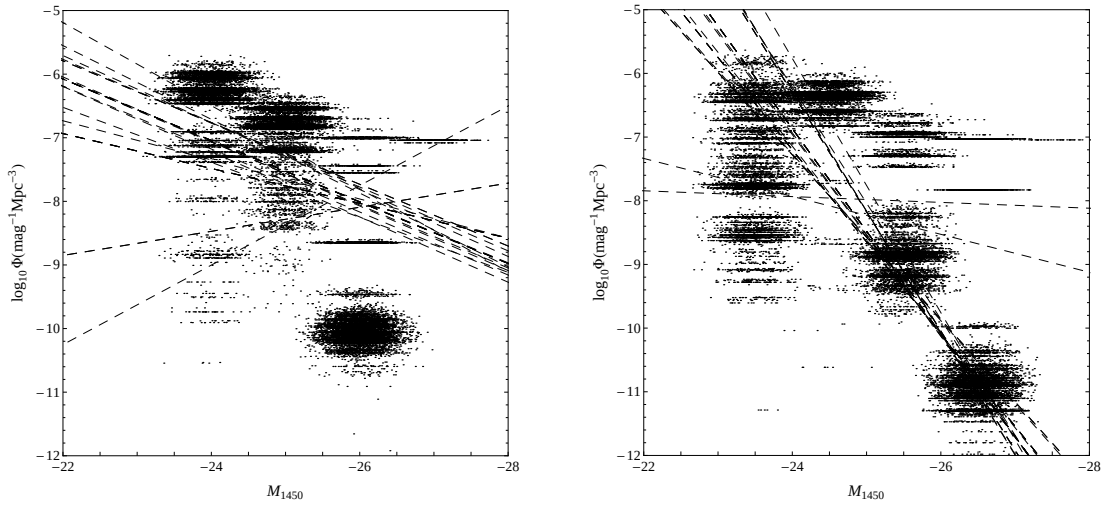

Figure 9.6: Binned QSO counts for Monte Carlo realizations of the QSO data set. Overplotted are 25 randomly-selected best-fit lines. Left and right panels show two different choices of bins.

included in Table 9.2 for comparison to the other analysis methods.

	β
Worst-case errors, binning A	-2.92 ± 1.88
Worst-case errors, binning B	-2.76 ± 2.52
Full Monte Carlo, binning A	-1.88 ± 0.92
Full Monte Carlo, binning B	-4.71 ± 1.11
Best-case errors, binning A	-2.95 ± 0.37
Best-case errors, binning B	-2.95 ± 0.37
Jiang (2009), samples I & II	-2.9 ± 0.4
Jiang (2009), all samples	-2.6 ± 0.3
Willott (2010)	$-2.8^{+0.5}_{-1.0}(2\sigma)$

Table 9.2: Single-power-law indices determined for the survey sample by various methods.

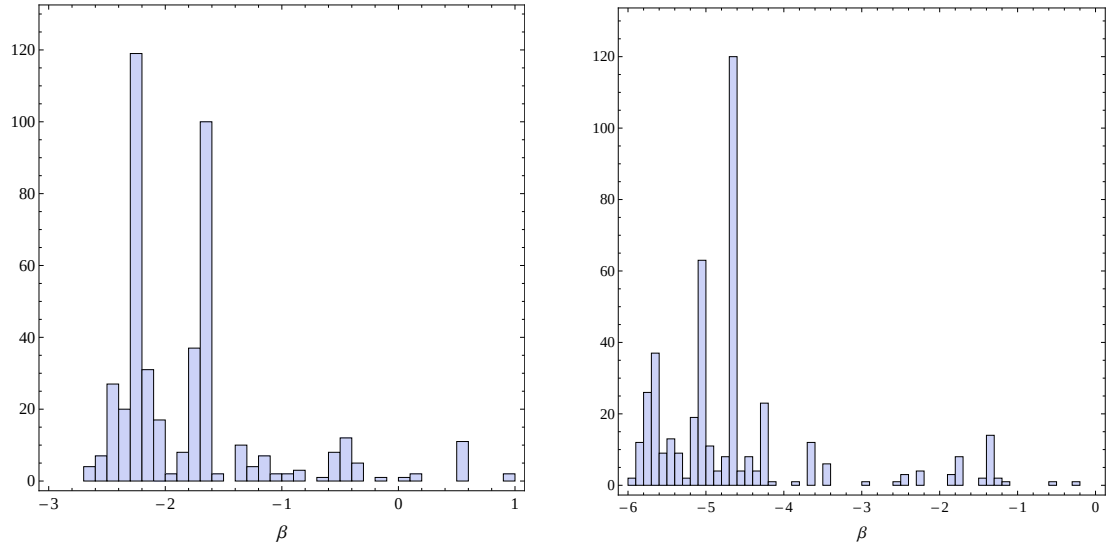

Figure 9.7: Histograms of the power law index for Monte Carlo realizations of the QSO data set. Left and right panels as in Figure 9.6. Although certain values of the power-law slope are favored, the small number of high-probability QSO candidates is evident in the scattered and discontinuous values of β, which can change dramatically based on the inclusion or exclusion of a single important candidate.

9.3 $1/V_a$ Estimator: F1 Complete Sample

Although the z' imaging of the DLS area is complete and unbiased, not having been selected for or against QSOs, the same cannot be said for the FLAMINGOS J-band imaging, which was targeted at red objects specifically. While other surveys have also used this technique, their complete J-band follow-up and ensuing spectroscopic QSO identification have ensured that they have a pure, complete QSO sample over their survey area. To make use of the J-band coverage of the 5.5 remaining DLS F1 subfields (2.4 deg^2), we must restrict ourselves to the area of search space where we are likewise complete. The FLAMINGOS imaging targeted red ($R - z'$) objects, but was not completed due to weather losses, and the situation is complicated by the recalibration of the DLS catalogs, performed after the 2006 FLAMINGOS observing run, which added new red candidates to the catalog. To ensure completeness, only QSO candidates which are *redder than the reddest object which went unobserved* will be considered. It can then fairly be said that if there were a QSO candidate in that discovery space, it would have been imaged in J and have a reliable probability estimate. (This procedure can be contrasted with that from Chapter 8, where cool dwarf candidates not imaged in J were assigned estimated probabilities based on their ($R - z'$) color and z' magnitude; the numbers of QSO candidates are simply too small to warrant that sort of estimation in this case, nor would the results contribute significantly to the luminosity function, given the intrinsic unlikelihood of a QSO detection.) The properties and number of additional candidates in each subfield are given in Table 9.3.

These candidates were analyzed in the same way as in the previous section, constructing a PDF in M_{1450} and integrating in bins, dividing each bin's integrated total by the matching V_a, calculated in this case by integrating from the lower limiting redshift up to a maximum of $z = 6.4$. The probabilities were calculated in the same manner as for the survey sample, then corrected for the change in search volume by

Subfield	$(R - z')$ completeness limit	Equivalent redshift	No. of add'l candidates
F1p12	3.53	5.63	1
F1p13	4.46	5.75	0
F1p22	3.81	5.67	1
F1p23	3.66	5.65	1
F1p31	3.72	5.66	0
F1p33	3.55	5.63	3

Table 9.3: Characteristics of FLAMINGOS imaging of DLS F1 subfields. Only candidates redder than the completeness limit were included in the analysis, and the equivalent redshift was used as the lower limit when calculating V_a.

multiplying by the luminosity-function-weighted ratio of the volumes (assuming the QLF of Willott et al. (2010)). The binned luminosity function is shown in Figure 9.8 with best-case and worst-case Poisson errors, calculated as above. The worst-case Poisson errors are particularly inapt in this case, as the addition of more data lowers the signal-to-noise ratio.

The full Monte Carlo analysis was also carried out for this sample, generating 21,000 random realizations, which were paired at random with realizations of the survey sample, then integrated in bins and fitted with a power law. Since these realizations were carried out over all FLAMINGOS subfields, the V_a used was that for all six subfields. Histograms for β are shown in Figure 9.9, and estimates from all three methods are shown in Table 9.4. As noted above, the Monte Carlo simulation should provide the best sense of the error distribution, while the best-case and worst-case errors recover a less-biased mean value.

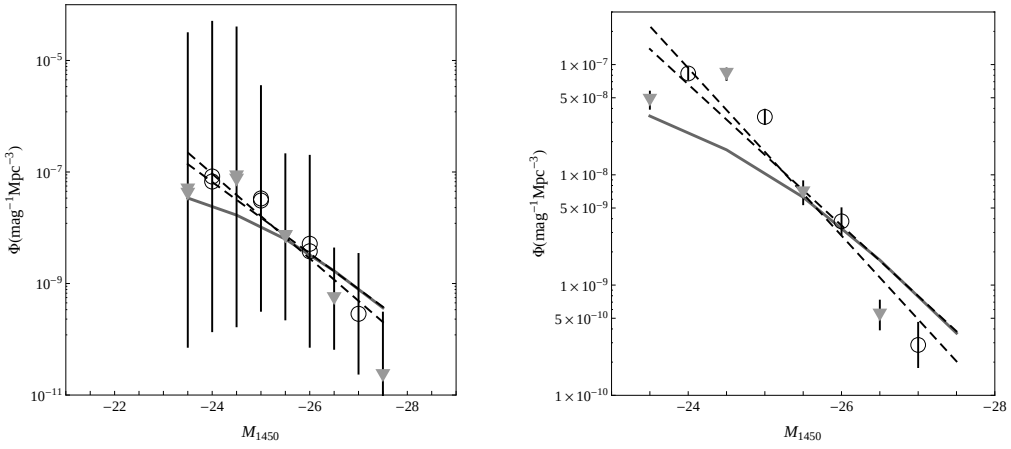

Figure 9.8: Binned QSO counts for combined survey and FLAMINGOS subfield samples. Circles and triangles represent different choices of bins, as above. Left and right panels show worst-case and best-case errors.

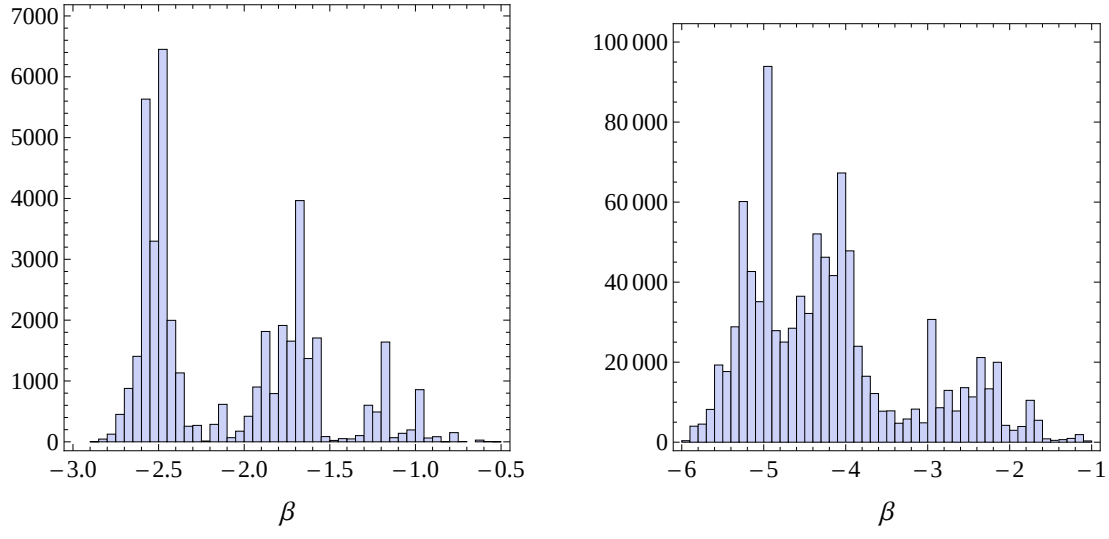

Figure 9.9: Histograms of the power law index for Monte Carlo realizations of the combined QSO data set. Left and right panels show different choices of binning. The peaks correspond to the inclusion or exclusion of a few high-probability objects, showing the effect of small number statistics.

	β
Worst-case errors, binning A	-3.94 ± 5.29
Worst-case errors, binning B	-3.13 ± 3.84
Full Monte Carlo, binning A	-2.38 ± 0.50
Full Monte Carlo, binning B	-4.34 ± 1.10
Best-case errors, binning A	-3.05 ± 0.46
Best-case errors, binning B	-3.18 ± 0.42
Jiang (2009), samples I & II	-2.9 ± 0.4
Jiang (2009), all samples	-2.6 ± 0.3
Willott (2010)	$-2.8^{+0.5}_{-1.0}(2\sigma)$

Table 9.4: Single-power-law indices determined for the combined QSO sample by various methods.

9.4 Parametric Luminosity Function

The usual maximum likelihood estimator (Marshall et al., 1983) used for luminosity functions is

$$\sum_{i=1}^{N} \ln[\Phi(M_{1450,i}, z_i)p(M_{1450,i}, z_i)] - \int \Phi(M_{1450}, z)p(M_{1450}, z)\frac{\mathrm{d}V}{\mathrm{d}z}\mathrm{d}M_{1450}\mathrm{d}z, \quad (9.8)$$

where $p(M, z)$ is the completeness of the sample for a particular magnitude and redshift, usually calculated from simulations. The sum is over all detected objects (representing the likelihood of detecting precisely those objects), while the penalty integral is over the entire range of possible magnitudes and redshifts (measuring the likelihood of all of those infinitesimal luminosity and redshift bins being empty). To this estimator, we will be adding two additional complications: the probability that a candidate is actually a QSO, $p(QSO|color)$, and the probability that the true absolute magnitude is M_{1450} given the measured z' magnitude, $p(M_{1450}|m_{z'})$. From the simulated point source recovery detailed in Chapter 8, we have $p(m_{z',true}|\ m_{z',measured})$, and the relation between $m_{z'}$ and M_{1450} is given by

$$M_{1450} = m_{z'} - DM(z) - K_{qr}(z)$$

where DM is the distance modulus and K_{qr} is the K-correction (which converts the measured magnitude in observed bandpass r to a source magnitude emitted in rest-frame bandpass q). The distance modulus can be calculated numerically from the standard cosmology, as outlined in Chapter 2, while the K-correction accounts for the difference in bandpass between the emission and detection reference frames (see Figures 2.7(a) and 2.7(b) for details). To determine the correct expectation value of $\Phi(M_{1450,i}, z_i)$, we integrate it over all possible values of the true magnitude, given the measured magnitude:

$$\langle\Phi(M_{1450,i}, z_i)\rangle = \sum_{m_{z',true}} p(m_{z',true}|m_{z',meas}) \times \Phi(M_{1450}(m_{z',true}, z), z) \quad (9.9)$$

As our redshifts are necessarily unknown, they have been estimated from the point of closest approach of the QSO color-color track to the color of each object (for J-detected objects), or from the $(R - z')$ color (for J-dropout objects).

However, the likelihood estimator in its current form assumes more than our data set can claim: it is inherently based on Poisson statistics, and assumes that we are quite sure which bins are occupied and which are empty. Under these circumstances, we will modify the estimator to consider only the normalized likelihood of each QSO being detected given the model; the total likelihood will be the sum of the individual log likelihoods. The single QSO likelihood is

$$p_j(\text{QSO}|\text{model}) \propto \frac{p(\text{QSO}|\text{color}) \times \Phi(\langle M_{1450,j} \rangle, z_j, \alpha, \beta, M^*, k, \Phi^*)}{\int\int \Phi(M, z, \alpha, \beta, M^*, k, \Phi^*) p(M, z) \frac{\mathrm{d}V}{\mathrm{d}z} \mathrm{d}z \mathrm{d}M}. \tag{9.10}$$

The normalization integral ensures that the QSO likelihood is being maximized relative to the total likelihood, not simply being inflated by inflating the total. Due to its numerical difficulty, this normalization integral was computed on a grid and interpolated. The QSO probabilities used for the survey sample are the same as above, normalized using Φ^* from Willott et al. (2010).

The resulting likelihood is shown in Figure 9.10. As with other data sets, our survey QSO sample cannot place a lower limit on M^*, meaning that the data are still consistent with no break in the luminosity function power law. The maximum-likelihood β is -3.25 ± 0.3, with all of our favored values of M^* lying fainter than our faintest observed objects, so our best-fit is still an unbroken power law. This value agrees with the best-fit bright-end slopes from both Willott et al. (2010) ($-2.8^{+0.5}_{-1.0}(2\sigma)$) and Jiang et al. (2009) (-2.9 ± 0.4) to within the joint errors; however, the Willott et al. (2010) β is calculated for $M^* = -25.13$, while their best-fit β for $M^* = -23.25$ is significantly shallower than ours.

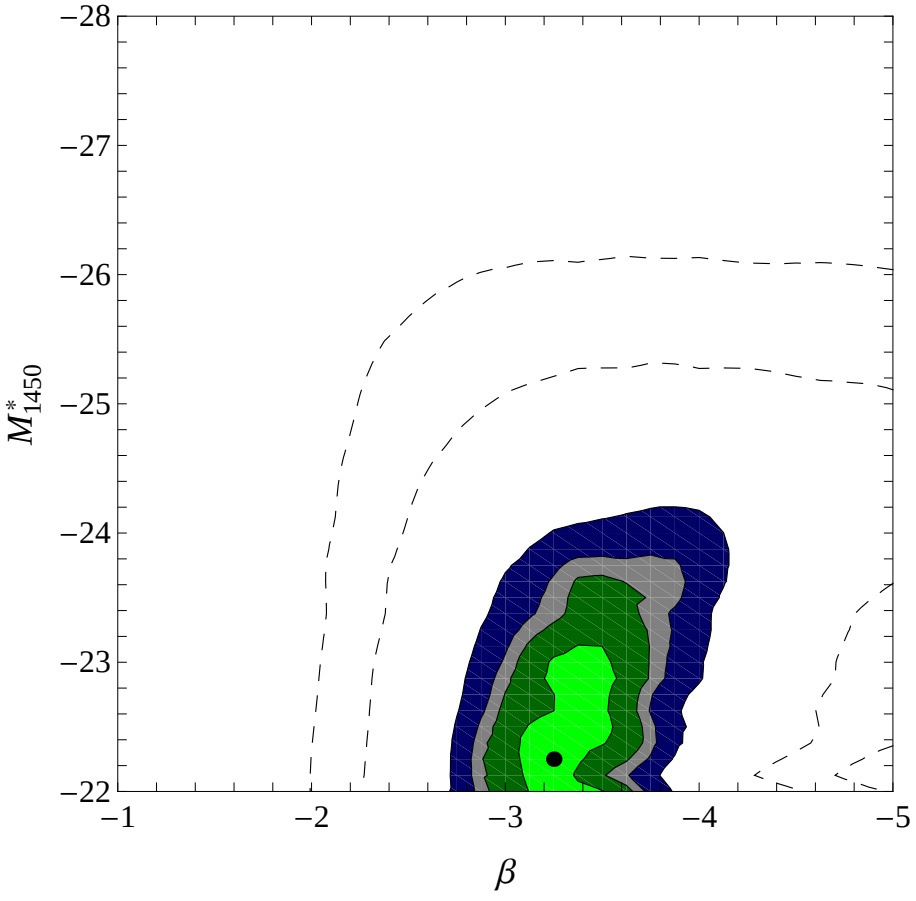

Figure 9.10: Likelihood plot for M^* and β, with solid contours at 68%, 90%, 95%, and 99%. The maximum likelihood is plotted as a point.

9.5 Discussion and Conclusions

Our values for the essential parameters of the luminosity function are mostly in agreement with earlier high-redshift QSO surveys, so the properties derived from our luminosity function will agree in general with earlier findings: primarily, that ionizing radiation from QSOs can supply only 1%–5% (Willott et al., 2010) of the ionizing flux necessary to keep the Universe ionized at $z = 6$ (under very optimistic assumptions, such as a 100% photon escape fraction). While we appear to find a slightly steeper slope and fainter break magnitude for QSOs, which would imply a larger number of faint QSOs (or a smaller population of bright QSOs, at a fixed Φ^*), the primary disagreement between this finding and Willott et al. (2010) is the location of M^*; in fairness, theirs is the first study to publish any evidence for a break luminosity at $z \simeq 6$, and their findings are strongly dependent on a single QSO detected at $M_{1450} = -22$. In bootstrap resamples where that QSO did not appear, they fitted a single power law which was consistent with Jiang et al. (2009) ($\beta \simeq -2.9$). For the range of magnitudes where our data overlap, the differences between our binned data and the predicted QLF are within the 1σ errors; however, the predicted total number of QSOs in the survey area is only 0.13, which should make the recovery of the QLF from our data difficult, if not impossible. The fact that our β is consistent with other studies, then, may be an indication that their Φ^* has been underestimated, meaning our field contains more than the predicted total number of faint QSOs.

The most important difference between this study and previous studies, for the purposes of future work, is the lack of spectroscopic follow-up for our QSO candidates. While spectroscopy is the only way to guarantee a pure sample, it is extremely time-consuming, and generally requires the use of a larger and more competitive telescope facility than the imaging survey. While that may be practical for the moment, upcoming surveys such as LSST and Pan-STARRS will be detecting candidate

QSOs and other exotic objects to such faint magnitudes that spectroscopy would be completely impractical, even assuming the continuing construction of larger ground-based telescopes (e.g. the Thirty Meter Telescope). For these surveys, calculation of luminosity functions based on only "photo-z" techniques, whereby the redshift of a QSO or galaxy is estimated from the broad-band colors, will be essential, and the techniques in this work can be revised and expanded to work on deeper imaging and different filter sets. Great advances have been made in the selection of QSOs by photometry alone (e.g. Richards et al., 2009a,b), which can be extended to the case of extremely rare outliers by application of the methods outlined here, particularly by not discarding the probability information when the time comes to calculate the luminosity functions, as is frequently done. If the probability estimates are sufficiently accurate, keeping low-probability objects in the sample should allow better estimation of the QLF parameters than a smaller sample with only high-probability objects (and a proper analysis of a photo-z sample with color cuts would have to include color modeling to determine false positive and negative rates, so very little additional work is required.) These techniques will be valuable and necessary to extract as much information as possible from deep surveys both now, and in the future.

Chapter 10

Gallery and Notes on Individual Objects

ID		R.A.			Decl.		R	R	z'	z'	J	J
	h	m	s	d	m	s		err		err		err
1	00	57	03.3	12	57	51	22.58	0.02	19.32	0.01	17.03	0.01
2	00	56	02.9	13	16	06	25.46	0.19	21.72	0.05	19.01	0.04
3	00	55	32.0	13	26	21	26.60	0.32	23.45	0.24	20.89	0.16
4	00	55	08.1	13	25	06	24.57	0.07	21.37	0.04	19.05	0.05
5	00	57	08.6	12	23	39	25.98	0.14	22.21	0.09	19.10	0.04
6	00	56	16.0	12	15	15	25.90	0.16	22.70	0.14	20.33	0.10
7	00	55	41.0	12	22	44	25.99	0.16	22.52	0.12	19.86	0.07
8	00	54	22.0	12	38	52	25.63	0.13	22.25	0.07	19.99	0.19
9	00	52	37.0	12	26	58	25.94	0.14	22.54	0.09	20.11	0.20
10	00	49	29.0	12	34	42	22.66	0.01	19.29	0.01	16.65	0.02
11	00	56	26.0	12	01	35	25.51	0.11	22.08	0.07	19.47	0.21
12	00	54	17.0	11	49	19	26.60	0.23	23.07	0.19	20.71	0.11
13	00	52	47.0	12	09	47	25.95	0.13	22.48	0.11	19.95	0.08
14	00	49	36.0	11	42	44	27.19	0.41	23.53	0.26	20.96	0.22

Table 10.1: J-detected brown dwarf candidates in DLS F1.

10.1 Brown Dwarf Candidates

In the final version of the catalog, there were 14 objects with matching J imaging for which the colors indicated most likely spectral types later than M9, i.e. red $(z' - J)$ colors to go along with their red $(R - z')$. Figures 10.1, 10.2, and 10.3 show composite BVR color images for these 14 objects, along with Vega-normalized grayscale Rz'J images, while Table 10.1 has basic data on each one. Objects 2, 5, and 7 have noticeable proper motion between the z' imaging (from the 1999 and 2001 DLS runs) and the WIRC or FLAMINGOS J imaging (from the 2004 and 2006 Palomar and Kitt Peak runs), but this should be regarded as a lower limit on the number of candidates with proper motions, as the centroids of the faint images can be difficult to determine, and the astrometric solution is good to only 0.3 pixels.

10.1.1 DLSJ0057+1258 (Brown Dwarf Candidate No. 1)

This cool dwarf is one of the nearest to the main sequence stellar locus, lying near the blue limits of the M9–L2 selection region in both $(R - z')$ and $(z' - J)$. Due to its brightness and reliable colors, it was selected for observation with the Hobby-Eberly Telescope's Low Resolution Spectrograph (HET LRS, Hill et al., 1998). Three 240 s exposures were taken on 26 Nov 2008, which were bias-subtracted, and flat-fielded using a nightly reference star spectrum for telluric absorption and wavelength response, and dome flats for pixel-to-pixel variations. The science spectra were rectified along both the x- and y-axes using a nearby bright star trace and the sky lines, then normalized for the constantly changing effective area of the HET using the sky lines, and the resulting sections combined with outlier rejection. The spectrum was then extracted using a least-squares fit to the sky and object profiles (determined from the summed spatial profile) at each wavelength column. The 2-D spectrum and extracted spectrum are shown in Figure 10.4. The TiO bandheads at 7100Å, 7600Å, and 8400Å are present (albeit weakly), marking this object out as earlier than type L2 (Kirkpatrick et al., 1999), and the nearly equal strength of the NaI feature near 8200Å and the 8400Å TiO bandhead argues for a spectral type near L1. A prominent absorption feature for CrH can be clearly seen near 8600Å, which is a sure indicator of an L dwarf. Taken together, these features identify DLSJ0057+1258 as an early L dwarf, in agreement with the spectral type assigned based on its photometry.

10.1.2 DLSJ0056+1316 (Brown Dwarf Candidate No. 2)

This brown dwarf was originally considered one of the most promising candidates for a $z > 7$ QSO, as it was clearly pointlike in J-band, and slightly offset from a mildly extended z'-band source, consistent with it being a gravitationally-lensed background QSO near a foreground galaxy. However, the multi-epoch DLS imaging proved useful in this case, as separate stacks of the 1999 and 2001 z' images, showed a point source

with proper motion, rather than an extended galaxy. The proper motion of 0.6″/yr definitively ruled out the possibility that this object was a QSO, but not before Dr. D.J. Thompson carried out J & K imaging with the NIRC camera[1](Matthews and Soifer, 1994) on Keck I. The resulting infrared colors, $(z' - J)$=2.70, $(J - K)$=1.39, are significantly redder than any variety of M or early L dwarf, more consistent with a mid-L spectral type. On the same observing run, this object was imaged with a medium-band filter, centered on the CH_4 absorption feature between 2.19 μm and 2.35 μm. Comparison of the flux in this filter to the surrounding K_s filter flux should be a measure of the strength of methane absorption; this target showed a stronger absorption signal than the median object ($\Delta K - \overline{\Delta K} = 1.09^m$) in the field, but the standard deviation of ΔK was also large, ≈ 0.8 ($n = 6$), so this result is only marginally significant. Given these mixed results, the spectral type could be anything between L2 and L8, with corresponding most-likely distances of 190 pc and 95 pc, which would translate to velocities of 260 km/s and 550 km/s in the plane of the sky. The components of this motion relative to the local standard of rest are shown in Figure 10.5; the object appears to be leading the Sun in rotational velocity, a feature quite inconsistent with advanced age (Population II stars tend to trail the Sun in rotation; Oort, 1926), but possible for an L dwarf ejected from its formational system. If the galactic disk of brown dwarfs must be constantly replenished to replace cooling members, we might expect this sort of wider variation in uv-velocities than for field stars.

10.1.3 DLSJ0057+1223 (Brown Dwarf Candidate No. 5)

This is a definite brown dwarf with a measured proper motion of 0.06″/yr between the z' stacked image (in this case, created from images taken between 1999 and 2004) and the 2004 J-band image. We can be quite certain of the spectral type identification in this case, both from the NIRC J & K imaging which yielded $(J - K) = 1.71$,

[1]http://www2.keck.hawaii.edu/inst/nirc/

a very red color consistent with only a late L dwarf, and from a concurrent HK grism spectrum taken by Dr. D.J. Thompson (see Figure 10.6). This yields a slightly more accurate distance estimate (since we can be sure what spectral type bin the object is drawn from) of 118^{+33}_{-20} pc, which translates to a velocity of 31^{+9}_{-5} km/s in the plane of the sky. The components of the motion relative to the local standard of rest are shown in Figure 10.7; this object seems to be in a lagging orbit, very consistent with the older Population II kinematics, regardless of the unknown radial velocity. If the dwarf's motion is a correct indicator of its age ($\simeq$ 10 Gyr), it should be extremely close to the hydrogen-burning limit, having begun its existence as a 70–75 M_J late-M dwarf and cooled to its present condition. This old age would also be most likely based on the underlying age-luminosity relation, as the largest objects take the longest to cool, and would predominate in any given spectral type bin. This surmise can be tested using optical spectroscopy to determine the object's metallicity and radial velocity, and hopefully check for lithium depletion (although for this class of objects, the lithium test is not conclusive as to hydrogen-burning status.) However, if the object were found to have solar or super-solar metallicity, then it would be possible to consider its motion a mere coincidence.

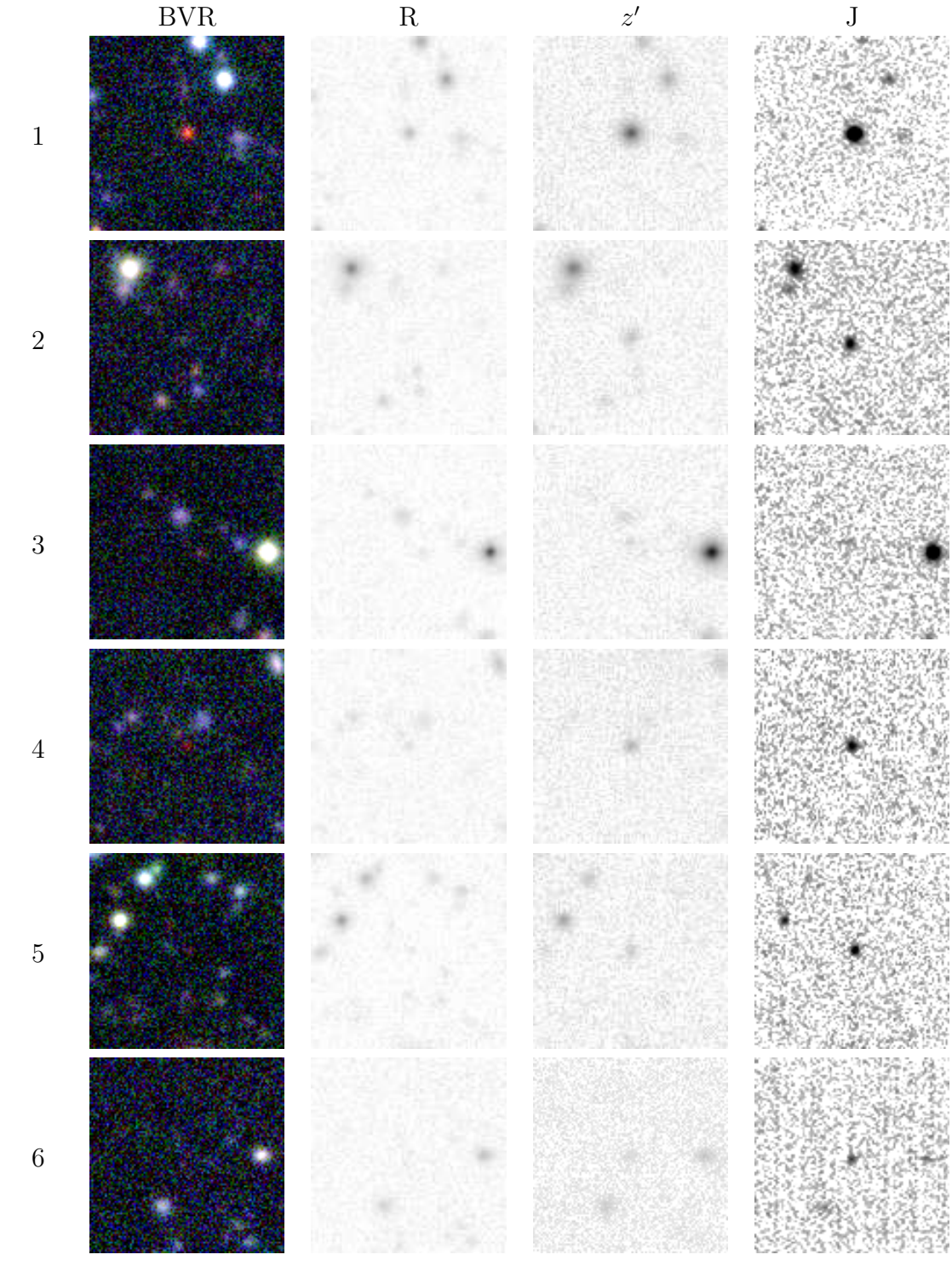

Figure 10.1: J-detected brown dwarf candidates. Grayscale images are normalized such that Vega would appear the same brightness in all three bands.

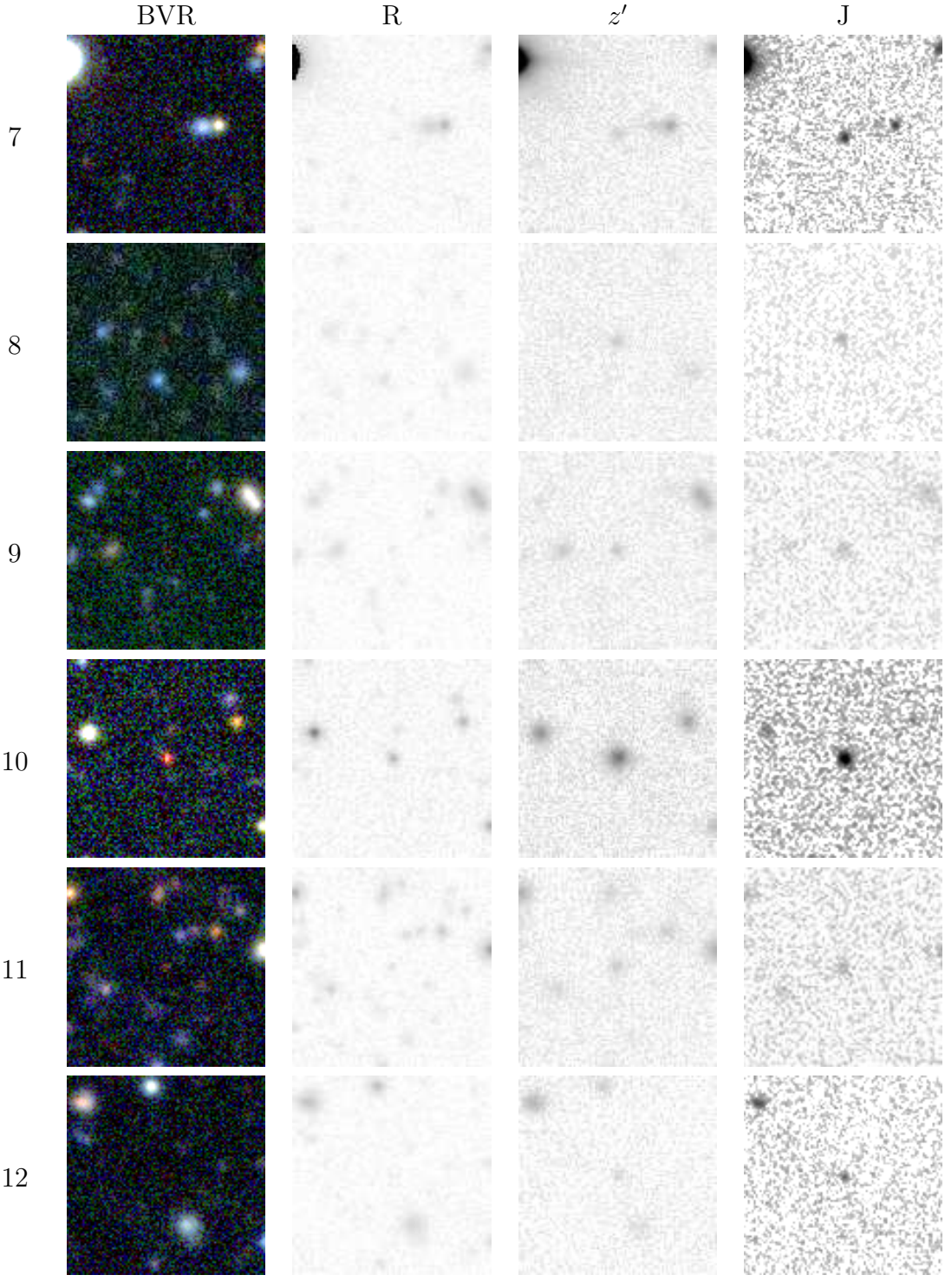

Figure 10.2: J-detected brown dwarf candidates. Grayscale images are normalized such that Vega would appear the same brightness in all three bands.

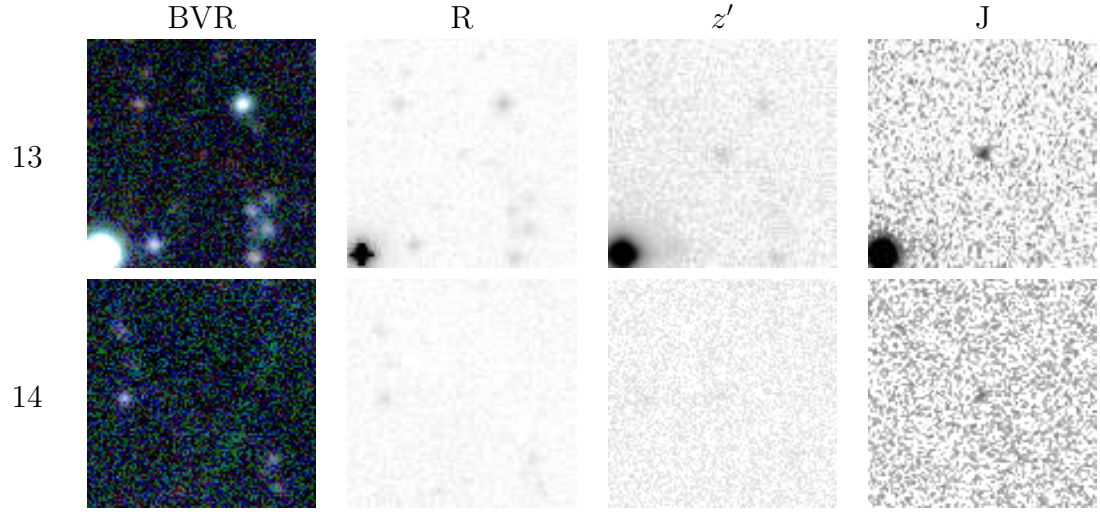

Figure 10.3: J-detected brown dwarf candidates. Grayscale images are normalized such that Vega would appear the same brightness in all three bands.

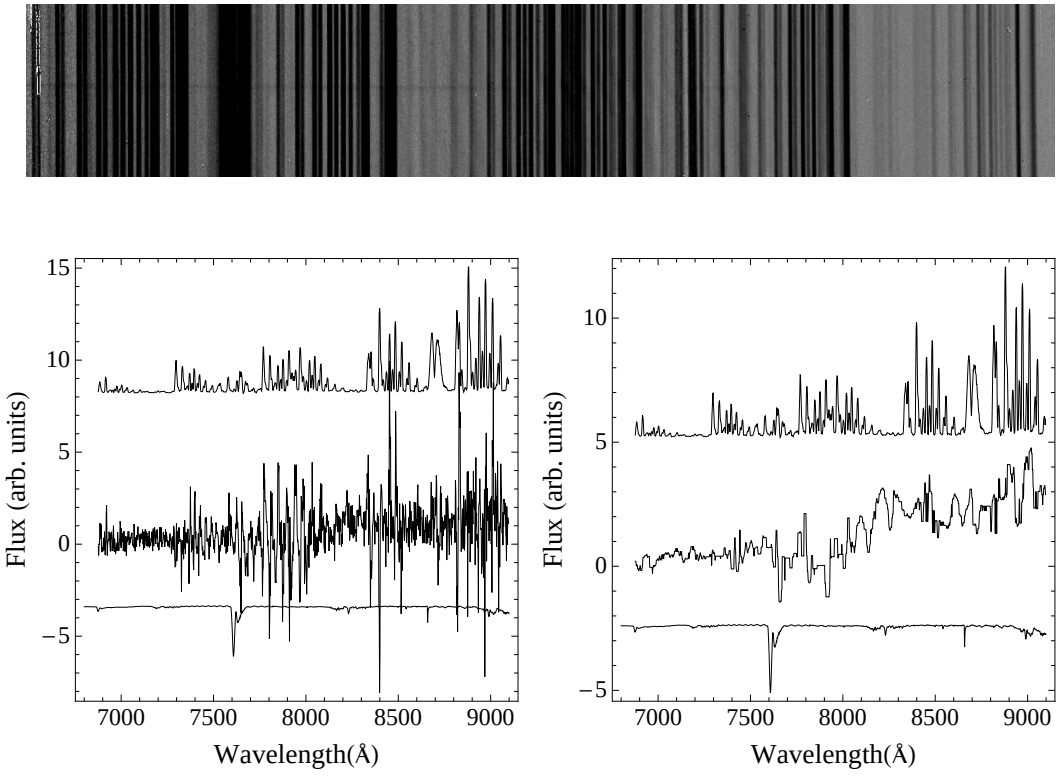

Figure 10.4: HET LRS spectrum of DLSJ0057+1258 (Brown Dwarf Candidate No. 1). The upper image is the 2-D median-combined spectrum from HET, shown in negative, with red wavelengths to the left. The target spectrum appears as a dark band near the center of the image. The extracted spectrum is shown with the sky emission (above) and absorption (below) to indicate regions where the spectrum may be untrustworthy. The spectrum in the right-hand panel has been smoothed with a median filter of width 21 pixels (40Å). Note the very weak TiO bandheads at 7100Å and 7600Å, the stronger one at 8400Å, and the prominent absorption feature for CrH near 8600Å. The overall spectral features are consistent with an early L dwarf.

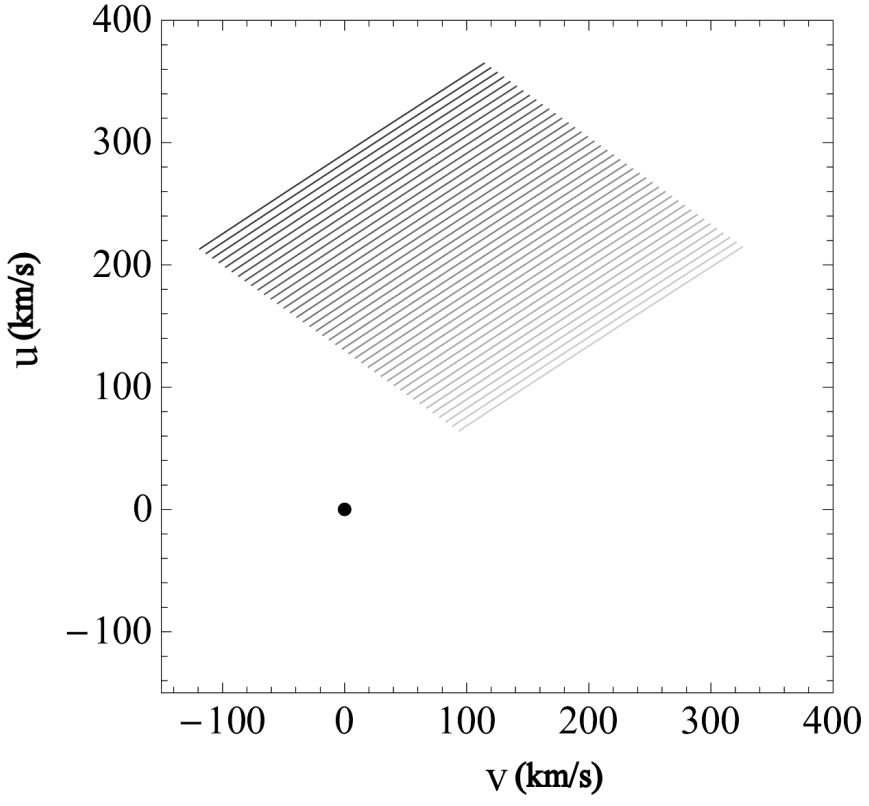

Figure 10.5: Possible peculiar motions of DLSJ0056+1316. u and v are the velocity away from the center of the Galaxy and the tangential velocity relative to a circular orbit at the Sun's location, respecitvely, so a positive u-velocity indicates that an object is moving away from the center of the Galaxy, while a positive v-velocity indicates that the object moving more quickly than the local circular rotation velocity (overtaking the Sun, for example). The uncertainty in the velocity due to the uncertain distance to the object is represented by the lines, with each line tracing out the distance from 90 pc to 190 pc. The unknown $\frac{dr}{dt}$ is represented by the darkness of the line: the darkest line shows the velocity assuming $v_r = -200$ km/s, the lightest is $v_r = +200$ km/s.

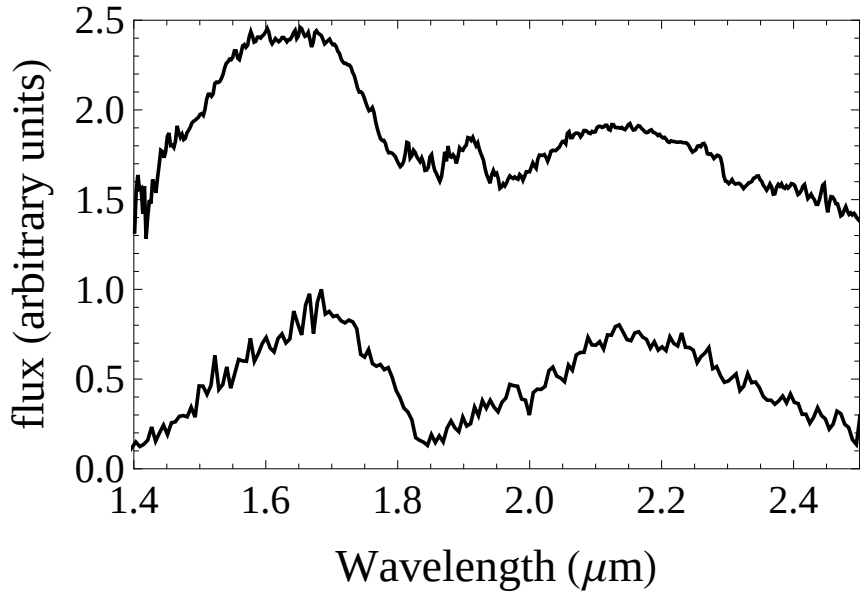

Figure 10.6: An H- and K-band spectrum (lower) of DLSJ0057+1223 (Brown Dwarf Candidate No. 5) and a typical L7 dwarf (upper). The slope of the spectrum, particularly the $(H-K)$ color, is indicative of a late L dwarf; however, our spectrum does not specifically show the onset of CH_4 absorption at 2.3 μm, which occurs near the L-T transition. The absorption features at the blue end of the H-band may be telluric H_2O, but otherwise have no obvious counterpart in brown dwarf spectra.

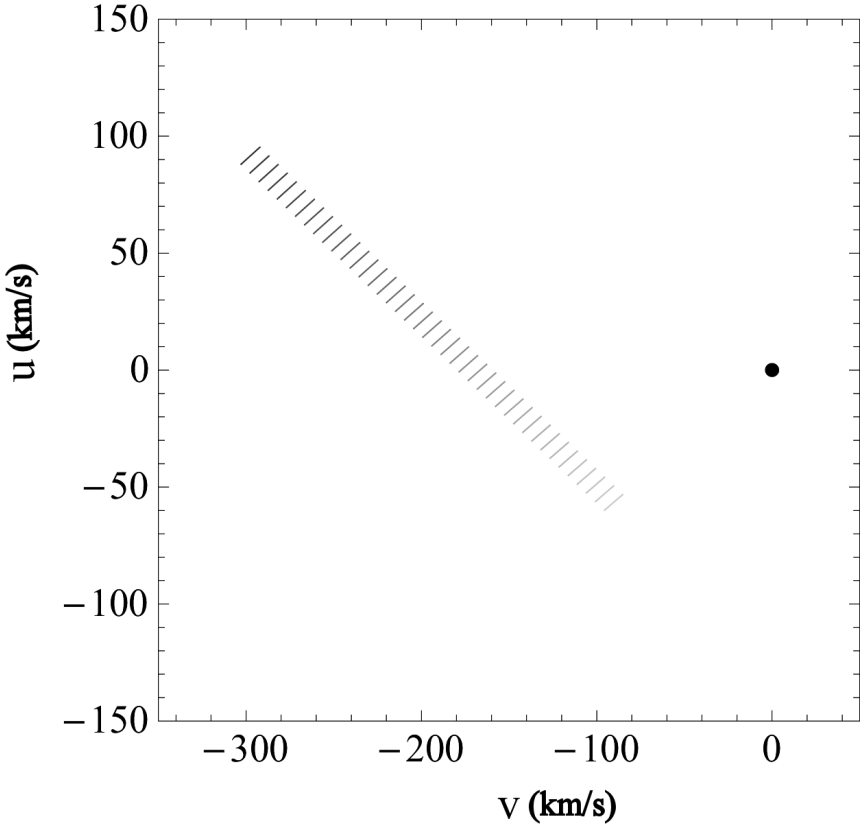

Figure 10.7: Possible peculiar motions of DLSJ0057+1223. u and v are the velocity away from the center of the Galaxy and the tangential velocity relative to a circular orbit at the Sun's location, respecitvely, so a positive u-velocity indicates that an object is moving away from the center of the Galaxy, while a positive v-velocity indicates that the object moving more quickly than the local circular rotation velocity (overtaking the Sun, for example). The uncertainty in the distance to the object is represented by the lines, with each line tracing out the 1σ distance range from 98 pc to 151 pc. The unknown $\frac{dr}{dt}$ is represented by the darkness of the line: the darkest line shows the velocity assuming $v_r = -200$ km/s, the lightest is $v_r = +200$ km/s.

10.2 QSO Candidates

In the final version of the catalog, there were 117 J-detected objects which lay more than 1σ blueward of the stellar locus in $(z' - J)$, many of which are doubtless merely unusual or poorly-measured stars. One of the brightest of these candidates is shown at position 1 in the following figures and tables, due to its follow-up spectroscopy; the remaining 19 are the J-selected QSO candidates with the highest odds ratios, p(QSO)/p(dwarf). Figures 10.8, 10.9, 10.10, and 10.11 show composite BVR color images for these 20 objects, along with Vega-normalized grayscale Rz'J images, while Table 10.2 has basic data on each one. In addition, 170 objects with very red $(R - z')$ colors were not detected in J to the 5σ limit; the 20 of those with the highest odds ratios are shown in Figures 10.12, 10.13, 10.14, and 10.15, with their pertinent data in Table 10.3.

10.2.1 DLSJ0050+1227 (QSO Candidate No. 1)

This object is a marginal QSO candidate, lying relatively close to the mid-M part of the stellar locus, but was selected for spectroscopic follow-up due to its relative brightness. Spectra of the object were obtained from HET LRS in October and November of 2008, bias-subtracted, and flat-fielded using a reference star spectrum for telluric absorption and wavelength response, and dome flats for pixel-to-pixel variations. The science spectra were rectified along both the x- and y-axes using a nearby bright star trace and the sky lines, then normalized for the constantly changing effective area of the HET using the sky lines. This allowed the use of all of the spectra which were taken on the western track, for a total of 90 minutes of exposure time. The 2-D spectrum and extracted spectrum are shown in Figure 10.16. The TiO bandheads at 7100Å, 7600Å, and 8400Å are present, marking this object out as a dwarf earlier than type L2 (Kirkpatrick et al., 1999) (and not a QSO), but the absorption lines near 8000Å may be RbI, which would argue for the latest

ID		RA			Dec		R	R	z'	z'	J	J
	h	m	s	d	m	s		err		err		err
1	00	49	44.0	12	27	29	23.78	0.04	20.72	0.02	19.72	0.00
2	00	55	55.0	13	05	57	25.06	0.10	22.12	0.07	21.70	0.31
3	00	54	48.0	12	56	28	24.61	0.07	21.85	0.06	21.03	0.18
4	00	51	30.0	13	08	43	23.86	0.04	20.77	0.03	19.83	0.05
5	00	56	44.0	12	48	29	23.73	0.03	21.09	0.03	20.22	0.11
6	00	56	03.0	12	47	48	24.29	0.05	21.75	0.06	21.20	0.17
7	00	54	37.0	12	23	28	23.03	0.01	20.31	0.01	19.75	0.12
8	00	54	28.0	12	55	13	26.37	0.19	21.91	0.05	21.01	0.29
9	00	54	18.0	12	31	44	24.60	0.06	21.81	0.05	21.33	0.35
10	00	54	13.0	12	48	2	23.73	0.03	21.19	0.03	20.49	0.17
11	00	52	35.0	12	52	59	24.01	0.04	21.01	0.02	20.15	0.15
12	00	54	28.0	12	55	15	25.92	0.18	21.68	0.04	20.31	0.25
13	00	54	46.0	12	25	38	24.48	0.04	21.13	0.03	20.30	0.18
14	00	49	49.0	12	44	28	21.26	0.00	18.39	0.00	17.94	0.03
15	00	56	36.0	11	52	38	22.08	0.01	19.17	0.01	18.40	0.01
16	00	56	02.1	11	58	11	24.20	0.04	21.28	0.04	20.46	0.06
17	00	54	55.0	11	34	2	22.47	0.01	19.37	0.01	18.71	0.01
18	00	54	08.5	11	38	42	25.09	0.07	22.35	0.10	21.63	0.27
19	00	53	44.0	11	49	28	25.15	0.08	22.44	0.11	21.69	0.22
20	00	52	15.0	12	05	13	23.99	0.02	21.43	0.04	20.62	0.11

Table 10.2: J-detected QSO candidates in DLS F1.

part of that spectral type range. Absorption features for CsI and FeH can also be tentatively identified near 8500Å and 8600Å. However, the overall shape of the spectrum is flatter than expected for M9 or later objects, which should have a more steeply ascending underlying black-body spectrum. This mix of features from M and L dwarfs is sometimes attributed (e.g. Cushing and Vacca, 2006) to a low metallicity or "subdwarf" star, which has unusually blue colors for its luminosity (Kuiper, 1939; Jao et al., 2008) due to changes in opacity (not to be confused with the subdwarfs of Adams and Joy (1922), which are underluminous due to their small size). If this is the correct explanation, it might help explain some of the intrinsic spread in the colors of M dwarfs in our sample, which is currently simply being modeled, but is

ID		RA			Dec		R	R	z'	z'	J
	h	m	s	d	m	s		err		err	5σ
1	00	54	45.0	13	12	06	23.64	0.03	20.57	0.02	19.36
2	00	54	09.9	13	29	53	26.31	0.23	22.64	0.13	21.70
3	00	53	53.0	13	16	43	26.34	0.23	22.83	0.15	21.71
4	00	53	03.2	13	22	14	24.80	0.11	21.79	0.06	20.76
5	00	52	07.1	12	56	43	24.32	0.06	20.84	0.02	19.54
6	00	51	60.0	12	57	48	23.91	0.04	20.86	0.02	19.57
7	00	51	20.0	13	16	37	25.42	0.13	21.97	0.08	20.56
8	00	51	07.5	13	20	53	25.21	0.11	22.17	0.10	20.95
9	00	53	38.0	12	52	26	25.42	0.08	22.09	0.06	21.05
10	00	53	24.0	12	14	38	25.90	0.28	21.69	0.04	18.99
11	00	53	19.0	12	15	21	23.41	0.02	20.05	0.01	19.12
12	00	53	00.9	12	31	11	25.04	0.08	22.30	0.08	21.61
13	00	52	29.0	12	36	10	25.54	0.09	22.34	0.08	21.00
14	00	53	17.0	12	53	35	25.33	0.11	22.31	0.08	21.30
15	00	49	56.0	12	19	05	23.17	0.02	20.41	0.02	19.89
16	00	49	44.0	12	27	29	23.78	0.04	20.72	0.02	19.72
17	00	56	21.0	12	14	16	25.55	0.16	22.67	0.13	21.51
18	00	54	42.0	11	33	39	23.82	0.03	20.41	0.02	19.31
19	00	52	07.0	12	11	40	24.75	0.05	20.97	0.02	19.17
20	00	52	03.7	11	55	05	25.45	0.08	21.51	0.04	19.22

Table 10.3: J-dropout QSO candidates in DLS F1.

significantly larger than the corresponding error in the color-color diagrams of hotter stars (High et al., 2009).

10.2.2 QSO candidates in DLS F2

Using the existing IRAC 4-band imaging, as outlined in Chapter 2, we have made a preliminary selection for the 6 subfields of F2 that had been released as of 2006. Our deeper optical and IRAC imaging made it impossible to use the color cut from Cool et al. (2006), as it would have contained > 20 faint stars, so it was replaced with a much more stringent cut, centered on the QSO track. Even so, the results included 7

objects in 2.6 sq. deg., a higher density than the earlier study's 3 QSOs in 8 sq. deg. One candidate was eliminated based on its VRz' colors, which were typical of an M dwarf, and the brightest four of the remaning six were submitted for spectroscopy as part of a successful Gemini observing proposal; however, the observations did not occur due to poor weather during the semester. A more complete sample from all of F2 will be submitted for future observation, but the small sample of known high-z QSOs observed with IRAC is inadequate to characterize the population in the absence of spectroscopic follow-up. Images of the six candidates are shown in Figure 10.17, and the selection criteria are shown in Figure 10.18.

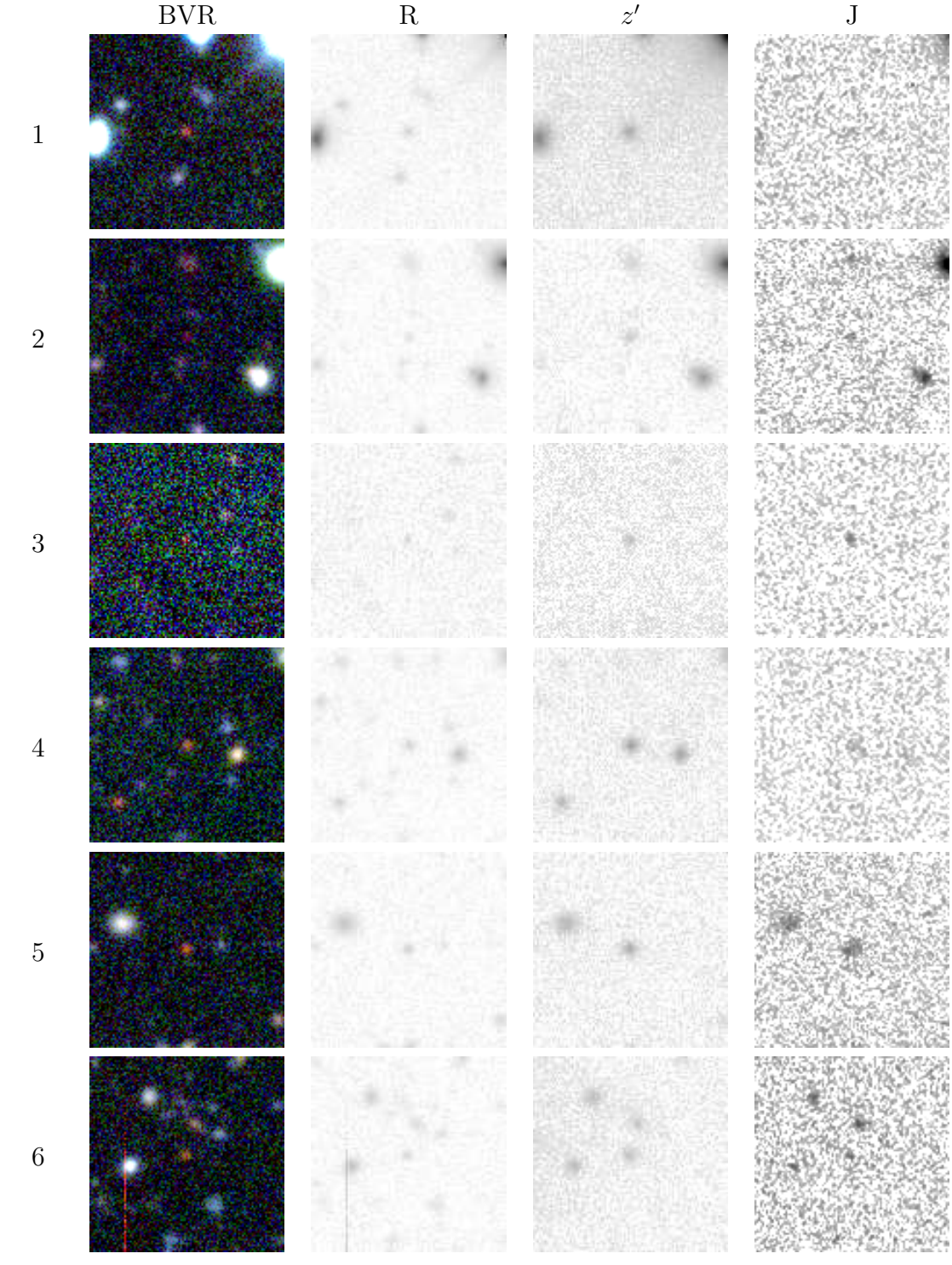

Figure 10.8: J-detected QSO candidates. Grayscale images are normalized such that Vega would appear the same brightness in all three bands.

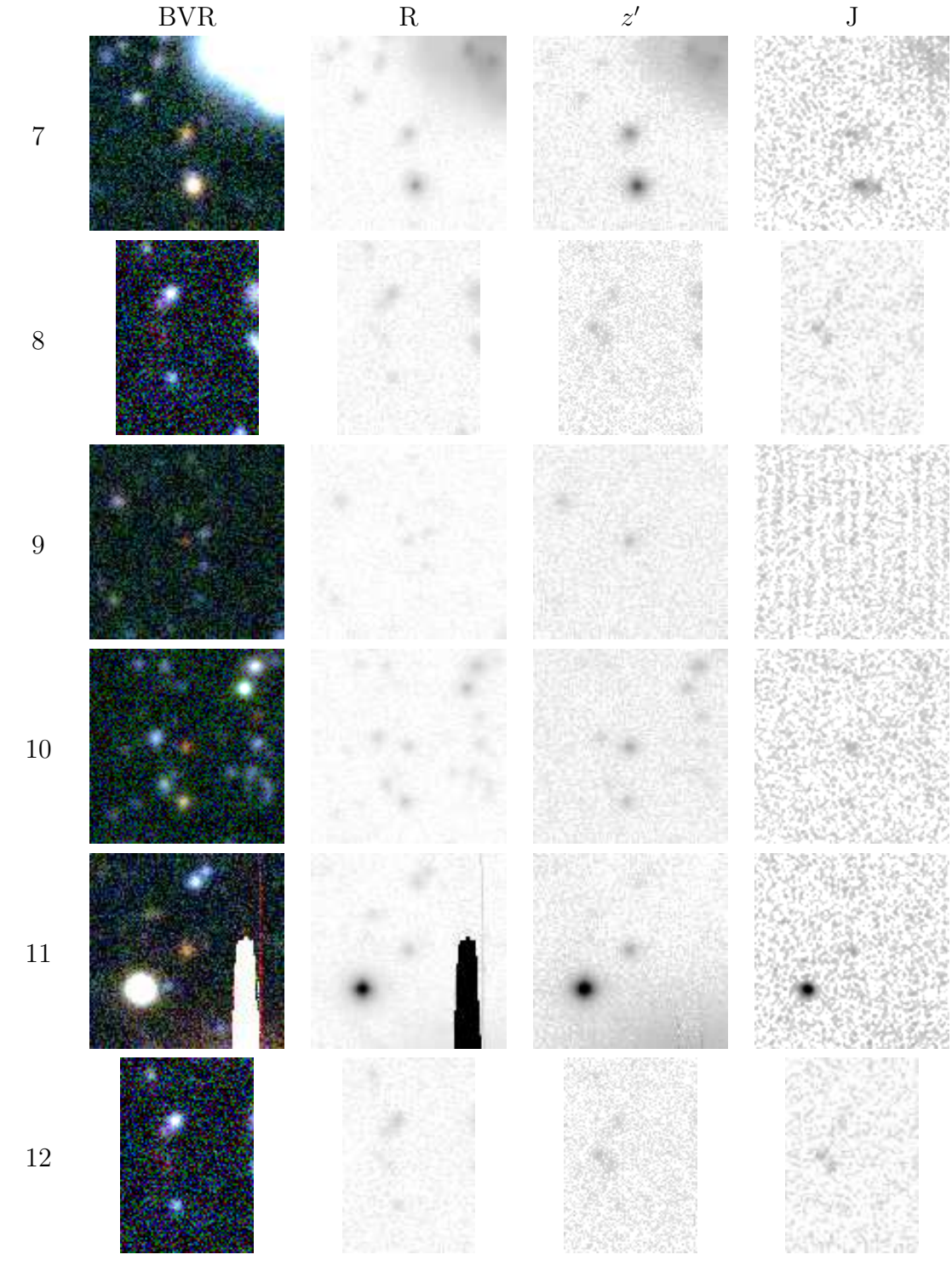

Figure 10.9: J-detected QSO candidates. Grayscale images are normalized such that Vega would appear the same brightness in all three bands.

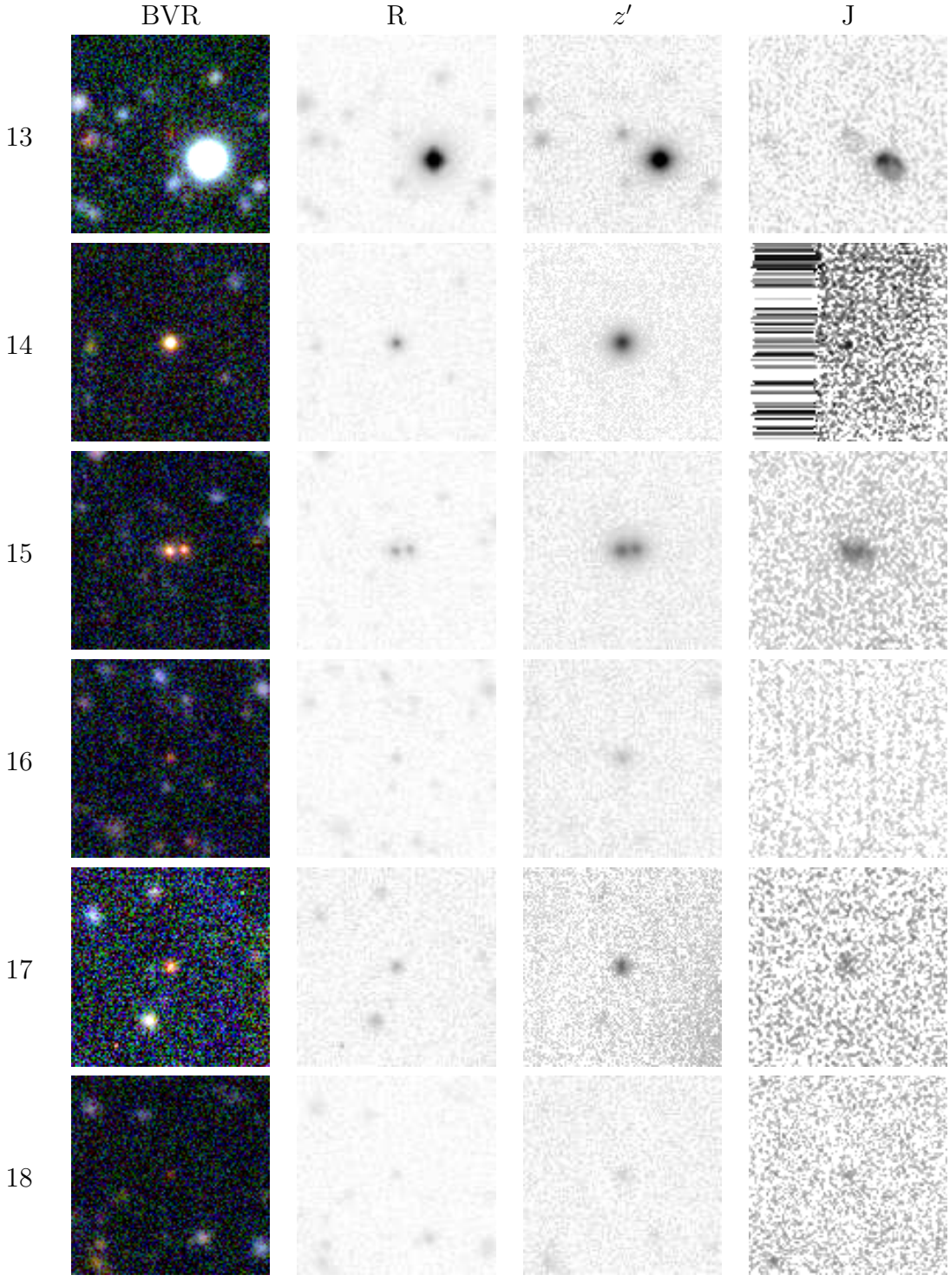

Figure 10.10: J-detected QSO candidates. Grayscale images are normalized such that Vega would appear the same brightness in all three bands.

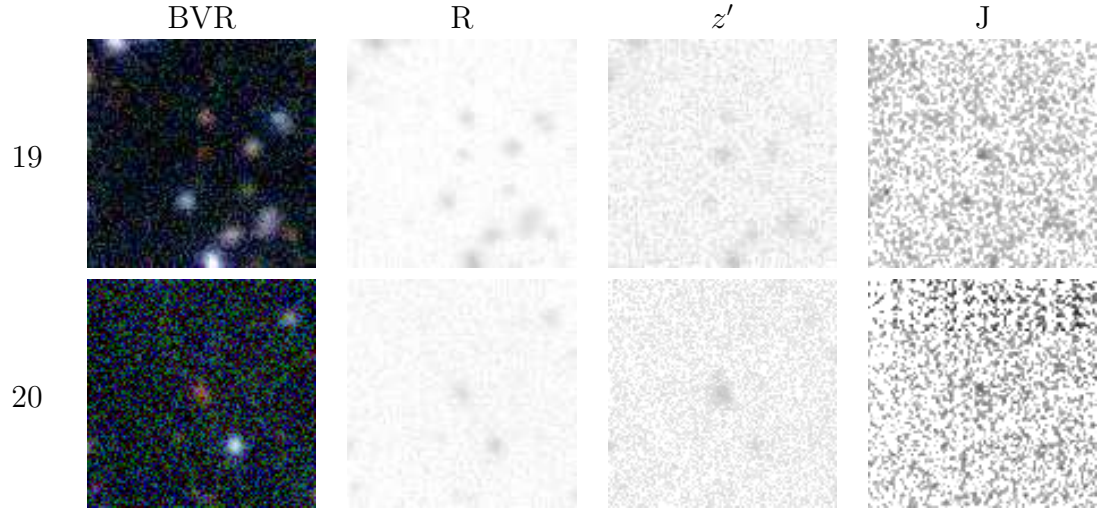

Figure 10.11: J-detected QSO candidates. Grayscale images are normalized such that Vega would appear the same brightness in all three bands.

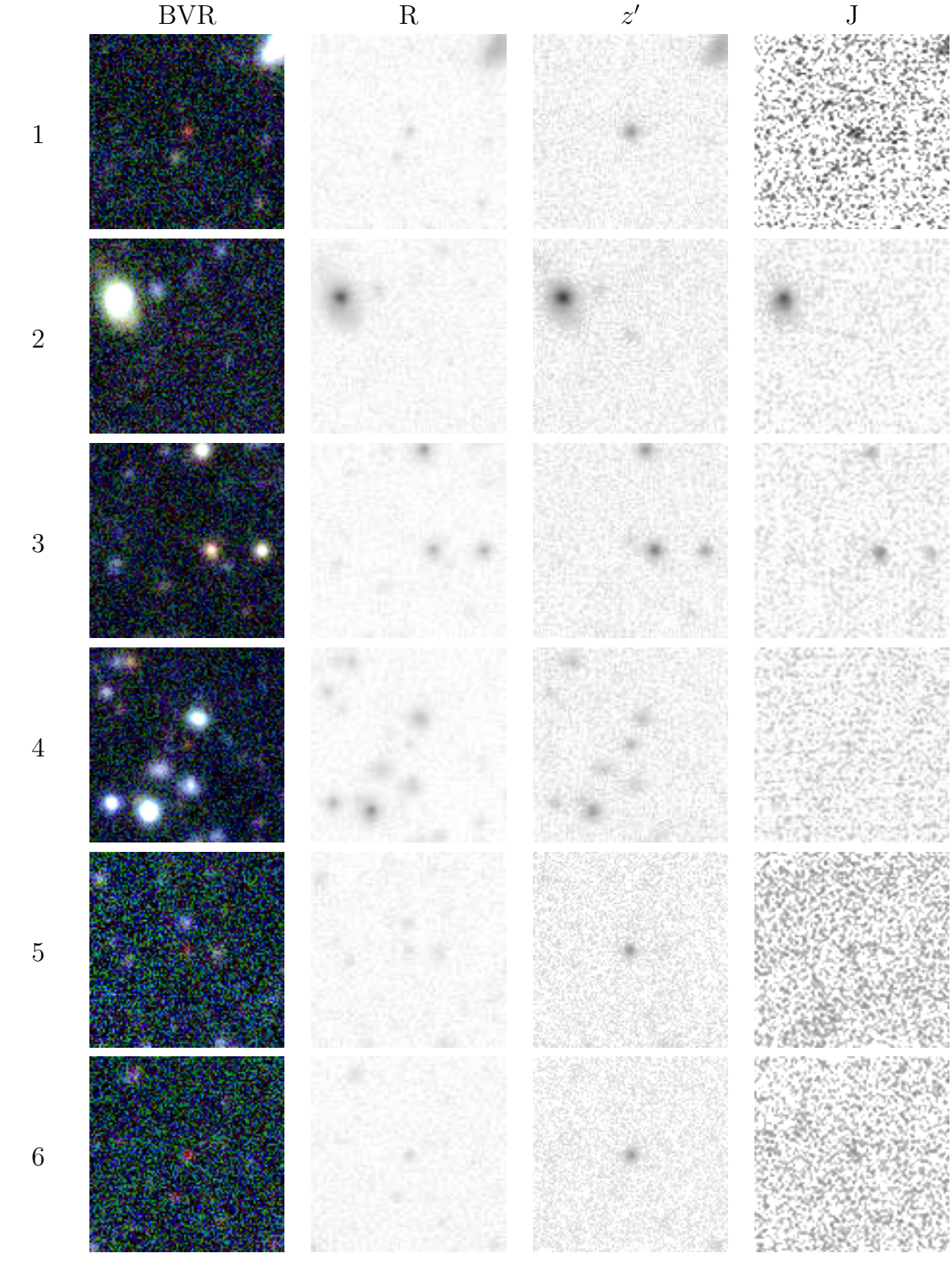

Figure 10.12: J-dropout QSO candidates. Grayscale images are normalized such that Vega would appear the same brightness in all three bands.

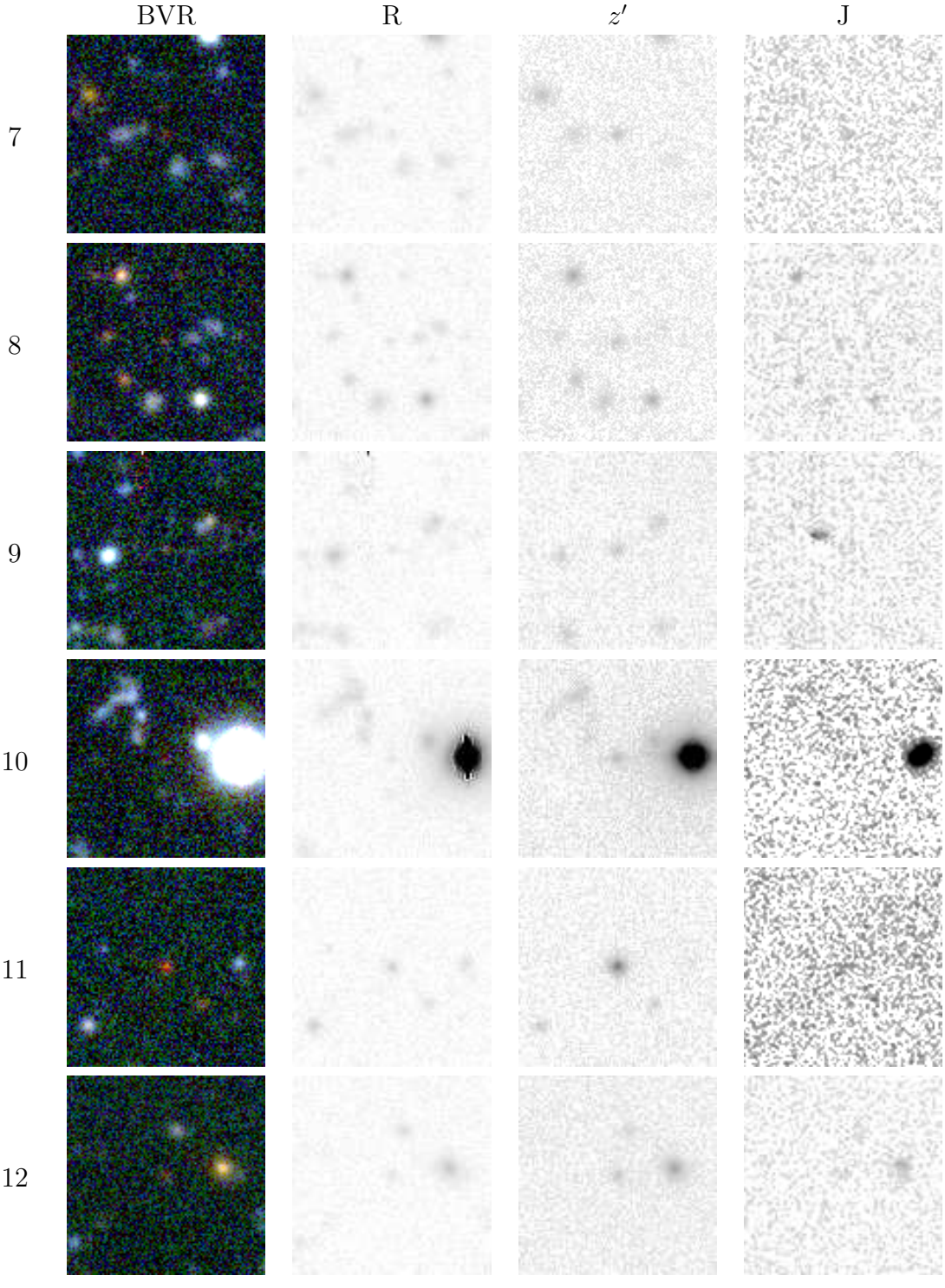

Figure 10.13: J-dropout QSO candidates. Grayscale images are normalized such that Vega would appear the same brightness in all three bands.

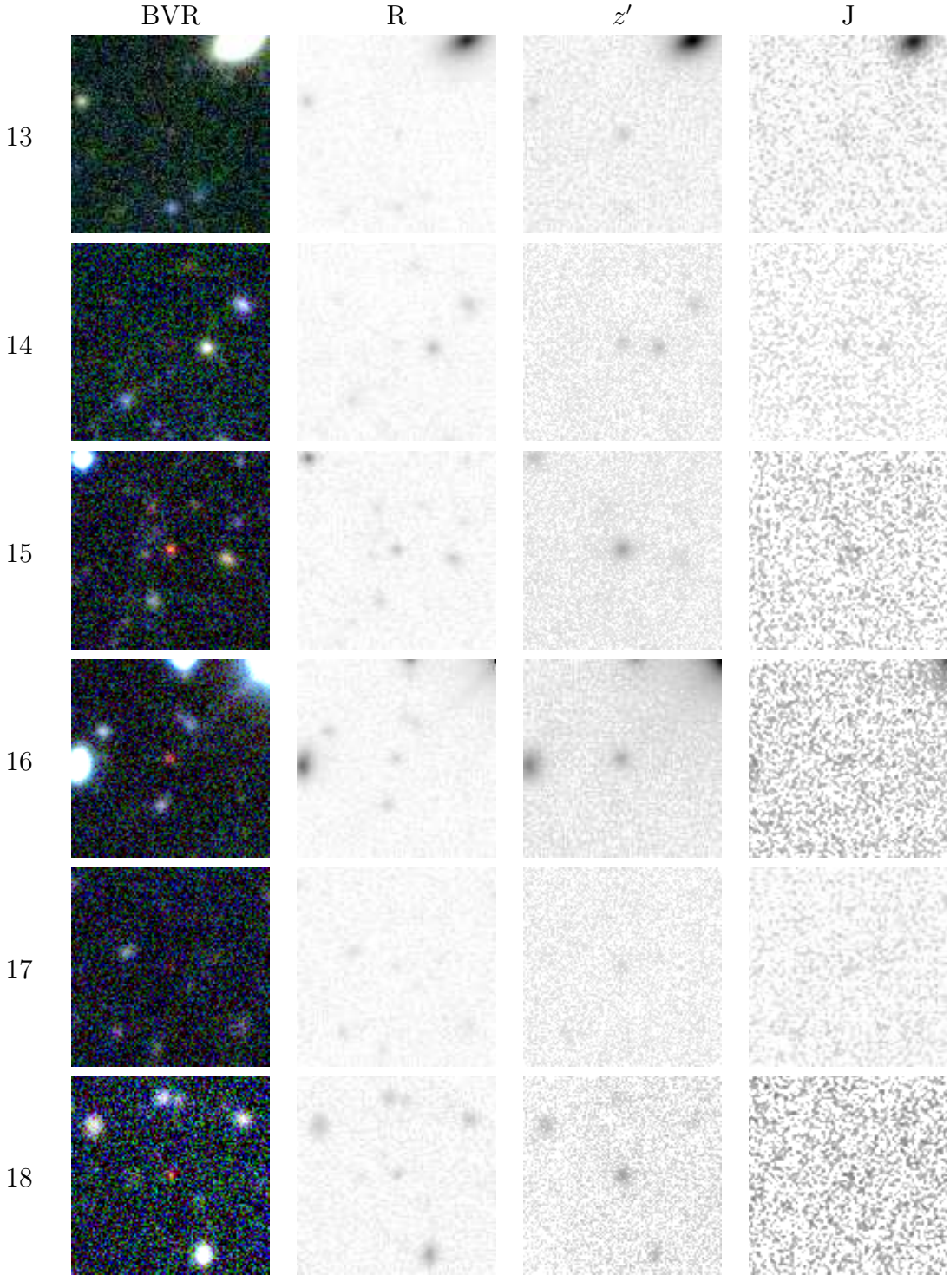

Figure 10.14: J-dropout QSO candidates. Grayscale images are normalized such that Vega would appear the same brightness in all three bands.

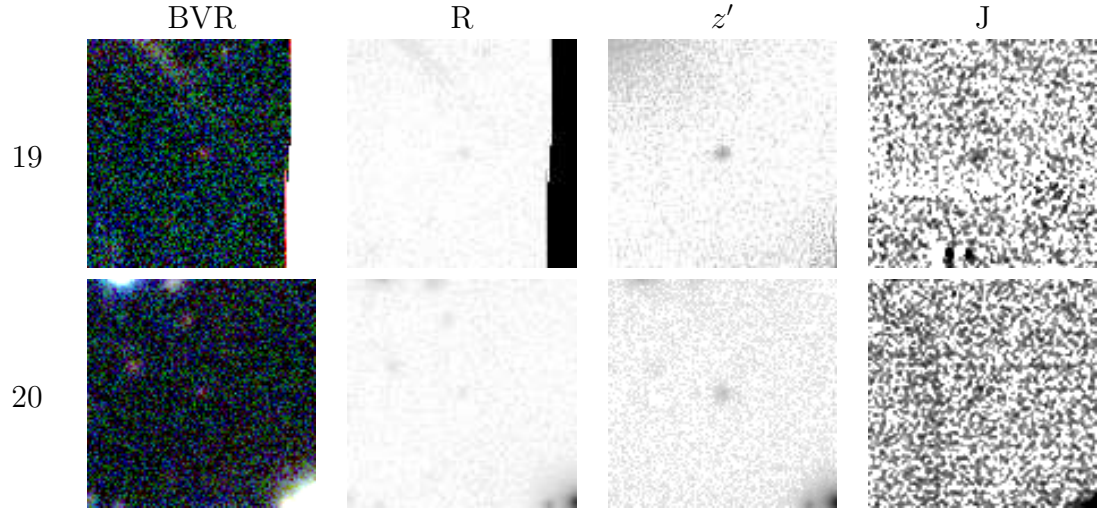

Figure 10.15: J-dropout QSO candidates. Grayscale images are normalized such that Vega would appear the same brightness in all three bands.

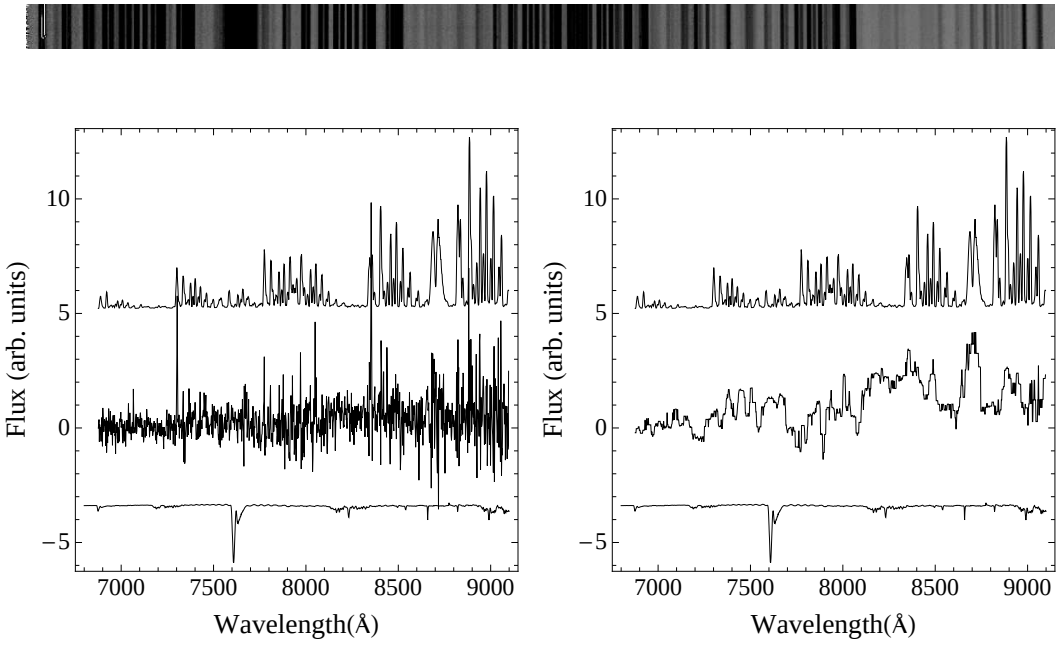

Figure 10.16: HET LRS spectrum of DLSJ0050+1227 (QSO Candidate No. 1). The upper image is the 2-D median-combined spectrum from HET, shown in negative, with red wavelengths to the left. The target spectrum appears as a faint dark band near the center of the image. The extracted spectrum is shown with the sky emission (above) and absorption (below) to indicate regions where the spectrum may be untrustworthy. The spectrum in the right-hand panel has been smoothed with a median filter of width 21 pixels (40Å). Note the characteristic TiO bandheads at 7100Å, 7600Å, and 8400Å, and possible absorption features for CsI and FeH near 8500Å and 8600Å. The absorption features are most consistent with a very late M or early L dwarf, but the relatively shallow red slope of the spectrum may indicate that the weakening of the TiO features is based on low metallicity rather than low temperature.

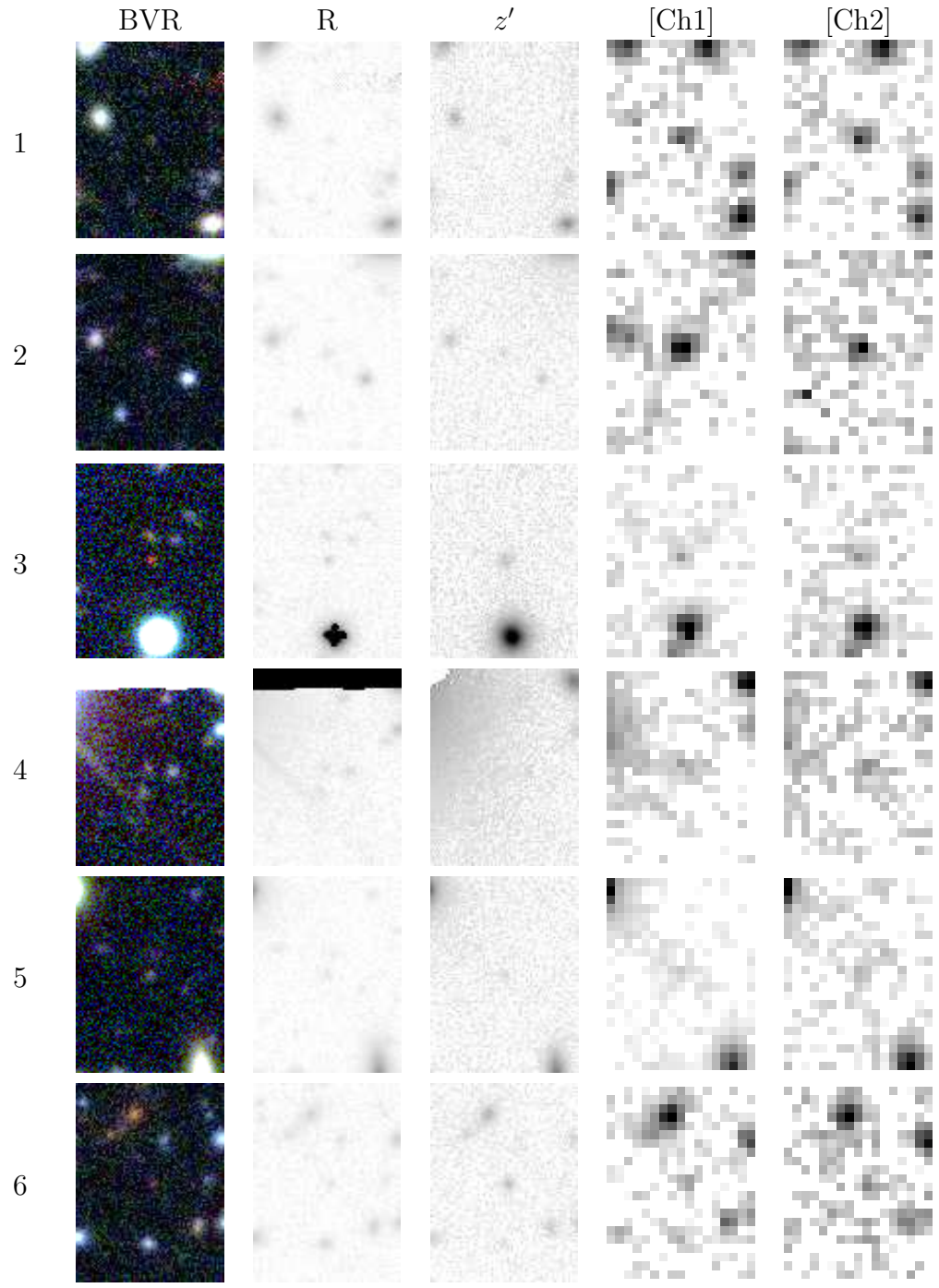

Figure 10.17: F2 QSO candidates, with IRAC 3.6 and 4.5μm imaging.

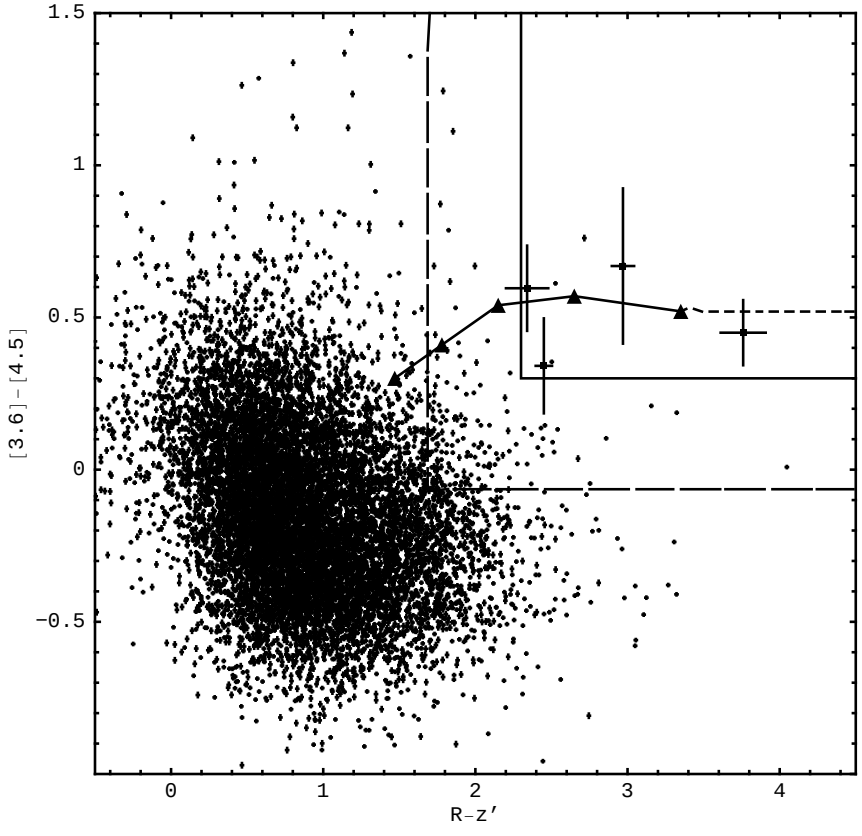

Figure 10.18: Selection criteria for QSO candidates in DLS F2, using IRAC [Ch1] and [Ch2] colors. The dashed line shows the less-stringent selection of Cool et al. (2006), while the solid line shows our selection box. The four points with error bars were submitted as part of a successful spectroscopy proposal, while the solid line with triangles marks the location of the QSO track in this color space, with triangles at 0.1 redshift intervals from 5.3 onward.

Chapter 11

Conclusions and Future Work

11.1 Conclusions

11.1.1 High-z QSOs

We proposed to measure the luminosity function of high-redshift QSOs to nearly unprecedented faintness, using the very deep optical imaging of the Deep Lens Survey as a starting point. By adding J-band imaging, we have created an unusually deep multi-band data set, which has been used to distinguish between cool dwarf stars and high-redshift QSOs. After correcting for systematic effects in the DLS data set, we assigned each visually-confirmed object a probability of belonging to one of our studied object classes. These probabilities were then used in a series of Monte Carlo simulations, to determine the likelihoods of the various underlying model parameters.

The resulting QSO luminosity function is in good agreement with other measurements of the QLF. From the SDSS sample, Jiang et al. (2009) found a bright-end slope of $\beta = -2.9$. We were able to measure a very similar value for the bright-end slope, $\beta = -2.92 \pm 0.92$, by using the binned $1/V_a$ estimator and assuming a single power-law form. Willott et al. (2010) added a fainter QSO sample from CFHTQS, and used a two-parameter model (varying M^* and β) to find a slightly different bright-end slope ($\beta = -2.81$), with a shallow ($\alpha = -1.5$) faint-end slope assumed on the far side of a break in the luminosity function which they found to be located at $M^* = -25.13$. Our own two-parameter fit could not duplicate the finding of a break luminosity (which was also the case for CFHTQS bootstrap resamples lacking their faintest QSO). We measured a best-fit value of $\beta = -3.25$, with 95% confidence limits of $-3.9 < \beta < -2.8$, similar in width to Willott's limits of $-3.8 < \beta < -2.3$. Based on agreement with these earlier results, there is some reason to believe that our probability-based methods are working.

While our results are not dramatically different than earlier studies, one important difference in method should be noted: the luminosity functions of SDSS

and CFHTQS are based on spectroscopically-confirmed QSOs, each one of which represents an investment of multiple hours of 8-m-class telescope spectroscopy (a very precious commodity). Our QLF was calculated based solely on photometric identification from 4 m and 5 m telescopes, with a careful eye on uncertainty and backgrounds, and produced a substantially similar result at significantly less cost in observing time (albeit with higher computational costs and a larger measurement uncertainty than a full spectroscopic survey would have.) As new all-sky surveys made with larger telescopes (e.g. LSST, Pan-STARRS) become available, photometric methods will be the *only* way to analyze large portions of the data set, as spectroscopic follow-up for more than a tiny handful of these extremely faint objects will be impossible for the foreseeable future. It is important to note, however, that our photometric methods have found success largely due to the existence of a photometrically distinctive QSO population, well-characterized with spectra from low-redshift QSOs, and a limited class of interlopers. The computational challenges of carrying out the same type of analysis with a more heterogeneous population, and one that is less well-studied (such as high-redshift galaxies), are still to be overcome. However, it should be possible to select narrow- or medium-band filters for particular future samples as an intermediate step between broad-band imaging and spectroscopy — as we have shown in this project, the addition of a properly chosen filter can sometimes break an existing degeneracy between targets and interlopers in color space.

11.1.2 Cool Dwarfs and Brown Dwarfs

Nearly all of our detected very red ($R - z'$) point objects are surely cool dwarfs and brown dwarfs from our own galaxy, seen along our line of sight out of the galactic disk. By converting existing photometric studies of M, L, and T dwarfs to our filter set, and by convolving published spectra with our response curves, we have generated colors and absolute magnitudes to characterize dwarfs of spectral type M9 and later.

These colors have been used to assign every object a probability of belonging to a given spectral type, and these photometric types have been confirmed both by spectroscopy from HET, and by photometry of cool dwarfs of known type from SDSS and earlier studies. Using the absolute magnitudes and types, we have constructed Monte Carlo realizations of the galaxy, which are compared to our observed data as a function of inferred heliocentric distance to determine the best-fit parameters for the distribution of cool dwarfs and brown dwarfs in the galaxy.

Earlier studies had found that field dwarfs later than M7 were distributed in an exponential disk of scale height $Z_S = 350 \pm 50$ pc (Ryan et al., 2005) or $Z_S = 400 \pm 100$ pc (Pirzkal et al., 2005). However, the lack of spectral type information in the former study and the small number of objects in the latter placed strong limits on how well they could measure the scale height as a function of spectral type. By characterizing a larger area of sky, we have access to more candidates than either study, and our photometric spectral types appear to be accurate to within a few subclasses. With this larger sample, we have measured the scale height of the different spectral types. First, we binned all late types together, as in earlier studies, which resulted in a scale height measurement of $Z_0 = 293^{+106}_{-93}$ pc. We then separated them by spectral type, which resulted in a peak scale height of $Z_0 = 575$ pc for the earliest sample of dwarfs (M9–L2), with the most likely scale heights decreasing for later spectral types: 175 pc for L2–L5 dwarfs, and 91 pc for L5–L9 dwarfs (albeit with large positive error bars).

These tentative measurements of the decreasing scale height with later spectral type could be caused by at least two physical phenomena: the gradual scattering of objects away from the Galactic plane over time (by interactions with giant molecular clouds or other massive structures in the disk), and the increasing odds of such scattering with decreasing mass. The objects in each spectral type bin will be a mixture of old high-mass dwarfs which have only recently cooled to that characteristic temperature and newer low-mass dwarfs which have not yet had a chance to cool to

even later spectral types. The older, high-mass dwarfs are likely to be the dominant population at any given time, as their higher mass leads to longer cooling times. For example, the L5–L9 spectral types should consist mostly of 75 M_J objects formed 2-4 Gyr ago, which have had more time to be scattered away from the Galactic mid-plane than their younger L2–L5 counterparts. Although this differential cooling means that each spectral type will contain objects with a range of masses, each spectral type nevertheless has a minimum mass: the mass of a newly formed object of that type. Because this minimum mass is smaller for cooler spectral types, we would expect cooler spectral types to have a greater equilibrium scale height, as their smaller average masses translate into a higher velocity dispersion at a given kinematic "temperature". This should be the dominant effect only for very cool brown dwarfs, as they are the only population likely to have survived long enough to reach thermal equilibrium with the disk. It is important to note that any spectral type dominated by brown dwarfs is certain to have a younger average age than one that contains mostly hydrogen-burning stars (which could well date back to the formation of the Galaxy), meaning that the decline in scale height should closely follow the crossing of the hydrogen-burning limit.

11.2 Future Work

In addition to the J-band imaging discussed herein, near-IR J- & K-band imaging is now complete on 2 sq. deg. of DLS F2, along with matching K-band imaging over the Palomar WIRC survey J-band imaging area in F1. These new observations will allow our photometric methods to be extended over nearly twice the current area, and the addition of K-band imaging should allow even better rejection of non-QSO interlopers from the QSO sample. The addition of JK imaging to F2, where IRAC imaging is already available, also makes it an excellent data set to search for brown dwarfs, which can be much more accurately typed using $Rz'JK$ colors than with J

alone.

Observing proposals are currently pending to carry out further spectroscopic follow-up with the LRIS spectrograph on Keck, which is a superior instrument for long-integration spectroscopy; to observe the remainder of the DLS in IRAC Channels 1 & 2; and to image the southern DLS in J & K. Successful spectroscopy of high-z QSOs detected in the mid-IR would allow for the sort of precise color modeling that is necessary to produce a photometrically-selected luminosity function for this population.

The photometric calibration of the DLS is also under review, using new techniques pioneered in SDSS (Padmanabhan et al., 2008) to automatically cross-calibrate neighboring subfields using overlapping imaging. Following this process, we will be reviewing and updating the z' response function, and making a more complete data release of the DLS. Once the DLS data are standardized, we plan to create a point-source catalog using more specialized software, which will allow higher-quality proper motion and color searches across the entire DLS. We expect to have thousands of stars of various spectral types available for study, many at very large distances out into the Galactic halo. Studying these distant stellar populations will make possible the modeling and planning necessary to interpret the deep surveys of the future, which will detect, not thousands, but millions of stars and brown dwarfs out into the thick disk and halo, and will need photometric algorithms for classifying them, and models of the Galaxy to interpret them. In this sense, this analysis of very red objects in the Deep Lens Survey can serve as a pilot project for future photometric analyses of LSST and Pan-STARRS over the entire sky — the methods learned from these samples can be extended from our small fields-of-view to the deep all-sky surveys of the future.

References

Adams, W. S. and Joy, A. H.: 1922, ApJ **56**, 242

Allard, F., Hauschildt, P. H., Alexander, D. R., and Starrfield, S.: 1997, ARA&A **35**, 137

Arfken and Weber: 2005, *Mathematical Methods for Physicists*, Elsevier Academic Press, sixth ed. edition

Arp, H.: 1966, *Science* **151**, 1214

Avni, Y. and Bahcall, J. N.: 1980, ApJ **235**, 694

Bahcall, J. N.: 1986, ARA&A **24**, 577

Baraffe, I., Chabrier, G., Barman, T. S., Allard, F., and Hauschildt, P. H.: 2003, A&A **402**, 701

Becklin, E. E. and Zuckerman, B.: 1988, Nature **336**, 656

Bernstein, G. M. and Jarvis, M.: 2002, AJ **123**, 583

Bertin, E. and Arnouts, S.: 1996, A&AS **117**, 393

Bochanski, J. J., Munn, J. A., Hawley, S. L., West, A. A., Covey, K. R., and Schneider, D. P.: 2007, AJ **134**, 2418

Boeshaar, P. C.: 1976, *Ph.D. thesis*, Ohio State Univ., Columbus.

Bouwens, R. J., Illingworth, G. D., Oesch, P. A., Stiavelli, M., van Dokkum, P., Trenti, M., Magee, D., Labbe, I., Franx, M., and Carollo, M.: 2009, *ArXiv e-prints*

Boyle, B. J., Shanks, T., Croom, S. M., Smith, R. J., Miller, L., Loaring, N., and Heymans, C.: 2000, MNRAS **317**, 1014

Boyle, B. J., Shanks, T., and Peterson, B. A.: 1988, MNRAS **235**, 935

Brett, J. M.: 1989, MNRAS **241**, 247

Burgasser, A. J.: 2004, ApJS **155**, 191

Burgasser, A. J., Kirkpatrick, J. D., Liebert, J., and Burrows, A.: 2003, ApJ **594**, 510

Burgasser, A. J., Vrba, F. J., Lépine, S., Munn, J. A., Luginbuhl, C. B., Henden, A. A., Guetter, H. H., and Canzian, B. C.: 2008, ApJ **672**, 1159

Burrows, A., Sudarsky, D., and Hubeny, I.: 2006, ApJ **640**, 1063

Burrows, A., Sudarsky, D., and Lunine, J. I.: 2003, ApJ **596**, 587

Butkevich, A. G., Berdyugin, A. V., and Teerikorpi, P.: 2005, MNRAS **362**, 321

Caballero, J. A., Burgasser, A. J., and Klement, R.: 2008, A&A **488**, 181

Chandrasekhar, S.: 1931, MNRAS **91**, 456

Chiu, K., Fan, X., Leggett, S. K., Golimowski, D. A., Zheng, W., Geballe, T. R., Schneider, D. P., and Brinkmann, J.: 2006, AJ **131**, 2722

Churchill, C. W., Rigby, J. R., Charlton, J. C., and Vogt, S. S.: 1999, ApJS **120**, 51

Clampin, M., Hartig, G. F., Ford, H. C., Sirianni, M., Purdue, G., Walkowicz, L., Golimowski, D. A., Illingworth, G., Blouke, M. M., Lesser, M. P., Burmester, W.,

Kimble, R. A., Sullivan, P., and Krebs, C. A.: 1998, in P. Y. Bely & J. B. Breckinridge (ed.), *Society of Photo-Optical Instrumentation Engineers (SPIE) Conference Series*, Vol. 3356 of *Society of Photo-Optical Instrumentation Engineers (SPIE) Conference Series*, pp 332–337

Coe, D., Benítez, N., Sánchez, S. F., Jee, M., Bouwens, R., and Ford, H.: 2006, AJ **132**, 926

Cohen, J. G., Blandford, R., Hogg, D. W., Pahre, M. A., and Shopbell, P. L.: 1999, ApJ **512**, 30

Colless, M., Dalton, G., Maddox, S., Sutherland, W., Norberg, P., Cole, S., Bland-Hawthorn, J., Bridges, T., Cannon, R., Collins, C., Couch, W., Cross, N., Deeley, K., De Propris, R., Driver, S. P., Efstathiou, G., Ellis, R. S., Frenk, C. S., Glazebrook, K., Jackson, C., Lahav, O., Lewis, I., Lumsden, S., Madgwick, D., Peacock, J. A., Peterson, B. A., Price, I., Seaborne, M., and Taylor, K.: 2001, MNRAS **328**, 1039

Cool, R. J., Kochanek, C. S., Eisenstein, D. J., Stern, D., Brand, K., Brown, M. J. I., Dey, A., Eisenhardt, P. R., Fan, X., Gonzalez, A. H., Green, R. F., Jannuzi, B. T., McKenzie, E. H., Rieke, G. H., Rieke, M., Soifer, B. T., Spinrad, H., and Elston, R. J.: 2006, AJ **132**, 823

Couchman, H. M. P.: 1985, MNRAS **214**, 137

Covey, K. R., Ivezić, Ž., Schlegel, D., Finkbeiner, D., Padmanabhan, N., Lupton, R. H., Agüeros, M. A., Bochanski, J. J., Hawley, S. L., West, A. A., Seth, A., Kimball, A., Gogarten, S. M., Claire, M., Haggard, D., Kaib, N., Schneider, D. P., and Sesar, B.: 2007, AJ **134**, 2398

Croom, S. M., Smith, R. J., Boyle, B. J., Shanks, T., Miller, L., Outram, P. J., and Loaring, N. S.: 2004, MNRAS **349**, 1397

Cruz, K. L., Reid, I. N., Kirkpatrick, J. D., Burgasser, A. J., Liebert, J., Solomon, A. R., Schmidt, S. J., Allen, P. R., Hawley, S. L., and Covey, K. R.: 2007, AJ **133**, 439

Cruz, K. L., Reid, I. N., Liebert, J., Kirkpatrick, J. D., and Lowrance, P. J.: 2003, AJ **126**, 2421

Cushing, M. C., Looper, D., Burgasser, A. J., Kirkpatrick, J. D., Faherty, J., Cruz, K. L., Sweet, A., and Sanderson, R. E.: 2009, ApJ **696**, 986

Cushing, M. C. and Vacca, W. D.: 2006, AJ **131**, 1797

Dahn, C. C., Harris, H. C., Vrba, F. J., Guetter, H. H., Canzian, B., Henden, A. A., Levine, S. E., Luginbuhl, C. B., Monet, A. K. B., Monet, D. G., Pier, J. R., Stone, R. C., Walker, R. L., Burgasser, A. J., Gizis, J. E., Kirkpatrick, J. D., Liebert, J., and Reid, I. N.: 2002, AJ **124**, 1170

de Grijs, R. and Peletier, R. F.: 1997, A&A **320**, L21

Delfosse, X., Tinney, C. G., Forveille, T., Epchtein, N., Bertin, E., Borsenberger, J., Copet, E., de Batz, B., Fouque, P., Kimeswenger, S., Le Bertre, T., Lacombe, F., Rouan, D., and Tiphene, D.: 1997, A&A **327**, L25

Doi, M., Tanaka, M., Fukugita, M., Gunn, J. E., Yasuda, N., Ivezić, Ž., Brinkmann, J., de Haars, E., Kleinman, S. J., Krzesinski, J., and French Leger, R.: 2010, AJ **139**, 1628

Douglas, L. S., Bremer, M. N., Stanway, E. R., Lehnert, M. D., and Clowe, D.: 2009, MNRAS **400**, 561

Eddington, A. S.: 1917, MNRAS **77**, 596

Eisenhardt, P. R., Stern, D., Brodwin, M., Fazio, G. G., Rieke, G. H., Rieke, M. J., Werner, M. W., Wright, E. L., Allen, L. E., Arendt, R. G., Ashby, M. L. N.,

Barmby, P., Forrest, W. J., Hora, J. L., Huang, J., Huchra, J., Pahre, M. A., Pipher, J. L., Reach, W. T., Smith, H. A., Stauffer, J. R., Wang, Z., Willner, S. P., Brown, M. J. I., Dey, A., Jannuzi, B. T., and Tiede, G. P.: 2004, ApJS **154**, 48

Elston, R.: 1998, in A. M. Fowler (ed.), *Society of Photo-Optical Instrumentation Engineers (SPIE) Conference Series*, Vol. 3354 of *Society of Photo-Optical Instrumentation Engineers (SPIE) Conference Series*, pp 404–413

Fan, X., Carilli, C. L., and Keating, B.: 2006, ARA&A **44**, 415

Fan, X., Hennawi, J. F., Richards, G. T., Strauss, M. A., Schneider, D. P., Donley, J. L., Young, J. E., Annis, J., Lin, H., Lampeitl, H., Lupton, R. H., Gunn, J. E., Knapp, G. R., Brandt, W. N., Anderson, S., Bahcall, N. A., Brinkmann, J., Brunner, R. J., Fukugita, M., Szalay, A. S., Szokoly, G. P., and York, D. G.: 2004, AJ **128**, 515

Fan, X., Narayanan, V. K., Lupton, R. H., Strauss, M. A., Knapp, G. R., Becker, R. H., White, R. L., Pentericci, L., Leggett, S. K., Haiman, Z., Gunn, J. E., Ivezić, Ž., Schneider, D. P., Anderson, S. F., Brinkmann, J., Bahcall, N. A., Connolly, A. J., Csabai, I., Doi, M., Fukugita, M., Geballe, T., Grebel, E. K., Harbeck, D., Hennessy, G., Lamb, D. Q., Miknaitis, G., Munn, J. A., Nichol, R., Okamura, S., Pier, J. R., Prada, F., Richards, G. T., Szalay, A., and York, D. G.: 2001a, AJ **122**, 2833

Fan, X., Strauss, M. A., Richards, G. T., Newman, J. A., Becker, R. H., Schneider, D. P., Gunn, J. E., Davis, M., White, R. L., Lupton, R. H., Anderson, Jr., J. E., Annis, J., Bahcall, N. A., Brunner, R. J., Csabai, I., Doi, M., Fukugita, M., Hennessy, G. S., Hindsley, R. B., Ivezić, Ž., Knapp, G. R., McKay, T. A., Munn, J. A., Pier, J. R., Szalay, A. S., and York, D. G.: 2001b, AJ **121**, 31

Fan, X., Strauss, M. A., Schneider, D. P., Becker, R. H., White, R. L., Haiman, Z., Gregg, M., Pentericci, L., Grebel, E. K., Narayanan, V. K., Loh, Y., Richards, G. T., Gunn, J. E., Lupton, R. H., Knapp, G. R., Ivezić, Ž., Brandt, W. N., Collinge, M., Hao, L., Harbeck, D., Prada, F., Schaye, J., Strateva, I., Zakamska, N., Anderson, S., Brinkmann, J., Bahcall, N. A., Lamb, D. Q., Okamura, S., Szalay, A., and York, D. G.: 2003, AJ **125**, 1649

Fukugita, M., Ichikawa, T., Gunn, J. E., Doi, M., Shimasaku, K., and Schneider, D. P.: 1996a, AJ **111**, 1748

Fukugita, M., Ichikawa, T., Gunn, J. E., Doi, M., Shimasaku, K., and Schneider, D. P.: 1996b, AJ **111**, 1748

Gamow, G.: 1938, *Zeitschrift fur Astrophysik* **16**, 113

Geballe, T. R., Knapp, G. R., Leggett, S. K., Fan, X., Golimowski, D. A., Anderson, S., Brinkmann, J., Csabai, I., Gunn, J. E., Hawley, S. L., Hennessy, G., Henry, T. J., Hill, G. J., Hindsley, R. B., Ivezić, Ž., Lupton, R. H., McDaniel, A., Munn, J. A., Narayanan, V. K., Peng, E., Pier, J. R., Rockosi, C. M., Schneider, D. P., Smith, J. A., Strauss, M. A., Tsvetanov, Z. I., Uomoto, A., York, D. G., and Zheng, W.: 2002, ApJ **564**, 466

Geballe, T. R., Kulkarni, S. R., Woodward, C. E., and Sloan, G. C.: 1996, ApJ **467**, L101+

Ginzburg, V. L. and Ozernoi, L. M.: 1966, *Soviet Astronomy* **9**, 726

Gizis, J. E., Monet, D. G., Reid, I. N., Kirkpatrick, J. D., Liebert, J., and Williams, R. J.: 2000, AJ **120**, 1085

Golimowski, D. A., Burrows, C. J., Kulkarni, S. R., Oppenheimer, B. R., and Brukardt, R. A.: 1998, AJ **115**, 2579

Golimowski, D. A., Henry, T. J., Krist, J. E., Dieterich, S., Ford, H. C., Illingworth, G. D., Ardila, D. R., Clampin, M., Franz, O. G., Wasserman, L. H., Benedict, G. F., McArthur, B. E., and Nelan, E. G.: 2004, AJ **128**, 1733

Gunn, J. E., Carr, M., Rockosi, C., Sekiguchi, M., Berry, K., Elms, B., de Haas, E., Ivezić, Ž., Knapp, G., Lupton, R., Pauls, G., Simcoe, R., Hirsch, R., Sanford, D., Wang, S., York, D., Harris, F., Annis, J., Bartozek, L., Boroski, W., Bakken, J., Haldeman, M., Kent, S., Holm, S., Holmgren, D., Petravick, D., Prosapio, A., Rechenmacher, R., Doi, M., Fukugita, M., Shimasaku, K., Okada, N., Hull, C., Siegmund, W., Mannery, E., Blouke, M., Heidtman, D., Schneider, D., Lucinio, R., and Brinkman, J.: 1998, AJ **116**, 3040

Gunn, J. E. and Peterson, B. A.: 1965, ApJ **142**, 1633

Hayashi, C. and Nakano, T.: 1963, *Progress of Theoretical Physics* **30**, 460

Hertzsprung, E.: 1910, *Astronomische Nachrichten* **185**, 89

High, F. W., Stubbs, C. W., Rest, A., Stalder, B., and Challis, P.: 2009, AJ **138**, 110

Hill, G. J., Nicklas, H. E., MacQueen, P. J., Tejada, C., Cobos Duenas, F. J., and Mitsch, W.: 1998, in S. D'Odorico (ed.), *Society of Photo-Optical Instrumentation Engineers (SPIE) Conference Series*, Vol. 3355 of *Society of Photo-Optical Instrumentation Engineers (SPIE) Conference Series*, pp 375–386

Hogg, D. W.: 1999, *ArXiv Astrophysics e-prints*

Hogg, D. W., Baldry, I. K., Blanton, M. R., and Eisenstein, D. J.: 2002a, *ArXiv Astrophysics e-prints*

Hogg, D. W., Baldry, I. K., Blanton, M. R., and Eisenstein, D. J.: 2002b, *ArXiv Astrophysics e-prints*

Hopkins, P. F., Hernquist, L., Cox, T. J., Robertson, B., Di Matteo, T., and Springel, V.: 2006, ApJ **639**, 700

Hora, J. L., Fazio, G. G., Willner, S. P., Ashby, M. L., Huang, J., Megeath, S. T., Stauffer, J. R., Tollestrup, E. V., Wang, Z., Glaccum, W. J., Pipher, J. L., Forrest, W. J., McCreight, C. R., McKelvey, M. E., Hoffman, W. F., Eisenhardt, P., Surace, J. A., Reach, W. T., Moseley, S. H., Arendt, R. G., Stewart, K. P., and Robinson, F. D.: 2000, in M. Strojnik & B. F. Andresen (ed.), *Society of Photo-Optical Instrumentation Engineers (SPIE) Conference Series*, Vol. 4131 of *Society of Photo-Optical Instrumentation Engineers (SPIE) Conference Series*, pp 13–25

Jao, W., Henry, T. J., Beaulieu, T. D., and Subasavage, J. P.: 2008, AJ **136**, 840

Jiang, L., Fan, X., Bian, F., Annis, J., Chiu, K., Jester, S., Lin, H., Lupton, R. H., Richards, G. T., Strauss, M. A., Malanushenko, V., Malanushenko, E., and Schneider, D. P.: 2009, AJ **138**, 305

Jiang, L., Fan, X., Ivezić, Ž., Richards, G. T., Schneider, D. P., Strauss, M. A., and Kelly, B. C.: 2007, ApJ **656**, 680

Jurić, M., Ivezić, Ž., Brooks, A., Lupton, R. H., Schlegel, D., Finkbeiner, D., Padmanabhan, N., Bond, N., Sesar, B., Rockosi, C. M., Knapp, G. R., Gunn, J. E., Sumi, T., Schneider, D. P., Barentine, J. C., Brewington, H. J., Brinkmann, J., Fukugita, M., Harvanek, M., Kleinman, S. J., Krzesinski, J., Long, D., Neilsen, Jr., E. H., Nitta, A., Snedden, S. A., and York, D. G.: 2008, ApJ **673**, 864

Kaiser, N., Aussel, H., Burke, B. E., Boesgaard, H., Chambers, K., Chun, M. R., Heasley, J. N., Hodapp, K., Hunt, B., Jedicke, R., Jewitt, D., Kudritzki, R., Luppino, G. A., Maberry, M., Magnier, E., Monet, D. G., Onaka, P. M., Pickles, A. J., Rhoads, P. H. H., Simon, T., Szalay, A., Szapudi, I., Tholen, D. J., Tonry, J. L., Waterson, M., and Wick, J.: 2002, in J. A. Tyson & S. Wolff (ed.), *Society of Photo-Optical Instrumentation Engineers (SPIE) Conference Series*, Vol. 4836

of *Society of Photo-Optical Instrumentation Engineers (SPIE) Conference Series*, pp 154–164

Kakazu, Y. K. M.: 2008, *Ph.D. thesis*, University of Hawai'i at Manoa

Kaufman, M.: 1965, Nature **207**, 736

Kirkpatrick, J. D., Beichman, C. A., and Skrutskie, M. F.: 1997, ApJ **476**, 311

Kirkpatrick, J. D., Henry, T. J., and Liebert, J.: 1993, ApJ **406**, 701

Kirkpatrick, J. D., Reid, I. N., Liebert, J., Cutri, R. M., Nelson, B., Beichman, C. A., Dahn, C. C., Monet, D. G., Gizis, J. E., and Skrutskie, M. F.: 1999, ApJ **519**, 802

Kirkpatrick, J. D., Reid, I. N., Liebert, J., Gizis, J. E., Burgasser, A. J., Monet, D. G., Dahn, C. C., Nelson, B., and Williams, R. J.: 2000, AJ **120**, 447

Knapp, G. R., Leggett, S. K., Fan, X., Marley, M. S., Geballe, T. R., Golimowski, D. A., Finkbeiner, D., Gunn, J. E., Hennawi, J., Ivezić, Z., Lupton, R. H., Schlegel, D. J., Strauss, M. A., Tsvetanov, Z. I., Chiu, K., Hoversten, E. A., Glazebrook, K., Zheng, W., Hendrickson, M., Williams, C. C., Uomoto, A., Vrba, F. J., Henden, A. A., Luginbuhl, C. B., Guetter, H. H., Munn, J. A., Canzian, B., Schneider, D. P., and Brinkmann, J.: 2004, AJ **127**, 3553

Kron, R. G.: 1980, ApJS **43**, 305

Kuiper, G. P.: 1939, ApJ **89**, 548

Kulkarni, S. R. and Rau, A.: 2006, ApJ **644**, L63

Kumar, S. S.: 1963, ApJ **137**, 1121

Kurucz, R. L.: 1970, *SAO Special Report* 309

Landolt, A. U.: 1992, AJ **104**, 340

Leggett, S. K., Allard, F., Geballe, T. R., Hauschildt, P. H., and Schweitzer, A.: 2001, ApJ **548**, 908

Leggett, S. K., Toomey, D. W., Geballe, T. R., and Brown, R. H.: 1999, ApJ **517**, L139

Liebert, J., Kron, R. G., and Spinrad, H.: 1978, PASP **90**, 718

Madau, P., Haardt, F., and Rees, M. J.: 1999, ApJ **514**, 648

Marshall, H. L., Tananbaum, H., Avni, Y., and Zamorani, G.: 1983, ApJ **269**, 35

Martín, E. L., Delfosse, X., Basri, G., Goldman, B., Forveille, T., and Zapatero Osorio, M. R.: 1999, AJ **118**, 2466

Matthews, K. and Soifer, B. T.: 1994, *Experimental Astronomy* **3**, 77

Matthews, T. A. and Sandage, A. R.: 1963, ApJ **138**, 30

McLean, I. S., McGovern, M. R., Burgasser, A. J., Kirkpatrick, J. D., Prato, L., and Kim, S. S.: 2003, ApJ **596**, 561

McLure, R. J., Dunlop, J. S., Cirasuolo, M., Koekemoer, A. M., Sabbi, E., Stark, D. P., Targett, T. A., and Ellis, R. S.: 2009, *ArXiv e-prints*

Metchev, S. A., Kirkpatrick, J. D., Berriman, G. B., and Looper, D.: 2008, ApJ **676**, 1281

Nakajima, T., Oppenheimer, B. R., Kulkarni, S. R., Golimowski, D. A., Matthews, K., and Durrance, S. T.: 1995, Nature **378**, 463

Noll, K. S., Geballe, T. R., Leggett, S. K., and Marley, M. S.: 2000, ApJ **541**, L75

Oke, J. B.: 1972, *Journal of the Optical Society of America (1917-1983)* **62**, 1342

Oort, J. H.: 1926, *Publications of the Kapteyn Astronomical Laboratory Groningen* **40**, 1

Oort, J. H.: 1952, ApJ **116**, 233

Oppenheimer, B. R., Kulkarni, S. R., Matthews, K., and Nakajima, T.: 1995, *Science* **270**, 1478

Oppenheimer, B. R., Kulkarni, S. R., Matthews, K., and van Kerkwijk, M. H.: 1998, ApJ **502**, 932

Padmanabhan, N., Schlegel, D. J., Finkbeiner, D. P., Barentine, J. C., Blanton, M. R., Brewington, H. J., Gunn, J. E., Harvanek, M., Hogg, D. W., Ivezić, Ž., Johnston, D., Kent, S. M., Kleinman, S. J., Knapp, G. R., Krzesinski, J., Long, D., Neilsen, Jr., E. H., Nitta, A., Loomis, C., Lupton, R. H., Roweis, S., Snedden, S. A., Strauss, M. A., and Tucker, D. L.: 2008, ApJ **674**, 1217

Page, M. J. and Carrera, F. J.: 2000, MNRAS **311**, 433

Patten, B. M., Stauffer, J. R., Burrows, A., Marengo, M., Hora, J. L., Luhman, K. L., Sonnett, S. M., Henry, T. J., Raghavan, D., Megeath, S. T., Liebert, J., and Fazio, G. G.: 2006, ApJ **651**, 502

Pei, Y. C.: 1995, ApJ **438**, 623

Pickles, A. J.: 1997, *VizieR Online Data Catalog* **7102**, 0

Pirzkal, N., Sahu, K. C., Burgasser, A., Moustakas, L. A., Xu, C., Malhotra, S., Rhoads, J. E., Koekemoer, A. M., Nelan, E. P., Windhorst, R. A., Panagia, N., Gronwall, C., Pasquali, A., and Walsh, J. R.: 2005, ApJ **622**, 319

Porcel, C., Garzon, F., Jimenez-Vicente, J., and Battaner, E.: 1998, A&A **330**, 136

Rajkanan, K., Singh, R., and Shewchun, J.: 1979, *Solid State Electronics* **22**, 793

Reid, I. N., Burgasser, A. J., Cruz, K. L., Kirkpatrick, J. D., and Gizis, J. E.: 2001, AJ **121**, 1710

Reid, I. N. and Hawley, S. L.: 2005, *New light on dark stars : red dwarfs, low-mass stars, brown dwarfs*, Praxis

Reid, I. N., Kirkpatrick, J. D., Gizis, J. E., Dahn, C. C., Monet, D. G., Williams, R. J., Liebert, J., and Burgasser, A. J.: 2000, AJ **119**, 369

Reid, I. N., Kirkpatrick, J. D., Liebert, J., Burrows, A., Gizis, J. E., Burgasser, A., Dahn, C. C., Monet, D., Cutri, R., Beichman, C. A., and Skrutskie, M.: 1999, ApJ **521**, 613

Richards, G. T., Deo, R. P., Lacy, M., Myers, A. D., Nichol, R. C., Zakamska, N. L., Brunner, R. J., Brandt, W. N., Gray, A. G., Parejko, J. K., Ptak, A., Schneider, D. P., Storrie-Lombardi, L. J., and Szalay, A. S.: 2009a, AJ **137**, 3884

Richards, G. T., Myers, A. D., Gray, A. G., Riegel, R. N., Nichol, R. C., Brunner, R. J., Szalay, A. S., Schneider, D. P., and Anderson, S. F.: 2009b, ApJS **180**, 67

Richards, G. T., Strauss, M. A., Fan, X., Hall, P. B., Jester, S., Schneider, D. P., Vanden Berk, D. E., Stoughton, C., Anderson, S. F., Brunner, R. J., Gray, J., Gunn, J. E., Ivezić, Ž., Kirkland, M. K., Knapp, G. R., Loveday, J., Meiksin, A., Pope, A., Szalay, A. S., Thakar, A. R., Yanny, B., York, D. G., Barentine, J. C., Brewington, H. J., Brinkmann, J., Fukugita, M., Harvanek, M., Kent, S. M., Kleinman, S. J., Krzesiński, J., Long, D. C., Lupton, R. H., Nash, T., Neilsen, Jr., E. H., Nitta, A., Schlegel, D. J., and Snedden, S. A.: 2006, AJ **131**, 2766

Ruiz, M. T., Leggett, S. K., and Allard, F.: 1997, ApJ **491**, L107+

Russell, H. N.: 1910, AJ **26**, 147

Ryan, Jr., R. E., Hathi, N. P., Cohen, S. H., and Windhorst, R. A.: 2005, ApJ **631**, L159

Sandage, A.: 1965, ApJ **141**, 1560

Schmidt, M.: 1963, Nature **197**, 1040

Schmidt, M.: 1968, ApJ **151**, 393

Schmidt, S. J.: 2007, *Ph.D. thesis*, AA(University of Pittsburgh)

Schweitzer, A., Hauschildt, P. H., Allard, F., and Basri, G.: 1996, MNRAS **283**, 821

Scientific Imaging Technologies Inc.: 1995, *Literature No. ST-002A*, 12/21/95 edition, Retrieved from http://www.ociw.edu/instrumentation/ccd/parts/ST-002a.pdf

Seyfert, C. K.: 1943, ApJ **97**, 28

Siana, B., Polletta, M. d. C., Smith, H. E., Lonsdale, C. J., Gonzalez-Solares, E., Farrah, D., Babbedge, T. S. R., Rowan-Robinson, M., Surace, J., Shupe, D., Fang, F., Franceschini, A., and Oliver, S.: 2008, ApJ **675**, 49

Songaila, A.: 2004, AJ **127**, 2598

Stephens, D. C. and Leggett, S. K.: 2004, PASP **116**, 9

Stockton, A., Wyckoff, S., and Wehinger, P. A.: 1979, ApJ **231**, 673

Strauss, M. A., Fan, X., Gunn, J. E., Leggett, S. K., Geballe, T. R., Pier, J. R., Lupton, R. H., Knapp, G. R., Annis, J., Brinkmann, J., Crocker, J. H., Csabai, I., Fukugita, M., Golimowski, D. A., Harris, F. H., Hennessy, G. S., Hindsley, R. B., Ivezić , Ž., Kent, S., Lamb, D. Q., Munn, J. A., Newberg, H. J., Rechenmacher, R., Schneider, D. P., Smith, J. A., Stoughton, C., Tucker, D. L., Waddell, P., and York, D. G.: 1999, ApJ **522**, L61

Sunyaev, R. A., Tinsley, B. M., and Meier, D. L.: 1978, *Comments on Astrophysics* **7**, 183

Tinney, C. G., Delfosse, X., Forveille, T., and Allard, F.: 1998, A&A **338**, 1066

Tsvetanov, Z. I., Golimowski, D. A., Zheng, W., Geballe, T. R., Leggett, S. K., Ford, H. C., Davidsen, A. F., Uomoto, A., Fan, X., Knapp, G. R., Strauss, M. A., Brinkmann, J., Lamb, D. Q., Newberg, H. J., Rechenmacher, R., Schneider, D. P., York, D. G., Lupton, R. H., Pier, J. R., Annis, J., Csabai, I., Hindsley, R. B., Ivesić, Ž., Munn, J. A., Thakar, A. R., and Waddell, P.: 2000, ApJ **531**, L61

Tyson, J. A.: 2002, in J. A. Tyson & S. Wolff (ed.), *Society of Photo-Optical Instrumentation Engineers (SPIE) Conference Series*, Vol. 4836 of *Society of Photo-Optical Instrumentation Engineers (SPIE) Conference Series*, pp 10–20

Tyson, J. A., Baum, W. A., and Kreidl, T.: 1982, ApJ **257**, L1

Vanden Berk, D. E., Richards, G. T., Bauer, A., Strauss, M. A., Schneider, D. P., Heckman, T. M., York, D. G., Hall, P. B., Fan, X., Knapp, G. R., Anderson, S. F., Annis, J., Bahcall, N. A., Bernardi, M., Briggs, J. W., Brinkmann, J., Brunner, R., Burles, S., Carey, L., Castander, F. J., Connolly, A. J., Crocker, J. H., Csabai, I., Doi, M., Finkbeiner, D., Friedman, S., Frieman, J. A., Fukugita, M., Gunn, J. E., Hennessy, G. S., Ivezić, Ž., Kent, S., Kunszt, P. Z., Lamb, D. Q., Leger, R. F., Long, D. C., Loveday, J., Lupton, R. H., Meiksin, A., Merelli, A., Munn, J. A., Newberg, H. J., Newcomb, M., Nichol, R. C., Owen, R., Pier, J. R., Pope, A., Rockosi, C. M., Schlegel, D. J., Siegmund, W. A., Smee, S., Snir, Y., Stoughton, C., Stubbs, C., SubbaRao, M., Szalay, A. S., Szokoly, G. P., Tremonti, C., Uomoto, A., Waddell, P., Yanny, B., and Zheng, W.: 2001, AJ **122**, 549

Varshni, Y. P.: 1967, *Physica* **34**, 149

Weymann, R.: 1967, ApJ **147**, 887

Willott, C. J., Delfosse, X., Forveille, T., Delorme, P., and Gwyn, S. D. J.: 2005, ApJ **633**, 630

Willott, C. J., Delorme, P., Omont, A., Bergeron, J., Delfosse, X., Forveille, T., Albert, L., Reylé, C., Hill, G. J., Gully-Santiago, M., Vinten, P., Crampton, D.,

Hutchings, J. B., Schade, D., Simard, L., Sawicki, M., Beelen, A., and Cox, P.: 2007, AJ **134**, 2435

Willott, C. J., Delorme, P., Reylé, C., Albert, L., Bergeron, J., Crampton, D., Delfosse, X., Forveille, T., Hutchings, J. B., McLure, R. J., Omont, A., and Schade, D.: 2009, AJ **137**, 3541

Willott, C. J., Delorme, P., Reylé, C., Albert, L., Bergeron, J., Crampton, D., Delfosse, X., Forveille, T., Hutchings, J. B., McLure, R. J., Omont, A., and Schade, D.: 2010, AJ **139**, 906

Wilson, J. C., Eikenberry, S. S., Henderson, C. P., Hayward, T. L., Carson, J. C., Pirger, B., Barry, D. J., Brandl, B. R., Houck, J. R., Fitzgerald, G. J., and Stolberg, T. M.: 2003, in M. Iye & A. F. M. Moorwood (ed.), *Society of Photo-Optical Instrumentation Engineers (SPIE) Conference Series*, Vol. 4841 of *Society of Photo-Optical Instrumentation Engineers (SPIE) Conference Series*, pp 451–458

Wilson, J. C., Kirkpatrick, J. D., Gizis, J. E., Skrutskie, M. F., Monet, D. G., and Houck, J. R.: 2001, AJ **122**, 1989

Wittman, D., Dell'Antonio, I. P., Hughes, J. P., Margoniner, V. E., Tyson, J. A., Cohen, J. G., and Norman, D.: 2006, ApJ **643**, 128

Wyckoff, S., Gehren, T., Morton, D. C., Albrecht, R., Wehinger, P. A., and Boksenberg, A.: 1980, ApJ **242**, L59